Springer Theses
Recognizing Outstanding Ph.D. Research

Kurt Brendlinger

Physics with Electrons in the ATLAS Detector

Springer

Springer Theses

Recognizing Outstanding Ph.D. Research

Aims and Scope

The series "Springer Theses" brings together a selection of the very best Ph.D. theses from around the world and across the physical sciences. Nominated and endorsed by two recognized specialists, each published volume has been selected for its scientific excellence and the high impact of its contents for the pertinent field of research. For greater accessibility to non-specialists, the published versions include an extended introduction, as well as a foreword by the student's supervisor explaining the special relevance of the work for the field. As a whole, the series will provide a valuable resource both for newcomers to the research fields described, and for other scientists seeking detailed background information on special questions. Finally, it provides an accredited documentation of the valuable contributions made by today's younger generation of scientists.

Theses are accepted into the series by invited nomination only and must fulfill all of the following criteria

- They must be written in good English.
- The topic should fall within the confines of Chemistry, Physics, Earth Sciences, Engineering and related interdisciplinary fields such as Materials, Nanoscience, Chemical Engineering, Complex Systems and Biophysics.
- The work reported in the thesis must represent a significant scientific advance.
- If the thesis includes previously published material, permission to reproduce this must be gained from the respective copyright holder.
- They must have been examined and passed during the 12 months prior to nomination.
- Each thesis should include a foreword by the supervisor outlining the significance of its content.
- The theses should have a clearly defined structure including an introduction accessible to scientists not expert in that particular field.

More information about this series at http://www.springer.com/series/8790

Kurt Brendlinger

Physics with Electrons in the ATLAS Detector

Doctoral Thesis accepted by
The University of Pennsylvania, Philadelphia, USA

Springer

Author
Dr. Kurt Brendlinger
Deutsches Elektronen-Synchrotron DESY
Hamburg
Germany

Supervisor
Prof. I. Joseph Kroll
Department of Physics
The University of Pennsylvania
Philadelphia
USA

ISSN 2190-5053 ISSN 2190-5061 (electronic)
Springer Theses
ISBN 978-3-319-73929-8 ISBN 978-3-319-73930-4 (eBook)
https://doi.org/10.1007/978-3-319-73930-4

Library of Congress Control Number: 2017963012

Printed on acid-free paper

This Springer imprint is published by Springer Nature
The registered company is Springer International Publishing AG
The registered company address is: Gewerbestrasse 11, 6330 Cham, Switzerland

Supervisor's Foreword

The title of this dissertation summarizes concisely the importance of this research. At hadron colliders, charged and neutral leptons with large components of momentum transverse to the beam line originate from the decay of the weak intermediate vector bosons—the $W^{\pm}$ and Z^0—which are the cornerstone of the vast majority of signatures of electroweak standard model processes and physics beyond the standard model (BSM). This dissertation describes the methods used to identify these so-called "prompt" electrons (and their antimatter counterparts positrons) produced in the proton-proton collisions at the Large Hadron Collider (LHC) at CERN in Geneva, Switzerland.

The research was performed using the ATLAS detector, one of two large multipurpose experiments at the LHC. At present, approximately 3000 scientists work on the ATLAS detector; about 1200 of these scientists are Ph.D. candidates from 182 institutions located in 38 countries from six continents. Kurt Brendlinger led the development and implementation of a new method used identify electrons, and he made major contributions to the methods used to measure the efficiency of the electron identification methods and to the techniques used to determine the backgrounds from hadrons mimicking the signature of electrons. His method—known as the "Likelihood identification"—replaced the selection-criteria-based selection, and is now the default electron identification method used in both real-time (or on-line) selection of the most potentially interesting proton-proton collisions and the subsequent off-line analysis of data for physics results. In a collaboration of 3000 physicists, it is still possible for a single individual to have a profound impact on the scientific output of the experiment.

Electrons have a distinct way of interacting in the detector, and the combination of various detector quantities are used to distinguish electrons from more commonly produced charged particles such as pions, kaons and protons, collectively referred to has "hadrons." The distributions of some of these quantities look very different for electrons and hadrons, so much so that it is possible to examine such a distribution and draw a line or "cut:" on one side of the line the distribution is primarily electrons and on the other side of the line the distribution is primarily hadrons.

The "cut" or selection criteria can be used to distinguish electrons from hadrons. The number of hadrons produced exceeds the number of prompt electrons by many orders of magnitude, so a combination of several quantities must be used to ultimately identify electrons. This cut-based method was the basis of the earlier methods of electron identification with the ATLAS detector.

There are many detector quantities for which the distribution of these quantities is different for electrons and hadrons, but not so different that it is straightforward to draw a line that distinguishes the two distributions. The likelihood technique was designed to address this problem. It is based on a product of the probability distributions of these various detector quantities for electrons and hadrons. More quantities can be used in the identification, and the likelihood approach achieves a better separation of the signal electrons from the background hadrons than the cut-based approach. Specifically this means that for a given signal identification efficiency, the likelihood identification achieves better background rejection than the cut-based method, typically a factor of two better rejection.

Kurt used the likelihood in two physics analyses. The first was the measurement of the coupling properties of the newly discovered Higgs boson in the $H \rightarrow ZZ^*$ final state, where the Z bosons decay to either muon-antimuon pairs ($\mu^-\mu^+$) or electron-positron pairs e^-e^+. To maximize the size of the statistically-limited sample of Higgs bosons in this decay mode, the minimum transverse momentum required for the muons and electrons was made as low as possible, where backgrounds become problematic. Introducing the electron likelihood identification reduced the backgrounds to the prompt electrons by a factor of two. This work was carried out using Run 1 data from the LHC, collected at center-of-mass energies of $\sqrt{s} = 7$ TeV (in the year 2011) and $\sqrt{s} = 8$ TeV (in the year 2012).

The second analysis used the first data from Run 2 of the LHC collected at $\sqrt{s} = 13$ TeV in the year 2015. The discovery of a Higgs boson with a mass of 125 GeV opened up several rich avenues of investigation. Perhaps the most important of these avenues is the search for BSM physics that would explain why the Higgs boson has such a small mass. Quantum-mechanical corrections to this mass should push its value to be many orders of magnitude larger than 125 GeV. One of the most popular extensions of the standard model that offers an explanation to this "hierarchy" problem is known as "supersymmetry." In supersymmetry, each known boson and fermion in the standard model has a supersymmetric partner that is a fermion or a boson, respectively. The gauge bosons and the Higgs boson have supersymmetric partners known as "gauginos," and one of the most important signatures of the production of gauginos is the production of $W^{\pm}Z^0$ boson pairs. There is also standard model production of $W^{\pm}Z^0$, which forms the most important background to these particular gaugino searches.

Insufficient data was collected in 2015 to make improvements on limits on gaugino production from Run 1 data at the LHC. However, at the new center-of-mass energy, it was imperative to measure the standard model production rate of $W^{\pm}Z^0$ boson pairs to quantify the expected contribution of this background in searches for supersymmetry. Kurt was one of the main contributors to this analysis.

Along with developing an expertise in electron identification, he also became a leading specialist in determining the rate of background hadrons contributing to the prompt electron signature. This work led to the first publication of the standard model $W^{\pm}Z^0$ boson pair production cross section in proton-proton collisions at $\sqrt{s} = 13$ TeV.

Kurt's dissertation includes chapters on two other major pieces of work. As I mentioned above, he was not only the leader in developing and implementing the likelihood identification of electrons, he was also a major player in developing improved methods to measure the efficiencies for identifying electrons using $Z^0 \rightarrow e^- e^+$ decays reconstructed in the data collected by the ATLAS detector. In particular he led the improvement of the systematic uncertainties associated with these efficiencies. Improvements in these systematics directly impact the precision of, for example, cross-section measurements that are based on prompt electrons as part of their experimental signatures.

Finally at the beginning of his tenure as a graduate student, Kurt also contributed to the operations of the ATLAS detector by working on the alignment of one of the three components of the ATLAS tracking detector or Inner Detector (ID). Specifically he worked on the alignment of the Transition Radiation Tracker or TRT, a tracking drift chamber constructed out of tubular drift-tubes (straws). The University of Pennsylvania was a leading institution in the design, production and commissioning of the 350,000 channels of on-detector electronics that read out and process the electronic signals from the TRT. It was a natural place for us to participate in the ID alignment.

The alignment refers to the process by which the precise locations of the various individual components of the ID is determined using the data. It is performed in stages. The initial stage focuses on large collections of detector elements, and then proceeds to align smaller and smaller collections of detector elements. The TRT alignment first adjusts the barrel and end cap detectors as whole rigid units; then it adjusts the 96 modules in the barrel and 80 wheels in the two endcaps. Kurt's contribution was to implement a third level of alignment that focused on the individual straws. This involved about 720,000 degrees of freedom—three orders of magnitude larger than the second stage of TRT alignment. The result is an average knowledge of the position of the individual straws to a level of about 100 μm, which is quite remarkable considering that the overall scale of the ATLAS detector is tens of meters!

The length of this *Foreword* is a testament to the large number of areas where Kurt contributed to the ATLAS experiment: detector operations, the building blocks of physics analysis, and two physics results that were central to the flagship measurements of the ATLAS experiment and the entire LHC physics program. The dissertation documents these contributions thoroughly and at a level that should be accessible to beginning graduate students in particle physics.

Philadelphia, USA I. Joseph Kroll
November 2017

Abstract

This thesis presents two diboson measurements with the ATLAS experiment. The first is a differential measurement of Higgs boson observables in the four-lepton decay channel at $\sqrt{s} = 8$ TeV. The second presents a first measurement of the *WZ* diboson production cross section in the three-lepton decay channel at $\sqrt{s} = 13$ TeV. Special emphasis is given to the identification techniques of prompt electrons, particularly the likelihood identification first introduced in 2012 data taking, and electron efficiency measurements in the ATLAS detector.

Preface

This thesis presents my work on ATLAS from July 2010 to March 2016. The central theme of my work was physics with electrons.

As a new member of the ATLAS collaboration I undertook a specific task to earn the right to be an author of publication, a process we call "qualification." My qualification task involved the alignment of the straws of the Transition Radiation Tracker, one of three subdetectors that compose the ATLAS Inner Detector (ID). The ID is used to reconstruct the trajectories of charged particles. Together with the ATLAS superconducting solenoid they form the spectrometer that is used to determine the trajectories and momentum of charged particles produced in the collision. The alignment of the TRT detector elements is a key ingredient for ensuring a precise momentum measurement. This was a natural place for me to get involved in ATLAS since the ATLAS group at the University of Pennsylvania played a leading role in the design, production, installation, and commissioning of the read-out electronics for the TRT.

The identification of electrons is a primary task of any general-purpose detector at a particle collider. Electrons are used, for example, to identify W and Z bosons through the decays $W \to e\nu$ and $Z \to e^+e^-$ and to search for more massive hypothetical partners of these intermediate vector bosons. The Penn ATLAS group has played a leading role in the identification of electrons and photons, in part because of the group's involvement in the TRT, which plays a critical role in their identification. In Fall 2011, I joined Penn graduate students John Alison and Chris Lester on improving the ATLAS electron identification. We began with the goal of developing a multivariate strategy to improve on the rectangular cut-based selection in use at the time, and settled on a likelihood construction.

Around this time, hints of a Higgs boson signal around 125 GeV were appearing. ATLAS and CMS reported modest excesses of events in the 115–130 GeV mass range in a public seminar in December 2011. By July the following year, the discovery of the Higgs boson with a mass of around 125 GeV was announced, energizing the field. The relatively low mass of the Higgs means that its decays via WW^* and ZZ^* feature leptons with low transverse momentum (p_{T}), which are harder to discriminate from background (which we call "fake" electrons).

The electron likelihood is particularly well-suited for identifying low-p_{T} electrons; my goal then was to develop the electron likelihood for the 2012 data set, and implement it in the $H \to ZZ^* \to 4\ell$ analysis.

During this time, I also began working on electron efficiency measurements. These measurements are critical to make on new identification criteria before they can be used by any analysis. As with any analysis, the efficiency measurement came with its own challenges. Our efforts to improve the precision of electron efficiency measurements reduced the uncertainty of all measurements with electrons in the final state.

By the fall of 2013 we had completed the electron efficiency measurements; we had also succeeded in implementing the electron likelihood in the $H \to ZZ^* \to 4\ell$ analysis. By then, I was also helping with the first Higgs fiducial and differential cross section measurements in that channel, running the latest theoretical predictions with which the data could be compared.

By the end of Run 1, the electron likelihood had improved the measurements in many analyses, including $H \to 4\ell$ [1], $H \to WW^* \to 2\ell 2\nu$ [2], and ttH multilepton [3] analyses. I worked with a team of Penn grad students and post-docs to prepare the likelihood for Run 2. That electron identification is now used by everyone on ATLAS.

With the discovery of the Higgs boson, one of the central remaining unknowns is the mechanism that stabilizes the Higgs mass. Supersymmetry (SUSY) offers one possible explanation, and some particularly well-motivated SUSY models involve "compressed" scenarios that have low-p_{T} leptons in their signature. I was eager to exploit my knowledge of electron identification to search for well-motivated SUSY scenarios with soft lepton signatures. In the fall of 2014 and beginning of 2015, we prepared to contribute to a sensitive three-lepton SUSY analysis using 2015 data. The signature featured low-momentum leptons and potentially difficult backgrounds from fake leptons. When it became clear that the LHC would fail to deliver enough data in 2015 to surpass the Run 1 sensitivity to our target SUSY signature, we pivoted toward measuring its largest Standard Model background, WZ. Studying this process allowed us to continue developing the strategy to estimate the backgrounds from fake leptons relevant to the SUSY search, and to understand WZ as a background to potential new physics.

This thesis presents the fiducial and differential measurements of the recently discovered Higgs boson decaying to two Z bosons in Run 1, as well as the Standard Model (SM) WZ diboson cross section at 13 TeV in Run 2. A lot of attention is paid to the construction and performance of the electron likelihood developed in 2012 data, and adapted for Run 2. Some of the motivation for measuring WZ is to prepare for 3ℓ searches; the theoretical motivations for these searches is presented as well.

The material presented in this thesis is based on a number of ATLAS conference notes[1] and journal publications. The improvements in TRT detector alignment are

[1] Conference notes document preliminary ATLAS physics results and undergo a similar level of collaboration review as papers that are submitted to refereed journals.

summarized in a 2012 conference note [4]. The Run 1 electron efficiency measurements and a description of the electron likelihood identification are described in a 2014 conference note [5], which is currently in preparation for journal submission. Run 2 methods of electron identification, including updates described in this thesis, are described in a conference note prepared for Moriond 2016 [6]. The Higgs production and couplings measurement in the 4ℓ channel, for which I was involved in electron identification optimization, was published in January 2015 in Phys. Rev. D [1]. The $H \rightarrow 4\ell$ fiducial and differential cross section measurements, featuring the same event selection as in [1], were published in Physics Letters B in November 2014 [7]. Finally, the *WZ* measurement at 13 TeV described in this thesis has been submitted to Phys. Lett. B and is currently available on arXiv.org [8].

June 2016

Kurt Brendlinger
CERN, Geneva, Switzerland

References

1. ATLAS Collaboration, *Measurements of Higgs boson production and couplings in the four-lepton channel in pp collisions at center-of-mass energies of* 7 *and* 8 *TeV with the ATLAS detector*, Phys. Rev. D **91** (2015) 012006, arXiv:1408.5191 [hep-ex].
2. ATLAS Collaboration, *Observation and measurement of Higgs boson decays to WW* with the ATLAS detector*, Phys. Rev. D **92** (2015) 012006, arXiv:1412.2641 [hep-ex].
3. ATLAS Collaboration, *Search for the associated production of the Higgs boson with a top quark pair in multilepton final states with the ATLAS detector*, Phys. Lett. B **749** (2015) 519, arXiv:1506.05988 [hep-ex].
4. ATLAS Collaboration, *Study of alignment-related systematic effects on the ATLAS Inner Detector track reconstruction*, ATLAS-CONF-2012-141, 2012. http://cdsweb.cern.ch/record/1483518.
5. ATLAS Collaboration, *Electron efficiency measurements with the ATLAS detector using the 2012 LHC proton–proton collision data*, ATLAS-CONF-2014-032, 2014. http://cdsweb.cern.ch/record/1706245.
6. ATLAS Collaboration, *Electron efficiency measurements with the ATLAS detector using the 2015 LHC proton-proton collision data*, ATLAS-CONF-2016-024, 2016. https://cds.cern.ch/record/2157687.
7. ATLAS Collaboration, *Fiducial and differential cross sections of Higgs boson production measured in the four-lepton decay channel in pp collisions at* $\sqrt{s} = 8$ *TeV with the ATLAS detector*, Phys. Lett. B **738** (2014) 234, arXiv:1408.3226 [hep-ex].
8. ATLAS Collaboration, *Measurement of the* $W^{\pm}Z$ *boson pair-production cross section in pp collisions at* $\sqrt{s} = 13$ *TeV with the ATLAS Detector*, Phys. Lett. **B762** (2016) 1–22, arXiv:1606.04017 [hep-ex].

Acknowledgements

There are too many people to thank for their support, guidance and camaraderie during these last six years. I can only highlight a few.

First and foremost, thanks to my advisor Joe Kroll for his tremendous support over these past years. Joe is the best advisor anyone could ask for, and I have learned so much in physics and life from working with him.

Thanks to the rest of the Penn HEP faculty: Brig Williams, Evelyn Thomson, and Elliot Lipeles. Your personal support and your fostering of a close-knit physics group will leave a lasting impression on me.

Thanks to Paul Tipton, Michael Zeller, Jahred Adelman, Richard Wall, and Andrei Loginov for their guidance during my formative years in physics. Andrei is a great friend and we will all miss him dearly.

Thanks to all of the students in my year at Penn for all the good times. Thanks to my roommates during graduate school: Lawrence Lee, Alexander Tuna, James Saxon, Benjamin Wieder, Javier Duarte, Phil Hebda, Bijan Haney, and Ryan Reece, who were there for the good times and the bad.

Thanks to my close Penn collaborators: in TRT alignment, John Alison, Jonathan Stahlman, William DiClemente; in e/γ, John Alison, Chris Lester, Sarah Heim, Rob Roy MacGregor Fletcher, Joseph Reichert, and Lucas Flores; in $H \rightarrow ZZ^* \rightarrow 4\ell$, Jonathan Stahlman, Sarah Heim, and Bijan Haney; in WZ, Joana Machado Miguéns, Keisuke Yoshihara, Will DiClemente, and Elodie Resseguie. I couldn't have done it without all your help, and physics was more fun with your collaboration. Thanks to the Penn distinguished post-docs and alumni not already mentioned who helped shape my graduate school experience and broadened my knowledge of physics: Douglas Schaefer, Elizabeth Hines, Dominick Olivito, Joshua Kunkle, Rami Vanguri, Christopher Meyer, and Brett Jackson.

Thanks to the office-mates in Cobra not already mentioned, especially Elena Villhauer and Dan Guest, for keeping life interesting during the work week. Thanks to the countless friends in Philadelphia, Geneva and around the world for their support. Thanks especially to Alexander Tuna, James Saxon and Lawrence Lee.

Thanks to my family, Lisa O'Mahony, Thurman Brendlinger Jr., Ross and Jane, for their endless support and understanding during this adventure. I love you all.

Finally, I want to thank Sarah Heim for her endless patience with me. This thesis is dedicated to her.

Contents

Chapter 1
Outline

This thesis is divided into three main topics: the alignment of the Transition Radiation Tracker subdetector, the performance of electron objects, and measurements of diboson processes, including the Higgs boson decaying to four leptons, and WZ diboson production.

The first topic covered is the alignment of the TRT. In order to reconstruct collision events, the ATLAS detector gathers information on charged particles that traverse the detector volume. Its Inner Detector is composed of high-granularity position sensors that record hits from these particles; the hits are constructed into tracks which are used to study the event. The TRT, which is composed of nearly 300,000 drift tubes (straws) containing an ionizable gas mixture, records track positions and can also be used to help identify different types of particles. The position of the straws in this subdetector must be known to a very high precision to deliver accurate particle momentum measurements. This thesis describes the methods used to align the individual detector elements using collision data, and the subsequent improvements in measured track parameters. In particular, I document our work to remove large-scale detector deformations by individually aligning over 350,000 TRT drift tubes using in-situ collision data.

The second part of this thesis is dedicated to electron performance. The electron is one of the fundamental particles that the ATLAS detector was built to detect, and it plays a critical role in many ATLAS physics analyses. The ATLAS Collaboration maintains a group, the e/γ Combined Performance (CP) Group, dedicated to the preparation of electron physics objects, including their reconstruction from the raw detector data, discrimination against backgrounds with similar responses in the detector, measurements of the efficiency of those discriminating criteria, and electron energy measurements. I worked on electron discrimination against backgrounds and electron efficiency measurements. Improving these methods and measurements can have a far-reaching effect because it can improve the sensitivity of any analysis using electrons. The improvements outlined in this thesis have been demonstrated to benefit ATLAS analyses, most notably measurements of the Higgs boson using Run 1 data. The methods in this thesis are also currently in use as Run 2 continues.

K. Brendlinger, *Physics with Electrons in the ATLAS Detector*, Springer Theses,
https://doi.org/10.1007/978-3-319-73930-4_1

Both of the physics measurements presented in this thesis were performed after the Higgs discovery at the LHC, and both are examples of important areas of focus in the field of experimental high-energy particle physics in the post-Higgs world. The first goal is the description and characterization of the new particle, and comparison with theoretical predictions. In this thesis, I present my work on the fiducial and differential cross section measurements in the four-lepton decay channel, and comparisons of kinematic observables with theoretical predictions. Deviations with respect to the predictions can be an indicator of possible new physics. Though the differential cross sections in the 4ℓ decay channel suffer from large statistical uncertainties, our measurement paved the way for more precise calculations in the future.

The second measurement presented in this thesis is the measurement of a well-established SM process: WZ diboson production. Initially I had intended to work on a search for new physics, motivated by a supersymmetry signature with decays to leptons via intermediate W and Z bosons to a three-lepton decay channel. This channel is one of the most sensitive to superpartners of the SM electroweak sector, and the LHC was expected to deliver enough collision data in 2015 to surpass the sensitivity of the Run 1 dataset. However, the delivered integrated luminosity fell short of this projection.

Adjusting, we decided to turn our efforts to measuring the largest SM background to the 3ℓ search, namely WZ diboson production. This process had not yet been measured at this p–p collision energy, and previous measurements at smaller center-of-mass collision energies had shown a discrepancy between theoretical predictions and measurements. The measurement is a means to constrain an important background to our intended search, but SM diboson physics is interesting in its own right as a test of the predictive power of the Standard Model.

Chapter 2 provides the theoretical context for the following material, with a focus on the Higgs boson and Standard Model diboson physics. Chapter 3 describes the experimental apparatus, namely the Large Hadron Collider and the ATLAS detector. Chapter 4 describes the straw-by-straw alignment of the Transition Radiation Tracker subdetector. Chapter 5 introduces the subject of electron identification on ATLAS, and describes the development, commissioning and performance of the electron likelihood identification. Chapter 6 describes the in-situ electron identification efficiency measurements using $Z \to ee$ events.

Chapter 7 describes the Higgs fiducial and differential cross section measurements in the 4ℓ channel, made in 2014 using the Run 1 data set, with a focus on the impact of analysis improvements in electron identification and comparisons of differential distributions to theoretical predictions. Finally, Chap. 8 describes the fiducial cross section measurement of WZ diboson production using $\sqrt{s} = 13\,\text{TeV}$ data collected in the first year of Run 2.

Chapter 2
Introduction to the Theory

This section presents the theoretical background necessary to motivate and understand the content of the rest of the thesis. The focus is on the electroweak sector of the Standard Model of particle physics, electroweak symmetry breaking and the Higgs boson, and diboson physics with a focus on the WZ process. To further motivate the study of diboson physics, the theory of supersymmetry and the prospects for its discovery are briefly discussed, with a focus on signatures with diboson final states.

2.1 The Standard Model of Particles

The Standard Model (SM) of particle physics was constructed over the course of roughly the last century and has successfully described the vast majority of particle interactions. The SM is based on the existence of local (gauge) symmetries that motivate the structure of interactions of fermions (quarks and leptons) by means of force-mediating fields. Quantum field theories have been developed to describe the behavior of low-energy electromagnetic interactions (quantum electrodynamics, or QED), the strong nuclear force (quantum chromodynamics, QCD), and the weak nuclear force, which in fact is unified with electrodynamics at higher energies.

The first quantum field theory, QED, was developed to describe the interactions between electrons and photons, and its construction revealed features that are common to all field theories, as well as features characteristic of a "well-behaving" theory. A key field theory concept is that requiring local gauge invariance under Lorentz transformations of the fermionic field implies the existence of a spin-1 gauge field (the photon for QED). QED is also perturbative: the coupling constant $\alpha = e^2/4\pi$ is small enough that cross section calculations can be described as a power series in orders of α, with small higher-order corrections. Another property of QED (and of a "good theory" in general) is its validity at all energy scales; this property was lacking in early versions of QED, with infinities (ultraviolet divergences)

K. Brendlinger, *Physics with Electrons in the ATLAS Detector*, Springer Theses,
https://doi.org/10.1007/978-3-319-73930-4_2

appearing in cross section calculations. This problem was solved by a process called renormalization: physical parameters such as the masses and coupling constants of the theory are redefined to absorb the infinities, resulting in a finite cross section calculation.

The quantum field theory approach could be applied to the strong nuclear force. The study of hadrons accelerated during the era of bubble and spark chambers in the 1950s leading to an explosion of particle discoveries. These particles could be arranged according to their properties in a way suggestive that they were in fact composites of smaller constituents, later named quarks [1–3]. Because some of these hadronic bound states seemed to be composed of multiple quarks in the same state, in violation of the Pauli exclusion principle, it was recognized that quarks required a new quantum number, called color [4]. QCD theory is based on quark invariance under color transformations, an SU(3) symmetry, where gluons are the massless generators of the SU(3) group. An important feature of this gauge theory (and indeed any non-Abelian gauge theory) is that while the coupling constants are high enough at low energy scales to confine quarks to colorless hadrons, these "constants" in fact decrease at higher energy scales [5, 6]. This feature transforms QCD into a perturbative field theory at high energies, such as the energies accessible using today's accelerators.

Difficulties arose when trying to cast the weak force into a gauge theory. Weak interactions were proposed to explain nuclear β decay; the phenomenon has properties of an SU(2) symmetry, but its short interaction scale implies a massive gauge boson mediator. However, this would break the Lorentz invariance of the theory, which requires massless bosons. A solution was required to explain the masses of the weak gauge bosons, and preferably one that preserved the nice properties of the field theory: Lorentz invariance and renormalizability.

2.2 Electroweak Symmetry Breaking

The solution to the problems in the weak sector involved starting with a larger $\mathrm{SU}(2) \times \mathrm{U}(1)$ symmetry group with massless gauge bosons and spontaneously breaking this symmetry to obtain the structure of the electromagnetic and weak forces seen in nature. To do this, a complex scalar field doublet is introduced. However, instead of being invariant under SU(2) symmetry with a ground state (vacuum expectation value or vev) at the origin, it has a non-zero vev, and SU(2) transformations change the ground state—the symmetry is "spontaneously broken."

The consequences of this complex scalar field breaking SU(2) symmetry are profound. The generators of $\mathrm{SU}(2) \times \mathrm{U}(1)$ (B_μ for U(1) and W^0_μ, W^1_μ, W^2_μ of SU(2)) mix with each other and with degrees of freedom of the complex scalar field, resulting in a massless gauge boson (the photon), two massive vector bosons W^+ and W^- (the charged weak currents) and a third massive, neutral vector boson (Z) which had not yet been observed, amounting to a prediction of the theory of electroweak symmetry breaking (EWSB). The photon, a superposition of B_μ and W^0_μ, is associated with an unbroken U(1) symmetry that reproduces QED. The mechanism also predicts a massive scalar boson that couples to particles in proportion to their mass.

The mechanism described above was developed in the 1960s, including the spontaneous symmetry breaking mechanism (the Brout–Englert–Higgs or BEH mechanism [7–9]) and the unification of the electromagnetic and weak forces [10–12]. The new theory has all the desirable properties of a quantum field theory: the Lagrangian is Lorentz invariant and the theory is renormalizable [13]. The theory also provides mass terms (Yukawa couplings) for fermions in its Lagrangian, thus solving another theoretical problem.

The predictions of the new theory were confirmed in the following years: weak neural currents were observed in the Gargamelle bubble chamber experiment at CERN in 1973 [14, 15], supporting the existence of the proposed Z boson. The massive W and Z bosons themselves were discovered in 1983 at CERN by the UA1 and UA2 experiments using collisions at the Super Proton Synchrotron collider, and their properties were extensively studied at the LEP and SLC colliders [16–19]. These discoveries fueled the success of the unified electroweak theory; the remaining missing piece was the predicted massive scalar boson, the Higgs boson.

2.3 The Higgs Boson

One of the unknown parameters of EWSB was the mass of the Higgs boson, which is not predicted by the theory. Previous to the construction of the LHC, various constraints on the mass of the Higgs boson were placed. A Higgs with mass lower than the TeV scale is required to keep the WW scattering probability below one (or risk the electroweak theory becoming non-perturbative) [20]. Constraints from LEP and the Tevatron provided a lower bound on the mass [21]. The discovery of the Higgs boson was eventually made using collisions at the LHC. On July 4, 2012, ATLAS and CMS experiments announced the discovery of a particle with Higgs-like properties, with a mass of about 125 GeV [22, 23].

The production modes of the Higgs boson at a hadron collider are depicted in Fig. 2.1. At the LHC, Higgs production is dominated by gluon fusion (ggF), representing 87% of Higgs production at $\sqrt{s} = 8$ TeV.[1] Vector boson fusion has a distinct signature featuring two forward jets and plays an important role in determining Higgs boson couplings [24]. Higgs production in association with top quarks (ttH) offers direct access to the top Yukawa coupling.

The decays of the Higgs boson are illustrated in Fig. 2.2; production and decay modes are summarized in Table 2.1.

Measurements of the Higgs boson using the Run 1 data set are so far consistent with the SM predictions. Figure 2.3 shows the measured couplings to vector bosons and fermions in the ATLAS and CMS detectors, demonstrating their dependence on the mass of the Higgs boson as predicted by the SM.

Part of the LHC program in the coming years will be to measure the properties of the newly discovered Higgs boson and compare them to the theoretical

[1] Higgs cross sections are quoted given a mass of 125.4 GeV.

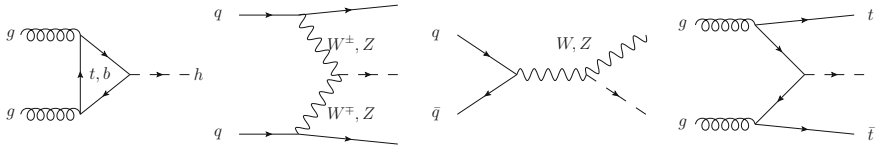

Fig. 2.1 Leading-order Feynman diagrams of Higgs boson production modes. From left: gluon-gluon fusion via heavy quark loops; vector boson (Z or W) fusion with two forward jets; radiation of a Higgs (Higgstrahlung) from a W or Z boson; Higgs production in association with top quarks

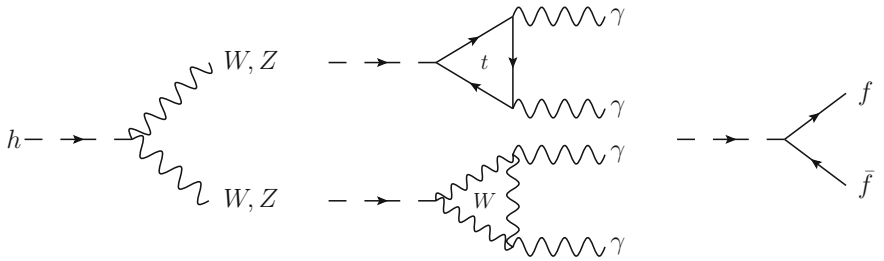

Fig. 2.2 Higgs decay modes. Left: decay to WW or ZZ spin-1 boson pairs; middle: decays to photons via virtual top and W loops; right: decays to fermion-antifermion pairs. Accessible (distinguishable from background) $f\bar{f}$ pairs at the LHC include $\tau^+\tau^-$, $\mu^+\mu^-$, and $b\bar{b}$

Table 2.1 Predicted Higgs production cross sections (σ) and decay branching ratios, given a Higgs with mass 125.4 GeV

Production mode	σ (pb)	% of total σ
Gluon-gluon fusion	19.15	87
Vector boson fusion	1.573	7
WH	0.6970	3
ZH	0.4112	1.9
bbH	0.2013	0.9
ttH	0.1280	0.6

Decay mode	Branching ratio (%)
$H \to b\bar{b}$	57.1
$H \to WW$	22.1
$H \to \tau\tau$	6.25
$H \to ZZ$	2.74
$H \to \gamma\gamma$	0.228
$H \to Z\gamma$	0.157
$H \to \mu\mu$	0.021
$H \to$ other	11.4
(gg, cc, ss, tt)	

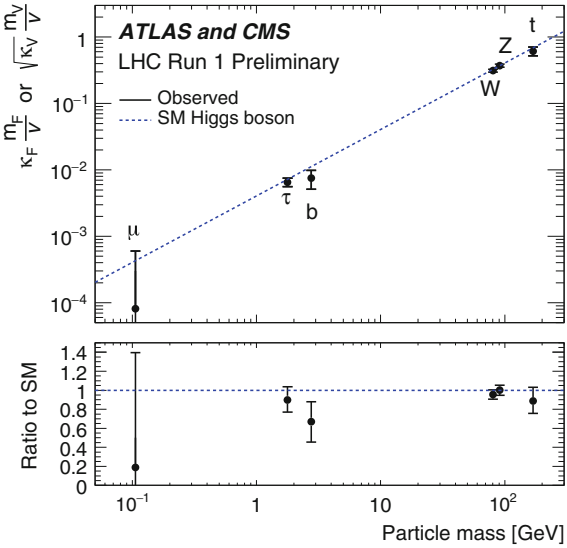

Fig. 2.3 Measurements combining ATLAS and CMS analyses of best-fit couplings to fermions and bosons, using the coupling modifiers $\kappa = \sigma/\sigma_{\mathrm{SM}}$. The results illustrate the mass dependence of particle couplings to the Higgs boson [25]

predictions. Deviations in cross section measurements, or differences in differential cross sections, can point to new physics. As an example, an additional heavy particle that couples to the Higgs can add an additional production mode to the list in Fig. 2.1 and increase the production of Higgs bosons with a higher p_{T}. It is for this reason that the theory community has made efforts to improve the understanding of the SM prediction of the Higgs p_{T} spectrum.

2.4 Diboson Physics, Triple Gauge Couplings and WZ

The non-Abelian nature of the electroweak sector allows for triple and quartic gauge couplings—vertices with three and four gauge bosons. The triple gauge couplings (TGCs) allowed by the SM correspond to the WWZ and $WW\gamma$ vertices, accessible via the WW, $W\gamma$ and WZ production processes.[2] Production of WW is available at both hadron and e^+e^- colliders, whereas the $W\gamma$ and WZ processes are only accessible at hadron colliders. Quartic gauge couplings (QGCs) can be probed using vector boson scattering (VBS), including $W^{\pm}W^{\pm}jj$ production, $WW\gamma$ and $WZ\gamma$ production, and the $\gamma\gamma \rightarrow WW$ process [26]. Measurements of triple and quartic gauge couplings and comparisons with theoretical predictions are an important test of the predictions of the SM.

Any deviation from the SM predictions of diboson production rates can originate from what are referred to as anomalous triple gauge couplings and can point to new physics. The most notable example of this was the dedicated search for and discovery

[2] $ZZ\gamma$ and $Z\gamma\gamma$ vertices are disallowed by the SM; photons only couple to charged particles.

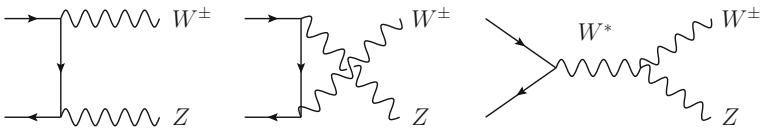

Fig. 2.4 Leading-order Feynman diagrams for WZ production at the LHC. From left, the t- and u-channel production, and the s-channel production, which features a triple gauge coupling vertex

of the Higgs boson decaying to WW [27], which manifested in an increase of events above the SM WW production cross section, and in differences between certain kinematic observables and the theoretical prediction from SM WW production.

2.4.1 WZ Production and Decay Modes

The WZ diboson production process is particularly useful to study because its cross section is influenced by a triple gauge coupling vertex in the s-channel. Furthermore, its backgrounds are relatively small in contrast to the WW process, which has large backgrounds due to $t\bar{t}$ that can necessitate a jet veto requirement. Figure 2.4 depicts the three leading-order Feynman diagrams for WZ production at p–p colliders.

The W boson decays to $e\nu_e$, $\mu\nu_\mu$, $\tau\nu_\tau$, and $q\bar{q}'$, with branching fractions of roughly 11, 11, 11, and 67%, respectively. The Z boson decays to ee, $\mu\mu$, $\tau\tau$, $\nu\nu$, and $q\bar{q}$ with branching fractions 3.4, 3.4, 3.4, 20, and 70%, respectively. The WZ diboson cross section is typically measured using the $\ell\nu_\ell\ell'\ell'$ ("fully leptonic") decay channels, with $\ell, \ell' = e$ or μ, because leptons have fewer backgrounds compared to jets at hadron colliders. The WZ channels including taus are typically excluded because the tau is unstable and largely decays hadronically, and thus also has large backgrounds compared to e and μ.

Searches for diboson resonances often use the $\ell\ell qq'$ channel, with the Z decaying leptonically and the W decaying to quarks. This channel has several advantages compared to the purely leptonic channel: all decay products are visible which allows for the mass of a heavy resonant peak to be reconstructed, the branching ratio is much larger than the fully leptonic decay modes, and backgrounds from multijet, Z + jet and W + jet production are much smaller for the high-p_{T} decay products of a heavy resonant particle.

2.5 Supersymmetry and Diboson Physics

Diboson channels, and particularly signatures with both a W and a Z in the final state, are a well-motivated place to search for new physics, and in particular for traces of a theory known as supersymmetry (SUSY).

The discovery of the Higgs boson was a milestone in particle physics, providing an important piece of the SM. However, loop corrections to the Higgs mass are divergent and suggest a Higgs mass on the order of the Planck scale ($\sim 10^{19}$ GeV), unless these corrections come in pairs that conveniently cancel in poorly-motivated ways. Problems of this nature are suggestive of a new symmetry that protects the Higgs mass scale. A symmetry which relates fermions and bosons and arranges the SM particles into multiplets—supersymmetry—can effectively solve this fine-tuning problem. In the past few decades a large number of theories have developed under the basic SUSY assumptions to try to explain existing phenomena and suggest new phenomenology beyond the SM.

The electroweakino sector—the superpartners to the electroweak force carriers and the Higgs—is a well-motivated place to look at the LHC. Fine-tuning arguments suggest that these SUSY particles must have masses at or near the electroweak scale [28].

The electroweakino spectrum consists of the superpartners of the SU(2) × U(1) gauge group: a neutral bino, and neutral and charged wino components; in addition, it contains the superpartners to the two Higgs doublets, resulting in two neutral and two charged higgsinos. These gauge eigenstates may mix; the mass eigenstates are called neutralinos ($\tilde{\chi}_1^0$, $\tilde{\chi}_2^0$, $\tilde{\chi}_3^0$, $\tilde{\chi}_4^0$, in order of increasing mass) and charginos ($\tilde{\chi}_1^\pm$ and $\tilde{\chi}_2^\pm$). The electroweakino spectrum is controlled by four variables, M_1, M_2, μ and $\tan\beta$, which dictate the hierarchy of states (and degree of mixing) [29].

At the LHC, direct production of electroweakinos proceeds mainly through s-channel production via W's and Z's, and cross sections can be on the order of 1–10 pb. Searches focus on the production of lighter states, namely $\tilde{\chi}_1^\pm \tilde{\chi}_2^0$ and $\tilde{\chi}_1^\pm \tilde{\chi}_1^\pm$ production. As illustrated in Fig. 2.5, the primary decays are $\tilde{\chi}_1^\pm \to \tilde{\chi}_1^0 W$ and $\tilde{\chi}_2^0 \to \tilde{\chi}_1^0 Z$, which can result in signatures with two or three leptons and large missing transverse momentum. These signatures are very similar to the SM WW and WZ processes—they can have on-shell W and Z bosons—and differ most significantly in their additional $E_{\mathrm{T}}^{\mathrm{miss}}$. Because the production cross sections of electroweakino pair production are typically at least two orders of magnitude smaller than those of

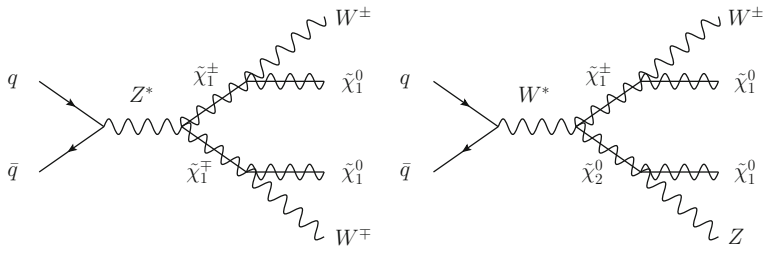

Fig. 2.5 Direct s-channel production and decay of $\tilde{\chi}_1^\pm \tilde{\chi}_1^\pm$ (left) and $\tilde{\chi}_1^\pm \tilde{\chi}_2^0$ (right), resulting in two- and three-lepton signatures (respectively) with $E_{\mathrm{T}}^{\mathrm{miss}}$. These signatures are the target of ATLAS direct electroweakino production searches, for which the WW and WZ SM diboson processes are the main irreducible backgrounds

SM WW and WZ production, analyses gain sensitivity by imposing a high $E_{\mathrm{T}}^{\mathrm{miss}}$ requirement in their signal region.[3] Understanding the SM backgrounds to these searches, namely WW and WZ, are essential to the success of searches for these SUSY signatures.

2.6 Physics at Hadron Colliders

Cross section calculations at hadron colliders require precise understanding of the dynamics of the proton constituents and the nature of the strong force governing quarks and gluons. Luckily, the high energies reached by modern-day colliders are in the perturbative limit of QCD.

The parton model of high-energy interactions with the proton (or other hadrons) takes the view that at relativistic energies, the proton length is contracted, resembling a disc, and interactions between its constituents are slowed due to time dilation such that it can be characterized as a collection of non-interacting constituent quarks and gluons ("partons") [30]. Then the proton can be described using form factors $f(x, Q^2)$ for each parton inside the proton, called parton distribution functions (PDFs). Here, x is the fraction of the proton momentum carried by the parton and Q^2 is the momentum transfer. The form factor has a strong dependence on x, and only a small dependence on Q^2. PDFs cannot be calculated perturbatively; instead, they are fit to measurements from deep inelastic scattering, Drell–Yan, and jet production cross section data, and evolved as a function of Q^2 with what are referred to as the DGLAP equations [31–33]. Several collaborations provide PDFs that can be used to make QCD cross section predictions; Fig. 2.6 shows the PDF distributions for the valence quarks, sea quarks, and gluons found inside a proton.

The cross section calculation of a p–p process can be factorized into two parts: the perturbative QCD calculation in orders of α_s of the hard-scatter process and the physics of the proton described by the parton model. The perturbative calculation can only be performed out to a few orders in α_s, resulting in a scale dependence μ_R related to the renormalization process required to remove ultraviolet divergences. This scale dependence is typically set to the scale of the hard-scatter process (for e.g. Higgs production μ_R is set to m_H) and varied by factors of 2 and 1/2 to get a sense of the uncertainty related to this choice. The scale dependence should diminish if the calculation is carried out to higher orders of α_s.

Another complication arises in the calculation of corrections real and virtual gluon emissions. These emissions can be thought of as either being part of the perturbative calculation or as part of the proton structure and thus incorporated into the PDF. A scale parameter μ_F is introduced to separate the physics of the proton and the hard scatter process which should not affect the result (it is also typically set to the scale of the hard-scatter process). Uncertainties due to this factorization scale are estimated

[3] Though it is possible that SUSY could appear in SM diboson measurements, such signatures would appear first in the dedicated searches commonly conducted by ATLAS and CMS.

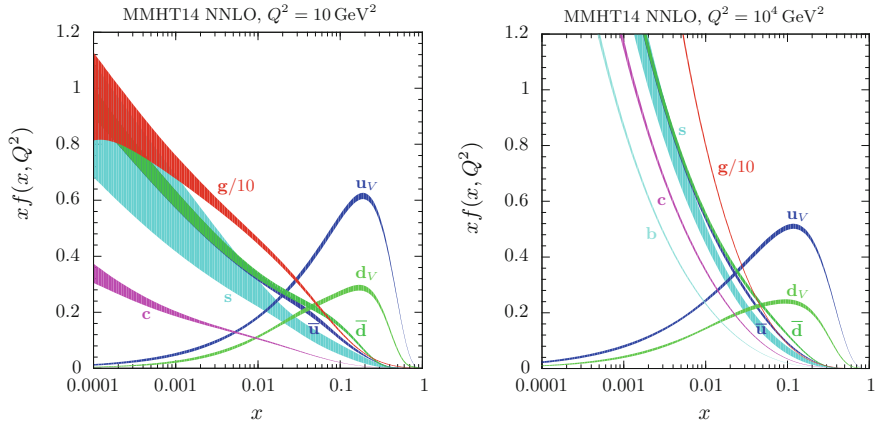

Fig. 2.6 PDFs from the MMHT14 NNLO prediction [34]

by varying it up and down, typically by factors of 2 and 1/2. The cross section can then be written as such:

$$\sigma_{AB} = \int dx_a dx_b \; f_{a/A}(x_a, \mu_F^2) \; f_{b/B}(x_b, \mu_F^2) \times \left[\hat{\sigma}_0 + \alpha_S(\mu_R^2)\hat{\sigma}_1 + \cdots\right]_{ab\to X} , \tag{2.1}$$

integrated across all possible momentum fractions x_a and x_b for each of the partons, with associated scale and factorization dependences [35].

References

1. M. Gell-Mann, A schematic model of baryons and mesons. Phys. Lett. **8**, 214–215 (1964). https://doi.org/10.1016/S0031-9163(64)92001-3
2. G. Zweig, An SU(3) model for strong interaction symmetry and its breaking. Version 1, Cern-th-401 (1964), https://cdsweb.cern.ch/record/352337
3. G. Zweig, An SU(3) model for strong interaction symmetry and its breaking. Version 2, in *Developments in the Quark Theory of Hadrons. Vol. 1. 1964–1978*, ed. by D. Lichtenberg, S.P. Rosen (1964), pp. 22–101, http://inspirehep.net/record/4674/files/cern-th-412.pdf
4. M.Y. Han, Y. Nambu, Three-triplet model with double SU(3) symmetry. Phys. Rev. **139**, B1006–B1010 (1965). https://doi.org/10.1103/PhysRev.139.B1006
5. D.J. Gross, F. Wilczek, Asymptotically free gauge theories. I. Phys. Rev. D **8**, 3633–3652 (1973). https://doi.org/10.1103/PhysRevD.8.3633
6. D.J. Gross, F. Wilczek, Asymptotically free gauge theories. II. Phys. Rev. D **9**, 980–993 (1974). https://doi.org/10.1103/PhysRevD.9.980
7. F. Englert, R. Brout, Broken symmetry and the mass of gauge vector mesons. Phys. Rev. Lett. **13**, 321–323 (1964). https://doi.org/10.1103/PhysRevLett.13.321
8. P.W. Higgs, Broken symmetries, massless particles and gauge fields. Phys. Lett. **12**, 132–133 (1964). https://doi.org/10.1016/0031-9163(64)91136-9
9. P.W. Higgs, Broken symmetries and the masses of gauge bosons. Phys. Rev. Lett. **13**, 508–509 (1964). https://doi.org/10.1103/PhysRevLett.13.508

10. S. Glashow, Partial symmetries of weak interactions. Nucl. Phys. **22**, 579–588 (1961). https://doi.org/10.1016/0029-5582(61)90469-2
11. S. Weinberg, A model of leptons. Phys. Rev. Lett. **19**, 1264–1266 (1967). https://doi.org/10.1103/PhysRevLett.19.1264
12. A. Salam, Weak and electromagnetic interactions, Svartholm: elementary particle theory, in *Proceedings of the Nobel Symposium held at Lerum, Sweden, Stockholm* (1968), pp. 367–377
13. G. 't Hooft, Renormalizable Lagrangians for massive yang-mills fields. Nucl. Phys. B **35**, 167–188 (1971). https://doi.org/10.1016/0550-3213(71)90139-8
14. F.J. Hasert et al., Observation of neutrino-like interactions without muon or electron in the Gargamelle neutrino experiment. Phys. Lett. B **46**, 138–140 (1973). https://doi.org/10.1016/0370-2693(73)90499-1
15. F.J. Hasert et al., Observation of neutrino-like interactions without muon or electron in the Gargamelle neutrino experiment. Nucl. Phys. B **73**, 1–22 (1974). https://doi.org/10.1016/0550-3213(74)90038-8
16. UA1 Collaboration, Experimental observation of isolated large transverse energy electrons with associated missing energy at $\sqrt{s} = 540$ GeV. Phys. Lett. B **122**, 103–116 (1983). https://doi.org/10.1016/0370-2693(83)91177-2
17. UA2 Collaboration, Observation of single isolated electrons of high transverse momentum in events with missing transverse energy at the CERN pp collider. Phys. Lett. B **122**, 476–485 (1983). https://doi.org/10.1016/0370-2693(83)91605-2
18. UA1 Collaboration, Experimental observation of lepton pairs of invariant mass around 95 GeV/c^2 at the CERN SPS collider. Phys. Lett. B **126**, 398–410 (1983). https://doi.org/10.1016/0370-2693(83)90188-0
19. UA2 Collaboration, Evidence for $Z^0 \to e^+e^-$ at the CERN pp collider. Phys. Lett. B **129**, 130–140 (1983). https://doi.org/10.1016/0370-2693(83)90744-X
20. P. Langacker, The standard model and beyond. AIP Conf. Proc. **150**, 142–164 (1986). https://doi.org/10.1063/1.36182
21. Tevatron Electroweak Working Group, CDF, DELPHI, SLD Electroweak and Heavy Flavour Groups, ALEPH, LEP Electroweak Working Group, SLD, OPAL, D0, L3 Collaboration, L. E. W. Group, Precision electroweak measurements and constraints on the standard model, arXiv:1012.2367 [hep-ex]
22. ATLAS Collaboration, Observation of a new particle in the search for the standard model Higgs boson with the ATLAS detector at the LHC. Phys. Lett. B **716**, 1 (2012). https://doi.org/10.1016/j.physletb.2012.08.020, arXiv:1207.7214 [hep-ex]
23. CMS Collaboration, Observation of a new boson at a mass of 125 GeV with the CMS experiment at the LHC. Phys. Lett. B **716**, 30–61 (2012). https://doi.org/10.1016/j.physletb.2012.08.021, arXiv:1207.7235 [hep-ex]
24. M. Duhrssen, S. Heinemeyer, H. Logan, D. Rainwater, G. Weiglein, D. Zeppenfeld, Extracting Higgs boson couplings from CERN LHC data. Phys. Rev. D **70**, 113009 (2004). https://doi.org/10.1103/PhysRevD.70.113009, arXiv:hep-ph/0406323 [hep-ph]
25. ATLAS and CMS Collaborations, Measurements of the Higgs boson production and decay rates and constraints on its couplings from a combined ATLAS and CMS analysis of the LHC pp collision data at $\sqrt{s} = 7$ and 8 TeV, Atlas-conf-2015-044 (2015), https://cdsweb.cern.ch/record/2052552
26. T. Kubota, Overview of triple and quartic gauge coupling measurements at the LHC, in *Proceedings, 2nd Conference on Large Hadron Collider Physics Conference (LHCP 2014)* (2014), arXiv:1408.6604 [hep-ex], https://inspirehep.net/record/1312758/files/arXiv:1408.6604.pdf
27. ATLAS Collaboration, Observation and measurement of Higgs boson decays to WW^* with the ATLAS detector. Phys. Rev. D **92**, 012006 (2015). https://doi.org/10.1103/PhysRevD.92.012006, arXiv:1412.2641 [hep-ex]
28. R. Barbieri, G.F. Giudice, Upper bounds on supersymmetric particle masses. Nucl. Phys. B **306**, 63–76 (1988). https://doi.org/10.1016/0550-3213(88)90171-X
29. S.P. Martin, A supersymmetry primer. Adv. Ser. Direct. High Energy Phys. **21**, 1–153 (2010). https://doi.org/10.1142/9789814307505_0001, arXiv:hep-ph/9709356 [hep-ph]

30. R.P. Feynman, The behavior of hadron collisions at extreme energies. Conf. Proc. C **690905**, 237–258 (1969)
31. V. Gribov, L. Lipatov, Deep inelastic e-p scattering in perturbation theory. Sov. J. Nucl. Phys. **15**, 438–450 (1972)
32. G. Altarelli, G. Parisi, Asymptotic freedom in parton language. Nucl. Phys. B **126**, 298 (1977). https://doi.org/10.1016/0550-3213(77)90384-4
33. Y.L. Dokshitzer, Calculation of the structure functions for deep inelastic scattering and e^+e^- annihilation by perturbation theory in quantum chromodynamics. Sov. Phys. JETP **46**, 641–653 (1977)
34. L.A. Harland-Lang, A.D. Martin, P. Motylinski, R.S. Thorne, Parton distributions in the LHC era: MMHT 2014 PDFs. Eur. Phys. J. C **75**(5), 204 (2015). https://doi.org/10.1140/epjc/s10052-015-3397-6, arXiv:1412.3989 [hep-ph]
35. J.M. Campbell, J.W. Huston, W.J. Stirling, Hard interactions of quarks and gluons: a primer for LHC physics. Rep. Prog. Phys. **70**(1), 89 (2007), http://stacks.iop.org/0034-4885/70/i=1/a=R02

Chapter 3
Experimental Apparatus

The following chapter describes the experimental apparatus used in this thesis. In addition, the software techniques used to reconstruct[1] and identify key particles are described, including track reconstruction, jet, electron and photon reconstruction, and muon reconstruction.

Special emphasis is placed on elements of the ATLAS detector and LHC collision conditions that affect electron reconstruction and identification.

3.1 The Large Hadron Collider

The LHC [1] was built to meet the challenges facing particle physics in the post-LEP (1989–2000), post-Tevatron (1987–2011) era. It is designed to produce a large variety of physics processes with very high center-of-mass (c.o.m.) energies, and it collides particles at a high rate to allow the study of rare processes. The LHC provides proton-proton (p–p) and heavy-ion (Pb–Pb) collisions to four primary detectors: ALICE [2], LHCb [3], CMS [4] and ATLAS [5].

Protons are injected into the LHC using a chain of particle accelerators as depicted in Fig. 3.1. Hydrogen atoms are ionized and the protons are accelerated to 50 MeV with the Linac, a linear accelerator. The protons continue to the Proton Synchrotron Booster (PSB), followed by the Proton Synchrotron (PS) and Super Proton Synchrotron (SPS); each accelerates the protons to energies of 1.4, 25 and 450 GeV respectively, before they are delivered to the LHC. The PS and SPS deliver protons

[1] "Reconstruction" refers generally to the process of both determining the trajectory (position, momentum and energy) of a particle and assigning a hypothesis of its fundamental origin using the raw hit information from the detector. Typical particle hypotheses include photon, electron, muon, and jet, or even kaon, pion, quark-initiated jet, and gluon-initiated jet (this is not a comprehensive list).

K. Brendlinger, *Physics with Electrons in the ATLAS Detector*, Springer Theses,
https://doi.org/10.1007/978-3-319-73930-4_3

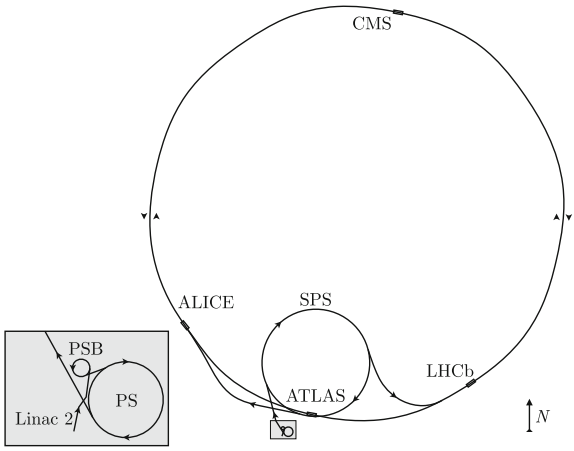

Fig. 3.1 The Large Hadron Collider, its injection chain, and the four main experiments, ATLAS, ALICE, CMS, and LHCb, to which it delivers collisions

in "bunches" separated by roughly 25 ns each; in total 2808 bunches can be injected into the LHC ring.[2] There are about 10^{11} protons per bunch.

Once inside the LHC, the proton bunches are kept circulating using superconducting magnets cooled to 1.9 K with liquid helium. Radiofrequency cavities with a maximum oscillation of 400 MHz are used to accelerate the particles from 450 GeV to a maximum of 7 TeV. Other magnets are dedicated to focusing and colliding the beam in the center of each of the four detectors.

In order to rapidly collect data, the LHC must deliver a high instantaneous luminosity, the number of p–p interactions per second, to an experiment. Instantaneous luminosity is historically measured in $\mathrm{cm}^{-2}\mathrm{s}^{-1}$. The instantaneous luminosity depends on the square of the number of protons in a bunch, the number of circulating bunches, the energy of the beam, the spread of particles in a beam (beam emittance), how tightly the magnets are focused at the interaction points (β^*), and the crossing angle of the beams. Figure 3.2 shows the instantaneous luminosity delivered to ATLAS between 2010 and 2012, reaching nearly $8.0 \times 10^{33}\,\mathrm{cm}^{-2}\mathrm{s}^{-1}$. The peak instantaneous luminosity in 2015 was $5.0 \times 10^{33}\,\mathrm{cm}^{-2}\mathrm{s}^{-1}$; already in 2016 the peak luminosity has exceeded $1 \times 10^{34}\,\mathrm{cm}^{-2}\mathrm{s}^{-1}$, its design luminosity [1]. For reference, the process $pp \to W^{\pm} \to e\nu$, with a cross section of about 10 nb at 8 TeV, occurred about 80 times per second at the end of 2012. Figure 3.3 reports the integrated luminosity delivered to ATLAS in each year of data taking from 2011 to 2016. In 2012 alone, the process $pp \to W^{\pm} \to e\nu$ would have occurred at the ATLAS interaction point around 230 million times.

As a consequence of the high instantaneous luminosity delivered by the LHC, the number of inelastic p–p interactions in a single bunch crossing at the detector interaction point is much greater than one. Figure 3.4 depicts the average number of

[2]There is space for 3564 bunches in the LHC ring, but gaps are required to allow the "kicker" magnets that inject beam into the SPS or the LHC to ramp up. A large gap (3 μs) is required to allow the LHC Dump Kicker to turn on and dump the beam.

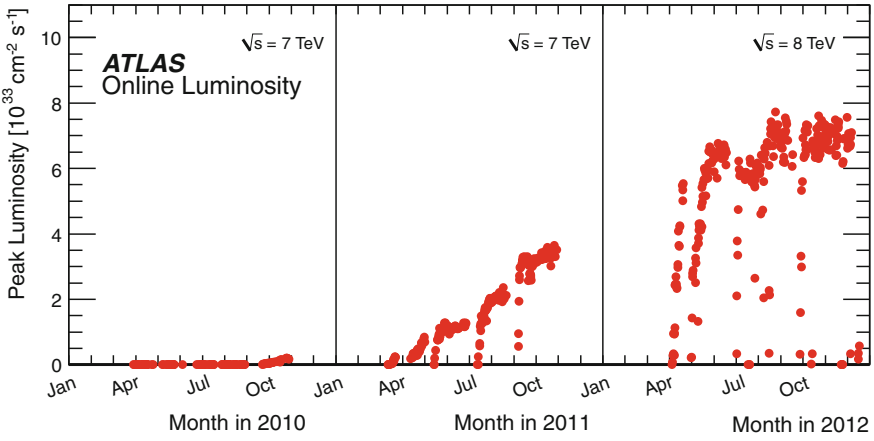

Fig. 3.2 Peak instantaneous luminosity delivered to ATLAS between 2010 and 2012 (Run 1) [6]

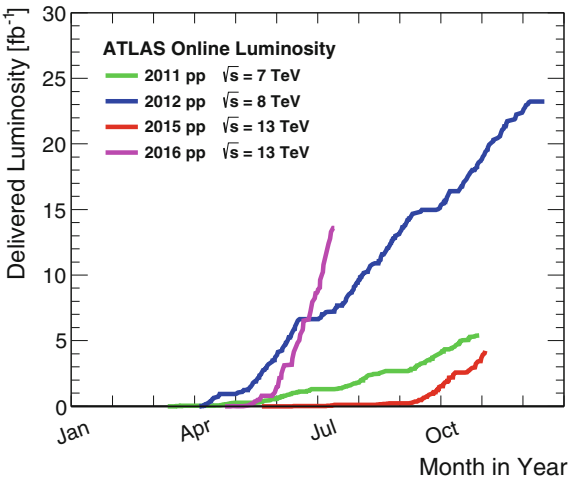

Fig. 3.3 Cumulative p–p collision luminosity delivered to the ATLAS detector versus day of the year, separately for years between 2011 and 2016 (ongoing) [6]

interactions per bunch crossing in 2011, 2012, and 2015. The multiple interactions per crossing poses a challenge for detectors that must resolve the properties of individual interactions. Compounding the issue, the 25 ns spacing between interactions is much faster than the response time of many calorimeter systems, meaning the effects of events from adjacent bunch spacings are present in an event as well. These conditions introduce challenges with which the detector collaborations must cope.

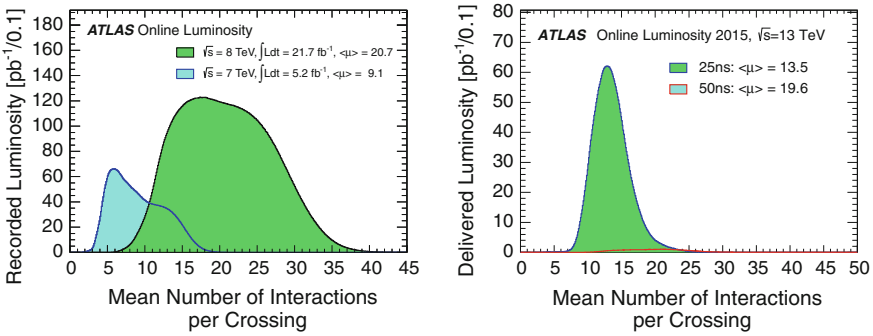

Fig. 3.4 Mean number of interactions per bunch crossing in 2011–2012 data taking (left) and 2015 data taking (right). The 2015 dataset is split into two periods: one in which the bunch spacing is 50 ns, as in Run 1, and one in which the bunch spacing is decreased to 25 ns, during which the bulk of 2015 data was taken [6]

3.2 The ATLAS Detector

The ATLAS detector measures the energy and momentum of light, electromagnetically interacting particles (electrons and photons), hadronic jets, and muons. To achieve this, the detector is composed of several nested, cylindrical sub-systems. Closest to the interaction point (IP), a tracking system is used to measure the momentum of charged particles while absorbing as little of a particle's energy as possible. Next, a system of calorimeters is used to stop electrons, photons and hadronic jets, measuring their energy in the process. An electromagnetic calorimeter is closer to the IP, and absorbs nearly all the energy from electrons and photons. Hadronic jets are fully stopped by the hadronic calorimeter. Muons escape the calorimeter; the outermost layer of the ATLAS detector is a spectrometer composed of tracking detectors and toroidal magnets designed to measure their momenta. The sub-systems are designed in ways to make it easier to identify electrons, photons, hadronic jets and muons and discriminate between the different classes in order to understand the fundamental interaction in the p–p collision.

In some of the following schematic diagrams presented, ATLAS uses a right-handed coordinate system with its origin at the nominal interaction point (IP) in the center of the detector and the z-axis along the beam pipe. The x-axis points from the IP to the center of the LHC ring, and the y-axis points upward. Because the detectors are constructed using a cylindrical geometry, cylindrical coordinates (r, ϕ) are often useful, where ϕ is the azimuthal angle around the beam axis. It is common in particle physics to use ϕ and the pseudorapidity η, defined in terms of the polar angle θ as $\eta = -\ln\tan(\theta/2)$, to describe the trajectory of particles.

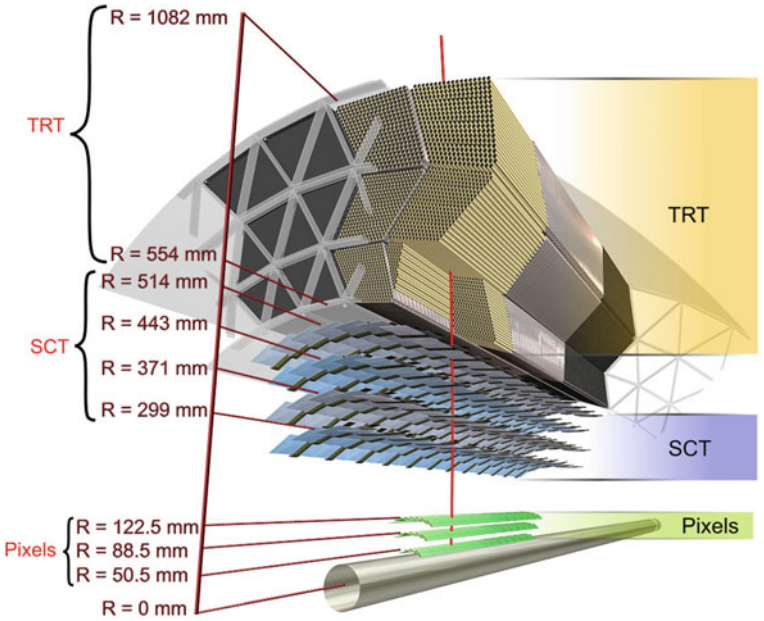

Fig. 3.5 View of the Inner Detector barrel detectors. The active elements of the Insertable B-Layer, not pictured, is positioned at a distance $R = 33.25\,\text{mm}$ from the interaction point

3.2.1 The Inner Detector and Solenoid

The inner detector (ID) is a tracking system designed to reconstruct the trajectories of charged particles at pseudorapidities of up to $|\eta| < 2.5$. It is surrounded by a solenoid coil delivering a 2 T axial magnetic field that bends charged particles and allows for a precise measurement of their momentum. The inner detector is composed of three sub-detectors which use different technologies: a pixel detector, a silicon strip detector and a transition radiation tracker. The position of a charged particle traversing the inner detector will be measured about 41 times (3 hits in the pixel detector, 8 hits in the SCT, and 30 hits in the TRT). Figures 3.5 and 3.6 depict the inner detector sub-systems.

3.2.1.1 Pixel Detector

The pixel detector consists of three layers of pixel sensors arranged in a barrel and two endcaps, covering a range of $|\eta| < 2.5$. The plane of each pixel sensor is $50\,\mu\text{m} \times 400\,\mu\text{m}$ in size, and there are 1744 total pixel sensors with a total of 80 million readout channels. The pixel sensors provide a resolution of $10\,\mu\text{m}$ in the $r - \phi$ plane, and $115\,\mu\text{m}$ in the z direction (r direction) of the barrel (endcap) modules.

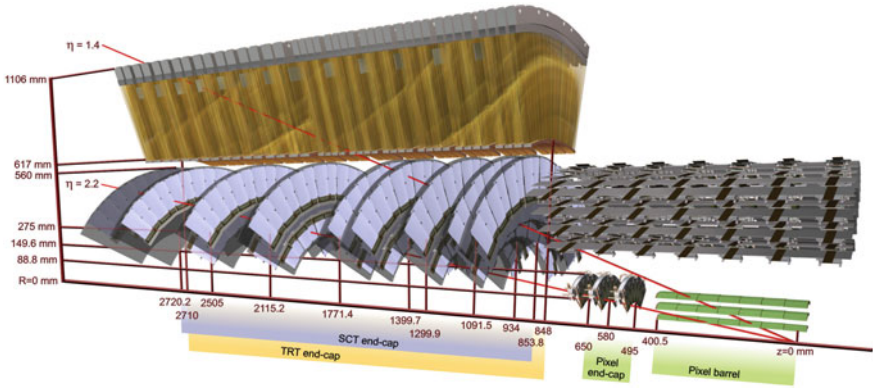

Fig. 3.6 View of the Inner Detector endcap detectors

During the shutdown between 2012 and 2015 data taking periods, the Insertable B-Layer [7] was installed, adding a fourth layer of pixel sensors. The beam pipe inside the ATLAS detector was replaced, reducing its radius from 29 to 25 mm, and the newest layer is positioned at a radius of around 33 mm from the interaction point, compared to 50 mm of the original closest layer. This layer allows higher-precision tracking including an increased ability to detect displaced vertices from b-jets.

3.2.1.2 Silicon Strip Detectors

The silicon microstrip tracker (or SCT—standing for SemiConductor Tracker) consists of four barrel and nine end-cap layers, located at radii between ∼288−560 mm and covering a range of $|\eta| < 2.5$. Each layer consists of silicon microstrip sensors: two sensors are arranged back-to-back at a relative angle of 40 mrad to provide precise position measurements, with a resolution of about 17 μm in the $r - \phi$ plane. The resolution in the z (r) direction of the barrel (endcap) modules is worse—580 μm. The SCT has 6 million readout channels.

3.2.1.3 Transition Radiation Tracker

The Transition Radiation Tracker (TRT) is the outermost subdetector in the inner detector, located at a radius of ∼550–1100 mm and covering a range of $|\eta| < 2.0$ [8]. The element providing measurements in the TRT is a proportional drift tube ("straw") with a diameter of 4 mm. The straws consist of an aluminum cathode deposited on electrically insulating Kapton; the straw is mechanically reinforced with carbon fiber bundles. Running along the center of the straw is a gold-plated tungsten wire anode from which the signal is read out. A voltage difference 1500 V is kept between anode

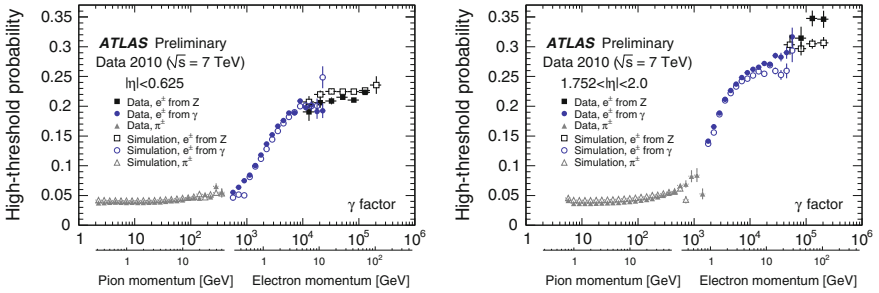

Fig. 3.7 The high threshold probability in a region of the barrel ($|\eta| < 0.625$, left) and in the endcap ($1.752 < |\eta| < 2.0$, right). Particles with a low γ factor such as pions have small high threshold probabilities, and those with a high γ factor (electrons) have larger high threshold probabilities [9]

and cathode. The straws are filled with a mixture of gas (70% Xe, 27% CO_2, 3% O_2); Xenon provides the ionizing radiation used to create the signal pulse.

In the TRT, a polyethelene fiber (barrel) or polypropylene foil (endcap) is arranged between the straw layers. The material has a different dielectric constant than its surroundings; and a particle traversing the matrix of foil boundaries has a probability of emitting a photon (called "transition radiation") proportional to the γ-factor of the particle—lighter particles are more likely to emit transition radiation than heavier particles. The radiated photons have ~keV-scale energies that can ionize Xenon, leading to larger signals in the TRT drift tube. The TRT has a ternary threshold output: zero, low-threshold and high-threshold. Electrons—which are much lighter than their backgrounds, are more likely to induce high-threshold hits along their trajectory, as illustrated by Fig. 3.7. This phenomenon is used in electron identification to discriminate against backgrounds.

3.2.2 The Calorimeters

ATLAS has two main calorimeter systems, the liquid Argon calorimeter (LAr calorimeter) and the Tile Calorimeter (TileCal), for inducing and measuring electromagnetic and hadronic showers. Its system of forward calorimeters, designed based on similar principles and instrumenting the region $1.5 < |\eta| < 3.2$, are not described in detail here. Calorimeter showers can be characterized according to their longitudinal depth and its lateral width, which vary according to the type of incident particle and the nature of the absorber used in the calorimeters.

Electrons and photons passing through an absorber will shower electromagnetically: photons produce e^+e^- pairs and electrons emit bremsstrahlung photon radiation; the daughter electrons and photons also interact, resulting in a particle shower. Most of the energy will have been absorbed after traversing about 20 radiation lengths X_0 of absorber (longitudinal depth). The lateral width of the shower in a material is

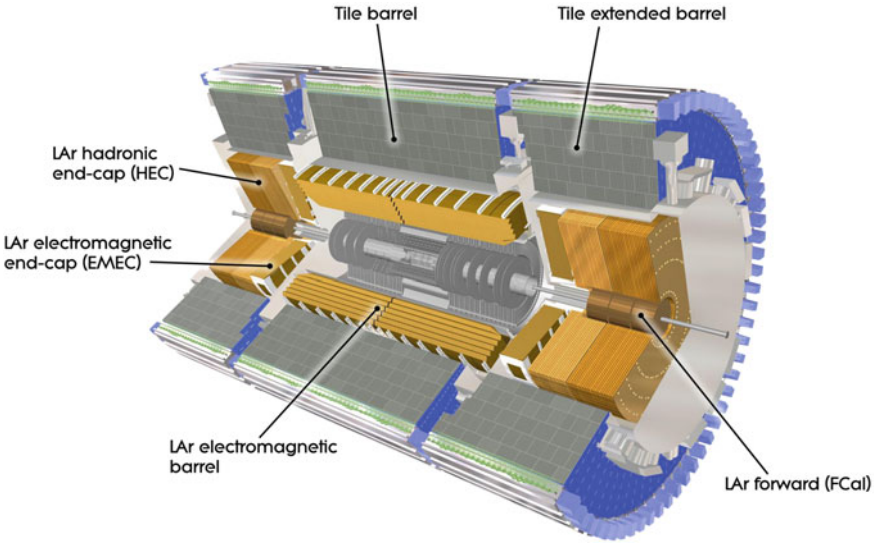

Fig. 3.8 The LAr and Tile calorimeters [11]

characterized by its Molière radius, the radius of a cone in which 90% of the shower energy is contained.

Hadrons, on the other hand, shower mostly via strong interactions. The shower develops in a similar cascade of decay products, about 1/3 of which are π^0 which decay electromagnetically, initiating an electromagnetic shower component to the total shower. Hadronic showers are characterized by a core energy deposit, partially due to the electromagnetic showering, and a larger tail of energy deposition [10].

The LAr and Tile calorimeters, depicted in Fig. 3.8, are both sampling calorimeters, alternating absorber and active layers. The LAr was specifically designed to aid electron and photon discrimination against hadronic jets. It uses liquid argon as an active material, whose relatively small Molière radius (10 cm) results in compact electromagnetic showers from electrons and photons. These local shower deposits can be identified against the more diffuse showers of hadronic jets.

3.2.2.1 Liquid Argon Calorimeter

The Liquid Argon Calorimeter is an electromagnetic calorimeter consisting of alternating lead+steel absorber sheets ranging from 1.1−2.2 mm, liquid argon in a space of 2.1 mm, and copper-polyimide readout boards arranged in an accordion geometry. The lead absorber has a small X_0 (about 0.5 cm) allowing for a compact calorimeter design. The LAr barrel is split into four layers: a presampler to correct for upstream energy loss, a finely segmented first sampling layer for accurate η pointing ($\delta\eta = 0.003$), a second layer with interaction length $X_0 \sim 16$ and granularity

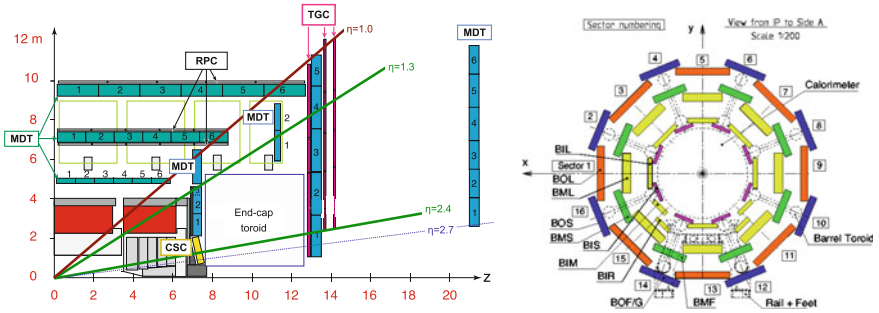

Fig. 3.9 Left: schematic of the muon detectors, including MDT, CSC, RPC and TGC chambers [13]. Right: view along the beam axis of the MDT chambers [5]

0.025×0.0245 ($\eta \times \phi$), and a final sampling to assist in characterizing the shower development. Electrons and photons showering in the LAr calorimeter deposit most of their energy in a cone contained in a 5×5 block of cells in the second layer. The entire LAr Calorimeter is encased in a cryostat held at around 90 K. The transition region between the LAr barrel and endcaps located at roughly $1.37 < |\eta| < 1.52$ is dedicated to detector services and is thus not fully instrumented.

3.2.2.2 Tile Calorimeter

The Tile Calorimeter (TileCal) [12] is a hadron calorimeter located at a radius $\sim$2.3−3.9 m from the IP, composed of alternating steel plate absorber and plastic scintillators. Light from the scintillators is channeled through fiber optics, which run to PMTs located in the outer structural element of the TileCal. The calorimeter barrel (endcap) consists of 3 or 4 layers of cells of roughly 0.1×0.1 ($\eta \times \phi$), allowing for three-dimensional energy deposit readout. The TileCal material represents about 8–10 hadronic interaction lengths.

3.2.3 The Muon Spectrometer and Toroid

The muon spectrometer (MS) [5] is a system of tracking detectors surrounding the calorimeters, designed for measuring muon momenta with the aid of three air-core toroidal magnets to bend particles. Several detector technologies are used to record spatial measurements of muons (Fig. 3.9). Three layers of Monitored Drift Tube Chambers (MDTs) cover the region $|\eta| < 2.7$. Due to high radiation levels in the region $2.0 < |\eta| < 2.7$ the innermost layer of MDTs is replaced by multi-wire proportional chambers called Cathode Strip Chambers (CSCs).

Muons with $|\eta| < 2.4$ can be triggered using two technologies: Resistive Plate Chambers (RPCs) cover the barrel region $|\eta| < 1.05$ and multi-wire proportional chambers called Thin Gap Chambers (TGCs) are used in the endcap $1.0 < |\eta| < 2.4$. Muon triggers are based on coincidences in two or more layers with a pattern fitting the description of a muon track above a minimum p_{T} threshold.

During the shutdown between Run 1 (end of the 2012) and the beginning of Run 2 (2015), additional muon detectors were added to the barrel-endcap transition region, $1.0 < |\eta| < 1.4$, and in additional regions to increase the acceptance compared to Run 1 [14].

3.2.4 Reconstruction Algorithms and Identification Techniques

ATLAS identifies electrons, photons, muons, jets and taus[3] by converting raw detector data to fundamental physics objects using a dedicated set of algorithms, collectively referred to as event reconstruction. The basic building blocks for constructing these objects are the particle trajectories (tracks) reconstructed from hits in the inner detector and muon spectrometer (in the case of muons), providing an estimate of a particle's momentum, and topological clusters constructed from energy deposits in the calorimeters. A second clustering algorithm for determining local energy deposits in the EM calorimeter, the sliding window algorithm, is used in the reconstruction of electrons and photons.

Track Reconstruction. Track reconstruction can be characterized in terms of three steps: a seeding step performed with hits in the silicon detectors, a pattern recognition step where the track seeds are extended to the rest of the ID, and a final track fitting step using the result of the pattern recognition. The tracking makes specific accommodations to increase the efficiency of finding tracks from electrons and converted photons.

The tracking steps are as follows:

- Segments of 3 silicon hits are found that meet basic p_{T} and spatial requirements.
- The pattern recognition step is run with an algorithm based on the Kalman Filter [15] with a pion track hypothesis (meaning that minimal energy loss is expected as the particle traverses the ID material).
- If the first pattern recognition fit fails, a second fit is attempted with a modified algorithm that allows for energy loss at each hit surface. This procedure recovers electrons with significant energy loss due to bremsstrahlung.
- Successful tracks from the Kalman Filter are rerun using the ATLAS Global χ^2 Track Fitter [16]. A pion or an electron hypothesis is used, depending on which was used successfully in the previous step.

[3] Tau reconstruction and identification is not discussed here.

The track reconstruction process described above can be described as an "inside-out" algorithm, with tracking seeded by the silicon hits close to the interaction point and extrapolated outward toward the calorimeters. A complementary "outside-in" algorithm, in which tracks are seeded using segments in the TRT and extended inward, is run to aid in the reconstruction of converted photons.

Topological Energy Clusters. Energy clusters used for defining jets are reconstructed using a topological clustering algorithm [17, 18]. Topological clusters are formed using the three-dimensional energy deposits in the EM and hadronic calorimeters. The process is iterative: beginning with a list of seed cells with a high signal-to-noise ratio $|E_{\text{cell}}| > 4\sigma_{\text{noise}}$, all cells touching the border of a seed cell (neighboring cells) are added to the cluster. If the neighboring cell has a signal-to-noise ratio $|E_{\text{cell}}| > 2\sigma_{\text{noise}}$ then the border of the cell becomes part of the seed border for the next iteration. The process repeats with the neighbors of the newly-defined border, until the border stops increasing. Jets are then formed using the anti-k_t algorithm [19] with radius parameter $R = 0.4$[4] using the topological clusters as an input.

The topological clustering algorithm is also used to construct lepton variables describing how isolated the lepton candidate is in the calorimeter (described later). For these applications the noise thresholds of the algorithm are slightly modified, but the basic principle is similar.

The Sliding Window Algorithm. Electromagnetic clusters for electron and photon reconstruction are formed using the sliding-widow algorithm [17]. Cells in the EM calorimeter from all four layers are grouped into $\Delta\eta \times \Delta\phi$ towers of 0.025×0.025, and a window of 3×5 towers is moved across the detector to identify local maxima above 2.5 GeV to form a collection of seed clusters. A rectangular tower with its larger dimension in ϕ is preferred over a square template to accommodate electrons with bremsstrahlung energy loss. The electron bends in the ϕ direction due to the axial magnetic field, but its collinear photon emissions are unaffected by the field, thus smearing the energy disproportionately in the ϕ direction. The 5×7 window attempts to capture the full electron energy, including losses from bremsstrahlung.

Electrons. Electrons are formed by matching tracks reconstructed in the ID with electromagnetic clusters found using the sliding window algorithm. Tracks and clusters are required to be within a tolerance of $|\Delta\eta| < 0.05$, and $-0.2 < \Delta\phi < 0.05$, where positive values of $\Delta\phi$ are associated with the case in which the fitted track is bending away from the cluster barycenter.[5] Failing these criteria, the track momentum is rescaled to match the measured cluster energy, and tested for the tolerances $|\Delta\eta| < 0.05$ and $-0.1 < \Delta\phi < 0.05$ [20].

Tracks are then refit using the Gaussian Sum Filter tracking algorithm, which further improves the track measurement in light of bremsstrahlung losses [21]. Infor-

[4] Other collections of jets defined with different radius parameters are available as well.

[5] As with the choice of a 5×7 window for the sliding window algorithm, the greater tolerance on one side of the $\Delta\phi$ distribution is to accommodate electron energy loss due to bremsstrahlung.

mation from the cluster and track are combined to measure the track momentum. Further corrections are applied to fully calibrate the electron energy [22].

Photons. Electromagnetic clusters formed using the sliding window algorithm and without an associated track are automatically classified as photons. However, roughly 30–50% of all photons convert inside the detector material, occurring more often in the endcaps where the photons traverse more material. Clusters with an associated track are initially classified as electrons, and a procedure is run to disambiguate converted photons and electrons by trying to find a two-track vertex inside the detector, or by checking whether the track leaves a hit in the innermost layer of the inner detector. Converted photons classified as electrons are a main electron background.

Muons. Muons can be reconstructed in one of several ways, depending on the instrumentation of the detector in the region traversed by the muon:

- Combined muons: a MS track is matched to a reconstructed track in the ID, and the measurements of the momenta are combined.
- Segment-tagged muons: a partial MS track is matched to an ID track, and the muon momentum is taken from the ID measurement.
- Standalone muons: MS tracks found outside the ID acceptance ($2.5 < |\eta| < 2.7$) and momentum taken from the MS track.
- Calorimeter-tagged muons: in the non-active "crack" of the MS at $|\eta| < 0.1$ and dedicated to services, tracks in the ID with $p_{\mathrm{T}} > 15\,\mathrm{GeV}$ and an associated calorimeter deposit consistent with a minimum ionizing particle.

A number of quality requirements can be imposed on the reconstructed muons, including minimum requirements on the number of hits in each of the ID subdetectors and the MS, where applicable.

Prompt versus non-prompt leptons. Leptons (muons and electrons—excluding taus) can be separated into two types. *Prompt* leptons are participants in the hard-scatter process, such as decay products of the short-lifetime ($\ll 1\,\mu\mathrm{m}$) W, Z and Higgs bosons. *Non-prompt* leptons are the weak decay products of b-jets and c-jets, whose lifetimes are relatively long ($c\tau \approx 450\,\mu\mathrm{m}$ for b-jets, and as much as $c\tau \approx 300\,\mu\mathrm{m}$ for c-jets). As a result, their decay products can be traced back to a vertex that is displaced from the hard-scatter process. ATLAS lepton identification is designed to identify the prompt leptons involved in electroweak physics and to reject the non-prompt leptons from these heavy-flavor jets.

Lepton Impact Parameter Requirements. To reject non-prompt leptons, requirements are placed on the distance of closest approach between the lepton's track and the primary collision vertex.[6] Two variables from the track fit are used. The first is the transverse impact parameter, d_0, defined as the track's distance of closest approach to the collision vertex in the transverse plane.[7] This variable can also be formulated

[6]The primary vertex is defined as the vertex with the highest $\sum p_{\mathrm{T}}^2$ summed over all tracks in the vertex.

[7]In 2011 and 2012, the d_0 is calculated with respect to the measured position of the primary vertex. Beginning in 2015, the d_0 is calculated with respect to the beam line (labeled d_0^{BL}).

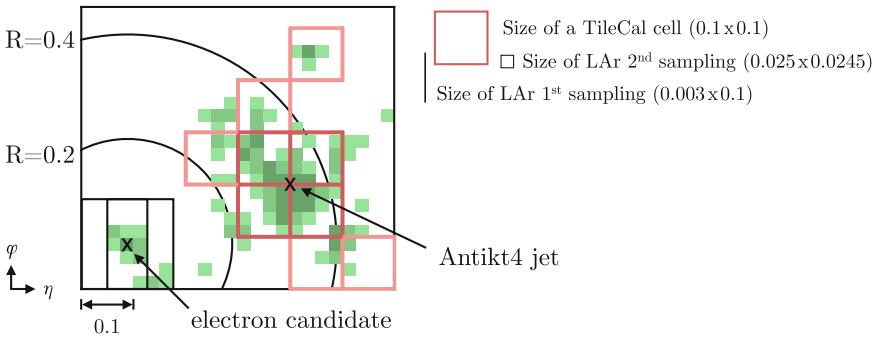

Fig. 3.10 Depiction of isolation cones ($\Delta R = 0.2$, 0.3 and 0.4) in relation to detector element sizes. The cone sizes are compared to LAr and Tile calorimeter cells, as well as the 7×7 cell block used to construct electron calorimeter variables. An artist's rendition of energy deposits from an electron and a hadron is depicted, simulating energy deposits in the 2nd layer of the LAr calorimeter (green) and energy deposits in the hadronic calorimeter (red)

into an impact parameter significance: $|d_0/\sigma_{d_0}|$, where σ_{d_0} is the defined by the error matrix of the track fit. The second variable used is $|z_0 \sin\theta|$, where z_0 is the distance between the z-position of the vertex and the z-position of the point on the track at which d_0 is defined, and $\sin\theta$ is the polar angle of the track. The d_0 and $|z_0 \sin\theta|$ of non-prompt leptons will have distributions with large tails, allowing many of them to be rejected.

Lepton Isolation. Calorimeter and track isolation variables reflect the ambient energy in a cone surrounding a lepton candidate, and are used as a powerful discriminant for selecting prompt leptons against the non-isolated lepton decay products in heavy-flavor jets, or from light-flavor jets (including u, d, and s-quark-initiated jets or gluon-initiated jets). Figure 3.10 relates the cone sizes used to describe these isolation variables, and their relation to calorimeter cell sizes.

For both electrons and muons, track isolation is defined as the scalar sum of all track momenta above a certain p_{T} threshold (typically around 0.4–1 GeV) in a cone $\Delta R = 0.2$, 0.3 or 0.4 around the electron candidate, excluding the track matched to the lepton candidate. Track isolation variables are typically formulated relative to the p_{T} of the associated object, e.g. $p_{\mathrm{T}}^{\mathrm{iso}}/p_{\mathrm{T}}$ to improve the efficiency of isolation requirements for higher-p_{T} objects.

There are two types of calorimeter-based isolation: "cell-based" and "topological" isolation. Cell-based calorimeter isolation is computed using the energy in the electromagnetic and hadronic calorimeters in a cone of $\Delta R = 0.2$, 0.3 or 0.4, excluding energy in the calorimeter associated with the lepton.[8] This energy in the surrounding cone is referred to as the "isolation energy," $E_{\mathrm{T}}^{\mathrm{iso}}$. The small amount of electron

[8] In the electron case, the energy in the 5×7 cell window surrounding the cluster in the EM calorimeter is associated with the electron (corresponding to 0.125×0.172 in $\eta - \phi$ space). In the muon case, the energy associated to the muon object is optimized on a layer-by-layer basis in the EM and hadronic calorimeters [23].

energy leaking out of its 5×7 window, typically just a few percent, is subtracted from $E_{\mathrm{T}}^{\mathrm{iso}}$. Furthermore, a correction term representing the ambient energy density of the event due to underlying event and pileup events is also subtracted from $E_{\mathrm{T}}^{\mathrm{iso}}$ [24]. As in the case of track isolation, calorimeter isolation variables are often formulated relative to the E_{T} of the associated object, e.g. $E_{\mathrm{T}}^{\mathrm{iso}}/E_{\mathrm{T}}$ to improve the efficiency of isolation requirements for high-E_{T} objects.

Topological isolation is an improvement over cell-based isolation, which has a dependence on out-of-time pile-up that changes the variable's behavior as a function of the position of the collision in the bunch train. The topological isolation variable, which constructs topological clusters in a cone $\Delta R = 0.4$ around the electron candidate and computes the isolation using these clusters, is much more stable as a function of bunch train position [25].

3.2.5 The Trigger System

ATLAS cannot save all 40 million brunch crossings ("events") delivered per second for further analysis; it would take too long to reconstruct every event and too much storage space. The collaboration has resources to save about 1000 events per second, and it must prioritize the events that it saves in the development of its physics program. To achieve this, the ATLAS trigger system is a dedicated system of hardware and fast-processing algorithms run immediately after the event occurs to determine which events to save. (If the event is deemed interesting enough for further study, it is said to have "fired" a trigger.)

The trigger system consists of algorithms that run in three consecutive decision-making steps. The first step, called the "Level 1" (L1) trigger system, is run on coarse-grained information from the sub-detectors using fast-processing electronics. Decisions on candidate electrons, photons, muons, jets, and missing transverse energy must be made by the L1 trigger within 1 μs, and reduce the 40 MHz collision rate down to 75–100 kHz events passed to the next step.

Events passing the L1 trigger are passed to the L2 trigger step. Fragments of the detector data that had been waiting in buffers are read out to a computer farm for further analysis. The data correspond to regions of interest (ROIs) in cones of $\eta \times \phi$ space of the detector volume. The data is unpacked and more sophisticated algorithms are run. The L2 system has a latency of 40 ms and an output rate of around 3–5 kHz.

The final step is the event filter (EF—the L2 and EF steps are collectively referred to as the HLT). The full event is read out from the detector buffers, and the algorithms used to reconstruct and select objects are as close to the offline reconstruction software as possible. The EF step reduces the output to 500–1000 Hz in about 4 s. Figure 3.11 shows the output trigger rates of the HLT in 2015. The plot indicates the prioritization of the ATLAS physics program; about 1/3 of the program is dedicated to physics with electrons and muons.

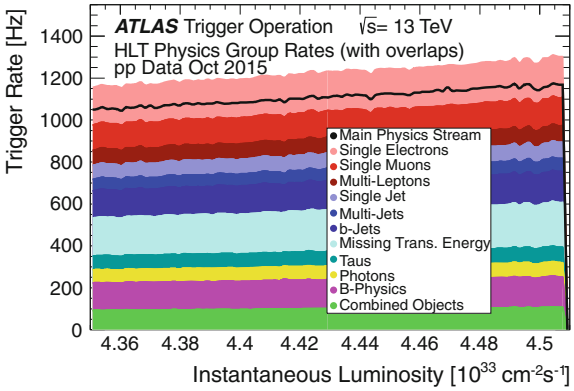

Fig. 3.11 Output trigger rate at the HLT in 2015. The total output ("Main Physics Stream") is less than the individual physics group rates due to events firing more than one trigger [26]

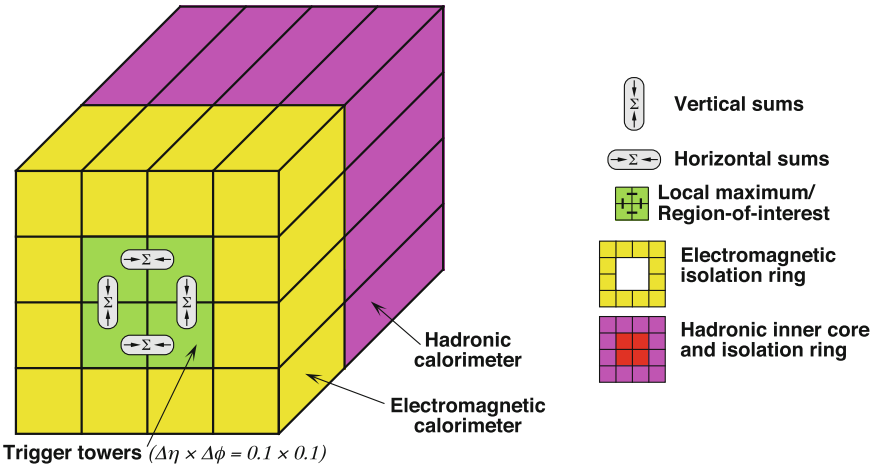

Fig. 3.12 The components of the Level 1 Calorimeter Trigger [27]

3.2.5.1 Electron Trigger Algorithms

Because of the emphasis in this document on electrons, the electron trigger strategy is briefly reviewed. The Level 1 Calorimeter trigger [27] used to select electrons and photons at L1 ("EM" objects) is executed using the analog sums of cells grouped into coarsely-grained "towers" of size $\eta \times \phi = 0.1 \times 0.1$. The basic building block of a L1EM trigger is a 2×2 block of electromagnetic trigger towers, depicted in Fig. 3.12.

A L1EM trigger is fired if any two adjacent trigger towers ("vertical sums" and "horizontal sums") in the 2×2 block satisfy a certain energy threshold. L1EM triggers can have variable thresholds as a function of η. An isolation requirement can

also be applied at L1 by requiring that the 12 cells of the surrounding electromagnetic isolation ring not be above a maximum programmable value. Finally, the amount of hadronic activity can be limited by requiring that the energy in the 2×2 hadronic core behind the EM towers be below a threshold.[9]

References

1. L.R. Evans, P. Bryant, LHC machine. JINST **3**, S08001 (2008)
2. ALICE Collaboration, K. Aamodt et al., The ALICE experiment at the CERN LHC. JINST **3**, S08002 (2008). https://doi.org/10.1088/1748-0221/3/08/S08002
3. LHCb Collaboration, A.A. Alves Jr. et al., The LHCb detector at the LHC. JINST **3**, S08005 (2008). https://doi.org/10.1088/1748-0221/3/08/S08005
4. CMS Collaboration, The CMS experiment at the CERN LHC. JINST **3**(08), S08004 (2008)
5. ATLAS Collaboration, The ATLAS experiment at the CERN Large Hadron Collider. JINST **3**, S08003 (2008). https://doi.org/10.1088/1748-0221/3/08/S08003
6. ATLAS Collaboration, Luminosity public results (2016), https://twiki.cern.ch/twiki/bin/view/AtlasPublic/LuminosityPublicResults
7. M. Capeans, G. Darbo, K. Einsweiller, M. Elsing, T. Flick, M. Garcia-Sciveres, C. Gemme, H. Pernegger, O. Rohne, R. Vuillermet, ATLAS insertable B-layer technical design report. Technical report, CERN-LHCC-2010-013. ATLAS-TDR-19, Sept 2010, https://cds.cern.ch/record/1291633
8. ATLAS TRT Collaboration, The ATLAS transition radiation tracker (TRT) proportional drift tube: design and performance. J. Instrum. **3**(02), P02013 (2008), http://stacks.iop.org/1748-0221/3/i=02/a=P02013
9. ATLAS Collaboration, Particle identification performance of the ATLAS transition radiation tracker, ATLAS-CONF-2011-128 (2011), http://cdsweb.cern.ch/record/1383793
10. M. Krämer, F.J.P. Soler, Large Hadron Collider phenomenology, in *Proceedings of the 33rd International Conference on High Energy Physics (ICHEP '06)* (IOP, Bristol, 2005), http://cds.cern.ch/record/602552
11. J. Pequenao, Computer generated image of the ATLAS calorimeter, Mar 2008
12. ATLAS Collaboration, ATLAS tile calorimeter: technical design report. CERN, Geneva, 1996, https://cds.cern.ch/record/331062
13. ATLAS Collaboration, Performance of the ATLAS muon trigger in pp collisions at $\sqrt{s} =$ 8 TeV. Eur. Phys. J. C **75**, 120 (2015), arXiv:1408.3179 [hep-ex]
14. ATLAS Collaboration, Muon reconstruction performance of the ATLAS detector in proton–proton collision data at $\sqrt{s} = 13$ TeV. Eur. Phys. J. C **76**(5), 292 (2016), arXiv:1603.05598 [hep-ex]
15. T. Cornelissen, M. Elsing, S. Fleischmann, W. Liebig, E. Moyse, A. Salzburger, Concepts, design and implementation of the ATLAS new tracking (NEWT), ATL-SOFT-PUB-2007-007 (2007), https://cds.cern.ch/record/1020106
16. T.G. Cornelissen, M. Elsing, I. Gavrilenko, J.-F. Laporte, W. Liebig, M. Limper, K. Nikolopoulos, A. Poppleton, A. Salzburger, The global χ^2 track fitter in ATLAS. J. Phys. Conf. Ser. **119**(3), 032013 (2008), http://stacks.iop.org/1742-6596/119/i=3/a=032013
17. W. Lampl et al., Calorimeter clustering algorithms: description and performance, ATL-LARG-PUB-2008-002 (2008), http://cds.cern.ch/record/1099735

[9] A shorthand is used to describe the L1EM triggers: the EM18 trigger has an energy threshold of 18 GeV. A "V" is appended if the threshold is variable as a function of η, an "H" is appended if the hadronic activity veto is applied, and an "I" is appended if the electromagnetic isolation requirement is applied.

18. ATLAS Collaboration, Topological cell clustering in the ATLAS calorimeters and its performance in LHC run 1, arXiv:1603.02934 [hep-ex]
19. M. Cacciari, G.P. Salam, G. Soyez, The anti-k_t jet clustering algorithm. JHEP **04**, 063 (2008), arXiv:0802.1189 [hep-ex]
20. ATLAS Collaboration, Electron efficiency measurements with the ATLAS detector using the 2012 LHC proton–proton collision data, ATLAS-CONF-2014-032 (2014), http://cdsweb.cern.ch/record/1706245
21. ATLAS Collaboration, Improved electron reconstruction in ATLAS using the Gaussian sum filter-based model for bremsstrahlung, ATLAS-CONF-2012-047 (2012), http://cdsweb.cern.ch/record/1449796
22. ATLAS Collaboration, Electron and photon energy calibration with the ATLAS detector using LHC run 1 data. Eur. Phys. J. C **74**, 3071 (2014), arXiv:1407.5063 [hep-ex]
23. B. Lenzi, C. Guyot, R. Nicolaidou, Search for the Higgs boson decaying to four leptons in the ATLAS detector at LHC and studies of muon isolation and energy loss. Ph.D. thesis, U. Paris-Sud 11, Dept. Phys., Orsay, France, 2010, https://cds.cern.ch/record/1301521. Accessed 17 Sept 2010
24. ATLAS Collaboration, Measurement of the inclusive isolated prompt photon cross section in pp collisions at $\sqrt{s} = 7$ TeV with the ATLAS detector. Phys. Rev. D **83**, 052005 (2011), arXiv:1012.4389 [hep-ex]
25. ATLAS Collaboration, Calorimeter isolation with topoclusters versus pile-up. Technical report, ATL-COM-PHYS-2012-362, CERN, Geneva, 2012, https://atlas.web.cern.ch/Atlas/GROUPS/PHYSICS/EGAMMA/PublicPlots/20120404/TopoIsolation/ATL-COM-PHYS-2012-362/index.html
26. ATLAS Collaboration, Trigger operation public results (2016), https://twiki.cern.ch/twiki/bin/view/AtlasPublic/TriggerOperationPublicResults
27. R. Achenbach et al., The ATLAS level-1 calorimeter trigger. J. Instrum. **3**(03), P03001 (2008), http://stacks.iop.org/1748-0221/3/i=03/a=P03001

Chapter 4
Alignment of the TRT

The actual position of detector elements in the inner detector (ID) will differ from the design geometry and the perfect description of the nominal position in the simulation software. Several effects can cause detector misalignments. Some activities cause entire detectors to move, such as turning on and off the ATLAS magnetic fields or changes in temperature conditions. Other sources of misalignment, such as limitations in precision during the detector machining process, can affect the relative position of individual detector elements with respect to one another. The purpose of alignment is to correct the position of the detector elements, whatever the cause, to improve the momentum measurements of particles traversing the ID.

Several survey systems have been developed to understand the position of subdetectors within ATLAS. However, an in-situ alignment procedure using tracks from cosmic rays or p–p collisions is a much more effective way to correct the position description of detector elements. The procedure relies on the collection of large samples of reconstructed tracks from particles that traverse multiple detector elements. A key characteristic of the reconstructed track is its track-to-hit residual, the distance between the position of the hit registered in the detector according to its current estimated location and the closest point on the trajectory describing the track. The alignment procedure updates the location description of detector elements with respect to one another (the "alignment constants") in order to minimize the residuals in the collection of tracks.

The ATLAS alignment constants have been updated many times to improve the ID geometry description. Before LHC collisions, The ID was aligned using cosmic ray data in preparation for first collisions [1]. The alignment was repeated using collision data in 2010 using $\sqrt{s} = 900\,\text{GeV}$ collision data [2]. Using collisions collected at $\sqrt{s} = 7\,\text{TeV}$, the alignment was repeated with much larger numbers of tracks, allowing more degrees of freedom to be individually aligned, and resulting in a significant improvement in key indicators of track parameter uncertainties.

Alignment can be performed at three different granularities of detector elements. The smallest detector unit in the pixel and SCT detectors is the silicon module; for the TRT, the smallest unit is the straw. These units are assembled into larger "modules" such as barrel layers or endcap discs. Modules are combined to form a full barrel or

K. Brendlinger, *Physics with Electrons in the ATLAS Detector*, Springer Theses,
https://doi.org/10.1007/978-3-319-73930-4_4

endcap sub-detector. ID alignment can be performed at three levels of granularity. Full subdetector barrels and endcaps can be aligned with respect to one another; this is referred to as Level 1 alignment. At a courser level, the modules inside each sub-detector can be aligned independently, referred to as Level 2 alignment. Finally, alignment can be performed at the level of the smallest units (silicon modules or TRT straws), called Level 3 alignment.

This chapter focuses on the alignment of the TRT during 2010 and 2011 to improve the TRT detector description. In particular, a full Level 3 alignment of the TRT was performed in 2010, correcting misalignments due to mechanical deformations in the detector that cannot be fixed using Level 1 or 2 alignment procedures. Following this, a Level 2 alignment of the endcap wheels was performed to correct translation misalignments along the beam axis and affecting low-p_{T} tracks. The result is an overall improvement in the track residuals in the TRT barrel and endcaps. Preceding the description of these alignment campaigns is a brief introduction to the alignment procedure and a review of the effects of Level 1 detector alignment.

4.1 Introduction to the Inner Detector Alignment

Track reconstruction requires a precise knowledge of the position of each active detector element in the tracking system. Figure 4.1 demonstrates the effect of a detector element that is misaligned compared to the perfect geometry description.[1] Misalignments, especially those in the plane perpendicular to the particle trajectory, impact the parameters of the reconstructed track and degrade the quality of the track fit.

Tracking is performed in the ID using the ATLAS Global χ^2 Track Fitter [3]. The track in the uniform magnetic field of the ID has a helical trajectory and can be defined by five parameters [4]:

$$\boldsymbol{\tau} = (d_0, z_0, \phi_0, \theta, q/p), \tag{4.1}$$

where d_0 and z_0 are the transverse and longitudinal impact parameters of the track with respect to the origin, ϕ_0 is the azimuthal angle of the track near the origin, θ is the polar angle, and q/p is the charge of the track divided by its momentum.

The residuals $\boldsymbol{r}$ of the track fit depend on the description of the track $\boldsymbol{\tau}$ and on the alignment constants describing the detector hit locations, $\boldsymbol{a}$:

$$\boldsymbol{r} = \boldsymbol{r}(\boldsymbol{\tau}, \boldsymbol{a}). \tag{4.2}$$

[1] The "perfect geometry" is the description of the detector in the software which assumes that it was constructed to match its exact specifications.

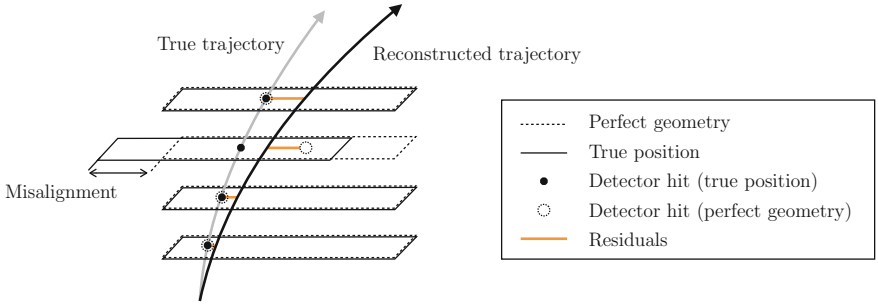

Fig. 4.1 Depiction of a detector element that is misaligned with respect to the perfect geometry, and the impact on the track fit to the particle trajectory

The χ^2 of the residuals associated with all tracks is defined as

$$\chi^2 = \sum_{\text{tracks}} \boldsymbol{r}^T V^{-1} \boldsymbol{r}, \tag{4.3}$$

where V is the covariance matrix of the residuals, as calculated by the Global Track Fitter. The correct track parameters and alignment constants can be found by minimizing this χ^2, or solving $d\chi^2/d\boldsymbol{a} = 0$, leading to the following formula:

$$2 \sum_{tracks} \left(\frac{\mathrm{d}\mathbf{r}}{\mathrm{d}\mathbf{a}} \right)^T V^{-1} \mathbf{r} = 0. \tag{4.4}$$

The residuals are a complex function of the track parameters and detector positions, so instead of solving this equation exactly, the residual can be Taylor expanded out to first order:

$$\mathbf{r} = \mathbf{r}_0 + \frac{\mathrm{d}\mathbf{r}}{\mathrm{d}\mathbf{a}} \delta\mathbf{a}, \tag{4.5}$$

where $\mathrm{d}\mathbf{r}/\mathrm{d}\mathbf{a}$ includes both the direct effect of the change in position of the detector element and the effect of the first-order change in the track parameter with the new detector position. Combining Eqs. 4.4 and 4.5 yields the following:

$$\left[\sum_{tracks} \left(\frac{\mathrm{d}\mathbf{r}}{\mathrm{d}\mathbf{a}} \right)^T V^{-1} \left(\frac{d\mathbf{r}}{d\mathbf{a}} \right) \right] \delta\mathbf{a} + \sum_{tracks} \left(\frac{\mathrm{d}\mathbf{r}}{\mathrm{d}\mathbf{a}} \right)^T V^{-1} \mathbf{r}_0 = 0, \tag{4.6}$$

which is of the form $\mathcal{M}_a \delta\mathbf{a} = \boldsymbol{\nu}_a$, a system of equations that can be solved by inverting the matrix $\mathcal{M}_a$.

The alignment constants $\boldsymbol{a}$ above refer to every degree of freedom involved in the alignment procedure, e.g. seven for a Level 1 alignment of all subdetectors; in this case, the matrix $\mathcal{M}_a$ is a 7×7 matrix that can easily be inverted. The alignment with full matrix inversion is referred to as the Global χ^2 procedure. In the case of many

Table 4.1 Description of alignment Levels 1, 2 and 3, the number of aligned structures at each level, and a description of the degrees of freedom [5]. The degrees of freedom correspond to the ATLAS coordinates described in Chap. 3. The TRT Level 3 alignment degrees of freedom are described in Sect. 4.4

Alignment level	Detector	Structures	Degrees of freedom	
			Used	Number
Level 1	Pixel: whole detector	1	All	6
	SCT: barrel and 2 end-caps	3	All	18
	TRT: barrel	1	All (except T_z)	5
	TRT: 2 end-caps	2	All	12
	Total	7		41
Level 2	Pixel barrel: half shells	6	All	36
	Pixel end-caps: disks	6	T_x, T_y, R_z	18
	SCT barrel: layers	4	All	24
	SCT end-caps: disks	18	T_x, T_y, R_z	54
	TRT barrel: modules	96	All (except T_z)	480
	TRT end-caps: wheels	80	T_x, T_y, R_z	240
	Total	210		852
Level 3	Pixel: barrel modules	1456	All (except T_z)	7280
	Pixel: end-cap modules	288	T_x, T_y, R_z	864
	SCT: barrel modules	2112	T_x, T_y, R_z	6336
	SCT: end-cap modules	1976	T_x, T_y, R_z	5928
	TRT: barrel wires	105088	T_ϕ, R_r	210176
	TRT: end-cap wires	245760	T_ϕ, R_z	491520
	Total	356680		722104

degrees of freedom (a large matrix) with complex correlations among alignment constants, the inversion is computationally prohibitive. Instead, correlations among detector elements are discarded; the matrix becomes block diagonal, and elements are aligned locally. This is referred to as the Local χ^2 alignment procedure. Both Local and Global alignments require multiple iterations, to account for the Taylor expansion simplification. Typically Local alignment requires more iterations because of the neglected correlations among detector elements [5].

Table 4.1 summarizes the degrees of freedom used for alignment at levels 1, 2 and 3. Typically alignment at level 3 requires the use of the Local χ^2 algorithm, while levels 1 and 2 can be performed using the Global χ^2 procedure.

The alignment procedure described above is susceptible to *weak modes*: systematic misalignments that do not negatively impact the χ^2 of the procedure. Weak modes can be removed by applying additional constraints to the alignment procedure; the efforts to remove weak modes are documented in [6].

An alignment procedure is run as follows: after determining which degrees of freedom to align, ATLAS reconstruction is run over a collection of tracks (either

from collision data or using cosmic ray tracks) and the terms in Eq. 4.6 are populated. (This step can be parallelized across many sub-jobs). Once the matrix is constructed, it is inverted, resulting in a new set of alignment constants. This process is repeated with the new set of alignment constants. The following qualities or quantities are used as tools to assess the success of the alignment procedure:

- Convergence: the total $\chi^2/n_{\text{d.o.f}}$ should gradually decrease after successive iterations, until $\Delta\chi^2$ approaches 0 (meaning that χ^2 is approaching its minimum).
- Mean residuals: if the mean residual, averaged over many detector elements, is nonzero, then likely some misalignment remains. A mean residual of 0 is consistent with ideal alignment constants.
- Residual RMS (or σ of a Gaussian fit): similar to the mean, the RMS is an indicator of the behavior of level of accuracy of the constants. A large residual RMS can point to persistent misalignments.
- Position of elements before and after alignment: often visualizing the detector movements or "straw displacements" can confirm whether the alignment is correcting an expected effect, or if e.g. weak modes have been introduced.

These criteria are each addressed in the following discussion of the Level 2 and 3 TRT alignment campaigns.

4.2 TRT Geometry

Figure 4.2 depicts the layout of the ATLAS ID. Each TRT Endcap consists of 80 "wheels" of straws, each one straw in thickness and consisting of 3072 straws each. Straws are assembled in groups of four wheels; this mechanical group is referred to as a "four-plane wheel" or occasionally "endcap ring." There are two types of four-

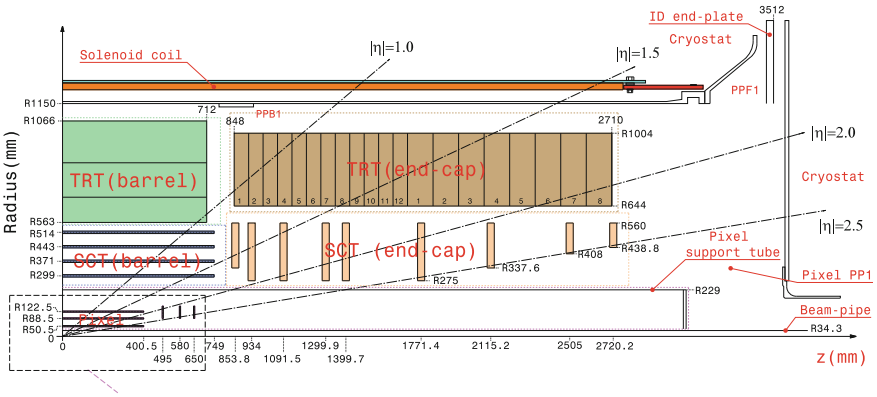

Fig. 4.2 Schematic of the ATLAS inner detector. The first twelve divisions in the endcap correspond to the six Type A-wheels, and the last eight divisions correspond to the eight Type B-wheels [7]

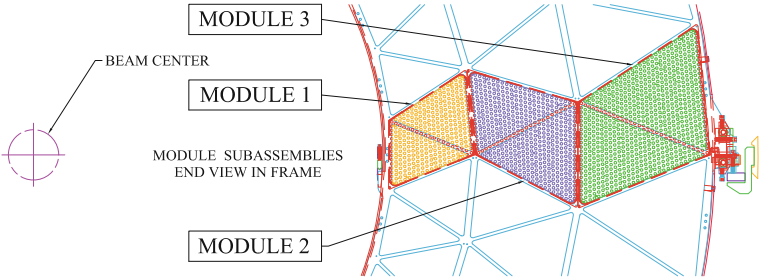

Fig. 4.3 End-view schematic of a single ϕ sector of the TRT Barrel [8]

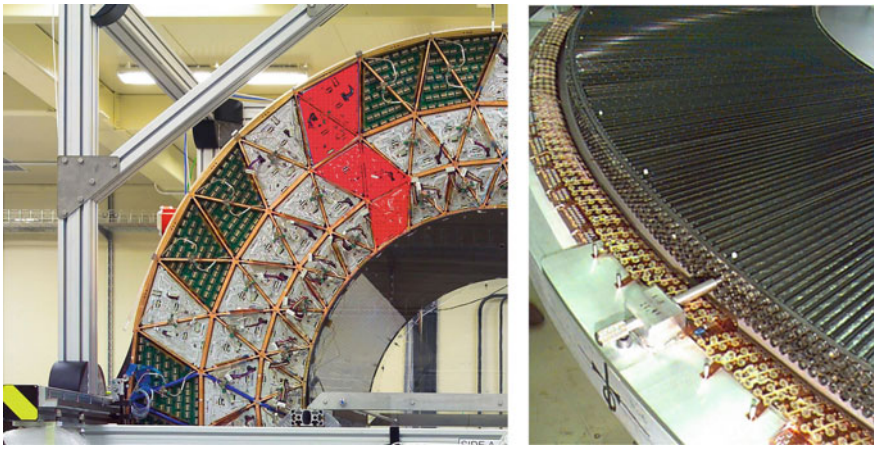

Fig. 4.4 The TRT Barrel (left) and a single four-plane wheel of the TRT Endcap (right) [7]

plane wheel—in which the straw wheels are separated by either 8 or 15 mm. Four groups of four-plane wheels with 8 mm spacing are referred to as "Type A-wheels" and positioned closer to the interaction point. Two groups of four-plane wheels with 15 mm spacing are referred to as "Type B-wheels," farther from the interaction point. A TRT Endcap consists of six Type-A wheels and 8 Type-B wheels.

A cross section of the TRT Barrel is depicted in Fig. 4.3. Three types of module are shown, which represent one of the 32 ϕ-sectors of the barrel. The barrel contains 96 modules in total. Collectively there are 73 layers of straws in the TRT Barrel, arranged to maximize the number of hits along a particle track. Straws run along the entire length of the barrel (144 cm); an insulating glass wire joint is placed at the center of each wire to split the readout into two sides (A side and C side). Because of the expected high occupancy, the nine innermost layers of the barrel are split into three sections by glass joints, where the center section is inactive.

The Level 2 alignment structures correspond to the 96 modules in the TRT Barrel and the 40+40 four-plane wheels in TRT Endcap A+C. Level 3 alignments occur at the individual straw level. Crucially, it is important to note that the TRT straw is not

sensitive to the location of the hit along the length of the straw. Therefore, the Level 3 alignment omits translations and rotations along the straw axis. This is also the reason why Level 1 and 2 alignments of the TRT barrel modules omit the translation degree of freedom along the beam (z) axis.

Figure 4.4 displays images of the TRT barrel before being lowered into the ATLAS cavern and a four-plane wheel of the endcaps during assembly.

4.3 Level 1 Alignments

Level 1 alignments are designed to correct large-scale subdetector shifts relative to one another. Beginning in 2012, time-dependent Level 1 alignment constants were introduced to correct for detector movements between LHC collision runs. The result provides a good illustration of the level of detector movements relative to one another over time. Figure 4.5 shows the evolution of the T_x degree of freedom in the alignment constant in 2012. The alignment constants were re-derived for each run, and movements are depicted with reference to the pixel subdetector, taken during a period of relative stability indicated on the image with two dashed lines [6].

Detector movements are on the order of 10 μm in 2012. These movements can be attributed to changes in the detector conditions and environment: turning on and off the ATLAS magnetic fields, changes in cooling conditions, power failures, and human

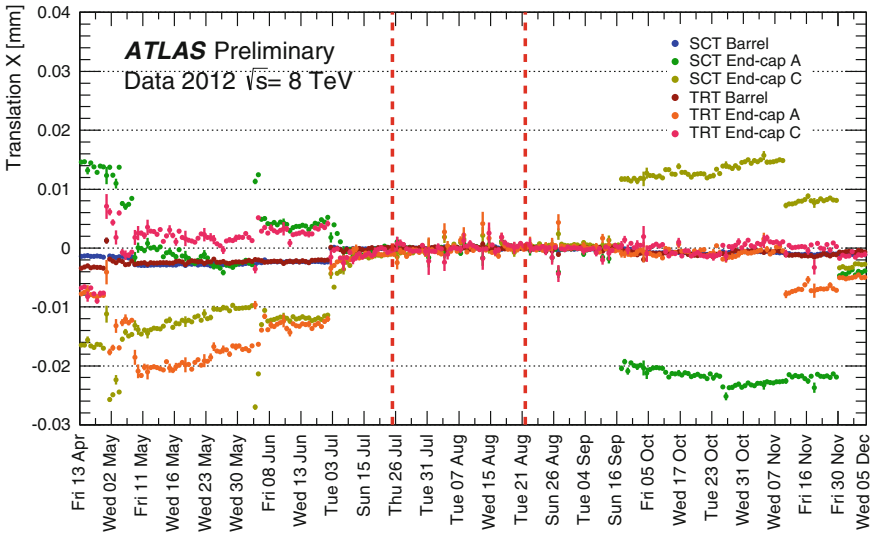

Fig. 4.5 Time-dependent alignment constants in the T_x degree of freedom during 2012 data taking, relative to the pixel detector. The Level 1 alignment procedure is repeated for every run in 2012; error bars on the detector movements reflect the statistical uncertainty due to the number of events in each run [6]

technical interventions can all cause detector movements on the scale observed. Gradual movements have been attributed to mechanical relaxation after a subdetector experiences a larger movement. Beginning in 2012, a Level 1 alignment procedure is performed on data collected in a dedicated "express stream," and new alignment constants are available a within 48 h of data collection. If the procedure detects large-scale shifts in the alignment constants, the online database used for collecting events is updated to reflect the new detector positions.

4.4 TRT Straw-Level Alignment

The Level 1 alignment procedure addresses large-scale misalignments and movements of the TRT with respect to the rest of the ID sub-detectors, and Level 2 alignment can correct the position of modules in relation to one another inside the barrel or the endcaps induced during their assembly. However, these procedures cannot correct other forms of mechanical deformation, including individual straw placement, deformations in the support structure, or from stress applied to the module after assembly. The Level 3 alignment can thus be viewed as correcting two different types of misalignment: the random misalignment of individual straws and systematic deformations. The latter, often referred to as "Level 2.5" effects, are recognizable by observing mean residuals as a function of the geometric position of collections of straws.

To simplify the Level 3 alignment process, only the straw degrees of freedom are aligned that most affect the track fit. These are the degrees of freedom that move the straw perpendicular to the particle trajectory, and correspond to one rotation and one translation in the barrel and endcaps, depicted in Fig. 4.6. The four other degrees of freedom (two translations and two rotations) have little or no effect on the measurement of the track parameters. The Level 3 TRT alignment procedure is executed using the Local χ^2 procedure described in Sect. 4.1.

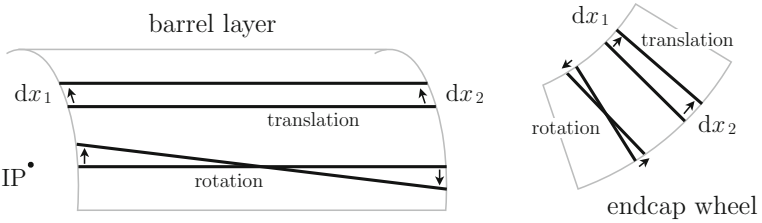

Fig. 4.6 Depiction of the local straw-level rotation and translation degrees of freedom in the barrel and endcap. The displacements dx_1 and dx_2 of the ends of each straw are referenced later in the text

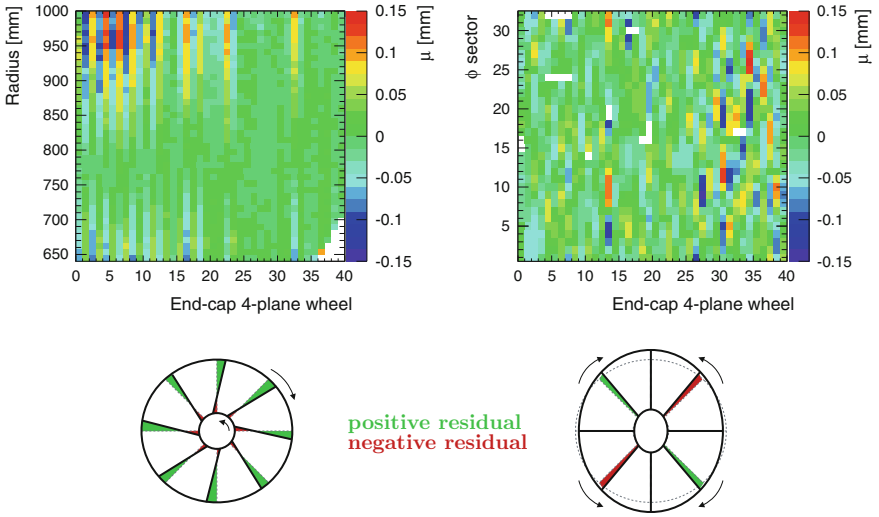

Fig. 4.7 Mean residuals of straws in Endcap A, grouped into four-plane wheels and as a function of radius from the beam pipe (left) and phi sector (right). Below, sketches of the deformations that can explain the behavior of the residuals

4.4.1 Level 3 Endcap Alignment

Before performing the Level 3 alignment procedure it is instructive to understand trends in the track residuals. Figure 4.7 depicts the mean residuals in each four-plane wheel of Endcap A, both as a function of the residual's radial distance from the beam pipe and as function of its ϕ sector position. Coherent trends can be seen in both dimensions, and the residual behavior changes sharply at the boundaries between four-plane wheels. Residuals in localized areas are as large as $\pm 150\,\mu\text{m}$.

The behavior as a function of radial distance is consistent with a ϕ rotation ("twist") of the inner support wheel with respect to the outer support structure. The sketch below depicts the deformation of the wheel and the effect on the residual positions. This behavior is consistent with an imperfection in the assembly table transmitted to the wheel geometry. Adjacent wheels were constructed on the same table and glued back-to-back, explaining the fact that the direction of the rotation is often inverted in neighboring four-plane wheels.

The residual behavior as a function of ϕ resembles an oscillation with two periods around the entire wheel, consistent with an elliptical deformation as depicted in the accompanying sketch. (Four-plane wheel number 30 best exhibits this behavior, for example.) Both of these "Level 2.5" deformations should be corrected by the Level 3 alignment procedure, moving the individual straws to match the deformation patterns and thus removing the structures visible in the mean residual distributions.

The Level 3 alignment procedure was performed using 4.3 million collision tracks from data collected in 2010 at $\sqrt{s} = 900\,\text{GeV}$ c.o.m. energy. The detector was aligned

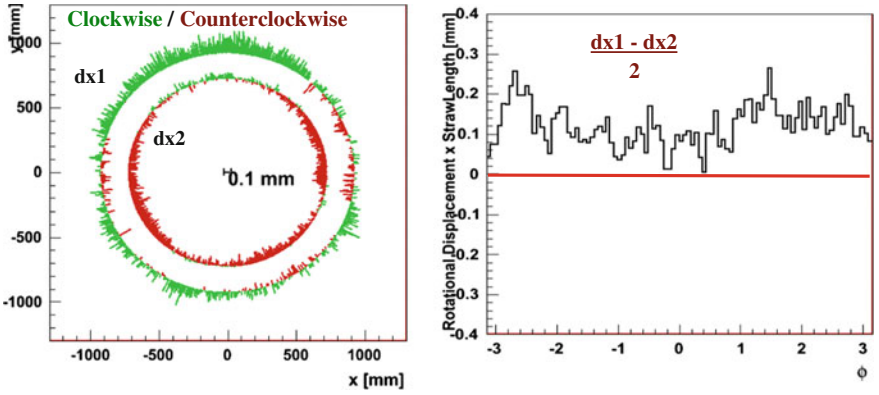

Fig. 4.8 Summary of straw movements during Level 3 Endcap alignment for a single plane in Endcap A. Left: At the (x,y) position of the outer (x_1) and inner (x_2) end of each straw, the magnitude of the tangential displacement is indicated in the radial direction. Clockwise movement is indicated using a green line pointed outward and counterclockwise movement with a red line pointed inward. Right: the rotational displacement $(\mathrm{d}x_1 - \mathrm{d}x_2)/2$ of each straw as a function of ϕ

at Levels 1 and 2 before conducting the Level 3 alignment, and only TRT degrees of freedom were allowed to float. The local χ^2 alignment algorithm was used, and the procedure converged was found after around 15 iterations.

The effects of the Level 3 Endcap alignment can be visualized by illustrating the magnitude of straw movements in each endcap plane. Figure 4.8 illustrates the straw movements of a straw plane suffering from a twist deformation. The ends of the straws on the inner edge of the wheel move in a counterclockwise direction while the outer straw ends move coherently clockwise.

Figure 4.9 illustrates the movements of straws in a plane suffering from an elliptical deformation. Straw displacements are mostly translational, with the inner and outer ends of each straw moving in the same direction. The oscillating displacement pattern completes the two periods characteristic of this deformation. Finally, Fig. 4.10 depicts the movement in eight consecutive straw planes. Straw planes within the same four-plane wheel have coherent patterns of movement, and different four-plane wheels have different movements. This effect is consistent with the Level 3 alignment correcting mechanical deformations at the four-plane wheel level.

The coherent residual patterns as a function of radius and ϕ are revisited in Fig. 4.11, with the residuals plotted using the same z-axis scale. The structures present in residuals using the previous alignment constants have been corrected, with variations in the residual means on the order of tens of microns instead of hundreds.

The effects of the Level 3 alignment on the overall hit resolution can be summarized in the aggregate residual distributions. Figure 4.12 displays the mean residual in each endcap ring (four-plane wheel) before and after the alignment procedure. The intrinsic resolution of straws in the endcaps improves from 166 μm to ∼148 μm as a consequence of the Level 3 alignment.

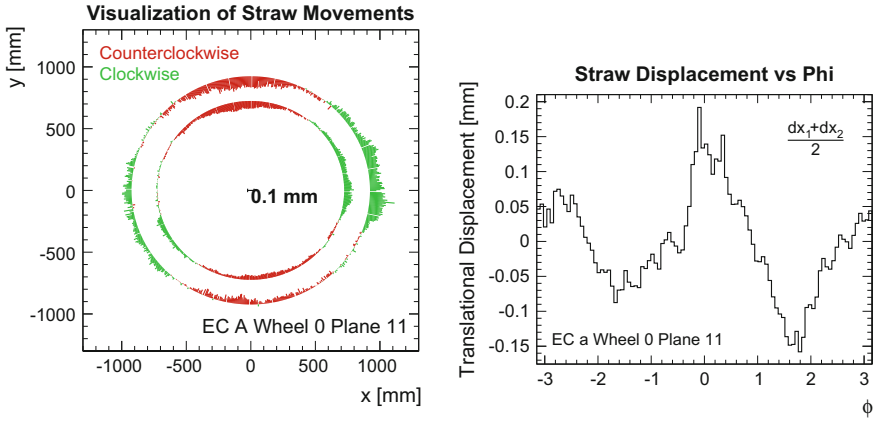

Fig. 4.9 Summary of straw movements during Level 3 Endcap alignment for a single plane in Endcap A. Left: At the (x,y) position of the outer (x_1) and inner (x_2) end of each straw, the magnitude of the tangential displacement is indicated in the radial direction. Clockwise movement is indicated using a green line pointed outward and counterclockwise movement with a red line pointed inward. Right: the average translational displacement $(\mathrm{d}x_1 + \mathrm{d}x_2)/2$ of each straw as a function of ϕ

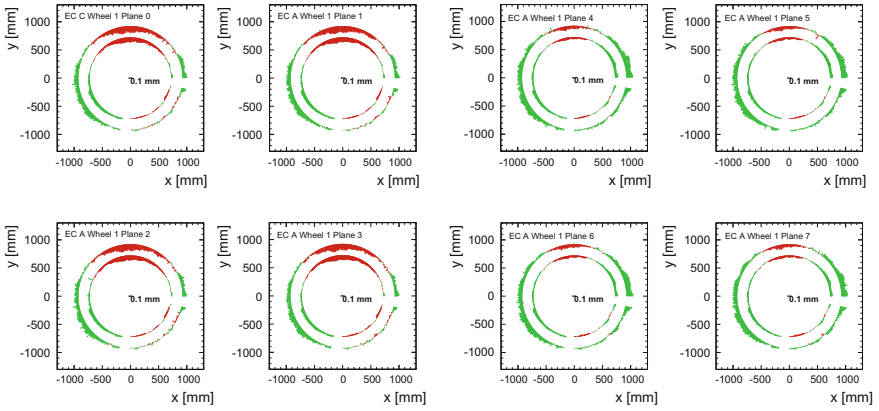

Fig. 4.10 Straw movements in eight consecutive plane wheels in Endcap A

4.4.2 Level 3 Barrel Alignment

The Level 3 alignment procedure was also applied to straws in the TRT barrel. Again, one rotation and one translation degree of freedom were allowed to float during the procedure, corresponding to straw displacements in the plane perpendicular to the particle path from the interaction point. The procedure was run using the same collection of tracks as were used for the endcap Level 3 alignment; convergence was achieved after 6 iterations.

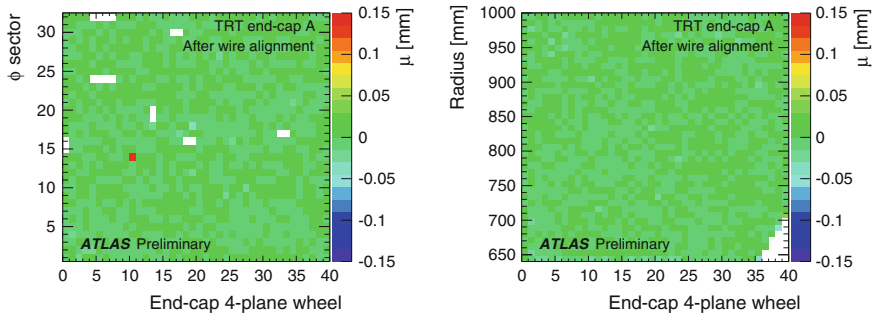

Fig. 4.11 Mean residual position as a function of ϕ sector (left) and radius from the beam line (right) in each end-cap 4-plane wheel of Endcap A, after TRT Level 3 alignment [5]

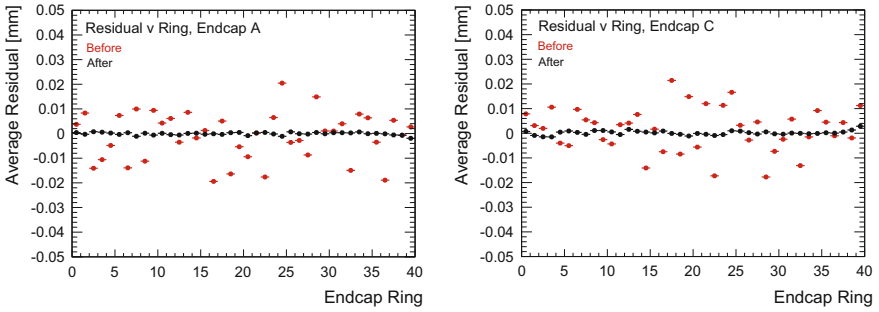

Fig. 4.12 Average residual as a function of endcap ring (four-plane wheel) in Endcap A (left) and C (right)

Figure 4.13 depicts the mean track residuals as a function of the z position and ϕ sector of each hit residual. In contrast with the TRT Endcaps, straws in the barrel do not display large coherent residual structures above the 50 μm level, though some distortions can be seen in the center of the barrel. After alignment, these small structures disappear.

Since the barrel modules do not display significant coherent residual patterns indicative of a mechanical deformation, movements of the individual straws during the Level 3 alignment procedure can be viewed as an in-situ measurement of the straw placement accuracy during assembly. Figure 4.14 reports the translational and rotational displacements of the straws in the barrel, indicating that the individual straw placement accuracy during assembly is better than 50 μm.

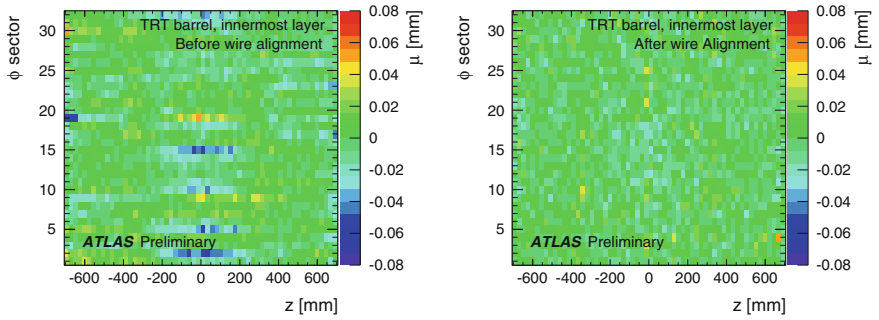

Fig. 4.13 Mean residuals in the TRT Barrel as a function of the z and ϕ position of the hit residual, before (left) and after (right) Level 3 barrel alignment

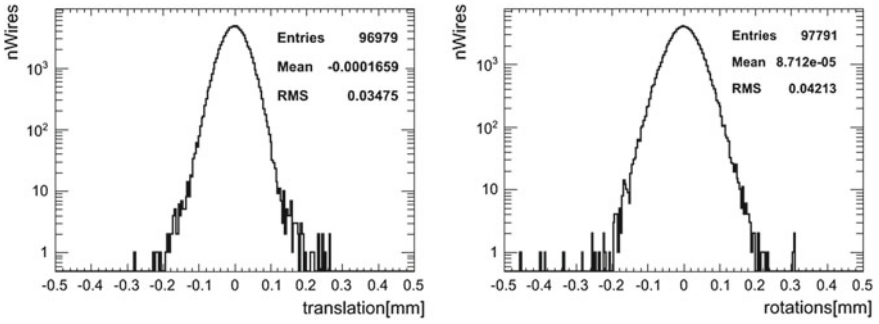

Fig. 4.14 Translational (left) and rotational (right) displacements of straws in the TRT barrel. Translations are defined as $(dx_1 + dx_2)/2$ and rotations as $(dx_1 - dx_2)/2$, where dx_1 and dx_2 are the tangential displacements of the two ends of each straw

4.4.3 Level 3 Alignment Summary

The result of Level 3 alignment is summarized in Fig. 4.15. In comparing with the previous ("Spring 2010") set of alignment constants, the new ("Autumn 2010") alignment constants improves hit resolutions, particularly in the Endcaps. These constants are the result of Level 3 TRT alignment along with alignment improvements in the other sub-detectors. The figure also compares TRT residuals with Monte Carlo simulation using a perfect geometry. In the barrel, the hit resolution has exceeded the simulation, while the resolution is still less ideal in the endcaps.

4.4.4 TRT Endcap Misalignment Along Beam Axis

In early 2011, studies of residuals in the endcaps revealed unexpected behavior. The average residual in each endcap was close to 0 μm, however the widths of the

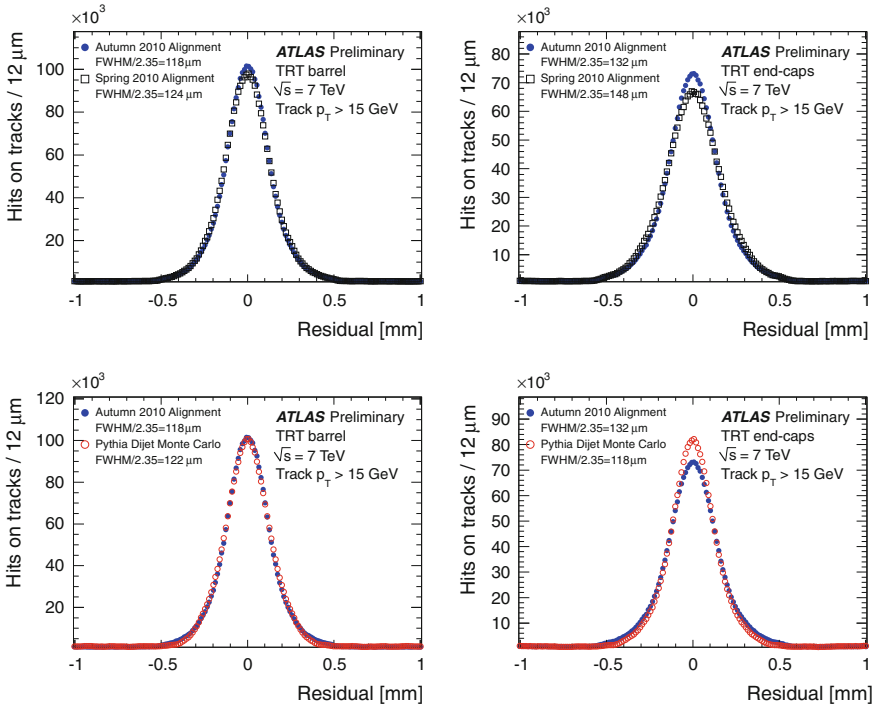

Fig. 4.15 Summary of residual distributions in the TRT Barrel (left) and Endcap (right). Top, improvement in residuals between the Spring 2010 alignment constants and the Autumn 2010 constants after TRT Level 3 alignment. Bottom, a comparison with Monte Carlo simulation

Gaussian fits to residuals were larger in some endcap wheels than in others. Figure 4.16 shows the endcap residual widths in individual endcap wheels; large structures are seen, particularly around wheels 0 and 24. When the residual σ was calculated in separately in sub-samples categorized according to track p_{T}, the structures disappear in samples of $p_{\mathrm{T}} > 10\,\mathrm{GeV}$ tracks and become more pronounced using $p_{\mathrm{T}} < 5\,\mathrm{GeV}$ tracks.

The type of misalignment that disproportionately affects low-p_{T} tracks is a misalignment of the endcap wheel structures along the beam (z) axis. Figure 4.17 illustrates the effect on low-p_{T} and high-p_{T} tracks, resulting in larger residuals for low-p_{T} tracks. The beam-axis misalignment hypothesis should also affect positively- and negatively-charged tracks differently. The effect is also shown in Fig. 4.17, resulting in a shift in the mean residual in opposite directions for oppositely-charged tracks. Figure 4.18 depicts the mean residual separately for positively- and negatively-charged tracks, confirming the suspicion of a z misalignment.

The z misalignments in the endcaps also manifest in physics measurements. Figure 4.19 shows the measurement of the J/ψ mass in $J/\psi \to \mu\mu$ events, as a function of the η of each muon. Measurements made with "combined tracks" (tracks

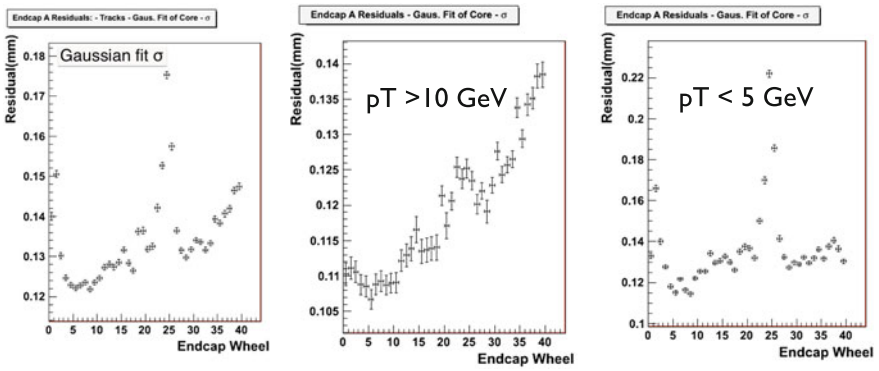

Fig. 4.16 Resolution (σ of the Gaussian fit of residuals) in each endcap wheel of Endcap A. Left: the resolution of all tracks. Center: resolution of tracks with $p_{\mathrm{T}} > 10\,\mathrm{GeV}$. Right: resolution of tracks with $p_{\mathrm{T}} < 5\,\mathrm{GeV}$ [9]

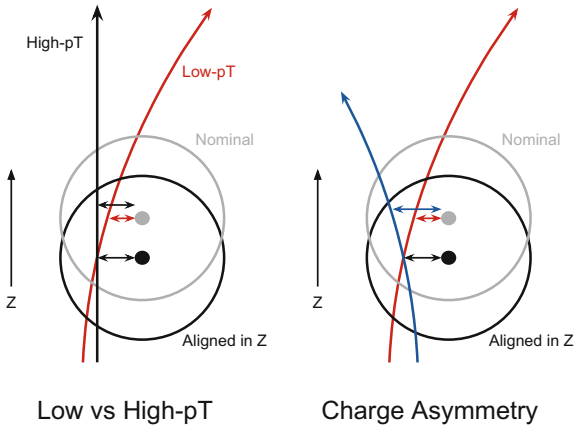

Fig. 4.17 Sketches depicting the effects of endcap misalignments in the z direction. Left, the track-to-wire distance has a small dependence on the z position of the straw for high-p_{T} tracks, but a large dependence for high-p_{T} tracks. Right, mismeasurements of the z-coordinate of the track hit position has the opposite effect on positively- and negatively- charged tracks

calculated using Silicon and TRT hits) are low in a specific positive η region, corresponding to the region with the large residual RMS in the TRT. When the J/ψ mass is recalculated by omitting TRT tracks ("silicon only"), the feature disappears, indicating an isolated problem in the TRT geometry.

To correct the z position of the TRT endcaps in the geometry description, a level 2 alignment of the TRT endcap wheels was performed allowing only the z-axis translation degree of freedom to vary. The χ^2 converged after roughly 6 iterations, though 38 iterations were performed to obtain the final constants. Figure 4.20 shows the change in the description of the detector position of each straw plane wheel after the alignment procedure. The corrections are large: as many as 5 mm, and the largest corrections correspond to the straw plane wheels that showed the largest differences in residuals between positively and negatively charged tracks.

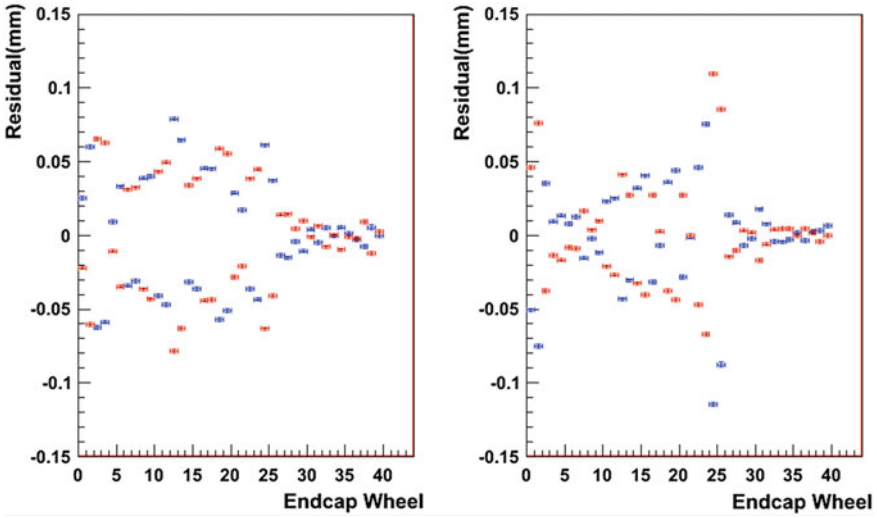

Fig. 4.18 Mean of residuals in Endcap C (left) and A (right) for low-p_T tracks ($p_T < 5$ GeV) shown separately for positively-charged (blue) and negatively-charged (red) tracks [9]

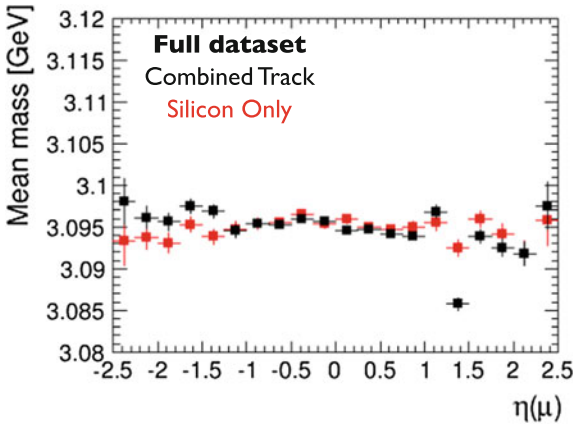

Fig. 4.19 $J/\psi \to \mu\mu$ mean reconstructed mass in an alignment geometry with z misalignments in the TRT endcaps. "Combined tracks" (tracks calculated using Silicon and TRT hits) in black have anomalous η-dependent features that are not present in "silicon only" tracks (where the track is recalculated without TRT hit information) in red [10]

Figures 4.21 and 4.22 confirm that the alignment procedure corrected the effects: tracks with $p_T < 5$ GeV no longer have a large charge asymmetry in the residual mean, and the RMS of residuals decreased significantly in areas where the bias had been the largest. Figure 4.23 revisits the J/ψ mass measurement as a function of the η of the muons; the new alignment removes the large mismeasurement in the $1.3 < \eta < 1.5$ region.

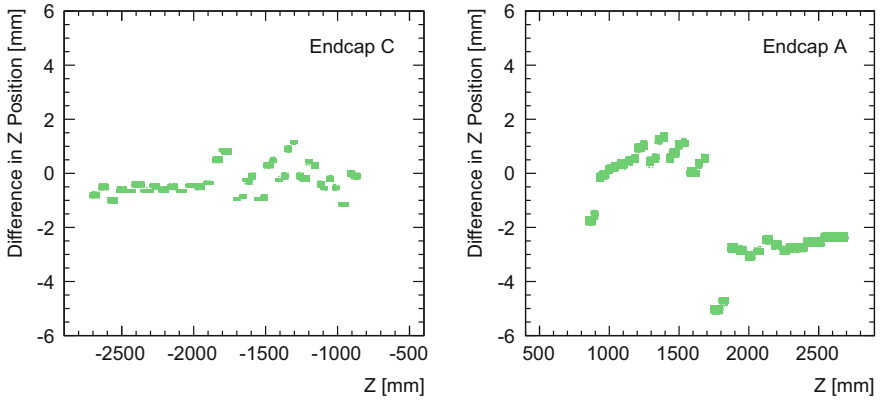

Fig. 4.20 Change in the alignment constant description of the z position of each straw after aligning endcap C (left) and A (right) at Level 2. Straws are visibly grouped into coherently moving straw plane wheels. The direction and magnitude of the movements correspond to the regions exhibiting large residual differences between positively and negatively charged tracks

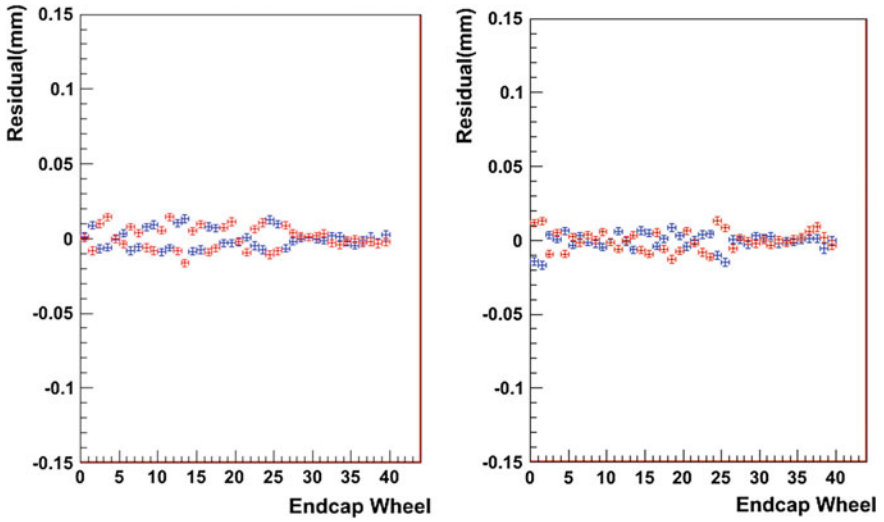

Fig. 4.21 Mean of residuals in Endcap C (left) and A (right) after the alignment procedure to correct endcap z misalignments, shown separately for positively-charged (blue) and negatively-charged (red) tracks [9]

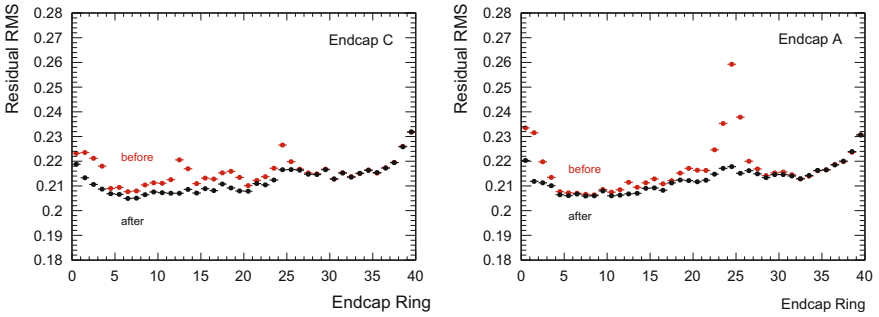

Fig. 4.22 RMS of residuals as a function of endcap ring (four-plane wheel) before (red) and after (black) aligning the TRT endcaps in the z direction

Fig. 4.23 $J/\psi \to \mu\mu$ mean reconstructed mass before (black) and after (red) aligning the TRT endcaps in the z direction [10]

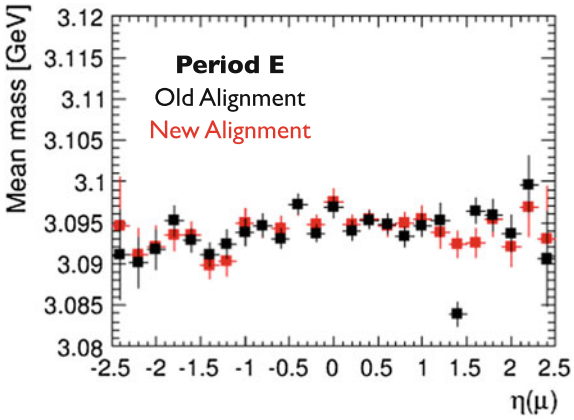

References

1. ATLAS Collaboration, The ATLAS inner detector commissioning and calibration. Eur. Phys. J. C **70**, 787 (2010). https://doi.org/10.1140/epjc/s10052-010-1366-7, arXiv:1004.5293 [hep-ex]
2. ATLAS Collaboration, Alignment performance of the ATLAS inner detector tracking system in 7 TeV proton–proton collisions at the LHC, ATLAS-CONF-2010-067, 2010, http://cdsweb.cern.ch/record/1281342
3. T.G. Cornelissen, M. Elsing, I. Gavrilenko, J.-F. Laporte, W. Liebig, M. Limper, K. Nikolopoulos, A. Poppleton, A. Salzburger, The global χ^2 track fitter in ATLAS. J. Phys. Conf. Ser. **119**(3), 032013 (2008), http://stacks.iop.org/1742-6596/119/i=3/a=032013
4. ATLAS Collaboration, Common framework implementation for the track-based alignment of the ATLAS detector, ATL-SOFT-PUB-2014-003, 2014, https://atlas.web.cern.ch/Atlas/GROUPS/PHYSICS/PUBNOTES/ATL-SOFT-PUB-2014-003/
5. ATLAS Collaboration, Alignment of the ATLAS inner detector tracking system with 2010 LHC proton–proton collisions at $\sqrt{s} = 7$ TeV, ATLAS-CONF-2011-012, 2011, http://cdsweb.cern.ch/record/1334582
6. ATLAS Collaboration, Alignment of the ATLAS inner detector and its performance in 2012, ATLAS-CONF-2014-047, 2014, http://cdsweb.cern.ch/record/1741021

7. ATLAS Collaboration, The ATLAS experiment at the CERN Large Hadron Collider. JINST **3**, S08003 (2008). https://doi.org/10.1088/1748-0221/3/08/S08003
8. ATLAS TRT Collaboration, The ATLAS TRT barrel detector. J. Instrum. **3**(02), P02014 (2008), http://stacks.iop.org/1748-0221/3/i=02/a=P02014
9. J. Stahlman, Plots from internal atlas presentation. Jonathan.Mark.Stahlman@cern.ch
10. M. Hurwitz, Plots from internal atlas presentation. Martina.Hurwitz@cern.ch

Chapter 5
Electron Identification

5.1 Introduction to Electrons

Electrons are excellent probes for studying physics at the LHC. Prompt electrons are a signature of weak decays such as the decays of the W and Z bosons (on-shell or off-shell). Electrons were instrumental in the discovery of the Higgs boson in the $H \rightarrow WW^*$ and $H \rightarrow ZZ^*$ decay channels. They are low-background and have well-measured momenta, and thus they are an indispensable tool for ATLAS precision electroweak measurements. Finally, searches for additional gauge bosons, supersymmetric partners to the Higgs and electroweak bosons, and numerous other BSM particles have signatures that include electrons. Figure 5.1 highlights electrons used in W, Z, and Higgs boson physics.

5.1.1 Electron Reconstruction

The detectors and algorithms used to reconstruct electrons are described in detail in Chap. 3 but are briefly revisited here. Figure 5.2 shows a depiction of an electron traversing elements of the ATLAS detector.[1] An electron traveling through the inner detector typically hits the IBL pixel layer (2015+), 3 pixel layers, 4 double-sided silicon strips, and it has an average of around 30 straw hits in the TRT, a large number of which are high-threshold hits. It traverses the solenoid and deposits its energy in four successive electromagnetic calorimeter layers: the presampler, then a layer finely segmented in η ("strips"), followed by a layer of roughly 16 radiation lengths and a backplane layer. Only small amounts of the electron's energy reach the hadronic calorimeter.

[1] The lowest-p_{T} electrons used during Run 1 data taking are 7 GeV; the following discussions refer to electrons satisfying roughly this threshold.

K. Brendlinger, *Physics with Electrons in the ATLAS Detector*, Springer Theses,
https://doi.org/10.1007/978-3-319-73930-4_5

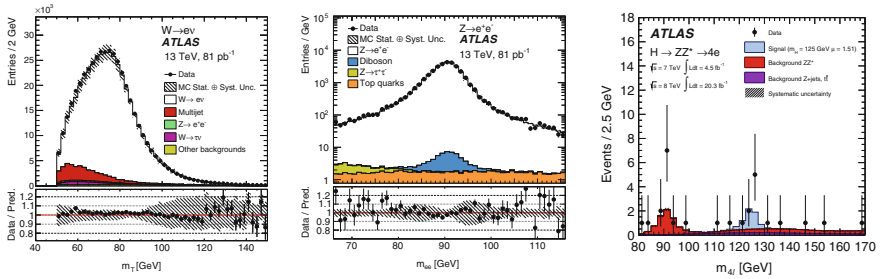

Fig. 5.1 Flagship analyses: events in the $W \to e\nu$, $Z \to ee$ and $H \to ZZ \to 4e$ channels of electroweak and Higgs boson production cross section measurements [1, 2]

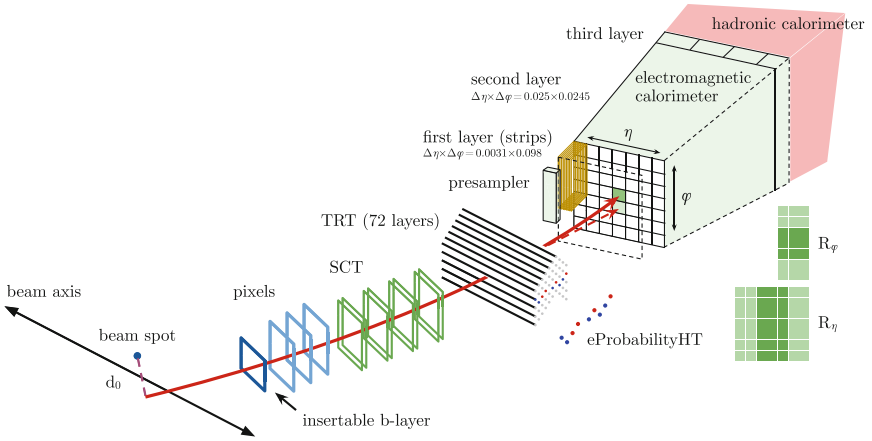

Fig. 5.2 Depiction of an electron traversing the ATLAS detector. The TRT extends to $|\eta| < 2.0$, and the SCT and pixel detectors out to $|\eta| < 2.47$. Electron discriminating variables are described in the text

Electron clusters are reconstructed using the sliding window algorithm [3], which searches for small-radius energy deposits contained in the EM calorimeter. A cluster matched to a track reconstructed in the inner detector is labeled an electron candidate. The electron track is refit using a Gaussian Sum Filter tracking algorithm which allows for large energy losses along the track due to bremsstrahlung radiation [4].

5.1.2 *Electron Backgrounds*

Once electrons are reconstructed they must be distinguished from backgrounds of other particle types. The largest backgrounds to electrons are charged hadrons, the most abundant of which are from light quarks jets (u, d, s) or gluon jets. These

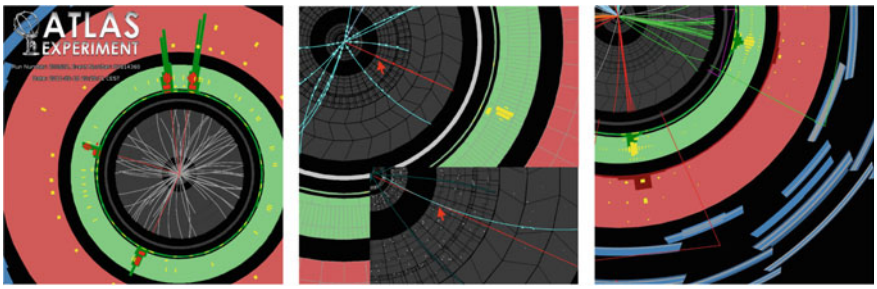

Fig. 5.3 Left: electron candidates in a $H \to ZZ^* \to 4\ell$ candidate event [5]. Middle: a converted photon [6]. The inset reveals a conversion vertex formed with two tracks. Right: two hadronic jets [7]

backgrounds, called light-flavor (LF) jets, are distinguishable from electrons by their hadronic shower, which is more diffuse than the narrow electromagnetic shower of an electron. Hadronic showers also deposit energy in both EM and hadronic calorimeters, where the electron's shower is typically fully contained inside the EM calorimeter.

The next most abundant background is from photon conversions. A photon that converts to an e^+e^- pair via interactions with material in the detector can have one of its electrons misidentified as a prompt electron from the p–p collision. (The $\pi^0 \to e^+e^-\gamma$ Dalitz decay can also mimic the electron signature.) Conversion backgrounds typically have a larger impact parameter, poor track-calorimeter matching, and slightly different shower signatures that can be used to distinguish them from electrons.

Finally, hadronic jets with a b- or c-quark that decay weakly to a non-prompt electron, called heavy flavor or HF jets, also serve as background. The real electron from the heavy-flavor decay typically has a large impact parameter compared to a prompt electron, which can be used to distinguish the two. The non-prompt electron will also be surrounded by the hadronic shower activity from its underlying jet.

Figure 5.3 contrasts the detector signatures of electrons, photons and jets in the ATLAS detector. The identification variables used to select electrons and reject the three types of background (LF jets, HF jets and converted photons) are described in the following sections.

5.1.3 Electron Identification

The ATLAS tracking and calorimetry detectors and the software reconstruction algorithms are designed specifically for the task of discriminating fundamental particles from one another. A set of tracking and calorimeter variables was developed to

discriminate electrons from background. The following sections describe the suite of variables used for electron identification, followed by a brief introduction to the multivariate discriminating techniques available to combine the variables into a single "menu" for identifying electrons.

5.1.3.1 Calorimeter Variables

Table 5.1 provides a description of the calorimeter variables calculated using the reconstructed electron cluster. The variables are designed to capture the difference in behavior of electrons and hadrons in the calorimeters, namely that electrons deposit their energy in a narrow shower contained inside the EM calorimeter, whereas hadrons showers are more diffuse and penetrate into the hadronic calorimeter. Calorimeter isolation variables used to identify electrons are described in Chap. 3.

Table 5.1 Definition of electron discriminating variables using the ATLAS calorimeters [8, 9]

Type	Description	Name	Rejects		
			LF	γ	HF
Strip layer of EM calorimeter	Total shower width, $\sqrt{(\Sigma E_i (i - i_{\max})^2)/(\Sigma E_i)}$, for all strips i in a window of $\Delta\eta \times \Delta\phi \approx 0.0625 \times 0.2$ (typically 20 strips in η). $i_{\max}$ is the index of the highest-energy strip	W_{stot}	✓	✓	✓
	Ratio of the energy difference between the largest and second largest energy deposits in the cluster over the sum of these energies	E_{ratio}	✓	✓	
	Ratio of the energy in the strip layer to the total energy	f_1	✓		
Middle layer of EM calorimeter	Ratio of the energy in $\Delta\eta \times \Delta\phi = 3 \times 7$ cells over the energy in 7×7 cells EM centered at the electron cluster position	R_η	✓	✓	✓
	Ratio of the energy in 3×3 cells over the energy in 3×7 cells centered at the electron cluster position	R_ϕ	✓	✓	✓
	Lateral shower width, $\sqrt{(\Sigma E_i \eta_i^2)/(\Sigma E_i) - ((\Sigma E_i \eta_i)/(\Sigma E_i))^2}$, with energy E_i and pseudorapidity η_i of cell i and the sum is calculated in a window of 3×5 cells	$W_{\eta 2}$	✓	✓	
Third layer of EM calorimeter	Ratio of the energy in the third layer to the total EM calorimeter energy	f_3	✓		
Hadronic leakage	Ratio of E_{T} in the first layer of the hadronic calorimeter to E_{T} of the EM cluster (the other hadronic layers are added for $0.8 < \lvert\eta\rvert < 1.37$)	R_{Had}	✓		✓

The ratio of energy deposited in the hadronic calorimeter to the energy deposited in the EM calorimeter, R_{Had}, is used to distinguish electrons and hadrons based on their shower depth. Other depth ratio variables inside the EM calorimeter, f_1 and f_3, seek to characterize the evolution of the shower as it traverses the EM calorimeter. The energy width variables W_{stot}, $W_{\eta 2}$, R_η, and R_ϕ distinguish narrow electron showers from diffuse hadronic showers. Finally, the difference between the two largest maxima (if two maxima exist) in the finely segmented strips layer of the cluster, divided by the sum of the two maxima, is calculated to check for multiple incident particles.

5.1.3.2 Tracking Variables

Table 5.2 summarizes the variables associated with the tracking detector, the track fit, and the track-calorimeter match. Tracking variables include the number of hits associated with the track for the pixel, strip, and TRT subdetectors. Variables related to the track's transverse and longitudinal impact parameters (d_0, d_0/σ_{d_0} and $|z_0 \sin\theta|$) help to distinguish electrons from b- and c-jets as described in Chap. 3, Sect. 3.2.4. The $\Delta p/p$ variable associated with the GSF track fit characterizes the track's energy loss due to bremsstrahlung and can help discriminate electrons from charged hadrons that do not lose as much energy in the ID. Variables that describe the quality of the match between the track and the cluster can be used to distinguish electrons from primarily converted photons or charged hadrons.

To further reject converted photons faking electrons, a tool is run during reconstruction to resolve electrons and photons. If the electron and any nearby track are consistent with an e^+e^- pair joined at a vertex inside the inner detector, then the electron is flagged as the product of a converted photon. This disciminant, called the ConvBit, was used in 2011 and 2012 data taking periods but not recommissioned for 2015 data taking.

The TRT provides discrimination between electrons and heavier objects based on the principle of transition radiation described in Chap. 3, Sect. 3.2.1. Particles with larger γ-factors (light particles, e.g. the electron) radiate more photons than those with lower γ-factors (heavy particles, such as pions and muons) when traversing the radiator foil inside the TRT. Those photons in turn induce more high-threshold hits in the detector. The high threshold ratio (F_{HT}) is the ratio of high-threshold hits to the total number of TRT hits along the reconstructed track, and should be larger for electrons than its hadronic backgrounds.

Beginning in 2012, cracks in the TRT gas system resulted in leaks and large losses of expensive xenon gas. To cope with this problem, the gas in some TRT modules was switched from xenon to argon, which is less expensive, for the 2015 data taking period. More modules will be switched to argon in the 2016 data taking period.

The use of argon gas leads to a lower high threshold probability. To compensate for the subsequent loss of performance, a tool was developed to calculate a likelihood ratio between electrons and backgrounds based on the high threshold hit information [10]. The high threshold probability of each hit is determined as a function of the location of the straw in the detector and the track-to-wire distance of the hit; the

Table 5.2 Definition of electron discriminating variables using the ATLAS tracking system (including variables matching the extrapolated track to the calorimeter cluster) [8, 9]

Type	Description	Name	Rejects		
			LF	γ	HF
Pixel	Number of hits in the B-Layer	nBlayerHits		✓	
	Number of hits in the pixel detector	nPixelHits		✓	
Pixel+SCT	Number of total hits in the pixel and SCT detectors	nSiHits		✓	
TRT	Total number of hits in the TRT	nTRTHits			
	Ratio of the number of high-threshold hits to the total number of hits in the TRT	F_{HT}	✓		
	Likelihood of the quality of TRT hits-on-track, including straw position, track-to-wire distance, and high-threshold status	eProbabilityHT	✓		
Track parameters	Transverse impact parameter	d_0		✓	✓
	Significance of transverse impact parameter, d_0/σ_{d_0}	σ_{d_0}		✓	✓
	GSF track momentum loss between the perigee and the last measurement point, divided by the track momentum at perigee	$\Delta p/p$	✓		
Track–cluster matching	$\Delta\eta$ between the cluster position in the strip layer and the extrapolated track	$\Delta\eta_1$	✓	✓	
	$\Delta\phi$ between the cluster position in the middle layer and the extrapolated track. In the $\Delta\phi_{\mathrm{Res}}$ case, the track momentum is rescaled to the cluster energy before extrapolating.	$\Delta\phi_{\mathrm{Res}}$ ($\Delta\phi_2$)	✓	✓	
	Ratio of the cluster energy to the track momentum	E/p	✓	✓	
Particle flow	Veto electron candidates matched to reconstructed photon conversion	ConvBit		✓	

probability is calculated separately for electron and pion hypotheses. The ratio of probabilities between the electron hypothesis and pion hypothesis is the discriminating variable. (In 2016 the high threshold probability will also be corrected as a function of the TRT occupancy local to the track.)

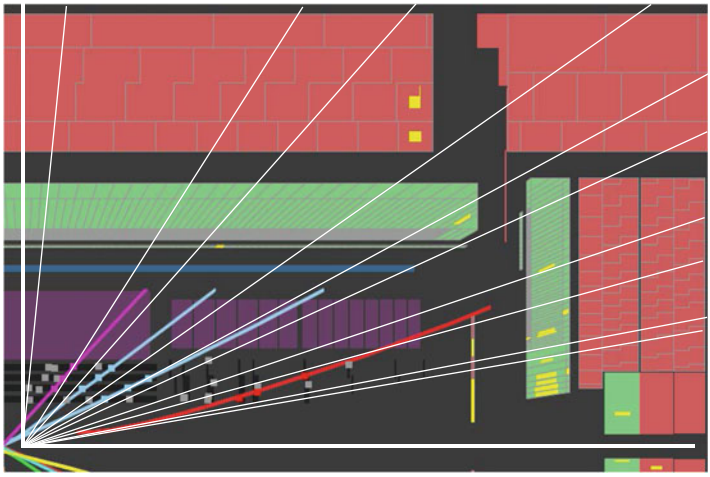

Eta	Angle
0	90°
0.1	84.3
0.6	57.5
0.8	48.4
1.15	35.1
1.37	28.5
1.52	24.7
1.81	18.6
2.01	15.3
2.37	10.7
2.47	9.7

Fig. 5.4 Cross section of the ATLAS inner detector, electromagnetic calorimeter (green), and hadronic calorimeter (red). White lines indicate η bin boundaries, whose values are reproduced on the right

5.1.3.3 Detector Geometry Considerations

The shape of the calorimeter variable distributions, and of the TRT discriminating variables, varies according to the detector geometry, whose features in η are dictated by the cylindrical nature of its barrel subdetectors, the transition to endcap detectors, the space dedicated to services, and the amount of material before the calorimeters. Consequently, electron identification is typically split into nine regions, or "bins" in η. Variable distributions also vary as a function of object E_{T}; thus, the phase space is split further into E_{T} bins, typically in 5 GeV increments. Variable distributions are roughly uniform across a single $\eta \times E_{\mathrm{T}}$ bin, and each region treated as a separate optimization problem for the purposes of defining an identification menu. Figure 5.4 shows a cross section of ATLAS subdetectors, with η bin boundaries indicated.

5.1.3.4 Multivariate Discrimination Techniques

A large range of classification techniques exist, and the field of classification is growing. Several classification methods are made readily available to the physics community via the Toolkit for Multivariate Data Analysis with ROOT (TMVA) [11]. Many of the methods implemented in this software have been tested for the problem of electron identification, including neural networks, boosted decision trees, and k-nearest neighbor methods.

Typically, the ATLAS e/γ Combined Performance Group provides a set of three "all-purpose" menus for identifying electrons, described as LOOSE, MEDIUM, or

TIGHT in order of decreasing electron efficiency, and increasing background rejection. These menus are intended to service all ATLAS analyses, and thus provide rejection for all types of electron backgrounds.

From 2010 to 2012, electrons were identified by the use of simple cuts on a set of electron variables (referred to as a "cut-based menu"), optimized using TMVA tools. The cut-based menu was re-optimized in 2011 to improve its performance and to account for differences between simulation and data. The menu was again re-optimized in 2012 to reduce the efficiency loss as a function of pile-up. The cut-based menus also served as the basis for the electron triggers during the 2010–2012 data taking periods.

The electron likelihood, which will be discussed in detail in the following section, was developed for offline reconstructed electron candidates in the 2012 8 TeV dataset. The likelihood was re-optimized for use in 2015, and was also adapted to trigger electrons in the HLT in 2015.

Nearly all variables can be combined in a multivariate analysis (MVA). However, track- and calorimeter-based isolation variables (described in Chap. 3) are typically regarded as a special discriminating variable that should be treated outside an MVA. This is because some physics processes (for instance $t\bar{t}$) have more particle activity (jets) in the event than other signatures, and thus may require specific isolation cuts (for instance, using a smaller cone size or a looser cut). Additionally, the isolation variable is an integral part of the current electron efficiency measurement (the "Z-Iso" method, described in Chap. 6), and correlations between the method and an isolation variable in the identification menu may bias that menu's efficiency measurement. For these reasons, isolation is kept outside of the standard ATLAS electron identification menus provided to the collaboration.

5.2 Samples for Electron Likelihood Menu Construction and for Performance Studies

The following section describes the data and MC samples used to develop electron identification criteria.

5.2.1 Electron Data Samples Using the Tag-and-Probe Method (2012)

To study electrons for the purposes of developing an identification menu, an unbiased selection of electrons is required. Unbiased electrons are obtained using Z boson events decaying to two electrons, by exploiting the tag-and-probe method. In the tag-and-probe method, described in detail in Chap. 6, events are collected using the single-electron trigger. Z boson candidate events are found by selecting pairs of

same-flavor, opposite-charge electrons: a triggered "tag" electron passing tight identification and isolation requirements, and a second, "probe" reconstructed electron candidate object passing basic track quality criteria cuts. (These events also include the subset in which the probe also passes the tag criteria, and in this case both electrons are counted as probes.) The tag-probe pair is required to be within 10 GeV of the PDG Z mass. Below a probe p_{T} of 20 GeV, the tag is required to originate from the barrel ($|\eta| < 1.37$). The set of electron probes is an unbiased, relatively clean source of electrons, at the reconstructed electron candidate level.

For the construction of PDFs in 2012, events were collected using the e24vhi_medium1 and e60_medium triggers in 20.3 fb^{-1} of 8 TeV data. To further reduce the amount of background in this sample, a loose calorimeter isolation cut is applied to the probe electrons: $\sum E_{\mathrm{T}}/E_{\mathrm{T}} < 0.5$ in a cone of $\Delta R = 0.3$. The effect of this cut is small in the high-E_{T} region, but significantly reduces background contamination for electrons below $p_{\mathrm{T}} = 20$ GeV. In principle, this isolation cut is correlated with other calorimeter variables; however, the cut value is more than 99% efficient in all bins, so the bias on the PDFs is minimal and has been shown to be negligible using MC. Additional steps to reduce background contamination in low-p_{T} electron candidates are discussed in Sect. 5.3.4.2.

5.2.2 *Background Data Samples Using Supporting Triggers (2012)*

The current formulation of the electron likelihood takes the simplistic approach of using a single set of PDFs to represent all sources of electron background, despite the fact that there are multiple types of electron background, each with their own distinct set of PDFs. (In the classification literature this is referred to as a one-against-one approach, as opposed to a one-against-all classifier.) In the one-against-one case, the exact mixture of background types (composition) of the PDFs affects the performance of the likelihood discriminant. As an example, if two background types have distinct sets of discriminating variables with equivalent discriminating power, and if their PDFs are combined in a single-background approach, then the type that is more represented in the PDFs will be rejected at a higher rate than the less represented type.

For the 2012 electron likelihood, the inclusive background is modeled using 20.3 fb^{-1} of 8 TeV data, collected using the electron and photon supporting triggers e5_etcut, e11_etcut, g20_etcut, and g24_etcut. The number represents the E_{T} threshold (in GeV); "g" triggers are photon triggers requiring only a reconstructed trigger cluster, and "e" triggers require a track matched within a loose ΔR window. To remove contamination by prompt electrons from Z boson production, a background candidate is rejected if it forms an invariant mass within 50 GeV of the PDG Z mass with any other electron candidate in the event. To remove prompt electrons from W boson production, events with $E_{\mathrm{T}}^{\mathrm{miss}} > 25$ GeV are rejected, and background

candidates with $M_T > 40\,\text{GeV}$ are rejected. Basic track quality criteria, matching the criteria required of the signal electron sample, is also applied on the offline reconstructed object. The offline reconstructed electron candidate that matches the trigger object firing the event within $\Delta R < 0.15$ is used as the background candidate. The composition of this sample is predicted by MC to be roughly 80–85% LF hadrons, 15–20% conversions, and ∼1% background electrons from HF decays.

5.2.3 Signal and Background MC Samples (2015)

In preparation for the 2015 data taking period, a new electron likelihood was necessary to adapt to the expected changes in conditions, including updates to core reconstruction algorithms; a newly-installed IBL and its corresponding tracking improvements; new gas conditions in the TRT; and a 25 ns LHC bunch spacing instead of 50 ns, causing changes to calorimeter responses. Since a version of the likelihood was required for the start of data taking, the 2015 electron likelihood would need to be constructed using PDFs obtained from MC.

For this purpose, a sample of $Z \rightarrow ee$ MC is used to obtain signal PDFs for electrons with $p_\text{T} > 15\,\text{GeV}$. Electrons are selected using the tag-and-probe method, and by requiring that the probe electron is matched to a true electron using the MC truth record. To obtain unbiased electrons below 15 GeV, a sample of $J/\psi \rightarrow ee$ is used as a source, with electrons identified by finding two reconstructed electrons whose invariant mass satisfies $2.8 < m_{ee} < 3.3\,\text{GeV}$ that both match to true electrons from the J/ψ in the MC truth record. Furthermore, to suppress highly collinear J/ψ electron pairs in which the electrons interfere with each other's shower shape variables, selected electrons must be a distance $\Delta R > 0.1$ away from any other electron candidate.

For background, PDFs are obtained using simulation of $2 \rightarrow 2$ QCD processes, including multijet, $qg \rightarrow q\gamma$, $q\bar{q} \rightarrow g\gamma$, electroweak and top production processes. The MC is filtered at truth level to enrich the sample in electron backgrounds: events are kept in which particles in the event (excluding neutrinos and muons) deposit $> 17\,\text{GeV}$ of energy into a square area $\eta \times \phi = 0.1 \times 0.1$, mimicking the highly localized energy deposits characteristic of electrons. The filter increases the number of high-p_T electron backgrounds; background objects with energy below 17 GeV are also abundant in this sample. The electron background constitutes objects in this sample that are reconstructed as electrons and that are not matched to a true electron in the truth record.

After obtaining signal and background samples from MC, differences between MC and data variable distributions must be corrected. These differences are from imperfect detector modeling in the MC, and are discussed in Sect. 5.3.4.3.

5.3 The Electron Likelihood

This section describes the electron likelihood discriminant as developed for use with the 2012, 2015 and 2016 ATLAS dataset.

5.3.1 The Generic Likelihood Method

The Neyman–Pearson Lemma [12] states that, for a set of variables $\mathbf{x}$, the most powerful discriminant between two hypotheses H_0 and H_1 that can be constructed is

$$d(\mathbf{x}) = \frac{p(H_s|\mathbf{x})}{p(H_b|\mathbf{x})} \tag{5.1}$$

where $p(H|\mathbf{x})$ is the conditional probability of the hypothesis H given $\mathbf{x}$ for signal s and background b. In practice, the conditional probability is found by constructing a set of one-dimensional probability density functions (PDFs), usually histograms, that are developed from clean sources of signal and background (the "training sample"). For a set of uncorrelated variables, the total conditional probability is the product of the PDFs evaluated at values x_i for each of the n variables in $\mathbf{x}$:

$$p(H|\mathbf{x}) = \prod_{i=1}^{n} p(H|x_i). \tag{5.2}$$

The likelihood can be transformed using a convenient function that is monotonically increasing for values > 0, namely $x \to x/(x+1)$ [13], allowing the signal to peak at 1 and background to peak at 0:

$$d_{\mathcal{L}}(\mathbf{x}) = \frac{p(H_s|\mathbf{x})}{p(H_s|\mathbf{x}) + p(H_b|\mathbf{x})}, \tag{5.3}$$

where $d_{\mathcal{L}}$ is the likelihood discriminant. An additional transform is applied to $d_{\mathcal{L}}(\mathbf{x})$ to allow the events to be more evenly distributed; this simplifies the technical aspect of choosing likelihood discriminant cut values [11]:

$$d'_{\mathcal{L}} = -\tau^{-1} d_{\mathcal{L}} \ln(d_{\mathcal{L}}^{-1} - 1) \tag{5.4}$$

where $\tau = 15$ is used in this case.[2] A cut can placed on this discriminant to separate signal from background; any electron whose discriminant is higher than this value passes the likelihood selection, while the rest fail. The cut on the likelihood can be combined with other rectangular cuts to define a full selection menu.

[2] $\tau = 15$ is the default value in TMVA.

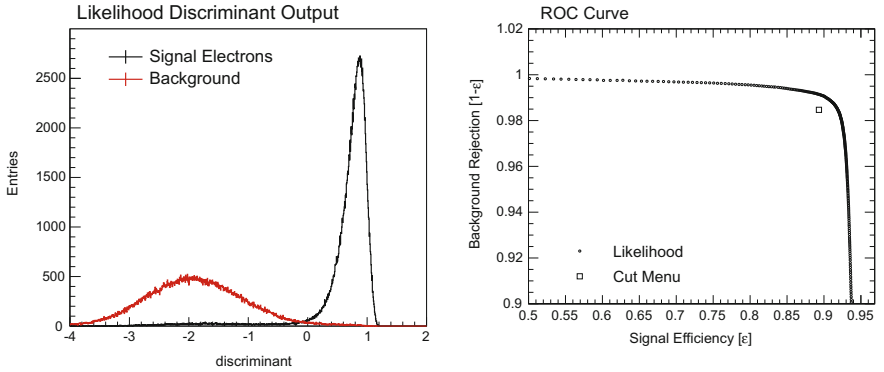

Fig. 5.5 Left: An example likelihood discriminant output, after having been transformed by Eq. 5.4, for data signal and background distributions. Right: The corresponding ROC curve, illustrating the continuum of operating points. A cut-based menu is plotted for comparison

An example likelihood discriminant and the continuum of corresponding signal efficiencies/background rejections are shown in Fig. 5.5 in the form of a receiver operating characteristic (ROC) curve. The corresponding optimized cut-based menu operating point is shown for comparison.

The benefit of the likelihood method of classification as compared to a rectangular cut-based method is two-fold. First, because it draws its discriminating power from many variables, the likelihood recovers electrons in the tails of some distributions, that otherwise look reasonable in other distributions. Cut-based menus naturally lose efficiency by removing electrons in the tails. Second, it becomes possible to use certain variables in a likelihood whose overlap between signal and background is sufficient to prevent applying hard cuts in a cut-based menu (due to excessive loss of efficiency), but that nonetheless have significant discriminating power. This opens up the opportunity for this type of electron variable, which had never been used in a cut-based menu, to be fully exploited by a likelihood particle identification. In the case of electrons, F_{HT},[3] f_1 and R_ϕ are three such variables; Fig. 5.6 shows the largely overlapping signal and background R_ϕ PDFs. The signal tail is too long for an efficient cut, but the PDFs contain a great deal of discriminating power that can be harnessed in the likelihood.

The likelihood method is the most powerful test if the set of variables is completely uncorrelated. In the case of electron classification this is not true, and more powerful techniques (boosted decision trees, neural networks, etc.) should outperform the likelihood. However, the simplicity of the likelihood is an asset: the method requires no training step, and the only parameters for its construction relate to the determination of the one-dimensional PDFs. The likelihood method is less susceptible or completely immune to smaller testing samples, over-training, training convergence at a local minimum, and other issues that more complicated multivariate techniques

[3]The F_{HT} variable is used in cut-based menus, however its cut is inefficient.

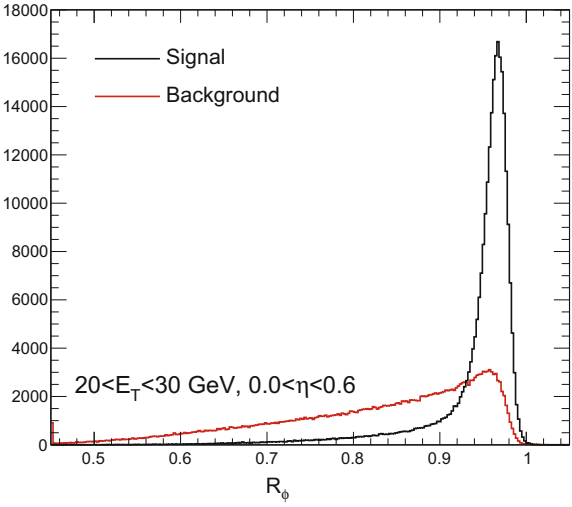

Fig. 5.6 An example of an electron variable, R_ϕ, which is inefficient when applied as a cut, but which nonetheless has significant discriminating power against background. Variables such as this can be used in a likelihood to improve the performance of the identification

must overcome. As such, it is much more easily maintainable, which is an asset in a field of study with continually changing personnel. These considerations shaped the decision to develop a likelihood electron identification.

The task of developing a likelihood test discriminant consists of the following steps: finding suitable sources of signal and background events for creating PDFs; constructing from these sources the PDFs of all variables that have some discriminating value; calculating the likelihood discriminant using different combinations of these variables; and finally settling on a likelihood with a list of variables that has the most discriminating power. The following sections discuss details related to how the electron likelihood performance was optimized.

5.3.2 *Structure of the ATLAS Electron Likelihood Menu*

Because the shape of the calorimeter and tracking PDFs vary as a function of the electron E_T and η, the likelihood menu is composed of 6×9 independent likelihood discriminants, each with its own set of variable PDFs and discriminant cuts. The η bin thresholds are influenced by detector geometry, as described in Sect. 5.1.3.3: [0.0, 0.6, 0.8, 1.15, 1.37, 1.52, 1.81, 2.01, 2.37, 2.47]. The E_T bins are: [7, 10, 15, 20, 30, 40, ∞] GeV.[4] The granularity of the discriminant cuts is slightly different, splitting the high-E_T bins further: [7, 10, 15, 20, 25, 30, 35, 40, 45, ∞].

The likelihood PDFs are obtained in 2012 using a data-driven method: unbiased electrons over a range of $10 < E_\mathrm{T} < 100$ GeV are gathered using the tag-and-probe method applied to $Z \rightarrow ee$ events, as described in Sect. 5.2. Thus, the 2012 likelihood

[4] A $4 < E_\mathrm{T} < 7$ GeV bin was added beginning in 2015.

is described as a "data-driven" likelihood. In 2015, the likelihood was constructed using PDFs derived from MC, and is described as a "MC-based" likelihood.

Several likelihood menus (LOOSE, MEDIUM and TIGHT) are provided to allow flexibility in optimizing the S/B ratio for a wide variety of ATLAS analyses using electrons. In 2012, LOOSE (alternately referred to as LOOSE_BL_PIX), MEDIUM, TIGHT (which is not used in analyses but which nonetheless appears in this text) and VERY TIGHT menus exist. LOOSE, MEDIUM and VERY TIGHT likelihood menus were designed to match the efficiency of LOOSE++, MEDIUM++, and TIGHT++ cut-based menus, respectively, and improve upon their background rejection. In 2015, the likelihood menus LOOSE, MEDIUM, and TIGHT were provided to roughly match the historical signal efficiencies of these menus.

An additional menu called VERYLOOSE, tuned to a higher efficiency than LOOSE, is provided as a tool for analysis background estimates which make use of a relaxed electron identification.

5.3.3 List of Likelihood Menu Details – Variable Content

The offline electron likelihood variable content is listed in Table 5.3, with 2012 cut-based menus listed as well for purposes of comparison. The choice of likelihood variable content, unless otherwise stated, is aimed at optimizing the likelihood performance; its optimization will be discussed in Sect. 5.3.5. The details of the 2012 and 2015 electron likelihood menus requiring additional explanation are enumerated below:

- nBlayerHits: 1 B-layer hit is required, if the expected hit is not masked in the detector. In 2012, nBlayerHits refers to the number of hits in the first pixel layer; in 2015, after the IBL was installed in ATLAS, it refers to the number of hits in the IBL.
- nPixelHits: at least 2 pixel hits are required. (For the VERYLOOSELH menu only one pixel hit is required.)
- nSiHits: at least 7 silicon hits are required.
- In 2012, the d_0 and σ_{d_0} variables were removed from LOOSE to accommodate the $H \to ZZ \to 4\ell$ analysis, whose reducible background estimation method relied on an anti-identification cut on these variables.[5]
- The f_3 variable is removed from the likelihood discriminant definition in the highest η bin ($2.37 < |\eta| < 2.47$) because of a large MC mismodeling that affects the data-MC efficiency agreement. The slightly reduced performance is preferred over a large data-MC scale factor. This approach is taken both in 2012 and 2015.

[5] Such requests were accommodated early in the development of the likelihood, since the number of customers was limited and experience with reducible background estimates with likelihood identification had not been studied. Experience has shown that background estimates do not generally require a special likelihood configuration.

Table 5.3 The variables used in the different selections of the electron identification menus, spanning 2012–2015. Cut-based, MULTILEPTON (ML) and likelihood menus are shown for comparison. Dashes indicate variables omitted because another nearly identical variable is already used in the menu. The $\Delta\phi_{\text{Res}}$ variable outperformed and replaced $\Delta\phi_2$ in 2012. The eProbabilityHT variable replaced F_{HT} in 2015 due to improved performance and compatibility with changing gas mixtures. The * refers to the fact that the E/p and W_{stot} variables are used as cuts for electrons with $E_{\text{T}} > 125\,\text{GeV}$ in a version of the 2015 TIGHT likelihood designed for high-mass exotic searches

	Cut-based		Likelihood	
Name	2012	ML	2012	2015
W_{stot}	C	C		*
E_{ratio}	C	C	$\mathcal{L}$	$\mathcal{L}$
f_1			$\mathcal{L}$	$\mathcal{L}$
R_η	C	C	$\mathcal{L}$	$\mathcal{L}$
R_ϕ			$\mathcal{L}$	$\mathcal{L}$
$W_{\eta 2}$	C	C	$\mathcal{L}$	$\mathcal{L}$
f_3	$\text{C}^{\text{!L}}$	C	$\mathcal{L}$	$\mathcal{L}$
R_{Had}	C	C	$\mathcal{L}$	$\mathcal{L}$
nBlayerHits	$\text{C}^{\text{!L}}$	C	C	$\text{C}^{\text{!L}}$
nPixelHits	C	C	C	C
nSiHits	C	C	C	C
nTRTHits	$\text{C}^{\text{!L}}$	C		
F_{HT}	$\text{C}^{\text{!L}}$	C	$\mathcal{L}$	–
eProbabilityHT	–	–	–	$\mathcal{L}$
d_0	$\text{C}^{\text{!L}}$		$\mathcal{L}^{\text{!L}}$	$\mathcal{L}$
σ_{d_0}			$\mathcal{L}^{\text{!L}}$	$\mathcal{L}$
$\Delta p/p$		C	$\mathcal{L}$	$\mathcal{L}$
$\Delta\eta_1$	C	C	$\mathcal{L}$	$\mathcal{L}$
$\Delta\phi_2$	$\text{C}^{\text{!L!M}}$	–	–	–
$\Delta\phi_{\text{Res}}$	–	C	$\mathcal{L}$	$\mathcal{L}$
E/p	$\text{C}^{\text{!L!M}}$			*
ConvBit	$\text{C}^{\text{!L!M}}$		$\text{C}^{\text{!L!M}}$	

- Due to inefficiencies identified in high-p_{T} electrons and associated with the f_3 variable, f_3 is removed from the likelihood for electrons with $p_{\text{T}} > 100\,\text{GeV}$ in 2015, and electrons with $p_{\text{T}} > 80\,\text{GeV}$ in 2016.
- Because of the limited coverage of the TRT, TRT variables are omitted in the range $2.01 < |\eta| < 2.47$. In 2015, gas leaks in the TRT caused certain barrel and endcap modules to be switched from Xe to Ar, degrading the F_{HT} discriminating power. Also in this year, the eProbabilityHT discriminant became available, partially compensating for the loss in F_{HT} performance. F_{HT} was used in the likelihood in 2012 and replaced by eProbabilityHT in 2015.

- The ConvBit variable was not recommissioned in 2015, and thus was not used in the 2015 likelihood menu.

5.3.4 Electron Probability Density Functions

The probability density function description of electron discriminating variables is essential to a well-performing electron likelihood identification menu. In 2012, electron signal and background PDFs were determined using the data-driven $Z \rightarrow ee$ event (signal) and supporting trigger (background) samples that are described in Sect. 5.2. In 2015, MC samples analogous to the 2012 data-driven ones are used as input samples to construct the likelihood.

To ensure that the one-dimensional PDFs are nonzero everywhere, raw histograms from data or MC must be "smoothed." The electron likelihood PDFs are smoothed using the kernel density estimation technique. Background contamination in data-driven PDFs can degrade the performance of the likelihood; therefore, additional criteria are added to the data $Z \rightarrow ee$ event selection for the probe sample to reduce this contamination, particularly for low-p_{T} electrons. Finally, data-MC differences due to imperfect modeling of the detector geometry and response require adjustment of MC PDFs to match data distributions–these corrections are applied to the MC-based PDFs for the 2015 likelihood. The following section describes the process of smoothing PDF distributions for constructing the likelihood, the additional selection applied to $Z \rightarrow ee$ signal to reduce background contamination, and the corrections applied to MC PDFs to construct MC-based likelihoods.

5.3.4.1 Smoothing PDFs Using the KDE Method

To first approximation, PDFs can be obtained by simply building a histogram of each variable using the signal and background samples described above. However, logistical issues of bin granularity and limited statistics could adversely affect the performance of the likelihood.

The electron likelihood should be constructed from PDFs containing only meaningful physical features. Random statistical fluctuations, particularly in the PDFs of likelihoods covering regions of $\eta \times E_{\mathrm{T}}$ where signal or background statistics are low, can cause suboptimal behavior, such as nearly identical electrons being assigned vastly different discriminant values. Likewise, the PDFs should be nonzero everywhere, to avoid undefined or unphysical results. Thus, raw histogram PDFs must be transformed to solve these issues. Adaptive kernel density estimation (KDE) is used to convert the histogrammed signal and background samples into PDF inputs for the likelihood.

The KDE method smooths a variable distribution in the following manner: first, the variable's values in the sample set are treated as a collection of δ-functions. Each δ function then replaced by a "kernel" function (in this case a Gaussian distribu-

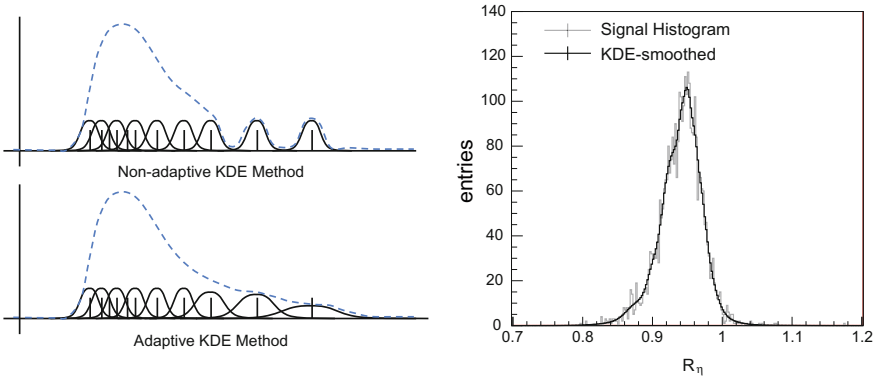

Fig. 5.7 The KDE method. Left: a cartoon depiction of the KDE and Adaptive KDE PDF smoothing technique. The adaptive method smooths areas of lower statistics. Right: an example of a raw variable distribution (R_η) and its KDE-smoothed PDF

tion) with a tunable width parameter, and the collection of Gaussian distributions are summed to form the final PDF. The adaptive KDE method follows the same procedure, but the Gaussian width parameter is increased in regions of low event yields (see Fig. 5.7) [11]. The PDFs developed for the electron likelihood tool were created using the TMVA adaptive KDE tool. In practice, the tool uses very finely binned histograms to approximate the δ functions of an unbinned dataset, in order to increase the algorithm speed, without loss of performance.

PDFs were hand-tuned to ensure that no real features were lost by the KDE-smoothing. This includes the choice of histogram range for each variable as well as the KDE smoothing parameters. In addition, certain variables (f_1 and E_{ratio} among them) exhibit discontinuities in their distributions, driven by detector geometry (e.g. a missing calorimeter layer in certain η regions for f_1, or no second maximum in the calorimeter cluster for E_{ratio}). These discontinuities were preserved by removing the discontinuity before applying KDE smoothing, and subsequently adding the discontinuity back into the KDE-smoothed distribution. Histogram overflow and underflow bins are treated in the same manner. Experiential evidence indicates that likelihood performance does not degrade significantly if the KDE approximation deviates somewhat from the true PDF.

5.3.4.2 Data-Driven PDFs at Low-E_{T}

The tag-and-probe method is effective at obtaining a sample of unbiased electrons for signal PDFs for the purposes of constructing a likelihood; however at low-E_{T} (below 20 GeV), background contamination significantly biases the PDFs. Figure 5.8 shows an example of an output discriminant in the $10 < E_{\text{T}} < 15$ GeV bin, illustrating the amount of background contamination in the PDFs. As mentioned earlier, an

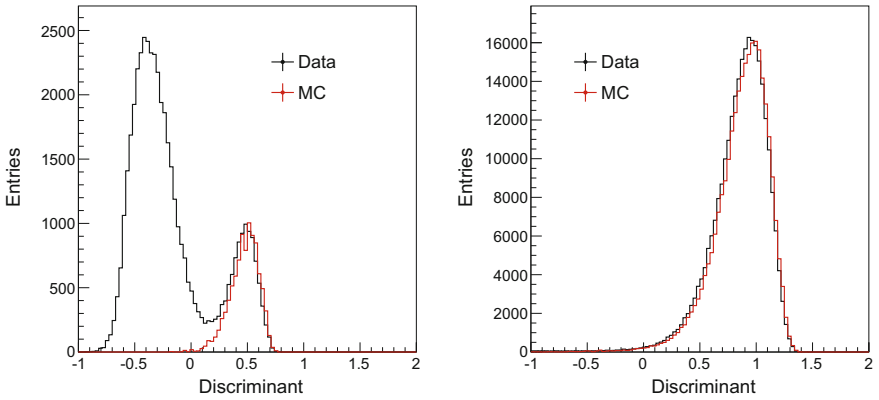

Fig. 5.8 Left: A plot of the output likelihood discriminant for probes (data and $Z \rightarrow ee$ MC) at 10–15 GeV, $0.80 < |\eta| < 1.15$. The data peak at high discriminant values comes from electrons (consistent with the $Z \rightarrow ee$ MC distribution), and the larger peak at low discriminant values is background, illustrating the high amount of contamination in the data sample at low-p_{T}. Right: the likelihood discriminant at 40–45 GeV, $0.80 < |\eta| < 1.15$; the fraction of background in the data sample is negligible

additional isolation cut is applied on the probe to reduce this background, but the signal PDFs remain polluted.

It is important to note that a likelihood constructed with contaminated PDFs can still provide adequate discrimination. Figure 5.8 is an illustration of this point. As a means of further improving the likelihood by obtaining purer PDFs, one can use a cut on the output discriminant itself (guided by the response of the MC) to drastically reduce the background contamination, while avoiding a cut on any one discriminating variable. This strategy was employed in constructing the 2012 likelihood with data-driven PDFs, in the following manner: A (data-driven) likelihood is constructed with the TIGHT-level likelihood variables (excluding the cuts). A $Z \rightarrow ee$ MC sample is then used to find the discriminant value that preserves 99.5% of the signal, to be used as the preselection. The procedure for obtaining the PDFs is then rerun on data, applying this discriminant cut, as well as additional tracking cuts (nSiHits$\geq$ 7 and nPixHits$\geq$ 1), before the KDE smoothing step. The resulting PDFs have significantly less background (see Fig. 5.9), and their bias is negligible because of the high efficiency of the pre-selection cuts.

While the low-E_{T} bins benefit the most from preselected PDFs, the method reduces the background contamination of the signal PDFs in all E_{T} regions. The procedure is therefore used for PDFs in all $E_{\mathrm{T}} \times \eta$ bins. The final PDFs have a purity of 98% or higher for electrons above 20 GeV, 85–98% between 10 and 20 GeV and 50–80% in the 7–10 GeV bin, depending on η. For the lowest-p_{T} bin in the calorimeter crack, $7 < p_{\mathrm{T}} < 10$ GeV and $1.37 < |\eta| < 1.52$, electron PDFs are highly contaminated with background, and signal and background contributions are difficult to

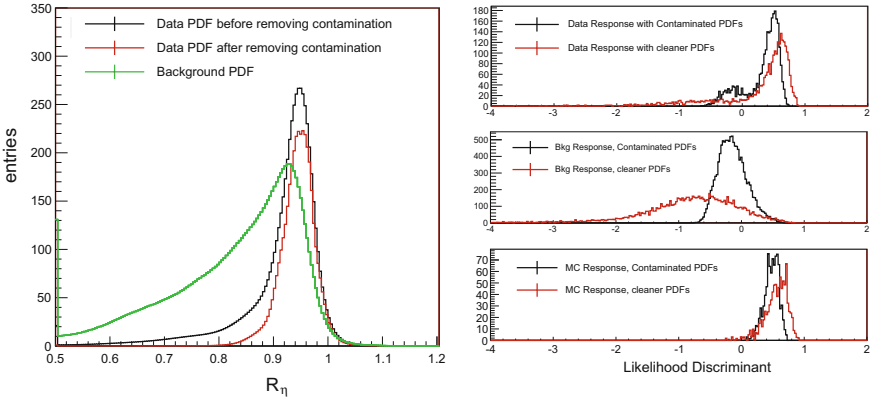

Fig. 5.9 Left: R_η distributions in data in the $10 < E_T < 15\,\text{GeV}$, $0.80 < |\eta| < 1.15$ bin, before and after removing background contamination using the procedure described in the text. The background PDF is plotted for reference. Right: A plot of the output discriminant for probes (from top to bottom: data, background, and $Z \to ee$ MC), from the same bin, comparing the performance of likelihoods with contaminated and cleaner PDFs

resolve. Thus, the PDFs have been replaced by PDFs from the $10 < p_T < 15\,\text{GeV}$ crack likelihood, resulting in improved performance.

The result of less contaminated signal PDFs is a better performing likelihood: the likelihood background rejection increases by 5–10%, compared to a likelihood tune with the same signal efficiency but using the original data PDFs.

5.3.4.3 Correcting MC Variable Mismodeling Using Constant Shift and Width Parameters

Imperfections in detector modeling causes differences between data and MC in the likelihood input variables. In order to use MC PDFs in place of data in a likelihood tune composed of MC PDFs, a correction must be made to bring the MC description closer to that of data. This can be achieved in two ways: one can investigate the source of the mismodeling (e.g. incorrect detector material descriptions, imperfect showering tune parameters, etc.), correct them, and re-simulate the propagation of particles through the detector in each MC sample; or one can find ways to manipulate the end-result variable distribution to more closely match data. In short-term identification development, the latter option is chosen due to time constraints.

Data-MC differences can typically be classified as constant offsets or as differences in the width (e.g. the full width at half-maximum, FWHM) between data and MC distributions, though there are exceptions to this rule. Comparisons between data and MC revealed that the variables f_1, f_3, R_η, $W_{\eta 2}$ and R_ϕ have constant offsets in bins of η; $\Delta\eta_1$ and $\Delta\phi_{\text{Res}}$ have different FWHM between data and simulation. Other

variables used for identification are sufficiently well-modeled by MC that they do not require adjustment.

The corrections are applied as follows: each electron's variable entry v is altered according to $v^*_{\text{MC}} = v_{\text{MC}} - a$ for constant offset a, or $v^*_{\text{MC}} = (v_{\text{MC}} - \bar{v}_{\text{data,MC}}) * w$ for width parameter w and mean value $\bar{v}_{\text{data,MC}}$ (in the electron variables shifted, $\bar{v}_{\text{data,MC}}$ is 0). To find the optimal corrections a, the following χ^2 test statistic is minimized:

$$\chi^2 = \sum_{\text{bins}} \frac{(n_{\text{data}} - n_{\text{MC}})^2}{\sigma_{\text{data}} + \sigma_{\text{MC}}} \tag{5.5}$$

To find the width corrections w, the ratio of the FWHM between data and MC is used. Correction parameters are derived using the same tag-and-probe datasets described in Sect. 5.2; to remove background, particularly among low-p_{T} electrons, the VERYLOOSE identification is applied to electrons (this reduces background while not significantly affecting the shape of input variables, since the menu is >95% efficient). This χ^2 minimization and FWHM ratio can be performed on PDFs either before or after the PDFs have been smoothed using the KDE procedure; the difference in results between the two approaches was found to be negligible.

The 2015 likelihood was developed using MC PDFs corrected using the above procedure using shifts and widths derived from 2012 8 TeV data that was reprocessed using the 2015 reconstruction software. The parameters derived using this procedure are reproduced in Appendix A.3. Corrections are derived and applied in each bin of η; the same corrections are assumed not to be dependent on electron E_{T}. The corrections derived in signal MC samples are also applied to the background MC samples used in constructing the 2015 likelihood. Figure 5.10 shows the data-MC agreement before and after applying the corrections. Note that corrections are η-dependent, however the distributions in the figure integrate over all η bins.

5.3.5 *Likelihood Variable Menu Optimization*

There are several ways to find the optimal likelihood given a list of variables, and they typically should all yield the same result. In constructing the 2012 electron likelihood, the "$n-1$" optimization method is used to determine the electron likelihood variables. In the method, a likelihood consisting of all n variables is evaluated using a sample of signal electrons and background, and a ROC curve is built from the output discriminants. Next, the process above is repeated on n likelihoods, each of which having the same likelihood construction as the original, minus one variable. If no $n-1$ likelihood performs better than the nominal, then the likelihood is already optimal. If one or more $n-1$ likelihoods performs better than the original, then the variable associated with the best-performing $n-1$ likelihood is removed from the list of variables, and the process is repeated with the new nominal menu. Variables are removed one-by-one until an optimal likelihood is reached.

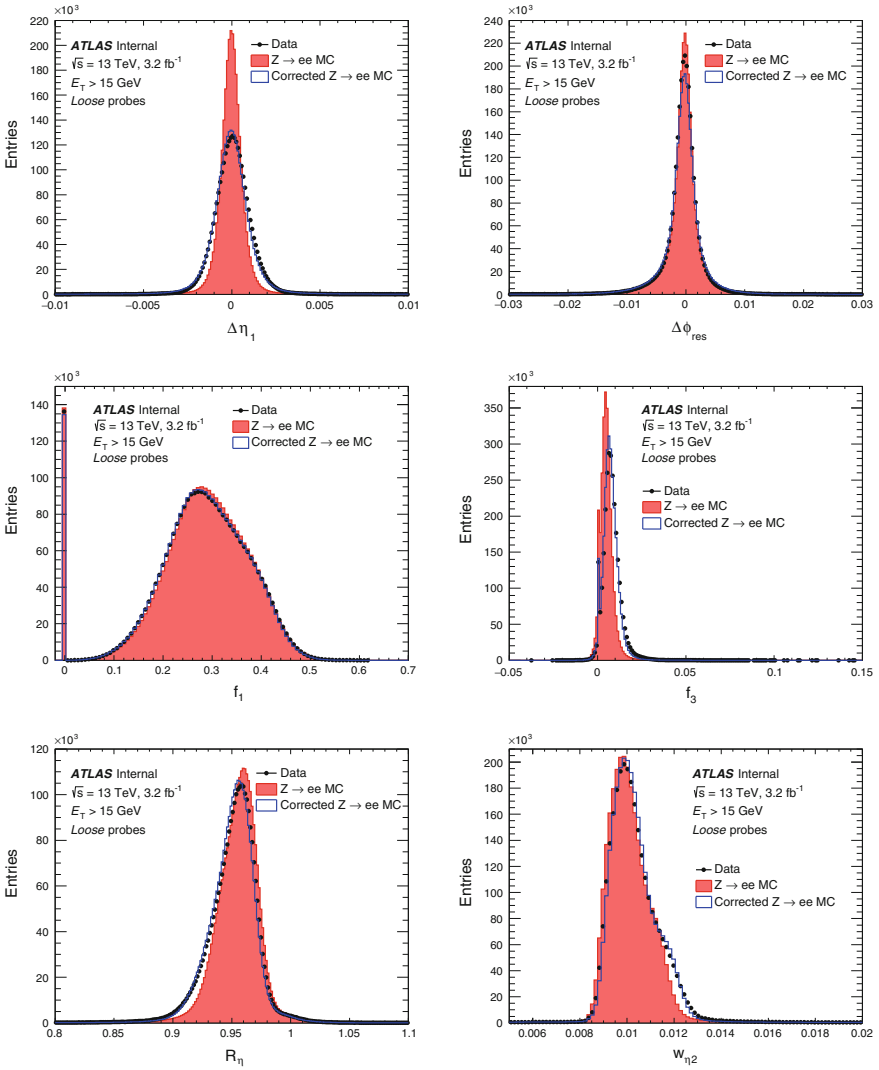

Fig. 5.10 Data and MC electron variable distributions obtained using the $Z \rightarrow ee$ tag-and-probe method, and integrated over E_{T} and η. MC is shown before and after applying the constant shift and width corrections described in the text

Figure 5.11 shows a baseline likelihood and a few corresponding $n-1$ likelihoods for some of the more powerful discriminating variables. If a particular menu performs much worse than the original, it indicates that the variable is a powerful discriminant. When removing a variable increases the likelihood's performance, it can be due to correlation effects with another variable in the likelihood, or problems with the PDF description of the variable.

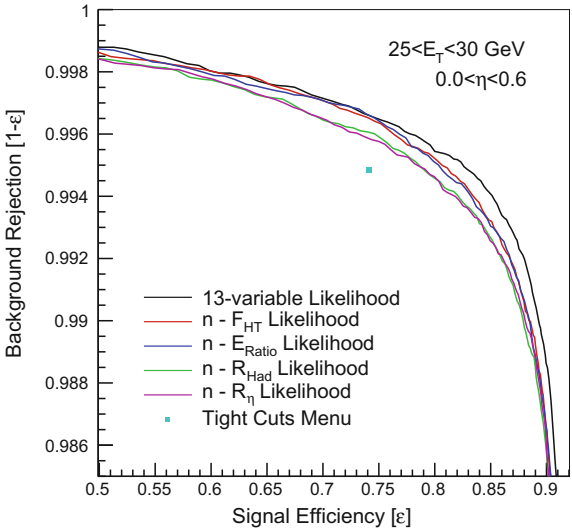

Fig. 5.11 The $n-1$ method used to optimize the choice of variables to use in the electron likelihood. Individual variables are removed from the nominal list of likelihood variables, and the likelihood recalculated to assess the relative power of each variable. The example shows the importance of F_{HT}, E_{ratio}, R_{Had} and R_{η}; the performance of the likelihood decreases when each is removed. The TIGHT cut-based operating point is shown for comparison

In theory, each of the 54+ likelihoods in bins of $\eta \times p_{\mathrm{T}}$ can have an individually optimized list of variables; in practice, the list of optimal variables is assumed to apply to all bins, and the performance of the full menu is used to determine the optimal list. Separate optimizations of the barrel and endcap do not result in significantly better performance, and thus for simplicity all likelihood bins feature the same variable content. Studies in which variables (such as tracking variables) are added as cut requirements, or a variable is removed and instead applied as a cut, were performed as well.

The $n-1$ variable optimization study was performed on the 2012 electron likelihood. The procedure was applied separately for LOOSE, MEDIUM and TIGHT regimes, as they lead to slightly different menus (particularly with regard to the cuts applied). Table 5.3 of Sect. 5.3.3 shows the resulting list of variables used in the likelihood and applied as cuts. (The removal of the d_0 and σ_{d_0} variables from the LOOSE likelihood was found not to significantly affect the menu's performance.)

Discriminant operating points in 2012 were determined the following way: For a certain operating regime (TIGHT, MEDIUM, LOOSE, or MULTILEPTON), operating points were selected to replicate the signal efficiency or background rejection of the corresponding cut-based menu. Typically, a likelihood constructed to have the same signal efficiency as a cut-based menu will have a better background rejection, and one which has the same background rejection as the cuts will have a higher signal efficiency. Discriminant cuts are determined on a bin-by-bin basis.

The five final likelihood menus in 2012 were adjusted slightly to have more natural spacing in overall efficiency: roughly 95% (VERYLOOSE), 92% (LOOSE), 87% (MEDIUM), 82% (TIGHT) and 77% (VERY TIGHT), to accommodate the needs of a wide range of analyses.

5.3.6 *Electron ID Pileup Dependence*

Electron discriminating variables are made less effective by several sources of activity (mostly jets) in the detector. Two types of activity exist: in-time pileup is the activity from the other p–p collisions in the same bunch crossing, and affects tracking and calorimeter detector response alike. Out-of-time pileup is the overlapping detector response from previous bunch crossings; this source only affects calorimeter detector responses. (Underlying Event (UE) is the activity from the same p–p collision point; this is typically small and can be ignored in the optimization process.)

Figure 5.12 shows the typical LAr calorimeter cell response, both before and after shaping. In 2011 and 2012, the bunch spacing was 50 ns (corresponding to a 20 MHz collision rate), arranged in Proton Synchrotron trains of 36; in 2015 and beyond the bunch spacing is 25 ns (40 MHz), arranged in PS trains of 72.

Pileup in the detector has increased in every year of ATLAS data taking (accounting for the change from 50 to 25 ns bunch spacing). Pileup affects a number of discriminating variables, typically degrading their discriminating power. The shower shape variables R_{Had} and R_{η} (see Fig. 5.13) are among the most affected variables, becoming wider (more background-like) and thus less discriminating with higher pileup. TRT variables (F_{HT}, eProbabilityHT) become more signal-like with higher pileup, in both signal and background; this variable is also less discriminating in dense environments.

The likelihood, whose PDFs are an average of pileup conditions over associated data or MC sample, is also affected by change in its input variables due to pileup. The efficiency of the likelihood operating points, which use R_{Had}, and R_{η}, has a dependence on n_{pv} (one which largely disappears when these two variables are removed

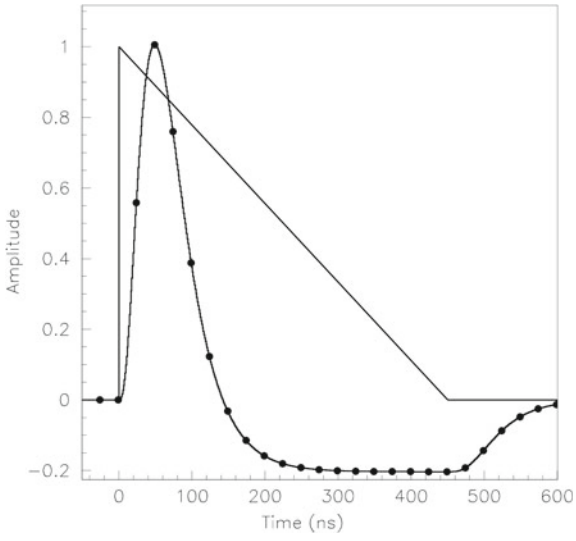

Fig. 5.12 Response of a LAr calorimeter cell, before (triangle) and after (curve) shaping [14]

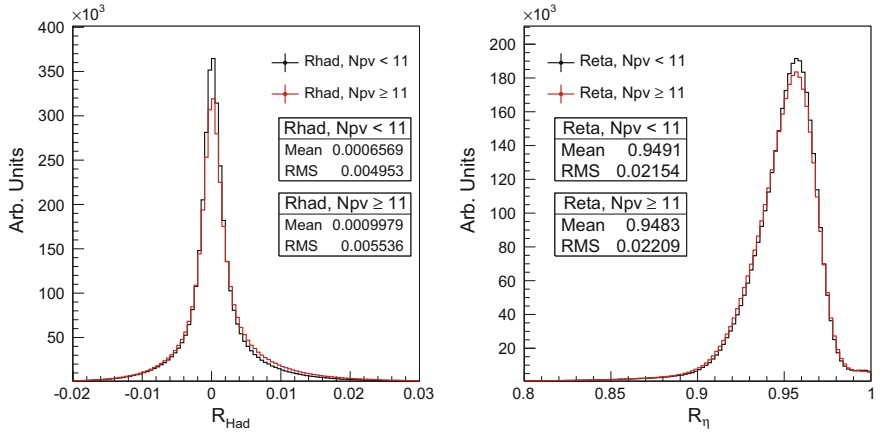

Fig. 5.13 The R_{Had} and R_{η} shower shapes, integrated over η, for electrons with $E_{\mathrm{T}} > 20\,\mathrm{GeV}$, divided into $n_{\mathrm{pv}} < 11$ and $n_{\mathrm{pv}} \geq 11$ regions. The electrons are obtained from data using the nominal tag and probe sample

from the likelihood menu). These two variables are among the most powerful, as shown in $n-1$ likelihood studies (see Sect. 5.3.5), and thus indispensable in the likelihood variable menu. However, the likelihood discriminant is systematically lower in higher pileup conditions, leading to a negative efficiency slope as a function of n_{pv}. (This negative slope is partially compensated by F_{HT} (2012) or eProbabilityHT (2015), which has the opposite effect on the likelihood discriminant, making the slope more positive as a function of n_{pv}.)

During the development of the likelihood, two approaches were considered to account for pileup conditions. The first approach is to make likelihood PDFs change as a function of n_{pv}. This approach replaces the $\eta \times E_{\mathrm{T}}$ binning of the likelihood with a set of likelihoods binned in $\eta \times E_{\mathrm{T}} \times n_{\mathrm{pv}}$, increasing the complexity of the tool. Furthermore, this approach leads to discontinuities in the electron efficiency as a function of n_{pv}. The second approach is to keep a single PDF set that is constant and averaged over all values of n_{pv}, but to correct the output likelihood discriminant as a function of n_{pv}. This is possible because most variables affected by pileup tend to simply have wider distributions, rather than having a changing mean. The effect on the output likelihood discriminant is smooth and can be approximated by linear corrections. Thus, the latter approach is taken, for its simplicity and smooth behavior.

In order to correct the efficiency for pileup dependence, the discriminant cut is made linearly dependent on the number of vertices, with the form $d''_{\mathcal{L}}(n_{\mathrm{pv}}) = d'_0 - a \cdot n_{\mathrm{pv}}$, where d'_0 is the original likelihood discriminant output, transformed by Eq. 5.4. In each η/E_{T} bin, d'_0 and a are chosen to meet the following condition:

$$\varepsilon = \varepsilon_{(n_{\mathrm{pv}}<11)} = \varepsilon_{(n_{\mathrm{pv}}\geq 11)} \tag{5.6}$$

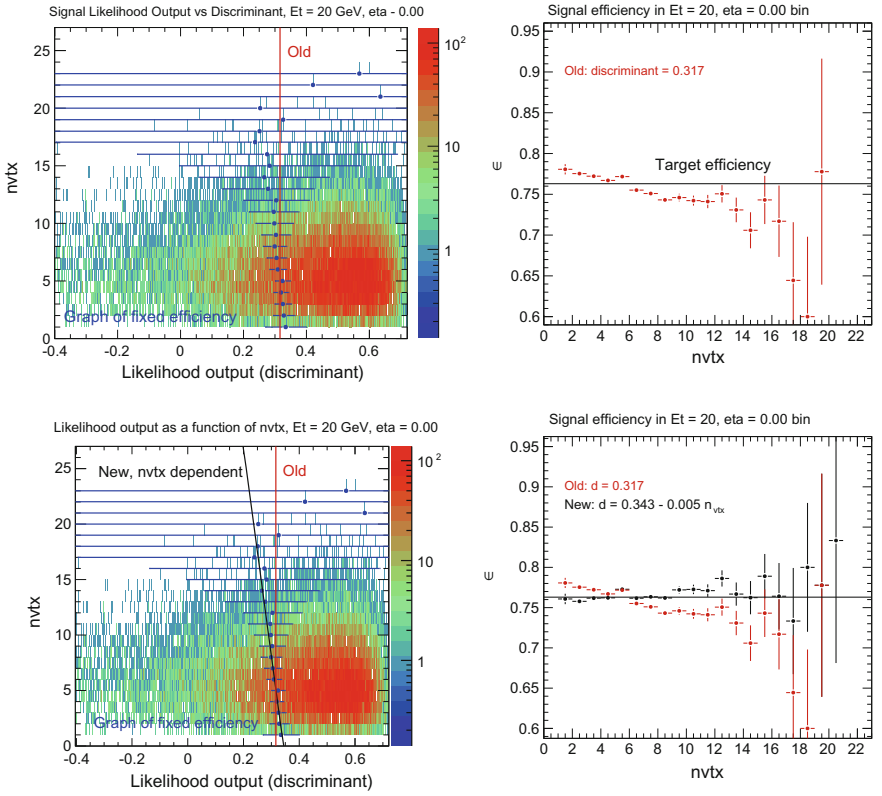

Fig. 5.14 An illustration of the n_{pv} dependence of the likelihood output discriminant. Errors on the left plot are estimates of the error on the discriminant, and are only meaningful relative to one another. The right plot shows the efficiency as a result of a constant discriminant cut. The bottom plots are the result of applying the n_{pv} correction. Efficiencies are roughly flat with n_{pv}

where ε is the desired operating point efficiency, and $n_{\text{pv}} = 11$ is roughly the central value of the n_{pv} distribution in 2012.

Introducing this discriminant dependence on n_{pv} softens the resulting effect of pileup on the signal efficiency (Fig. 5.14). It should be noted that the R_{Had} and R_{η} distributions are broader in the background, and the background response is less dependent on n_{pv}. As a result, correcting the signal efficiency might cause the background to develop an n_{pv} dependence, with worse rejection at higher n_{pv}. And in fact, a perfectly corrected signal efficiency in the TIGHT regime results in an untenably strong n_{pv} dependence in background rejection. The chosen values for d_0' and a balance these competing effects and the resulting behavior matches that of the corresponding 2012 cut-based menus (which still have a slight dependence - see Fig. 5.15). The corresponding background efficiencies are shown in Fig. 5.16. In the end, these n_{pv}-dependent cuts on the likelihood output are only applied for

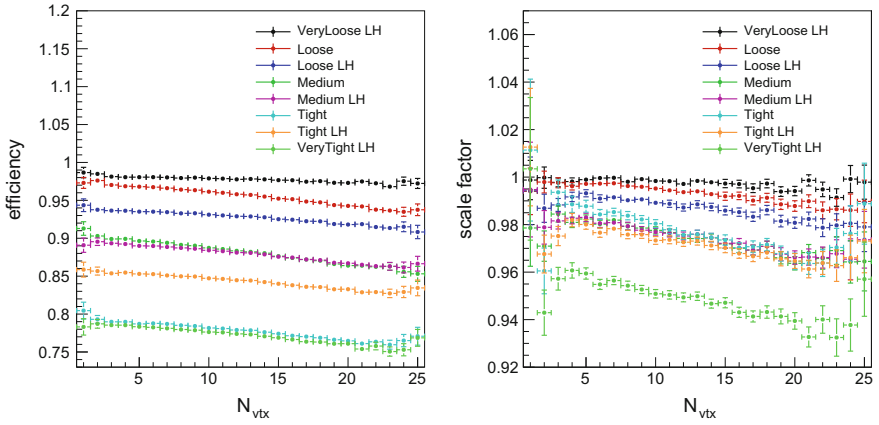

Fig. 5.15 $Z \to ee$ tag-and-probe data (left) efficiencies, as well as scale factors (right) as a function of n_{pv} for cut-based and likelihood operating points, for electrons with $20 < E_{\mathrm{T}} < 50\,\mathrm{GeV}$. The n_{pv} correction procedure for the likelihood has been applied to the MEDIUM, TIGHT and VERY TIGHT likelihood menus

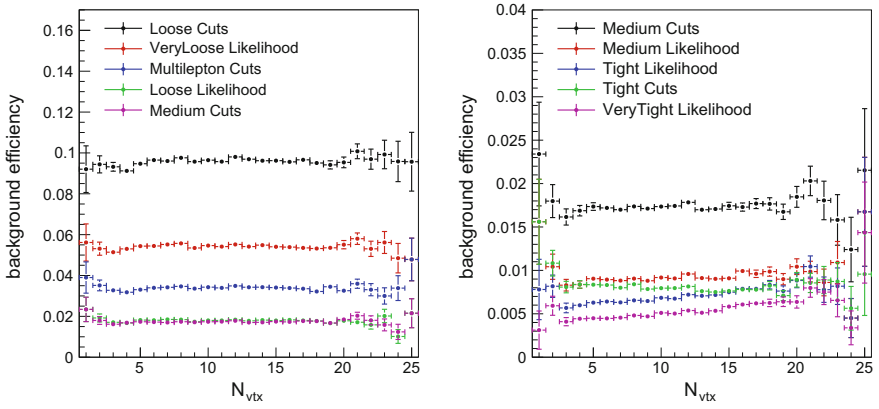

Fig. 5.16 Background efficiencies for likelihood and cut-based menus, as estimated in data using supporting triggers. The n_{pv} correction procedure for the likelihood has been applied to the MEDIUM, TIGHT and VERY TIGHT likelihood menus. The backgrounds for these menus exhibit up to a ∼40% efficiency increase across the bulk of the n_{pv} range

MEDIUMLH, TIGHTLH, and VERY TIGHT operating points. The dependence of the efficiency on the pile-up for the VERYLOOSE and LOOSE_BL_PIX operating points is small enough to not warrant a correction.

The 2012 electron likelihood menus are not arranged as exact subsets, for two reasons: the list of variables in the LOOSE menu is different from MEDIUM and TIGHT menus, and the n_{pv}-dependent cuts cross each other at high values of n_{pv}. The effect is small: electrons passing tighter operating points are almost entirely contained within

looser ones (the level of non-overlap in electrons has been found to be no larger than 0.05% between any two menus, for the 2012 pileup profile). However, to remove a chance of unexpected pathology caused by this effect, all 2015 likelihood menus have the same variable content, and the pileup dependence strategy has been changed slightly, as described below.

In 2015 we use a pileup-dependent correction that is not applied at all for the loosest electron menu, one that is applied maximally for the tightest menu, and whose effect turns on linearly between the two. Thus, the 2015 menus are corrected for n_{pv} dependence by applying a piecewise linear transformation in two dimensions (in the $d'_{\mathcal{L}}$–n_{pv} plane), ensuring a continuous output discriminant distribution $d''_{\mathcal{L}}$. The TIGHT menu in 2015 is corrected in the same way as in 2012, by finding d_{tight} and a_{tight} satisfying the condition in Eq. 5.6; this n_{pv}-dependent line is then taken as a reference point. The VERYLOOSE line (d_{loose}), with no n_{pv} correction, is taken as a second reference point; the correction will start here, increase linearly until it reaches a maximum at the TIGHT menu line, and then decrease linearly until it is again 0 at $d'_{\mathcal{L}} = 2$. The magnitude of the correction is 0 at $n_{\mathrm{pv}} = 0$, and reaches a maximum at $n_{\mathrm{pv}} = 50$, where it remains constant at $n_{\mathrm{pv}} > 50$.

The transform described is illustrated in Fig. 5.17. The mathematical description as implemented in the electron likelihood follows. Defining for convenience the following quantities:

$$n'_{\mathrm{pv}} = \min(n_{\mathrm{pv}}, 50) \tag{5.7}$$

and

$$d'_{\mathrm{tight}} = d_{\mathrm{tight}} - a_{\mathrm{tight}} \cdot n'_{\mathrm{pv}} \tag{5.8}$$

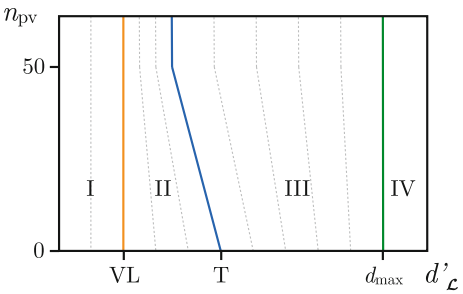

Fig. 5.17 The transform applied to the discriminant to correct for pileup dependence. Drawn are lines of equivalent $d''_{\mathcal{L}}(n_{\mathrm{pv}})$ on the $d'_{\mathcal{L}}$–n_{pv} plane. The transformed discriminant and the original discriminant are equal at $n_{\mathrm{pv}} = 0$. The highlighted lines are the VERYLOOSE (orange) and TIGHT (blue) discriminants, and d_{max} (green) from Eq. 5.9

The transform to correct for pileup dependence is then

$$d''_{\mathcal{L}}(d'_{\mathcal{L}}, n_{\mathrm{pv}}) = \begin{cases} d'_{\mathcal{L}}, & d'_{\mathcal{L}} \leq d_{\mathrm{loose}} \quad \text{(I)} \\ d_{\mathrm{loose}} + (d'_{\mathcal{L}} - d_{\mathrm{loose}}) \times \frac{d_{\mathrm{tight}} - d_{\mathrm{loose}}}{d'_{\mathrm{tight}} - d_{\mathrm{loose}}}, & d_{\mathrm{loose}} < d'_{\mathcal{L}} < d'_{\mathrm{tight}} \quad \text{(II)} \\ d_{\mathrm{tight}} + (d'_{\mathcal{L}} - d'_{\mathrm{tight}}) \times \frac{d_{\mathrm{max}} - d_{\mathrm{tight}}}{d_{\mathrm{max}} - d'_{\mathrm{tight}}}, & d'_{\mathrm{tight}} < d'_{\mathcal{L}} < d_{\mathrm{max}} \quad \text{(III)} \\ d'_{\mathcal{L}}, & d'_{\mathcal{L}} > d_{\mathrm{max}} \quad \text{(IV)} \end{cases} \tag{5.9}$$

with the regions corresponding to Fig. 5.17 indicated. Using this procedure, the n_{pv} dependence of LOOSE and MEDIUM operating points are determined automatically. The pileup correction described above was found to have nearly identical performance as compared to the 2012 strategy, with the added benefit that the menus now are exact subsets.

5.4 Electron Likelihood Menu Performance

The following section describes the performance of the 2012 electron likelihood, as measured in data and described by MC. The differences in response in data and MC, and the tools to understand their origin, are discussed here as well.

5.4.1 Performance in 2012 Data

The performance of the likelihood tool in 2012 was assessed using similar methods as were used for the construction of the signal and background PDF samples, described in Sect. 5.2. The electron signal efficiencies are measured using the Z, $Z\gamma$ and J/ψ tag-and-probe methods, as described in Chap. 6. Background efficiencies were determined using the supporting trigger sample described in Sect. 5.2; the signal contamination in this sample is subtracted using $Z \rightarrow ee$ and $W \rightarrow e\nu$ MC satisfying the selection criteria and scaled to the appropriate luminosity. Electron and background efficiencies are shown with respect to electron container objects that have additional track quality cuts applied (nSiHits $\geq$ 7, nPixelHits $\geq$ 1). In 2012, special attention is given to comparing cut-based menu and likelihood performance, to assess the utility of moving toward the more complex likelihood-based identification.

The electron efficiencies are shown in Fig. 5.18 as a function of η and E_{T}, alongside the cut-based menus. Likelihood menus in 2012 were tuned to roughly match the signal efficiency structures of their cut-based analogs; the ratios of efficiencies of backgrounds in the supporting trigger sample, comparing likelihood and cut-based menus with the same electron efficiency, is shown in Fig. 5.19. Background rejection

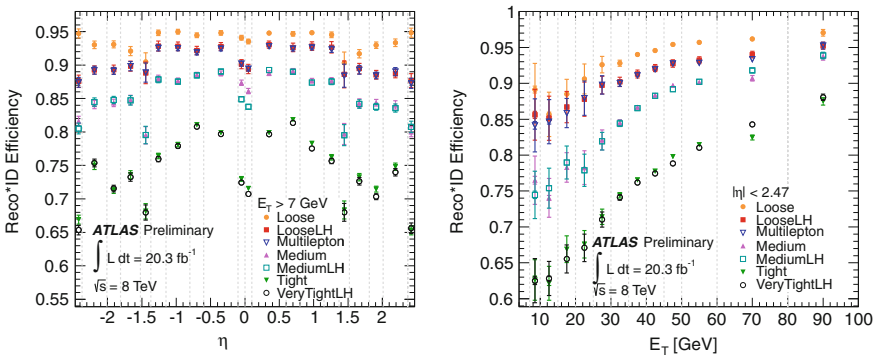

Fig. 5.18 Efficiencies of electron identification menus, measured by the tag-and-probe method in Z, $Z\gamma$ and J/ψ events using 2012 data. Likelihood LOOSE, MEDIUM and VERY TIGHT menus, and cut-based LOOSE, MULTILEPTON, MEDIUM and TIGHT menus are shown

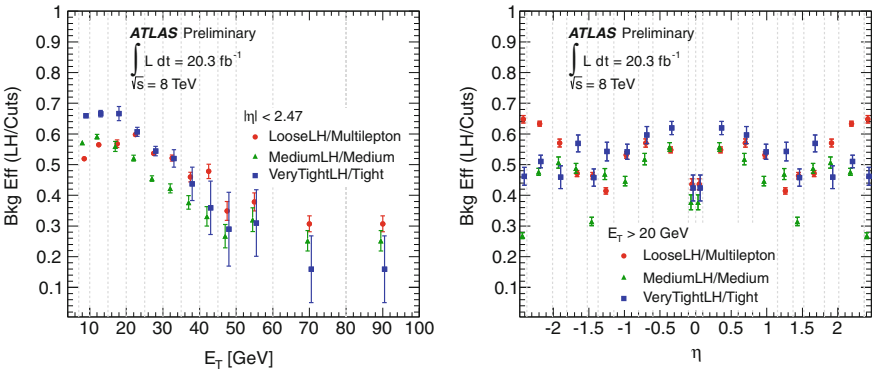

Fig. 5.19 Ratios of the background efficiencies of electron identification menus, comparing menus with the same electron efficiencies in 2012. The ratio is measured using a sample of background collected by electron supporting triggers

is typically improved by a factor of 2. Equalizing the efficiencies of cut-based and likelihood menus allows for easier comparison between the two approaches.

The VERYLOOSE likelihood (not shown in Fig. 5.18) features signal efficiencies close to 98% (as compared to ∼96% for the LOOSE cuts), with roughly 35% more rejection than the LOOSE cuts. The LOOSELH operating point closely resembles the MULTILEPTON cuts in efficiency, but reduces the backgrounds by around 40%. In the MEDIUM regime, the likelihood and cut-based menus have the same signal efficiency, but the likelihood reduces the background by half. The VERY TIGHT likelihood menu has signal efficiencies that are equivalent to the cut-based menu, but with half the background. (An additional likelihood menu, TIGHT, provided slightly better rejection than the cut-based TIGHT, but with roughly 5% more signal efficiency; this menu was not supported with scale factors.)

Beyond 2012, likelihood menus are assumed to out-perform cut-based menus; comparisons thus far have upheld this assumption, however the performance of both cut-based and likelihood menus can be affected by the specifics of their development or training, and thus cannot be assumed a priori to have the same behavior as in 2012. Nevertheless, comparisons between the 2015 cut-based and likelihood menus are not reproduced here.

5.4.2 Menu Characteristics Described by MC

The performance of a data-driven likelihood on simulated signal and background objects is nuanced. However, MC can in general be used to further understand the behavior of the likelihood. In particular, the composition of the background passing an identification menu can be studied using truth information from MC. (No comprehensive study has been made to verify the background composition of the MC samples or the response of different types of backgrounds to the Likelihood in data; studies of this nature will have to wait for another document.)

For the following composition studies, the jf17 MC sample (jf17) described in Sect. 5.2.3 is used; it contains $2 \rightarrow 2$ QCD processes and an emulated trigger requirement, enriched in electron backgrounds. The composition of the surviving candidates is categorized according to truth information: isolated electrons from electroweak processes, non-isolated electrons from heavy-flavor decays, background electrons from conversions and Dalitz decays, and hadrons.

Table 5.4 contains the compositions of surviving backgrounds for both cut-based and likelihood menus. The loose cut-based menus generally have equal parts hadrons and background electrons, with a small contribution due to electrons from heavy-flavor decays. As the cut-based menus get tighter, the heavy-flavor decays begin to dominate the remaining background, followed by background electrons. In contrast, the looser likelihood menus have much less hadronic background compared to their cut-based counterparts; instead, background electrons dominate in this regime. As the menu tightness increases, the hadron and background electron fractions decrease and the heavy flavor fraction increases.

Figure 5.20 shows the likelihood discriminant response for the different backgrounds; light-flavor jets are rejected most efficiently, followed by conversions. This behavior is driven mainly by the composition of the likelihood PDFs, which are dominated by light-flavor hadrons. Heavy flavor jets can contain real electrons from semi-leptonic decays and are therefore not effectively rejected. However, heavy flavor rejection is typically improved at the analysis level by adding an isolation cut on top of the likelihood identification criteria.

Figure 5.21 shows a comparison of background efficiencies between the LOOSE likelihood and the MULTILEPTON cut-based menu, which has the same signal efficiency. It can be seen that the likelihood provides most of its additional background rejection through suppression of light-flavor jets, although it also rejects more conversions.

Table 5.4 Background efficiencies (eff) of ID menus taken from an MC sample (jf17) containing all $2 \rightarrow 2$ QCD processes. The composition of the surviving candidates is categorized according to truth information: isolated electrons from electroweak processes, non-isolated electrons from heavy-flavor decays, background electrons from conversions and Dalitz decays, and hadrons. The background category efficiencies are also quoted. For the background efficiency numbers, prompt, isolated electrons are removed using the MCClassifierTool. All efficiencies are quoted with respect to a denominator of objects passing track quality requirements

Menu	$20 < E_T < 50$ GeV							
	Data eff (%)	MC eff (%)	Surviving candidates (%)			Category efficiencies (%)		
	$Z \rightarrow ee$	no sig electrons	non-iso	bkg	had	non-iso	bkg	had
Track quality	100.0	100.000	1.1	16.1	82.8	100.00	100.00	100.00
Loose cuts	95.68 ± 0.17	4.757 ± 0.039	7.4	48.4	44.2	32.46	14.27	2.54
Multilepton cuts	92.91 ± 0.16	1.643 ± 0.023	22.5	34.5	43.0	34.17	3.51	0.85
Medium cuts	88.09 ± 0.22	1.108 ± 0.019	25.8	50.5	23.7	26.50	3.46	0.32
Tight cuts	77.48 ± 0.24	0.456 ± 0.012	54.5	29.9	15.6	22.99	0.84	0.09
VERYLOOSE LH	97.77 ± 0.14	2.805 ± 0.030	16.2	69.5	14.3	42.06	12.07	0.49
LOOSE LH	92.82 ± 0.18	0.937 ± 0.018	40.2	42.0	17.9	34.79	2.44	0.20
MEDIUM LH	87.79 ± 0.25	0.513 ± 0.013	48.8	40.6	10.7	23.14	1.29	0.07
TIGHT LH	84.15 ± 0.27	0.389 ± 0.011	59.6	29.2	11.1	21.47	0.71	0.05
VERY TIGHT LH	76.97 ± 0.29	0.287 ± 0.010	63.7	28.9	7.4	16.93	0.51	0.03

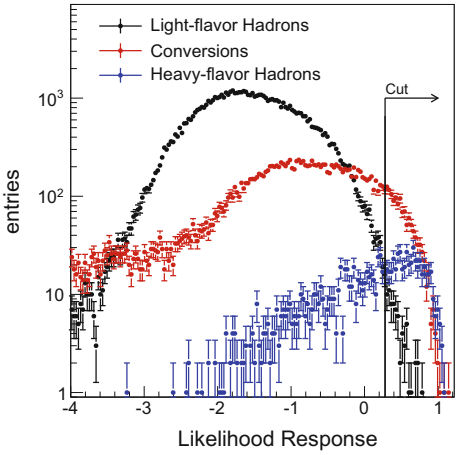

Fig. 5.20 Likelihood response for three categories of electron background in MC, for a LOOSE operating point. The sample (jf17) contains all relevant $2 \rightarrow 2$ QCD processes, and background objects are categorized using truth information. Shown are the backgrounds within the bin $20 < E_T < 25$ GeV, $0.0 < |\eta| < 0.6$, as well as the likelihood cut

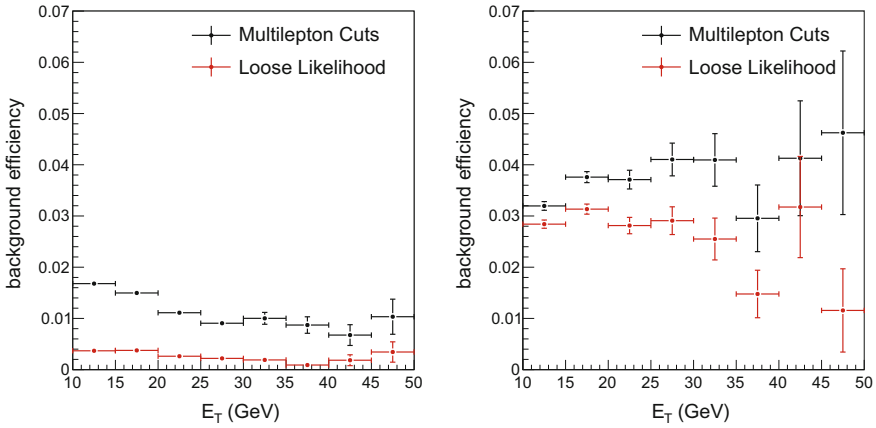

Fig. 5.21 MC efficiencies for light-flavor jets (left) and conversions (right) from the jf17 sample, comparing a cut-based menu (MULTILEPTON) to a likelihood with a similar electron efficiency. Heavy-flavor jet efficiencies are not shown due to low statistics

The purpose of Figs. 5.20 and 5.21 is in part to illustrate the very different efficiencies of different types of background. Thus, efforts to estimate background processes with one or more fake lepton using data-driven methods cannot a priori treat the electron background inclusively. Efforts to measure a background efficiency in a background-rich control region will encounter problems if the control region and the signal region have different compositions of light-flavor, heavy-flavor and conversion backgrounds. The analyzer is presented with two options: either he can carefully choose the numerator and denominator of his control region such that its composition matches that of his signal region, or he can choose numerator and denominator such that light-flavor, heavy-flavor and conversions all have the same efficiency in these regions. The latter can be achieved, for instance, by imposing additional isolation or other cuts on the denominator. Failing this, multiple background control regions would be required to effectively predict fake efficiencies which span over two orders of magnitude. The issue of predicting background processes with a background object faking an electron is discussed at length in a "real-world" scenario (the WZ cross section measurement) in Chap. 8.

5.5 Data-MC Comparisons and Tools

This section describes the general structure of the likelihood data-MC efficiency scale factors, how they differ from cut-based identification scale factors, and what causes these trends. Scale factor trends as a function of η are driven by MC mismodeling variations caused by a changing detector geometry. Likelihood and cut-based menu scale factors are both determined using the methods described in Chap. 6. Scale factors in this section are determined using the $Z \rightarrow ee$ tag-and-probe method.

Understanding the source of differences in data and MC responses to identification menus is important for building confidence in the electron program. Ideally, every scale factor trend should be matched to a known detector mismodeling, as a means of validating the efficiency measurement itself; otherwise, the efficiency measurement could instead be incorrect.

Another important reason for understanding data-MC differences is to improve identification performance. This is particularly important for a likelihood constructed using MC (as in 2015). Likelihoods built with MC PDFs will perform non-optimally if disagreements exist between the data and the MC input PDFs; a symptom of this type of problem would be data-MC disagreements in the scale factor.

First, it is prudent to address the scale factors being less than 1 for the likelihood, as can be seen in Fig. 5.22. As with the cuts, this can be explained by mismodeling resulting in narrower shower shape distributions in MC. For most cases this mismodeling will lead to better likelihood performance in MC, and thus a lower scale factor. This effect is especially evident for low-p_{T} electrons.

However, this is a simplified description, and shifted MC distributions can lead to scale factors both greater than and less than one, depending on the nature of the shift and the behavior of the background in that particular distribution. Figure 5.23 illustrates the possible MC mismodeling characteristics, and their effect on a likelihood scale factor. For cut-based menus, a mismodeling in MC will be reflected in the scale factor only if it occurs around the cut value. In the case of the likelihood, a mismodeling anywhere in the distribution can affect the scale factor. Furthermore, the effect also depends on the background distribution.

In the first example of Fig. 5.23, the MC is shifted with respect to data and the background distribution is flat. In this case, the peak of the MC distribution will be given a poor likelihood score, resulting in fewer passed MC events and a higher scale factor. However, the situation becomes more complicated if the background is not present in the region of non-overlap between MC and data (as is the case for $W_{\eta 2}$

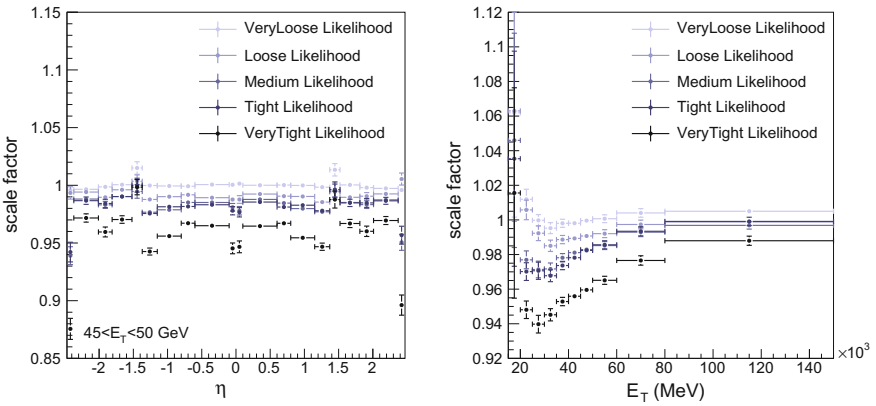

Fig. 5.22 Left: Comparing the scale factors of the five likelihood menus, as a function of η (left) and E_{T} (right)

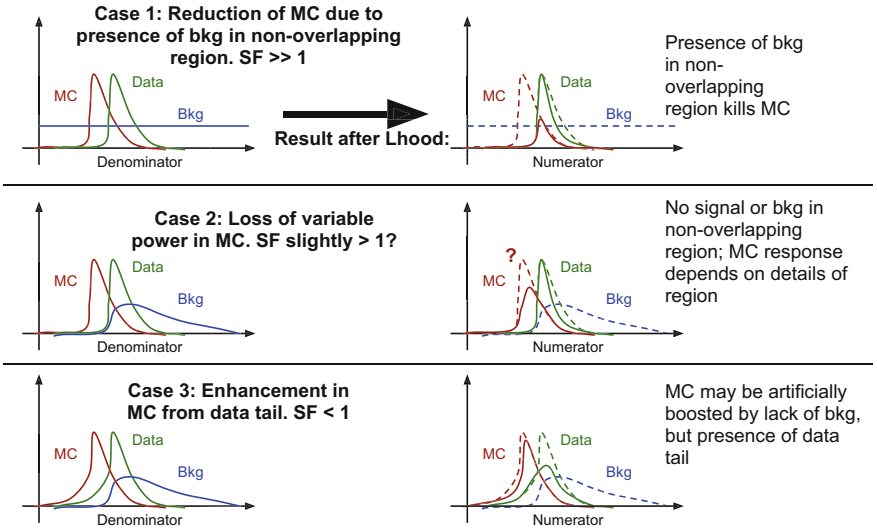

Fig. 5.23 A cartoon detailing variable distribution effects and how they can affect the scale factor. See text for description

and f_3). In this situation, which is shown as a second example, the behavior of the likelihood depends crucially on the ratio of signal to background in this previously unimportant region. In the third example, the peak of the MC distribution is enhanced by a tail in the data, because there is no background in the region. This will result in a scale factor <1.

The scenarios above describe the effect of a single distribution on the scale factor; however with 11–13 variables in the likelihood, competing effects obscure the underlying causes of a scale factor shape.

As previously mentioned, scale factors will generally be low for the likelihood if the MC shower shapes are narrower than in data. The problem can be compounded when cutting hard on the likelihood distribution. Figure 5.24 illustrates the potential for a scale factor very different from 1 when cutting hard on a particular discriminant. The VERY TIGHT operating point, which requires cutting into the discriminant distribution by as much as 30%, can be considered a hard cut value. In the figure, a shift can be seen between MC and data, more pronounced in the right plot; both regions have a scale factor <1, moreso in the right plot.

5.5.1 *Probing Scale Factor Trends Using $n-1$ Menus*

To understand the scale factor trends as a function of the electron η and E_{T} in the likelihood and cut-based menus, ad-hoc menus with special configurations were

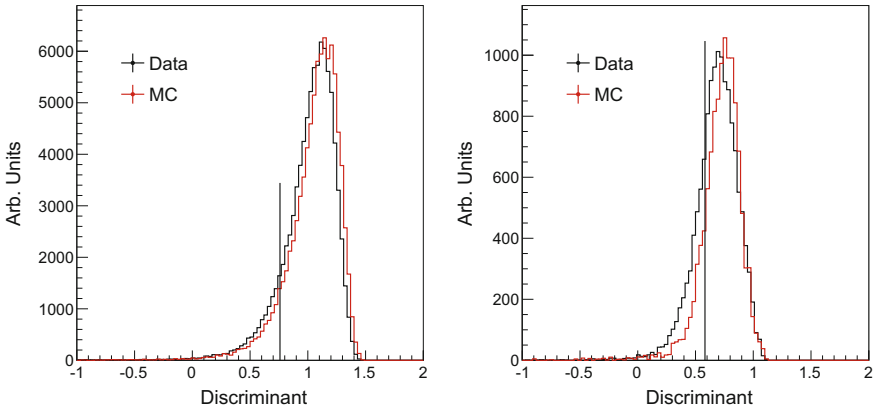

Fig. 5.24 Left: a plot of the VERY TIGHT output discriminant for the region $45 < E_T < 50\,\text{GeV}$, $0.6 < |\eta| < 0.8$. The vertical line represents the cut value for the VERY TIGHT operating point. Right: the same plot, for the region $45 < E_T < 50\,\text{GeV}$, $2.37 < |\eta| < 2.47$. In both cases, the MC is shifted with respect to the data (the effect is more pronounced in the right plot), consistent with a low scale factor. The discriminant distributions above support the scale factors measured by the $Z \to ee$ tag and probe methods

developed. The cut-based tight menu is compared to the same menu with the F_{HT} cut removed. For the likelihood menus, a menu is made with the same content as the VERY TIGHT likelihood, but with roughly 80% efficiency (and 65% efficiency at $2.37 < |\eta| < 2.47$). Then a second likelihood is produced, with the same configuration but removing a single variable from the likelihood training, to understand the effect of this variable on the scale factor trends in η. Figure 5.25 shows the results of this study for a few representative variables. The F_{HT} variable seems to be responsible for much of the structure in the cut-based menus, while for the likelihood menus F_{HT} seems to have little impact on the scale factor trend. Instead, shower shapes such as R_η seem to have more of an effect on the trend. The competing effects of each variable must be aggregated to gain a complete understanding of the scale factor trends; the issue is further complicated by correlations between variables.

5.5.2 *Probing Scale Factor Trends by Shifting MC Input Variables*

Perhaps a more powerful way to understand the behavior of the electron likelihood in data and MC is to compare scale factor trends before and after applying the shift and width adjustments described in Sect. 5.3.4.3.

Figure 5.26 shows the efficiency of the MC compared to data in the case where the mismodeled MC variables are shifted according to the methodology described in Sect. 5.3.4.3. The study shows that large data-MC differences in the unshifted MC are

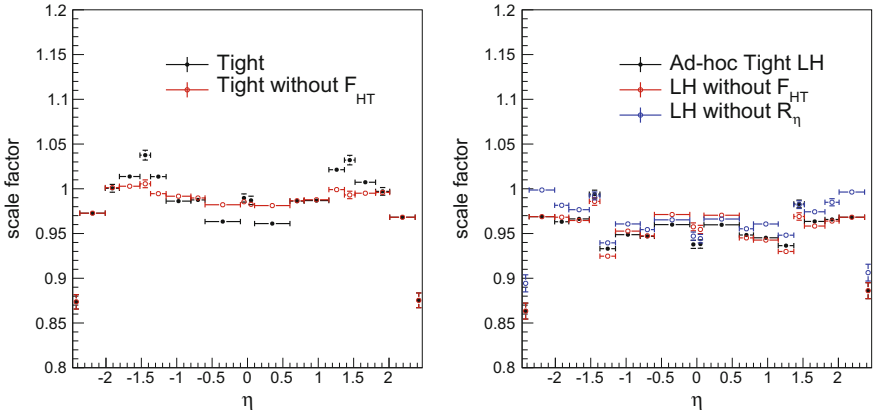

Fig. 5.25 Scale factors for electrons in the range $45 < E_T < 50$ GeV, for ad-hoc menus designed to probe the effects of certain variables on the scale factors trends. The Tight cut-based menu is compared with the same menu with the F_{HT} cut removed. The likelihood menus include all VERY TIGHT variables unless otherwise indicated, and were tuned to have roughly 80% efficiency, and 65% efficiency at $2.37 < |\eta| < 2.47$, to roughly match the efficiency of the official VERY TIGHT menu

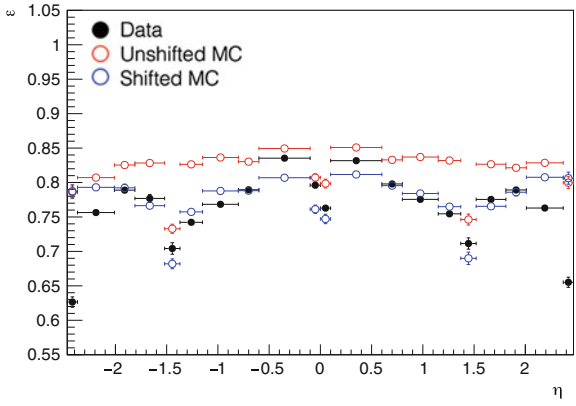

Fig. 5.26 TIGHT Efficiencies measured using the $Z \to ee$ tag-and-probe method, for electrons with $35 < E_T < 40$ GeV, using the shifts and width adjustments described in Sect. 5.3.4.3, using 1.7 fb^{-1} of 13 TeV data in 2015

reduced when the shifts are then applied, particularly in the region $0.6 < |\eta| < 2.01$. The regions $|\eta| < 0.6$ and $|\eta| > 2.01$ show persistent differences, requiring further study. Note that a scale factor that is exactly one does not guarantee that data and MC agree perfectly, and competing effects in two or more different variables can partially or completely cancel. Careful study of variable PDFs can be carried out alongside scale factor studies to obtain a full picture of the MC modeling.

Most importantly, manipulating distributions to improve data-MC efficiency agreement can improve the performance of a likelihood based on MC PDFs. In this scenario, MC PDFs that are shifted and widened to more closely match the data distributions will be verified by scale factors that are closer to one. The original MC-based likelihood can be rebuilt using the more accurate MC PDFs; the new likelihood

should outperform the original when applied to data. Similar procedures were run in preparation for the 2015 data taking period using 2012 data and MC, resulting in better-performing MC-based likelihoods.

5.6 Electron Quality Comparisons with Cut-Based Menus

Likelihood and cut-based menus differ qualitatively in both data and MC. Because the likelihood does not put a hard cut on any one distribution, a likelihood tuned to have the same signal efficiency as a cut menu will recover the tails of some distributions while discarding other electrons that fall within all of the cut values, but nevertheless appear more background-like. As a result, assuming the same signal efficiency, some fraction of events will fail the likelihood but pass the cuts, and an equal amount will do the opposite. For high-efficiency menus this fraction is small (a few percent), while at the tightest level this number approaches 10%.

An illustration of this concept is shown in Fig. 5.27, which shows distributions of electrons that pass the VERY TIGHT likelihood and fail the TIGHT cut-based menu, and vice-versa. The second of these two examples also shows the inefficiency of the f_3 cut, and illustrates the source of the low scale factor at high-η in the cut menus.

Efficiencies and scale factors for the TIGHT likelihood and the TIGHT cut-based menu were obtained using a very fine granularity in η to check for anomalies. Figure 5.28 shows the results of the efficiencies and scale factors binned in steps of $\Delta\eta = 0.1$. The source of cut-based and scale factor differences were discussed previously in Sect. 5.5.

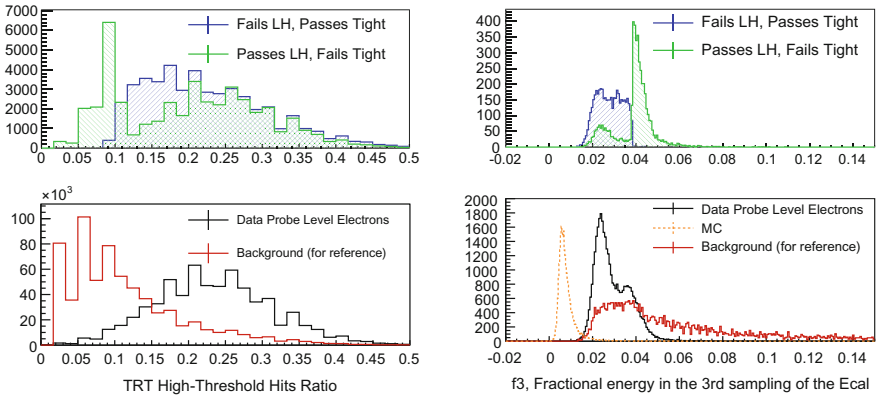

Fig. 5.27 Top: Comparing TRT high-threshold hits ratio (left; $40< E_T <50$ GeV; $0.00 < \eta < 0.60$) and f_3 (right; $40< E_T <50$ GeV; $2.37 < \eta < 2.47$) for electrons which pass the VERY TIGHT operating point but fail the Tight cuts, and vice-versa. Both the likelihood and cut-based menu have the same signal efficiency. The likelihood recovers some of the high-threshold hits ratio/f_3 tail that fail the Tight cut. Bottom: For reference, the raw signal and background distributions are shown. The particular sample is taken from a high-E_T bin, and thus has very little background contamination

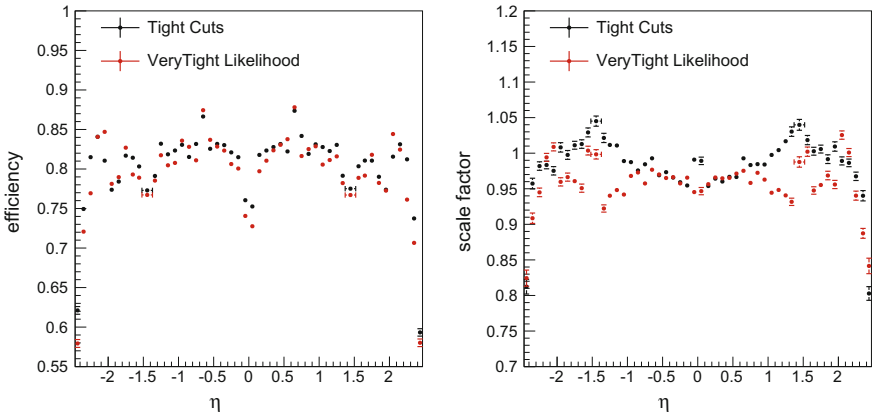

Fig. 5.28 Data efficiencies (left) and scale factors (right) from $Z \rightarrow ee$ tag-and-probe measurements, for 50 bins across η in the range $45 < E_{\mathrm{T}} < 50\,\mathrm{GeV}$. The menus shown are Tight cuts and VERY TIGHT likelihood. The VERY TIGHT likelihood was tuned to have roughly the same efficiency as the Tight cuts menu, but using a coarser binning than shown here

5.7 The Likelihood at Trigger Level in 2015

The motivation for using the electron likelihood to trigger electrons is straightforward: it improves the signal-to-background ratio for all analyses using triggered electrons, compared to a scenario where cut-based triggers are used, and it allows for a more pure electron trigger, allowing ATLAS to collect more events triggered by prompt electrons, or collect electrons with a lower p_{T} threshold. Trigger purity is especially essential given the luminosity increases expected in 2015 and beyond.

Because the likelihood derives its power by recovering signal efficiency normally lost in the tails of variable distributions, applying a likelihood to triggered objects, when the trigger is cut-based, will lead to inefficiencies. In 2012, the lowest single-electron trigger was e24vhi_medium1.[6] Figure 5.29 shows the loss in efficiency if one requires the electron to pass both the trigger requirements and the likelihood cut; a 5–8% loss in efficiency is seen. Figure 5.30 illustrates the inherent loss of efficiency when constructing a likelihood after requiring that electrons first pass a cut-based trigger. These studies suggest that the likelihood works best when it can be applied both online and offline.

However, there are challenges inherent in adapting the established offline electron likelihood to an online environment, caused by constraints in the trigger system. ATLAS analyses typically apply offline identification criteria on triggered electrons during event selection, on top of the (implicit) online identification criteria. Thus,

[6] Despite its name, this menu actually has an implicit online E_{T} threshold of 25 GeV.

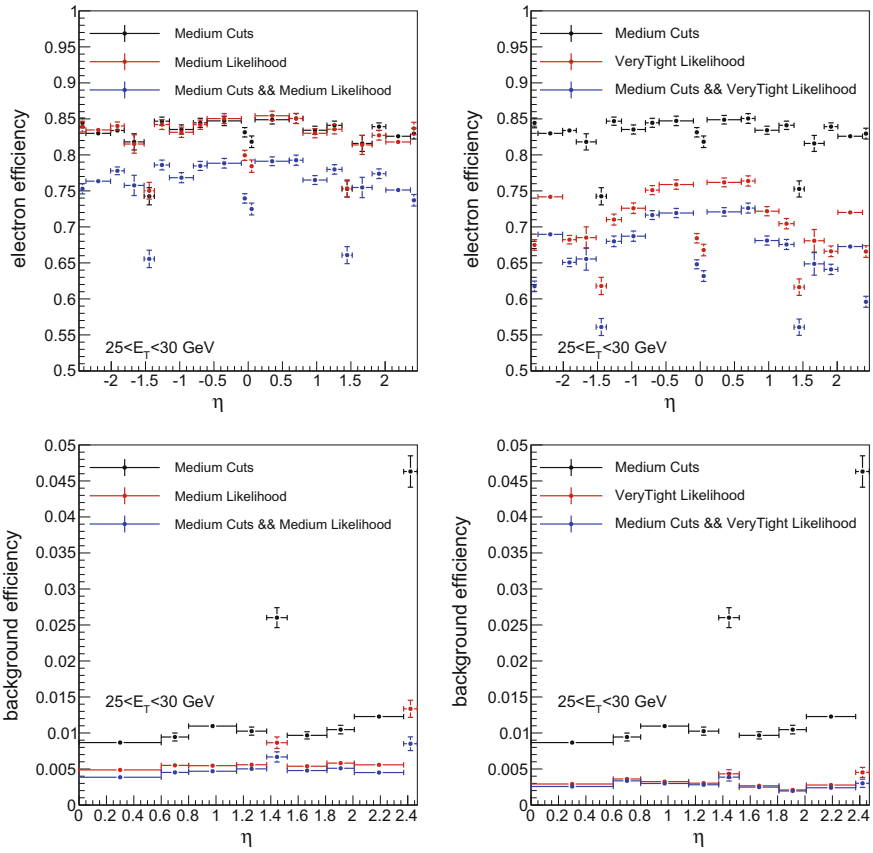

Fig. 5.29 Top left: A plot showing electron efficiencies in data for the MEDIUM cuts, MEDIUM likelihood, and the AND of the two in electrons with $25 < E_T < 30$ GeV. The Medium (offline) cuts used in this study are nearly identical to the ones used online. A 5–8% efficiency loss can be seen when requiring that electrons pass both menus. Top Right: The same plot, with the VERY TIGHT likelihood. A 4–5% loss is seen. Bottom: The corresponding background efficiencies (also estimated using data) of these menus

minimizing online-offline differences to reduce inefficiencies is a priority. These issues, and their resolution, are discussed in the following sections.

5.7.1 Online Reconstruction Algorithm Differences

During the reconstruction of electromagnetic clusters in the LAr calorimeter, certain cell corrections that are applied offline, such as the correction applied as a function

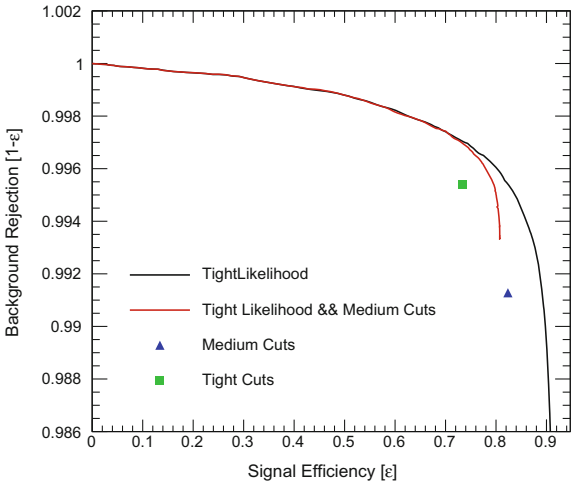

Fig. 5.30 A demonstration of the effect of requiring that electrons pass a cut-based menu before constructing the likelihood. The nominal TIGHT likelihood ROC curve is shown, as well as the ROC curve when the MEDIUM cut-based menu is required. The TIGHT and MEDIUM cut-based operating points are shown for reference. Since the MEDIUM operating point closely resembles the trigger requirement, this illustrates the effect of requiring a cut-based trigger before a likelihood

of the collision's position in the LHC bunch train, are not applied online, leading to differences in the calorimeter discriminating variables.

Another source of inefficiency is the L2 trigger decision. At L2, only a "fast algorithm" version of the cluster is available (in 2012—beginning in 2015 a track from a fast algorithm is available as well). The L2 trigger decision must take 100 K events from L1 and reduce it to 10 K events. Since tracking information is unavailable at L2, rectangular cuts are used to reduce the rate. In particular, the cuts mixed with a likelihood at HLT will cause inefficiencies. (These inefficiencies could be reduced in the future by replacing the rectangular cut approach with an MVA, such as a likelihood using only calorimeter variables.)

The time between a collision and the final ATLAS trigger decision is about 4 s. As a result, trigger reconstruction algorithms that are CPU-intensive must be altered with respect to their offline equivalents. The Gaussian sum filter tracking algorithm, used offline to reconstruct electrons, is too CPU intensive (as of 2015) to be run at the HLT. Instead, the standard tracking algorithm is applied with a pion particle hypothesis, and as a consequence the quality of the track fit degrades for prompt electrons. This impacts the resolution of the d_0 and σ_{d_0} tracking variables, as as well as the track-cluster matching variables $\Delta\phi_{\text{Res}}$ and $\Delta\eta_1$, as seen in Fig. 5.31. The variable $\Delta p/p$, which is output by the GSF algorithm, is unavailable altogether at the HLT.

Appendix A.5 includes a comparison of all electron identification variables and their online-offline differences. Differences in the construction of online and offline likelihoods, such as missing input variables, or differences between the online and

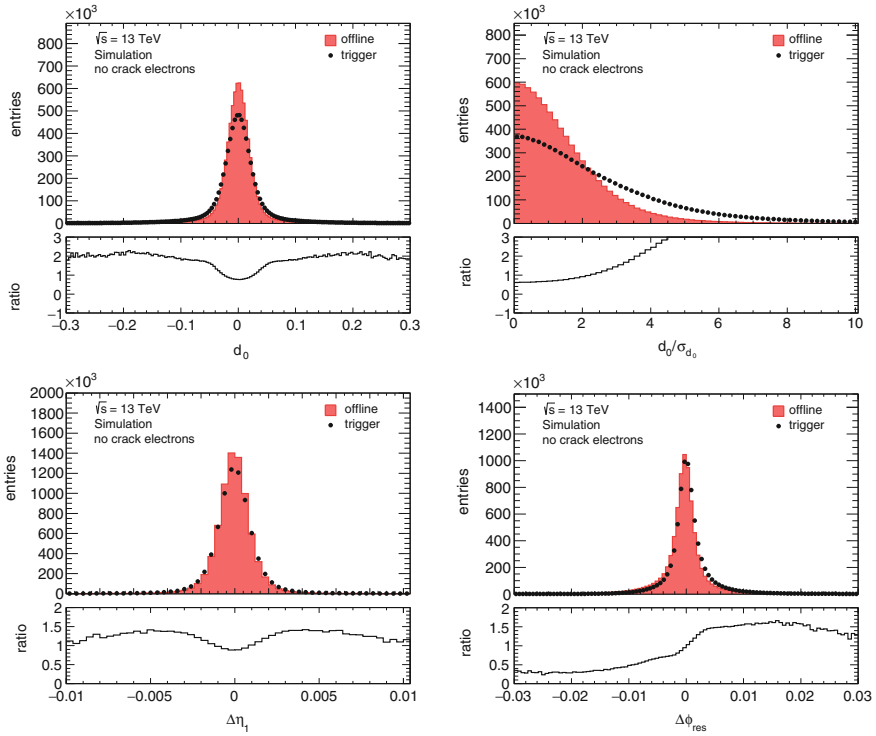

Fig. 5.31 Comparison of track parameter resolution at trigger and offline (2015 reconstruction)

offline input variables, leads to differences between the online and offline likelihood discriminants, which in turn causes inefficiencies during analysis selection. Figure 5.32 illustrates the online–offline inefficiencies induced by the different likelihood construction.

5.7.2 Pile-Up Conditions

The availability of pileup-related information is also limited online. Full event reconstruction is required to determine the number of primary vertices; this variable, which is used offline to correct for the electron likelihood's pileup dependence, must be replaced at the HLT with a different variable.

A reasonable replacement for n_{pv} at the trigger is the average number of collision vertices $\langle\mu\rangle$, measured online by a set of luminosity detectors (one dedicated detector LUCID, the Beam Conditions Monitor (2012), plus measurements from the Tile and Forward calorimeters and the ID. While the actual number of interactions in a bunch crossing fluctuates, and can depend on the location of the colliding bunch in the

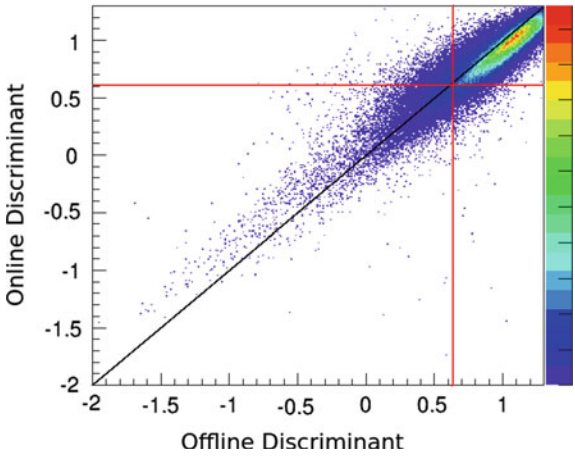

Fig. 5.32 Two-dimensional plot showing the online and offline output likelihood discriminants for a single $\eta \times E_{\mathrm{T}}$ bin, for an MC $Z \to ee$ sample. The z-axis scale shows the number of events, and the red lines indicate online and offline cuts of roughly equal efficiency. The online–offline inefficiency is the bottom right quadrant delineated by the cuts

bunch train, the $\langle\mu\rangle$ is the average over all BCIDs in a lumiblock (one minute of data taking) and acts as a reasonable proxy for the in-time and out-of-time activity in the detector.

5.7.3 *Implementing the Likelihood at the HLT in 2015*

The 2015 electron likelihood is constructed using data sets from MC simulation. For signal, the tag-and-probe method is applied to the $Z \to ee$ sample to obtain a set of unbiased offline electrons; these electrons are matched to HLT objects within $\Delta R = 0.15$. Since MC emulates all triggers, with no prescale, these correspond to electrons passing the basic "etcut" requirements at HLT. For background, the jf17 MC sample described in Sect. 5.2 is used, selecting candidates that pass an "etcut" trigger requirement and match to an HLT object. The MC signal and background samples are used to construct the likelihood PDFs, after applying the constant shift and width corrections derived using the offline selection. The samples are also used to derive discriminant cuts to achieve target signal efficiencies in bins of $\eta \times E_{\mathrm{T}}$.[7]

The likelihood is corrected for pileup using the linear transformation described in Sect. 5.3.6, using $\langle\mu\rangle$ in place of n_{pv} to make the correction. The difference in approach between the online and offline likelihood leads to a small inefficiency.

In 2015, the lowest unprescaled single-electron trigger is e24_lhmedium (triggered at L1 by L1EM20VH). The identification is relaxed at high-E_{T} using e120_lhloose. Multi-electron triggers 2e12_lhloose (dielectron, triggered at L1 by 2EM10VH) and e17_lhloose_2e9_lhloose (3-electron) round out the main trigger list. Supporting triggers for collecting backgrounds are listed in Appendix A.4. This

[7] In hindsight, the MC used to derive discriminant cuts should also be corrected using the shift and width parameters; however, this was not done in 2015.

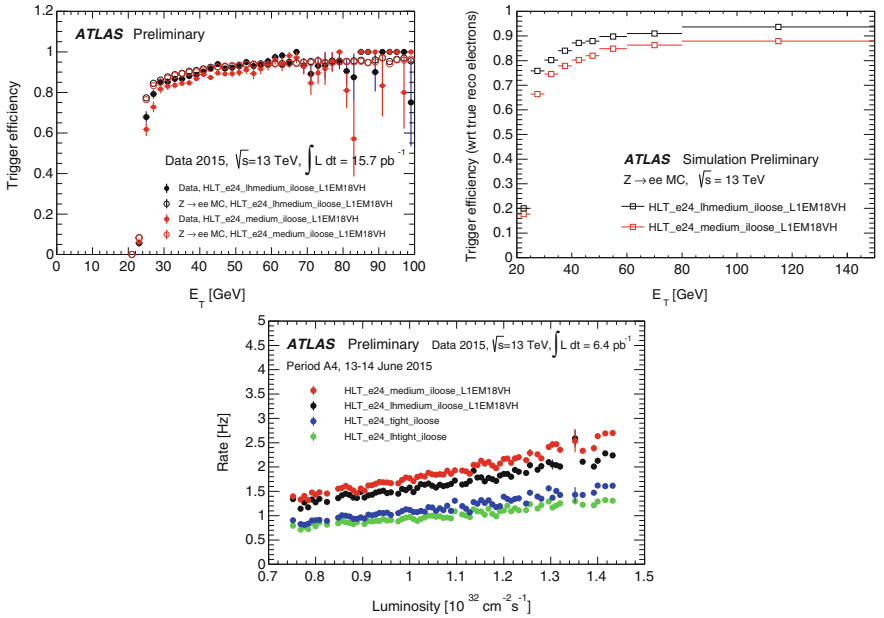

Fig. 5.33 Trigger performance of likelihood and cut-based menus. Shown is **a** trigger efficiencies of data and MC, collected using the tag-and-probe method, for cut-based and likelihood MEDIUM triggers, with respect to offline MEDIUM cut-based and likelihood identification (respectively); **b** trigger efficiencies with respect to true reconstructed electrons in MC; and **c** trigger rates for in 6.4 pb^{-1} of data taking, for likelihood and cut-based trigger menus [15, 16]. Likelihood trigger menus have higher electron efficiencies and lower trigger rates, indicating higher electron purities than cut-based menus. Inefficiencies in **a** are caused by L1 and L2 selection, and differences between the online and offline electron likelihood

list was developed in part to provide data backgrounds for the development of a data-driven likelihood for the 2015 data set.

During the 2015 startup, additional backup triggers were prepared in which the d_0 and σ_{d_0} variables are removed from the likelihood. These triggers are intended as backup to collect signatures such as long-lived particles decaying to electrons, or even taus decaying leptonically to electrons.[8] Removing these two variables causes a 10% increase in trigger rate, for a menu with the same electron efficiency.

5.7.4 Performance of the Likelihood Trigger in 2015

Figure 5.33 shows the performance of the likelihood trigger, with the cut-based trigger for comparison, in early 2015 data taking. The electron efficiency in MC with respect

[8]The τ has a lifetime of 87 μs, and electron triggers are traditionally used to collect electrons from taus. Tau efficiencies are not significantly affected by the inclusion of d_0 and σ_{d_0} in a likelihood.

to all truth electrons is about 7% higher in the likelihood menu compared to the cut-based menu. The trigger rate, however, is about 20% higher in the cut-based MEDIUM trigger than in the MEDIUM likelihood trigger.

The trigger inefficiency in Fig. 5.33a ranges from 20% at low-p_{T} to 5% at high-p_{T}. The inefficiency is caused by L1 and L2 trigger decision inefficiencies; the effect of missing $\Delta p/p$ at the HLT as a likelihood input variable; differences in the online and offline tracking and calorimeter algorithms, causing differences in the likelihood input variables; and the inefficiency due to the effect of using $\langle\mu\rangle$ instead of n_{pv} for the likelihood pileup correction.

5.8 Recent Improvements and Prospects

This section describes recent improvements in electron identification techniques in 2015, as well as ongoing projects and ideas.

5.8.1 High-p_{T} Electrons in 2015 MC-Based Likelihood

High-p_{T} electrons are used in searches for Z' and W' resonance searches. In 2015, the behavior of the electron likelihood TIGHT operating point became inefficient at high-p_{T} (starting around 500 GeV). The cause the inefficiency was traced to a non-ideal tuning of the eProbabilityHT input variable, as well as MC mismodeling of the R_{ϕ} distribution affecting the likelihood performance. These imperfections worsen the performance, especially with the hard cut of the TIGHT discriminant cuts.

To improve the behavior of the TIGHT operating point at high-p_{T}, the TIGHT discriminant cuts were relaxed to the MEDIUM discriminant values; to improve rejection, cuts on E/p and W_{stot}, variables that have stable behavior at high p_{T}, are added to the menu. The cuts applied to these two variables are summarized in Table 5.5. Additional uncertainties are added to the efficiency measurement of this menu, to account

Table 5.5 The E/p and W_{stot} cuts added to the TIGHT operating point in 2015, for electrons with $p_{\mathrm{T}} > 125$ GeV. These cuts, combined with the loosening of the likelihood discriminant cuts, maintain a stable efficiency and an adequate background rejection for very high-p_{T} electrons, and provided a solution to the large inefficiencies in the originally proposed TIGHT operating point

	$\lvert\eta\rvert$ range								
Variable	0.00–0.60	0.60–0.80	0.80–1.15	1.15–1.37	1.37–1.52	1.52–1.81	1.81–2.01	2.01–2.37	2.37–2.47
E/p	10	10	10	10	10	10	10	10	10
W_{stot}	2.45	2.70	3.00	3.10	–	3.05	2.10	1.45	–

for the non-ideal behavior when extrapolating out to electron energies where the number of events is too low to make an efficiency measurement.

5.8.2 Reducing Pileup Dependence Using the TRT Occupancy

So far, two variables have been used to estimate the amount of in-time and out-of-time activity in the detector: n_{pv}, the number of reconstructed primary vertices in an event, and $\langle\mu\rangle$, the average number of interactions in an event, as measured by ATLAS luminosity detectors. Only the latter is available at the trigger level, and it is averaged over all events in a one-minute lumiblock. However, electron identification is affected only by local tracking and calorimeter activity, and variables that average activity over the entire detector or across millions of events do not give information related to a particular region of the detector inside a particular event.

A proposed measurement of local activity in the detector in a single event is the local occupancy of the TRT detector. The TRT can be divided into 192 regions (two barrel regions, and two endcap regions on each side of the detector, multiplied by 32 phi modules). The occupancy of a region is defined as the number of hits recorded in that region, divided by the total number of straws in that region. The track occupancy is defined as the average of the occupancies of each region, weighted by the number of hits associated with the track in question from that particular region. This quantity represents the activity in a local detector region near the track, inside a single event (and thus it describes only in-time pileup activity). The local track occupancy has the added benefit that it is available both offline and online, at the time of the HLT electron trigger decision.

Local TRT occupancy was commissioned starting in mid-2014 and incorporated into ATLAS reconstruction in preparation for the 2016 data taking period. It will be studied as a means to efficiently account for pileup effects in electron identification, potentially replacing n_{pv} and $\langle\mu\rangle$.

5.8.3 Extending the Likelihood to Include Multiple Background Hypotheses

In the current implementation of the electron likelihood, a mixture of electron backgrounds collected using supporting electron triggers is used for the background PDFs. The mixture includes backgrounds from light-flavor hadrons, non-prompt electrons in heavy flavor decays, and converted photons. Each of these backgrounds has a different detector response; a good variable for discriminating hadrons from electrons may be a poor one for separating electrons and converted photons, for example. Typically, photons have a similar calorimeter response to electrons, but different tracking

signatures, owing to their displaced vertex; non-prompt background electrons from heavy flavor have slightly displaced vertices, and are typically non-isolated, which can affect calorimeter shower shapes and isolation variables. Light-flavor hadrons are also non-isolated, but typically do not have displaced vertices. Treating all three backgrounds using the same PDFs will make the likelihood less optimal.

The Neyman–Pearson lemma from Eq. 5.1 can be extended to a scenario in which the background is multi-source:

$$d(\mathbf{x}) = \frac{p(H_s|\mathbf{x})}{f_{b1} \cdot p(H_{b1}|\mathbf{x}) + f_{b2} \cdot p(H_{b2}|\mathbf{x}) + ...}, \tag{5.10}$$

where f_{b1} and f_{b2} are the relative abundances of each background in the sample. Following the same approach as before, the optimal likelihood discriminant is (substituting HF, LF and γ as the relevant electron backgrounds):

$$d_{\mathcal{L}} = \frac{\mathcal{L}_S}{\mathcal{L}_S + f_{\text{LF}}\mathcal{L}_{\text{LF}} + f_\gamma \mathcal{L}_\gamma + f_{\text{HF}}\mathcal{L}_{\text{HF}}} \tag{5.11}$$

A multi-background likelihood can be understood as having two benefits: first, PDF descriptions for individual background sources will become more pure. Thus, signal rejection with respect to LF background will perform more optimally for a likelihood constructed as $\mathcal{L}_S/(\mathcal{L}_S + \mathcal{L}_{\text{LF}})$ as compared to $\mathcal{L}_S/(\mathcal{L}_S + \mathcal{L}_{\text{inclusive}})$. The performance with respect to LF degrades when the additional $\mathcal{L}_{\text{HF}}$ and $\mathcal{L}_\gamma$ terms are added to the denominator in Eq. 5.11; however, the overall performance with respect to all backgrounds should be more optimal.

There is flexibility in choosing the factors f_{LF}, f_γ and f_{HF}—fractions that can vary depending on the analysis. For an all-purpose set of LOOSE, MEDIUM, and TIGHT menus made available to the ATLAS community, these factors can be chosen to reflect the general adage that light-flavor backgrounds are often most abundant, followed by conversions and heavy-flavor backgrounds, in the typical analysis with electron final states. In any case, even choosing $f_{\text{LF}} = f_\gamma = f_{\text{HF}}$ could improve the likelihood performance compared to the current inclusive single-background scheme. The optimization of background fractions f would then be another tunable parameter in the $\eta \times E_{\text{T}}$ likelihood optimization procedure.

One potentially paradigm-shifting benefit to a multi-background likelihood construction is the possibility to construct additional likelihood menus to aid in background studies, namely a likelihood constructed to distinguish conversion backgrounds from hadrons or electrons, $\mathcal{L}_\gamma/(\mathcal{L}_\gamma + \sum_i f_i \mathcal{L}_i)$, and a hadron likelihood, $\mathcal{L}_{\text{LF}}/(\mathcal{L}_{\text{LF}} + \sum_i f_i \mathcal{L}_i)$ (where $\mathcal{L}_i$ also includes electrons). With these tools, analyzers can quickly obtain control samples that are highly enriched in the three different electron backgrounds, and perform much more accurate reducible background estimates using these pure control samples.

References

1. ATLAS Collaboration, Measurement of $W^{\pm}$ and Z-boson production cross sections in pp collisions at $\sqrt{s} = 13$ TeV with the ATLAS detector, arXiv:1603.09222 [hep-ex]
2. ATLAS Collaboration, Measurements of Higgs boson production and couplings in the four-lepton channel in pp collisions at center-of-mass energies of 7 and 8 TeV with the ATLAS detector. Phys. Rev. D **91**, 012006(2015), arXiv:1408.5191 [hep-ex]
3. W. Lampl et al., Calorimeter Clustering Algorithms: Description and Performance, ATL-LARG-PUB-2008-002, 2008, http://cds.cern.ch/record/1099735
4. ATLAS Collaboration, Improved electron reconstruction in ATLAS using the Gaussian sum filter-based model for bremsstrahlung, ATLAS-CONF-2012-047 (2012), http://cdsweb.cern.ch/record/1449796
5. ATLAS Collaboration, Observation of an excess of events in the search for the Standard Model Higgs boson in the $H \to ZZ^{(*)} \to 4\ell$ channel with the ATLAS detector, ATLAS-CONF-2012-092 (2012), http://cdsweb.cern.ch/record/1460411
6. ATLAS Collaboration, Measurement of the isolated diphoton cross section in pp collisions at $\sqrt{s} = 7$ TeV with the ATLAS detector. Phys. Rev. D **85**, 012003 (2012), arXiv:1107.0581 [hep-ex]
7. ATLAS Collaboration, Search for squarks and gluinos using final states with jets and missing transverse momentum with the ATLAS detector in $\sqrt{s} = 7$ TeV proton–proton collisions. Phys. Lett. B **710**, 67 (2012), arXiv:1109.6572 [hep-ex]
8. ATLAS Collaboration, Expected electron performance in the ATLAS experiment, ATL-PHYS-PUB-2011-006, 2011, http://cdsweb.cern.ch/record/1345327
9. ATLAS Collaboration, Electron performance measurements with the ATLAS detector using the, LHC proton-proton collision data. Eur. Phys. J. C **72**(2012), 1909 (2010), arXiv:1110.3174 [hep-ex]
10. ATLAS Collaboration, Electron efficiency measurements with the ATLAS detector using the 2015 LHC proton-proton collision data, ATLAS-CONF-2016-024 (2016), https://cds.cern.ch/record/2157687
11. A. Hoecker, P. Speckmayer, J. Stelzer, J. Therhaag, E. von Toerne, H. Voss, M. Backes, T. Carli, O. Cohen, A. Christov, D. Dannheim, K. Danielowski, S. Henrot-Versille, M. Jachowski, K. Kraszewski, A. Krasznahorkay, Jr., M. Kruk, Y. Mahalalel, R. Ospanov, X. Prudent, A. Robert, D. Schouten, F. Tegenfeldt, A. Voigt, K. Voss, M. Wolter, A. Zemla, TMVA - Toolkit for Multivariate Data Analysis, arXiv:physics/0703039
12. J. Neyman, E.S. Pearson, On the problem of the most efficient tests of statistical hypotheses, in *Philosophical Transactions of the Royal Society of London. Series A, Containing Papers of a Mathematical or Physical Character*, vol. 231 (1933) pp. 289–337, http://www.jstor.org/stable/91247
13. O. Behnke, K. Krninger, G. Schott, T. Schrner-Sadenius, *Data Analysis in High Energy Physics: A Practical Guide to Statistical Methods* (Wiley-VCH, Weinheim, 2013), https://cds.cern.ch/record/1517556
14. ATLAS Collaboration, The ATLAS Experiment at the CERN Large Hadron Collider, JINST **3**, S08003 (2008)
15. G. Pasztor, R. White, C.Y. Shehu, J. Reichert, N.M. Hartmann, Electron trigger performance in 2015 ATLAS data, Technical Report ATL-COM-DAQ-2015-102, CERN, Geneva, July, 2015, https://cds.cern.ch/record/2034867. For upcoming conferences: EPS, DPF, LISHEP
16. G. Pasztor, R. White, F. Monticelli, Electron and photon trigger rates in 2015 ATLAS data, Technical Report ATL-COM-DAQ-2015-103, CERN, Geneva, July, 2015, https://cds.cern.ch/record/2034886. For upcoming conferences: EPS, DPF, LISHEP

Chapter 6
Electron Efficiency Measurements Using $Z \rightarrow ee$ Events

6.1 Overview of Electron Efficiency Measurements

Physics measurements with electrons in their final state signature usually require knowledge of the efficiency of electrons satisfying the identification criteria used to select them. Since we often use MC simulation to determine the fiducial acceptance or background rates of certain processes, we need to ensure that the simulation uses the correct efficiency. This is accomplished by measuring the efficiency in-situ using a relatively pure sample of electrons and then scaling the prediction of the Monte Carlo simulation so that the electron identification efficiency in MC matches the electron efficiency in the data.

In ATLAS the development of electron reconstruction and identification algorithms is carried out within one of the combined performance (CP) groups known as the e/γ CP group. This group determines several sets of electron identification criteria called "menus" at different levels of electron efficiency and background rejection. In 2012, the menus available were named LOOSE++, MULTILEPTON,[1] MEDIUM++, and TIGHT++ cut-based identification menus, and LOOSELH and VERY TIGHT likelihood-based menus.[2] As part of the support for analyses using electrons, the e/γ CP group measures efficiencies of these electron menus, as well as the "scale factors" of the form $\varepsilon_{\text{data}}/\varepsilon_{\text{MC}}$, with which analyses can correct prompt electrons in MC simulation.

The following description of the electron efficiency and scale factor measurements applies to the 2012 measurement of electron efficiencies; however, the major details (unless otherwise stated) are similar for electron efficiency measurements using data from 2011 and 2015.

[1] The MULTILEPTON menu is designed to have similar electron efficiency as LOOSE++ but with better background rejection. The better performance is achieved by optimizing rectangular cuts on variables that allow for electron energy loss due to bremsstrahlung.

[2] MEDIUMLH and TIGHTLH likelihood-based menus were also derived but efficiency and scale factor measurements were not derived due to lack of demand from analyses.

K. Brendlinger, *Physics with Electrons in the ATLAS Detector*, Springer Theses,
https://doi.org/10.1007/978-3-319-73930-4_6

The total efficiency for an electron used at analysis level is defined as the product of the efficiency of electron reconstruction, identification efficiency, the efficiency of any additional requirements, and (if the analysis electron is required to satisfy an online electron identification requirement as part of the trigger) the trigger efficiency:

$$\varepsilon_{\text{total}} = \varepsilon_{\text{cluster}} \times \varepsilon_{\text{reconstruction}} \times \varepsilon_{\text{identification}} \times \varepsilon_{\text{additional}} \times \varepsilon_{\text{trigger}} \tag{6.1}$$

The cluster efficiency is the efficiency with which an electron is found by the sliding window algorithm and reconstructed as an electromagnetic cluster. This efficiency is predicted by MC to be between 95% (7 GeV electrons) and 99.9% (45 GeV electrons), and more efficient in the barrel than in the endcaps [1]. No data-MC scale factor is measured for this efficiency. The reconstruction efficiency is the rate for reconstructed clusters to be reconstructed as electrons, e.g. to have a matched track that satisfies basic track quality requirements. Reconstruction-level electron tracks must have at least one pixel hit and at least seven silicon hits. All electrons must pass the same cluster and reconstruction requirements.[3]

The identification efficiency is the efficiency of any of the several identification menus designed to reject backgrounds, e.g. the cut-based and likelihood-based menus mentioned above. The efficiency of additional requirements, such as impact parameter and isolation requirements,[4] is measured with respect to electrons that satisfy ("pass") the criteria specified in the identification menu. Finally, the trigger efficiency is the rate at which an electron passing all cluster, reconstruction, identification and additional requirements will also satisfy the online requirements of a specific trigger.

To measure electron efficiencies in data, we must have a source of data enriched in electrons that are not biased by any electron identification. An electron collected using electron triggers are biased by the strict identification criteria applied by those triggers. However, in the di-electron resonances $J/\psi \rightarrow ee$ and $Z \rightarrow ee$, one electron can satisfy the trigger requirements and the other electron can serve as the unbiased source.[5] This method is referred to as the "tag-and-probe" method—the electron that satisfies the trigger selection is the "tag", and the other electron, on which the efficiency measurement is carried out, is the "probe".

The tag-and-probe method using $J/\psi \rightarrow ee$, $Z \rightarrow ee$, and $Z \rightarrow ee\gamma$ events is used to measure electron efficiencies at varying electron p_{T}. The $J/\psi \rightarrow ee$ events measure identification efficiencies of electrons with $7 < p_{\text{T}} < 20\,\text{GeV}$; $Z \rightarrow ee\gamma$ events measure identification efficiencies in the range $10 < E_{\text{T}} < 15\,\text{GeV}$. The remaining electron range, $E_{\text{T}} > 15\,\text{GeV}$, is measured using $Z \rightarrow ee$ events. Reconstruction efficiency is measured for electrons with $E_{\text{T}} > 15\,\text{GeV}$ using $Z \rightarrow ee$ tag-and-probe. These methods are described in [1]. Figure 6.1 illustrates the number of probes available that pass TIGHT identification in the 2012 data set, as a function

[3] In addition, the e/γ CP Group recommends that isolated electrons not overlap with jets: in 2012, jets within $\Delta R(e, \text{jet}) < 0.2$ are removed, as they are considered to be the same object; electrons are required to have $\Delta R(e, \text{jet}) > 0.4$ with the remaining set of jets, to ensure they are well-isolated.

[4] Impact parameter and isolation criteria are described in more detail in Chap. 3, Sect. 3.2.4.

[5] Some math, described momentarily, is required to make this work out.

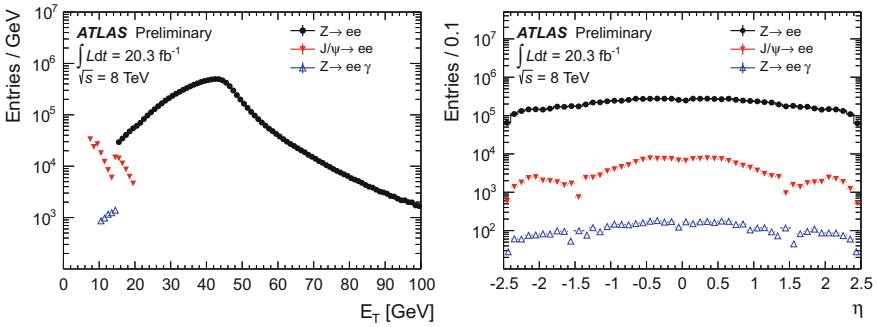

Fig. 6.1 Number of electron candidates used for the efficiency measurement passing TIGHT cut-based identification criteria using 20.3 fb^{-1} of 8 TeV data, for $J/\psi \to ee$, $Z \to ee$ and $Z \to ee\gamma$ events

of $E_{\mathrm{T}}$and η, to give a sense of the number of real electrons available for measurement in the $E_{\mathrm{T}} \times \eta$ phase space.

The remainder of this section is devoted to efficiency measurements using the tag-and-probe method with $Z \to ee$ events, and using the m_{ee} spectrum to estimate the background; this method is referred to as the Z_{mass} method. Another method called the Z_{Iso} method uses isolation to differentiate between the electron signal and background. The two methods use the same electrons from Z decays and thus are statistically correlated, but serve as cross-checks for each background subtraction technique. Both methods are combined for the final efficiency measurement, as described in Sect. 6.8.

6.2 Outline of Z-Mass Method

The Z_{mass} method is a tag-and-probe method using $Z \to ee$ events to measure electron efficiencies, with m_{ee} as the discriminating variable used to estimate and subtract background. The following section describes the event selection and the formalism of the tag-and-probe method using background templates derived from data.

Event Selection

The selection requirements are listed in Table 6.1 and described below. Events are selected by requiring that one of the main single-electron triggers fired (e24vhi_medium1 || e60_medium1). The event must have a primary vertex with at least three tracks and pass LAr calorimeter data quality requirements. In each event, a tag is sought that matches to an HLT object associated to the electron trigger(s) that fired the event. The tag must be a high-quality electron, with $p_{\mathrm{T}} > 25$ GeV and passing strict identification and isolation criteria. (The specific tag selection criteria is varied

Table 6.1 The $Z \to ee$ tag-and-probe event selection

Event preselection

LAr detector data quality
Trigger: e24vhi_medium1 || e60_medium1
At least 1 primary vertex (>= 3 tracks)

Tag selection	**Probe selection**
$E_{\mathrm{T}} > 25$ GeV	$E_{\mathrm{T}} > 15$ GeV
$\|\eta\| < 2.47$, !$(1.37 < \|\eta\| < 1.52)$	$\|\eta\| < 2.47$
detector data-quality criteria	detector data-quality criteria
trigger matched ($\Delta R < 0.15$)	
ID { MEDIUM++ && $E_{\mathrm{T}}^{\mathrm{cone40}} < 5$ GeV; TIGHT++; TIGHT++ && $E_{\mathrm{T}}^{\mathrm{cone40}} < 5$ GeV }	track quality (nPixelHits ≥ 1, nSiHits ≥ 7)
$p_{\mathrm{T}}^{\mathrm{cone20}}/p_{\mathrm{T}} < 0.1$	
	$\Delta R(e, \mathrm{jet}) > 0.4$

Further event selection

At least 1 Tag, 1 Probe (opposite sign)
Mass Window Requirement { $80 < m_{ee} < 100$ GeV; $75 < m_{ee} < 105$ GeV; $70 < m_{ee} < 110$ GeV }

as part of the determination of systematic uncertainty, as described in Sect. 6.6.) A second electron candidate (the probe) must exist in the event as well, falling inside the tracker volume and passing basic track quality criteria (nPixelHits $\geq$1, nSiHits $\geq$7). Both the tag and probe must satisfy data-quality criteria related to the proper functioning of the inner detector and calorimeters. The Z_{mass} method measures probes with $E_{\mathrm{T}} > 15$ GeV. If an opposite-charge tag-probe pair is found, then the probe is considered for the measurement. If both the objects pass the tag and the probe requirements (including the trigger matching), then both are considered as probes for the measurement.

This last point is a key detail required to ensure that the efficiency measurement is unbiased. An electron probe should be considered based only on the identification quality of the other electron in the event. If electron (a) satisfies the tag requirement, then electron (b) is counted as a probe. If electron (b) satisfies the tag, then electron (a) is a probe. If both are tags, then both are also probes.

If more than one tag-probe pairs are found, then the tag-probe pair with the highest m_{ee} is used, and the other tag-probe pairs are ignored.[6] Finally, to ensure that the tag-probe pair is consistent with a Z boson, their m_{ee} is required to fall within a mass window around the PDG Z mass (91.188 GeV).

Table 6.1 presents three options for the tag identification and the mass window requirement. Variations of the event selection are used to assess systematic uncertainties on the efficiency measurement. The uncertainty strategy is discussed later in Sect. 6.6.

Once the probes are selected, the efficiency of an identification selection menu can then be measured: out of the electron probes considered for the measurement, the efficiency is simply the number of electrons passing the identification menu divided by the total number of probes in the Z-mass peak:

$$\varepsilon_{\text{ID}} = \frac{n_{\text{electrons passing ID}}}{n_{\text{electron probes}}}. \tag{6.2}$$

This formula is in keeping with the principle that both electrons are counted as probes if both satisfy the tag criteria, as described earlier. A demonstration of the unbiased nature of the above equation can be found in Appendix B.1.

The above picture is simplified; in reality, non-electron background contaminates both the numerator and the denominator of the efficiency measurement. The equation can be rewritten to reflect the presence of background (real electron counts $n_{\text{electrons passing ID}}$ and $n_{\text{electron probes}}$ are replaced by S_{ID} and S_{probe}, respectively, and background terms are labeled with B):

$$\varepsilon_{\text{ID}} \equiv \frac{S_{\text{ID}}}{S_{\text{probe}}} = \frac{N_{\text{ID}}^{\text{peak}} - B_{\text{ID}}^{\text{peak}}}{N_{\text{probe}}^{\text{peak}} - B_{\text{probe}}^{\text{peak}}} \tag{6.3}$$

Background Subtraction Using Templates

Estimating the background in this efficiency measurement requires (1) obtaining a template shape of the m_{ee} spectrum to describe the background, (2) normalizing this shape in a background-enriched region, making sure to correct for signal leakage in that region, and (3) using the normalized template to determine the amount of background in the Z-peak. This procedure must be carried out for both the numerator and the denominator of Eq. 6.3.

The non-electron background satisfying the tag-and-probe criteria is due to hadrons and comes primarily from two sources. This first is multijet events in which two jets are misidentified as electron candidates, that is, as the tag and the probe. The second source is W bosons produced in association with jets. In this second case, the

[6] The choice to use one tag-probe pair per event should have a small impact on the result, especially since the same choice is made consistently throughout the procedure, e.g. when defining background templates or applying the same selection to MC.

W decays leptonically producing a prompt electron that is typically the tag electron candidate and a jet is misidentified as an electron candidate (usually the probe).

To estimate these backgrounds, a selection of the probes collected using the tag-and-probe method is enriched in background events using inverted electron identification requirements. This sample of probes is used to generate a template m_{ee} background shape. The template is normalized to background events in the m_{ee} spectrum of the numerator or the denominator in a region of the invariant mass spectrum that does not include the peak of the Z boson resonance, called the normalization region (abbreviated n.r.).

For determining the amount of background in the numerator, the same template used for the denominator is normalized to a selection of probes obtained using the same selection as above but requiring a same-charge tag-probe pair (these are referred to as "SS" probes):

$$B_{\text{ID}}^{\text{peak}} = N_{\text{templ}}^{\text{peak}} \times \left(\frac{N_{\text{ID}}^{\text{n.r,SS}}}{N_{\text{templ}}^{\text{n.r.}}} \right). \tag{6.4}$$

The m_{ee} spectrum of same-charge probes should be dominated by background away from the Z-peak; it should also roughly have the same magnitude as the opposite-charge background probes.[7] The subtraction of the background in the numerator is a small correction in comparison to the subtraction of background in the denominator.

The amount of background in the denominator can be estimated to first approximation by

$$B_{\text{probe}}^{\text{peak}} \sim N_{\text{templ}}^{\text{peak}} \times \left(\frac{N_{\text{probe}}^{\text{n.r.}}}{N_{\text{templ}}^{\text{n.r.}}} \right). \tag{6.5}$$

However, the normalization region can have contamination from signal; this contamination is approximated by taking the number of (cut-based) tight events in the normalization region and dividing by the tight efficiency measured in data. The background estimate in the denominator is then:

$$B_{\text{probe}}^{\text{peak}} \equiv N_{\text{templ}}^{\text{peak}} \times f_{\text{templ}} = N_{\text{templ}}^{\text{peak}} \times \left(\frac{N_{\text{probe}}^{\text{n.r.}} - \frac{1}{\varepsilon_{\text{tight}}} N_{\text{tight}}^{\text{n.r.}}}{N_{\text{templ}}^{\text{n.r.}}} \right). \tag{6.6}$$

where f_{templ} has been defined as the template normalization factor. The efficiency is then found using Eq. 6.3, with backgrounds estimated using Eqs. 6.4 and 6.6.

The astute reader will have noticed that the TIGHT efficiency is apparently used in Eq. 6.6, before it can be calculated using Eq. 6.3. In practice, the TIGHT efficiency is

[7] This is in general not the case for the W+jet background, which can have larger opposite-charge probe contributions from W+c where the c-quark decays weakly to a non-prompt lepton. W production in association with a quark-initiated jet will also produce more opposite-charge probes because of a correlation between the charge of the quark and the charge of the associated reconstructed probe electron. However, normalizing the background to the SS distribution is preferable to using the OS distribution, where signal contamination is much too high.

calculated iteratively—first using Eq. 6.5 to estimate the denominator background, and then using Eq. 6.6 with $\varepsilon_{\text{tight}}$ taken from the first estimate. Additional iterations of this procedure result in negligible changes; thus, a single iteration is used to calculate the TIGHT efficiency. This final TIGHT efficiency is used when calculating efficiencies of other menus; for these menus, no iterative procedure is required.

For the 2012 data set, the efficiency measurement is made in bins of $\eta \times E_{\text{T}}$:

$$\eta = [-2.47,\ -2.37,\ -2.01,\ -1.81,\ -1.52,\ -1.37,\ -1.15,\ -0.80,\ -0.60,\ -0.10,\ 0.00,\ 0.10,\ 0.60,\ 0.80,\ 1.15,\ 1.37,\ 1.52,\ 1.81,\ 2.01,\ 2.37,\ 2.47\,] \tag{6.7}$$

$$E_{\text{T}} = [7,\ 10,\ 15,\ 20,\ 25,\ 30,\ 35,\ 40,\ 45,\ 50,\ 60,\ 80,\ \infty] \tag{6.8}$$

Figure 6.2 demonstrates the application of the method described above. To measure the number of signal electrons in the denominator (probe level), a template describing background is normalized to the $120 < m_{ee} < 250\,\text{GeV}$ tail of the distribution. For illustrative purposes, the MC $Z \rightarrow ee$ signal is normalized to the signal estimate in the Z-peak; the sum of MC $Z \rightarrow ee$ signal and template background describes the total distribution well.

The numerator (ID level) distribution features the same template, normalized to the distribution of same-sign probes passing TIGHT cut-based identification. Again, when MC $Z \rightarrow ee$ is normalized to the signal estimate in the Z-peak, the sum of MC and background describes the full m_{ee} spectrum well.

Figure 6.2 is an example of the final result obtained after finding the optimal background templates to minimize potential biases. The following sections describe the process of template optimization, and the tools used to quantify and reduce bias in the measurement.

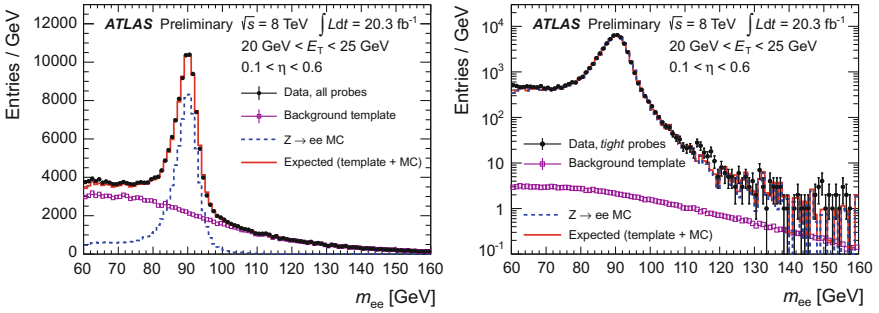

Fig. 6.2 Denominator (probe-level, left) and numerator (ID-level, right) of the Z_{mass} efficiency measurement of the TIGHT cut-based identification menu. Templates describing the background are normalized in the $120 < m_{ee} < 250\,\text{GeV}$ region although the x-axis is cut off at 160 GeV

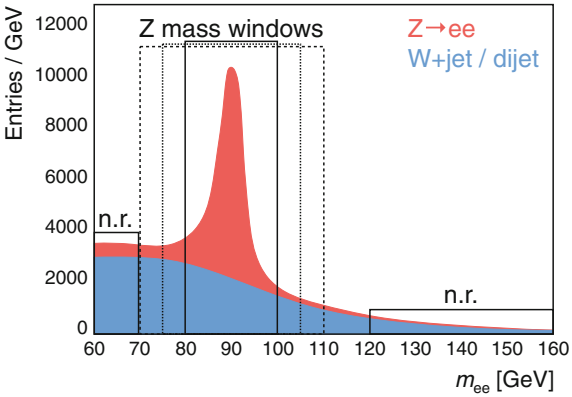

Fig. 6.3 Depiction of the Z_{mass} method regions: the three windows used in event selection, as well as the background normalization regions (labeled n.r.). The plot contains the m_{ee} of each probe used for the efficiency measurement, and shows the $Z \rightarrow ee$ and $W \rightarrow e\nu +$ jet/multijet background

6.3 Choice of Background Normalization Region

The choice of normalization region is deeply connected to the choice of background template. In the measurement using the 2011 data set, a normalization region of $120 < m_{ee} < 250\,\text{GeV}$ is used, since it is sufficiently far away from the Z-peak and enriched in background. However, studies in 2012 indicated that certain templates can have m_{ee} shape biases, causing too little background subtraction from the denominator distribution when normalized in the high-m_{ee} tail. The nature of these biases will be discussed during the description of the background templates.

To test these biases, a second normalization region is also considered: $60 < m_{ee} < 70\,\text{GeV}$. Figure 6.3 depicts the Z-peak windows and background normalization regions; both background normalization regions are used to assess systematic errors (see Sect. 6.6).

6.4 Template Optimization

Background templates are obtained by inverting the electron identification and isolation requirements on the selection of probes.[8] This template selection will naturally be contaminated with signal electrons. The signal contamination in the template S_{templ} is estimated using $Z \rightarrow ee$ MC, by applying the template selection to MC. These events are scaled to the correct luminosity/cross section, approximated by taking the ratio of TIGHT data events to TIGHT MC events in the in the Z-peak:

[8] "Inverting" a selection requirement designed to identify prompt electrons means to take the logical negation, i.e. inverting the LOOSE cut-based menu is to take !LOOSE, and inverting the isolation requirement $E_{\text{T}}^{\text{cone40}}/E_{\text{T}} < 0.05$ is to take $E_{\text{T}}^{\text{cone40}}/E_{\text{T}} > 0.05$.

Table 6.2 Identification menus considered for the background template criteria. They are ordered according to tightness (lowest to highest electron efficiency). Inverted identification menus are combined with inverted isolation requirements to obtain templates

ID Menu
!MULTILEPTON
!LOOSE
!VERYLOOSELH
!VERYLOOSELH || !MULTILEPTON
!2MULTILEPTON
!VERYLOOSELH || !LOOSE
!2LOOSE

$$S_{\text{templ}} = N^{\text{MC}}_{\text{templ}} \times \frac{N^{\text{peak}}_{\text{tight,data}}}{N^{\text{peak}}_{\text{tight,MC}}} \tag{6.9}$$

Once this distribution of MC events passing the template requirement is correctly scaled, it is subtracted from the template distribution, resulting in a template corrected for signal contamination.

Table 6.2 lists the identification criteria—built from various loose identification menus—that are considered in the template selection. Templates are built using identification and isolation criteria: events passing a template are required to fail an identification menu and fail an isolation requirement (for example, fail $E_{\text{T}}^{\text{cone40}}/E_{\text{T}} < 0.05$). New selection menus that more efficiently select background can be created by requiring that at least two selection criteria in the menu fail; these menus are referred to as !2LOOSE and !2MULTILEPTON.[9] The templates that produce the most unbiased efficiency measurement are sought from this list of available template criteria.

The choice of background template is a balance between two competing effects:

1. An adequate description of the background in the full m_{ee} spectrum
2. Minimal signal contamination in the templates.

The latter is crucial because the signal contamination is estimated using MC, and thus has a scale factor associated with it that is assumed equal to 1 in the method. However, the scale factor of inverted identification requirements has the potential to be very large compared to scale factors of the traditional (non-inverted) electron identification menus, because small modeling differences in the tails of identification variable distributions can have a fractionally large effect on the efficiency. Thus, keeping the signal contamination to a minimum is critical.[10]

[9] A list of selection criteria in the LOOSE and MULTILEPTON cut-based menus can be found in Table 5.3 of Sect. 5.3.3.

[10] An alternative would be to develop a means of assigning a systematic uncertainty on the signal contamination in the templates. In lieu of this, however, the uncertainty due to signal contamination must be as close to negligible as possible.

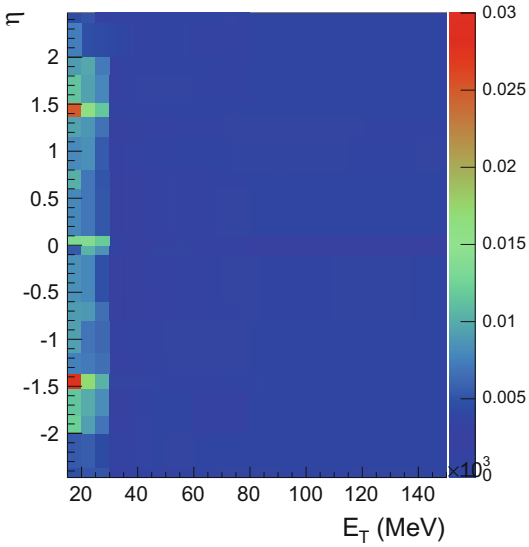

Fig. 6.4 An estimate the signal contamination in the official templates, presented as a fraction. The numerator of this fraction is the signal contamination yield estimate in the peak from MC, and the denominator is the denominator (base) signal estimate, also in the peak. Below 30 GeV, the template is !MULTILEPTON, $E_{\mathrm{T}}^{\mathrm{cone30}}/E_{\mathrm{T}} > 0.02$. Above 30 GeV, the template is !2LOOSE, $E_{\mathrm{T}}^{\mathrm{cone40}}/E_{\mathrm{T}} > 0.05$; the other high-$E_{\mathrm{T}}$ template will have less signal contamination than this one

Following the two criteria above, the template chosen should exhibit good agreement with the background in the probe-level distribution across the entire m_{ee} spectrum ($60 < m_{ee} < 250\,\mathrm{GeV}$), with minimal signal contamination. To quantify the potential signal contamination bias, the following metric is used:

- The fraction $\xi = S_{\mathrm{templ}}^{\mathrm{peak}} \cdot f_{\mathrm{templ}}/S_{\mathrm{probe}}$, which is the size of the template signal contamination component as a fraction of the total signal in the denominator, should be kept as close to 0 as possible to minimize the effect of template signal contamination. This quantity is used because it roughly corresponds to the percent effect on the efficiency measurement. In other words, if ξ is estimated by MC to be 1%, and in data the true value is 2%, then the measured efficiency is biased by ∼1%. (This quantity is demonstrated in Fig. 6.4.)

To evaluate template shape bias, two different metrics were used:

- The template shape can be compared to a reference template requiring !LOOSE, with no isolation requirement. While the !LOOSE template has too much signal contamination to be used itself, it should faithfully reproduce the shape of the background in the off-peak m_{ee} regions: the !LOOSE menu's efficiency for selecting background is very high, so the bias on the background shape is low. (Demonstrated in Figs. 6.5 and 6.6.)
- An unbiased template should give the same efficiency measurement regardless of the region in which it is normalized. Thus, the measurement is performed twice, using $120 < m_{ee} < 250\,\mathrm{GeV}$ and $60 < m_{ee} < 70\,\mathrm{GeV}$ normalization regions, and the result is compared. Good agreement between the measurement with low-m_{ee} and high-m_{ee} template normalization indicates a less biased template. (Demonstrated in Fig. 6.7.)

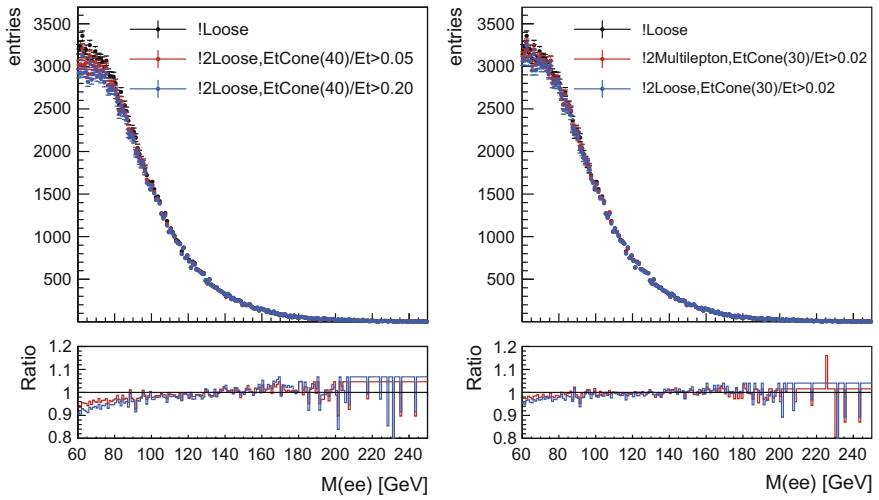

Fig. 6.5 Templates for the $20 < E_{\mathrm{T}} < 25\,\mathrm{GeV}$, $0.1 < \eta < 0.6$ efficiency measurement. Each template is normalized in the $120 < m_{ee} < 250\,\mathrm{GeV}$ region to the probe-level distribution. The template signal contamination is estimated and subtracted in the plots above, as described in the text. Templates are compared to the !LOOSE template, which is generally regarded as a good description of the background because it is highly efficient for all types of background

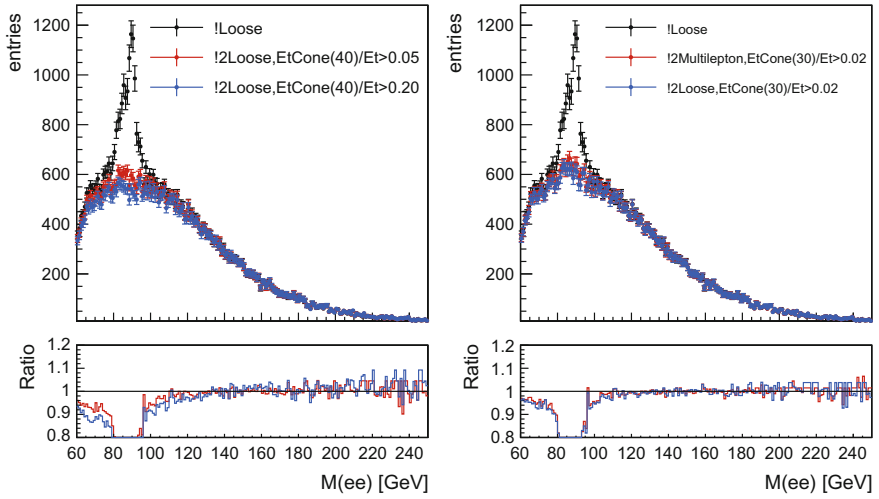

Fig. 6.6 Templates for the $35 < E_{\mathrm{T}} < 40\,\mathrm{GeV}$, $0.1 < \eta < 0.6$ efficiency measurement. Each template is normalized in the $120 < m_{ee} < 250\,\mathrm{GeV}$ region to the probe-level distribution. The template signal contamination is estimated and subtracted in the plots above, as described in the text. Templates are compared to the !LOOSE template, which is generally regarded as a good description of the background because it is highly efficient for all types of background

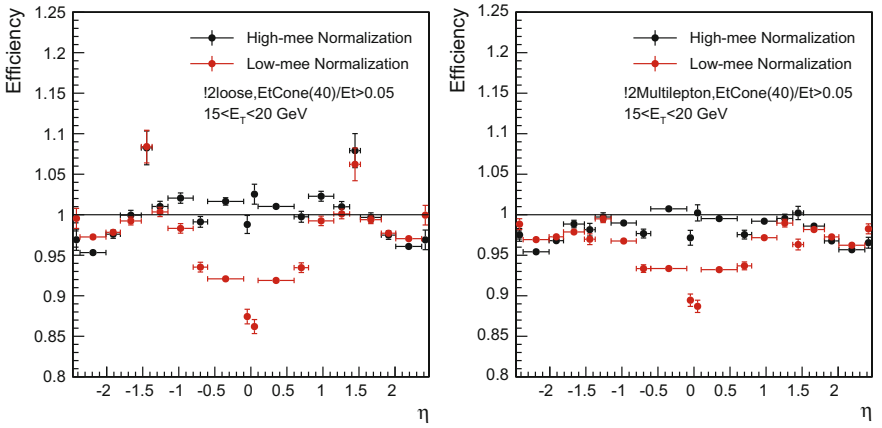

Fig. 6.7 The effect of using low- versus high-m_{ee} normalization regions on the measured efficiency, for electrons with $15 < E_{\mathrm{T}} < 20\,\mathrm{GeV}$. The ID menu studied here is a high-efficiency VERYLOOSE likelihood menu. The left (right) plot shows results using the !2LOOSE && $E_{\mathrm{T}}^{\mathrm{cone40}}/E_{\mathrm{T}} > 0.05$ (!2MULTILEPTON && $E_{\mathrm{T}}^{\mathrm{cone40}}/E_{\mathrm{T}} > 0.05$) template. The different results between normalization methods indicates a template bias; additionally, a >100% efficiency signals a problem with the background subtraction. !2MULTILEPTON-based template has less of a bias given these metrics

With these tests, we developed a better understanding of template behavior. In particular, it makes sense to treat template optimization separately for measurements of high- and low-E_{T}electrons. At low-E_{T}($<30\,\mathrm{GeV}$), the background is large compared to signal, and thus template biases have large impacts on the measurement. At high-E_{T}, the background is much smaller; template biases have a smaller effect on the measured efficiency, and instead signal contamination in templates can be a dominant effect. Below, the optimal template attributes are discussed.

Signal contamination. Figure 6.4 illustrates the template signal contamination metric ξ described above. Tests of this nature were performed to understand which template candidates keep ξ well below 1% at for high-E_{T}electron measurements, and below a few percent at low-E_{T}($<30\,\mathrm{GeV}$). Using this metric, we determined that each of the proposed identification menus (see Table 6.2) on its own has too much signal contamination to be considered as a template. Signal contamination can be reduced to an acceptable level by inverting both identification menu and isolation selection requirements.

Template bias. Figure 6.5 illustrates templates for low-E_{T}bins, combining inverted identification menu and inverted isolation requirements to define the templates. The templates are compared to the !LOOSE template, which has signal contamination in the Z-peak, but should be unbiased in the normalization regions of the m_{ee} spectrum because it is very efficient for background. By comparing the candidate templates to the !LOOSE template, biases can be exposed. Using, this, we determined that

applying an inverted isolation requirement (of the form $E_{\mathrm{T}}^{\mathrm{coneXX}}/E_{\mathrm{T}} > Y$) causes a shape deficit in the low-m_{ee} region of the template, with respect to the real background shape. Increasing the isolation threshold Y worsens the deficit at low-m_{ee}. Figure 6.5 (left) illustrates this effect, which is particularly visible for low-E_{T}electrons. Likewise, the !2LOOSE identification (which was the default in 2011) has a shape deficit at low-m_{ee}. !2MULTILEPTON also exhibits this feature, but the bias is smaller. Figure 6.5 (right) illustrates the effect.

Figure 6.6 shows the same comparison of templates with !LOOSE, but for measurements of higher-E_{T}electrons. The signal contamination mismodeling is evident in this plot—these templates are shown after correcting signal contamination using MC. The isolation bias effect is still evident, but the difference between !2LOOSE and !2MULTILEPTON templates is smaller. In addition, the background itself is smaller with respect to the amount of signal probes, so bias effects have a smaller impact on the measured efficiency.

To better quantify the effect of template bias on the efficiency measurement, we can compare the measured efficiency using the low-m_{ee} normalization region to the one using the high-m_{ee} normalization region. If no template bias exists, then the two efficiency measurements should agree. If the templates above indeed have a deficit at low-$m_{\ell\ell}$, then the efficiency measurement will be too low when normalizing background at high-$m_{\ell\ell}$, and too high when normalizing at low-$m_{\ell\ell}$, and the magnitude of the difference is a measure of the bias. Figure 6.7 shows this test, performed on the measurement of the VERYLOOSE likelihood menu. Measuring a very efficient menu has the added benefit that efficiency measurements above 1 (an unphysical efficiency) must be unequivocally flawed. The results expose the $E_{\mathrm{T}} \times \eta$ bins where the choice of template normalization dramatically affects the efficiency measurement, and allows the degree of template bias to be quantified.

The tools described above were developed to understand the characteristics of templates and their effect on the efficiency measurement, and to help choose templates with the least amount of bias. Based on the insights gained using these tools, we chose the template

$$\text{!2MULTILEPTON \&\& } E_{\mathrm{T}}^{\mathrm{cone30}}/E_{\mathrm{T}} > 0.02 \tag{6.10}$$

for efficiency measurements of electrons with $E_{\mathrm{T}} < 30\,\mathrm{GeV}$, to minimize template bias. For electrons with $E_{\mathrm{T}} > 30\,\mathrm{GeV}$, where template bias is less important but signal contamination is a concern, we chose to use the same two templates as were used in 2011:

$$\begin{aligned} &\text{!2LOOSE \&\& } E_{\mathrm{T}}^{\mathrm{cone40}}/E_{\mathrm{T}} > 0.05 \\ &\text{!2LOOSE \&\& } E_{\mathrm{T}}^{\mathrm{cone40}}/E_{\mathrm{T}} > 0.20 \end{aligned} \tag{6.11}$$

Understanding the Underlying Cause of Template Bias

What could be the cause of template biases causing a deficit at lower values of the m_{ee} spectrum? Two effects would have to contribute: a specific component of the background must have a different m_{ee} shape (more abundant at low-m_{ee}), and the template selection criteria must be less efficient for this background component than for the rest of the background elements.

Since the background is dominated by multijet and $W \rightarrow e\nu +$ jet, it is natural to investigate the difference between these two backgrounds. First, note that $W \rightarrow e\nu +$ jet LO production features quark jets; by comparison, multijet events at the LHC have a higher fraction of gluon jets. Quark-jets and gluon-jets have discernible differences, namely quark jets typically have a narrower shape and fewer tracks. These characteristics (narrower and more isolated energy deposits) are more closely aligned with electron signatures, and thus jets from W production may fail the template criteria more frequently than multijet events.

Studies using MC also indicate that, in the regions of $E_{\mathrm{T}} \times \eta$ with the largest template bias, $W \rightarrow e\nu +$ jet events have a more steeply falling m_{ee} spectrum than the rest of the background. Figure 6.8 shows the m_{ee} shape of $W \rightarrow e\nu +$ jet MC events that fail the template selection (and are thus not represented by the template), compared to the template (from data). Indeed, it appears that the missing $W \rightarrow e\nu$ + jet events are primarily at low-m_{ee}, supporting the postulate that quark jets from W production are the cause of the template bias.

Of course, the underlying cause of template bias is not critical to its treatment; however, it is useful to confirm the hypothesis, in case the apparent template bias was caused by some other unknown effect.

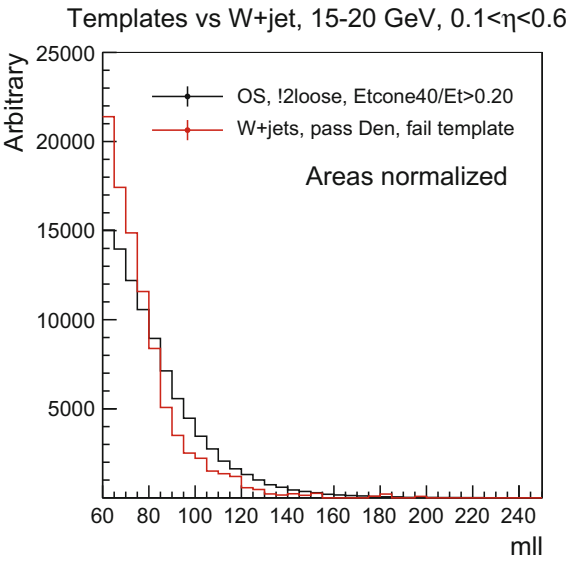

Fig. 6.8 Comparison of the m_{ee} shapes of the background template from data with the $W \rightarrow e\nu +$ jet events (from MC) failing the template criteria. The shape of the $W \rightarrow e\nu +$ jet events missing from the template is more steeply falling than the shape of the template

6.5 Shared Templates at High-E_{T}

When measuring electron identification efficiencies in two dimensions, a dedicated background template is used in each (E_{T}, η) bin. The high granularity of the measurements in η leads to background templates with low event yields in the normalization regions—particularly for bins with $E_{\mathrm{T}} > 30\,\mathrm{GeV}$.

In order to decrease the statistical uncertainty in this region, templates from adjacent η bins are added to the nominal template for the measurement in a particular $E_{\mathrm{T}} \times \eta$ bin—the new template is referred to as a "shared template".

The shared template technique is employed for efficiency measurements above $E_{\mathrm{T}} = 30\,\mathrm{GeV}$. The result is reduced statistical uncertainties, with a very small price in systematic uncertainty due to increased template bias. The boundaries for the templates used for these measurements are as follows:

$$\eta = [-2.47,\ -2.01,\ -1.52,\ -1.37,\ -0.80,\ -0.10,\ 0.10,\ 0.80,\ 1.37,\ 1.52,\ 2.01,\ 2.47\,] \tag{6.12}$$

6.6 Systematic Uncertainties

Systematic uncertainties on the efficiency measurements in each bin are assessed by varying a number of selection parameters. Table 6.3 summarizes the variations in background template, background normalization region, Z-mass window require-

Table 6.3 Event selection and background subtraction parameters in the Z_{mass} efficiency measurement that are varied to assess systematic uncertainties. For efficiency measurements of electrons with $E_{\mathrm{T}} > 30\,\mathrm{GeV}$, two template variations are used and normalized in the high-m_{ee} region; for $E_{\mathrm{T}} < 30\,\mathrm{GeV}$ electrons, a single template is used, and the template normalization region is varied. The systematic treatment has 18 total variations

Variation	Probe $E_{\mathrm{T}} < 30\,\mathrm{GeV}$	Probe $E_{\mathrm{T}} > 30\,\mathrm{GeV}$
Background template	!2MULTILEPTON && $E_{\mathrm{T}}^{\mathrm{cone30}}/E_{\mathrm{T}} > 0.02$	!2LOOSE && $E_{\mathrm{T}}^{\mathrm{cone40}}/E_{\mathrm{T}} > 0.05$!2LOOSE && $E_{\mathrm{T}}^{\mathrm{cone40}}/E_{\mathrm{T}} > 0.20$
Background normalization region	$120 < m_{ee} < 250\,\mathrm{GeV}$ $60 < m_{ee} < 70\,\mathrm{GeV}$	$120 < m_{ee} < 250\,\mathrm{GeV}$
Z-mass window	$80 < m_{ee} < 100\,\mathrm{GeV}$ $75 < m_{ee} < 105\,\mathrm{GeV}$ $70 < m_{ee} < 110\,\mathrm{GeV}$	
Tag identification	$p_{\mathrm{T}}^{\mathrm{cone20}}/p_{\mathrm{T}} < 0.1$ &&	MEDIUM++ && $E_{\mathrm{T}}^{\mathrm{cone40}} < 5\,\mathrm{GeV}$ TIGHT++ TIGHT++ && $E_{\mathrm{T}}^{\mathrm{cone40}} < 5\,\mathrm{GeV}$

ment, and tag identification criteria. For efficiency measurements of electrons with $E_{\mathrm{T}} < 30\,\mathrm{GeV}$, a single background template is used, and no systematic variation is applied. For electrons with $E_{\mathrm{T}} > 30\,\mathrm{GeV}$, the background normalization region $60 < m_{ee} < 70\,\mathrm{GeV}$ is omitted due to an insufficient number of events in that region. The efficiency measurement is repeatedly performed using a "grid" of all combinations of measurement parameter choices, resulting in $2 \times 3 \times 3 = 18$ measurements. The mean of these 18 measurements is taken as the central value of the efficiency measurement, and the RMS of the variations as the systematic uncertainty.

This method of making a measurement and assessing systematic uncertainties is not standard. Typically the central value of a measurement is determined using a single event selection that minimizes the background as much as possible. Here, the measurement with the smallest background, corresponding to the variation with the tightest tag identification requirements and smallest Z-peak mass window, is averaged with measurements having more background (looser tags, larger mass windows) to obtain the central value. Likewise, when making a measurement it is common to assess individual, uncorrelated sources of systematic uncertainty and add them in quadrature. In the efficiency measurement presented here, the individual variations are correlated; taking the RMS of the full grid of variations is more appropriate than adding the effect of each variation in quadrature, which would double-count sources of uncertainty.

Each variation is intended to capture certain effects that affect the electron efficiency measurement. All four variations effectively test the robustness of the background subtraction, either by increasing the amount of background (tag ID, Z-mass window), by slightly modifying the background subtraction procedure (normalization region), or by varying the background description (background template). Changing the tightness of the tag identification varies the relative contribution of $W \to e\nu +$ jet and multijet backgrounds (a tighter tag will reduce the multijet contribution, which consists of two background objects, compared to the $W \to e\nu +$ jet contribution, whose tag is a real electron). The only effect not related to background is the impact of electrons with large efficiency losses on the measured efficiency and data-MC scale factor. Increasing the Z-mass window variation includes more electrons with sufficient energy loss to decrease the measured m_{ee}, thus probing this effect.

Of the four types of variations, the background normalization variation is new as of the efficiency measurements at 8 TeV, and requires further discussion. Previously for electron efficiency measurements below $E_{\mathrm{T}} < 30\,\mathrm{GeV}$, the template variation was used to test the robustness of the background subtraction. However, as discussed in Sect. 6.4, all templates suffer from a deficit at the low end of the m_{ee} spectrum. As a result, both variations subtracted too little background from the denominator of distributions, and the efficiency measurements of both variations were lower than the true central value. Furthermore, in this scenario the systematic uncertainty band does not cover the true efficiency central value, since all variations are biased in the same direction (with efficiencies lower than the true value).

The low- and high-m_{ee} normalization variations are intended to correct the bias and non-coverage of the true central value. Figure 6.9 illustrates the effect of normal-

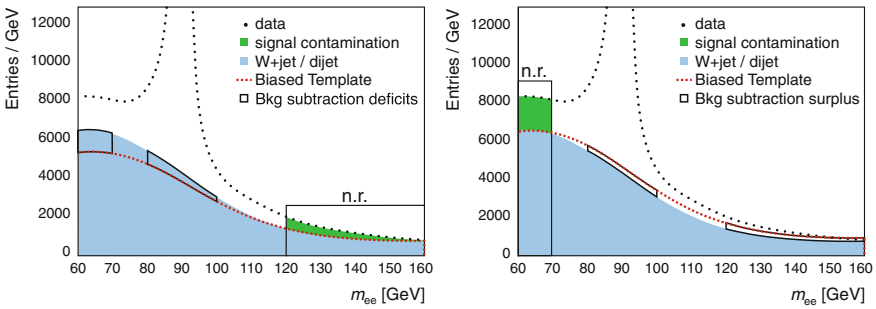

Fig. 6.9 Left: high-mass normalization, showing normalized templates plus signal contamination. The result is a deficit in the background subtraction under the Z peak, and thus a lower measured efficiency. A deficit is also seen in the low-mass region. Right: low-mass normalization, with templates plus signal contamination normalized in the low-mass tail. The result is an excess of background subtracted from the Z peak, and leading to a higher measured efficiency. An excess is also seen in the high-mass region

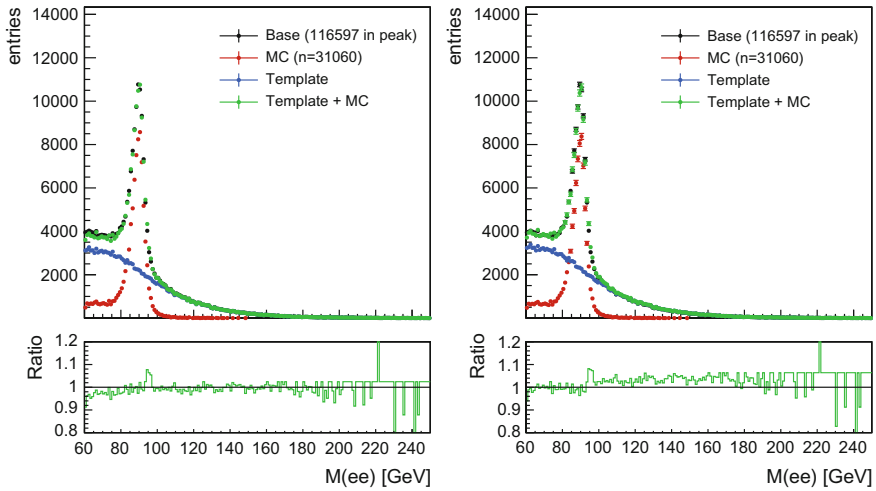

Fig. 6.10 Denominator m_{ee} distributions describing the method, for the tight scale factors, using an exemplary bin: $20 < E_{\mathrm{T}} < 25\,\mathrm{GeV}$, $0.1 < \eta < 0.6$. The left and right plots show cases where the templates are normalized to the high-m_{ee} ($120 < m_{ee} < 250\,\mathrm{GeV}$) and low-$m_{ee}$ ($60 < m_{ee} < 70\,\mathrm{GeV}$) regions, respectively. The ratio plotted below is between the base distribution and the final MC+template estimate, where the MC is scaled to match the total estimated signal yield in the Z-mass window. The variation shown here has tag cut-based MEDIUM + isolation

izing a template with a deficit at low-m_{ee} with respect to the true background shape. Normalizing to the high-m_{ee} region, the result is that too little background is subtracted from the denominator. Normalizing instead to the low-m_{ee} region, too much background will be subtracted from the denominator. The result is that the two variations should "straddle" the true value of the background under the Z-peak, and the

true efficiency will lie inside the uncertainty band of the subsequent efficiency measurement. This method effectively removes the issue of "bias in the same direction" of the template variations, in which the true efficiency value lies outside the uncertainty band of the measurement. Therefore the normalization region variation is used for $E_{\mathrm{T}} < 30\,\mathrm{GeV}$ electron measurements, where template biases are the dominant systematic effect. Figure 6.10 demonstrates in data the effect of using two different normalization regions to estimate background in the denominator distribution.

6.7 Statistical Uncertainties

Formula 6.13 is used to calculate the statistical uncertainties [2]:

$$\Delta\varepsilon = \frac{1}{S_{\mathrm{probe}}}\sqrt{(1-2\varepsilon)\,\Delta S_{\mathrm{ID}}^2 + \varepsilon^2\,\Delta S_{\mathrm{probe}}^2} \tag{6.13}$$

In the case of this measurement, however, events in the templates used for background subtraction are a subset of the total number of probes, and thus statistically correlated. We can rewrite these components into two uncorrelated quantities: events that fall into the template and events that fail the template selection:

$$N_{!\mathrm{templ}} = N_{\mathrm{probe}} - N_{\mathrm{templ}} \tag{6.14}$$

Then the equation for the number of signal probes can be rewritten in terms of these statistically uncorrelated quantities:

$$\begin{aligned} S_{\mathrm{probe}} =& N_{\mathrm{probe}}^{\mathrm{peak}} - N_{\mathrm{templ}}^{\mathrm{peak}} \times \left(\frac{N_{\mathrm{probe}}^{\mathrm{n.r.}} - \frac{1}{\varepsilon_{\mathrm{tight}}} N_{\mathrm{tight}}^{\mathrm{n.r.}}}{N_{\mathrm{templ}}^{\mathrm{n.r.}}} \right) \\ =& N_{!\mathrm{templ}}^{\mathrm{peak}} - N_{\mathrm{templ}}^{\mathrm{peak}} \times \left(\frac{N_{!\mathrm{templ}}^{\mathrm{n.r.}} - \frac{1}{\varepsilon_{\mathrm{tight}}} N_{\mathrm{tight}}^{\mathrm{n.r.}}}{N_{\mathrm{templ}}^{\mathrm{n.r.}}} \right) \end{aligned} \tag{6.15}$$

We neglect the correction term $N_{\mathrm{tight}}^{\mathrm{n.r.}}/\varepsilon_{\mathrm{tight}}$ in the calculation of the error; applying standard error propagation gives:

$$\Delta S_{\mathrm{probe}} = \sqrt{N_{!\mathrm{templ}}^{\mathrm{peak}} + \left(\frac{N_{!\mathrm{templ}}^{\mathrm{n.r.}}\, N_{\mathrm{templ}}^{\mathrm{peak}}}{N_{\mathrm{templ}}^{\mathrm{n.r.}}} \right)^2 \left(\frac{1}{N_{\mathrm{templ}}^{\mathrm{peak}}} + \frac{1}{N_{\mathrm{templ}}^{\mathrm{n.r.}}} + \frac{1}{N_{!\mathrm{templ}}^{\mathrm{n.r.}}} \right)} \tag{6.16}$$

For efficiency measurements with probes with $E_{\mathrm{T}} > 30\,\mathrm{GeV}$, the shared template technique is used to improve the statistical uncertainty. In this case, we make the assumption that the template events and the probe events are uncorrelated; the statistical uncertainty is then:

$$\Delta S_{\text{probe}} = \sqrt{N_{\text{probe}}^{\text{peak}} + \left(\frac{N_{\text{probe}}^{\text{n.r.}}\, N_{\text{templ}}^{\text{peak}}}{N_{\text{templ}}^{\text{n.r.}}}\right)^2 \left(\frac{1}{N_{\text{templ}}^{\text{peak}}} + \frac{1}{N_{\text{templ}}^{\text{n.r.}}} + \frac{1}{N_{\text{probe}}^{\text{n.r.}}}\right)} \tag{6.17}$$

The statistical uncertainty of the numerator is straightforward, since the template and numerator are disjoint selections:

$$\Delta S_{\text{ID}} = \sqrt{N_{\text{probe}}^{\text{peak}} + \left(B_{\text{ID}}^{\text{peak}}\right)^2 \left(\frac{1}{N_{\text{templ}}^{\text{peak}}} + \frac{1}{N_{\text{templ}}^{\text{n.r.}}} + \frac{1}{N_{\text{ID}}^{\text{n.r,SS}}}\right)}. \tag{6.18}$$

Eqs. 6.18 and 6.16 (or 6.16) are input into Eq. 6.13 to obtain the statistical uncertainty.

6.8 Measurement Combination and Results

The Z_{mass} method and the Z_{Iso} method (whose background subtraction is illustrated in Fig. 6.11) are statistically correlated. Thus, the Z_{mass} and Z_{Iso} methods are treated as variations of the same measurement. The central value of the efficiency measurement is the average of the 18 Z_{mass} and the 72 Z_{Iso} systematic variations, where the 18 Z_{mass} variations are given four times the weight of the Z_{Iso} variations such that the two methods are treated on equal footing. The systematic error is the RMS of the systematics (with Z_{mass} variations again given four times the weight); this value is multiplied by 1.2 to envelope roughly 68% of all variations, accounting for the fact that the systematic variations are not normally distributed. The joint Z_{mass} and Z_{Iso} measurements are used for the measurement of efficiencies and scale factors for $E_{\text{T}} > 20\,\text{GeV}$ electrons.

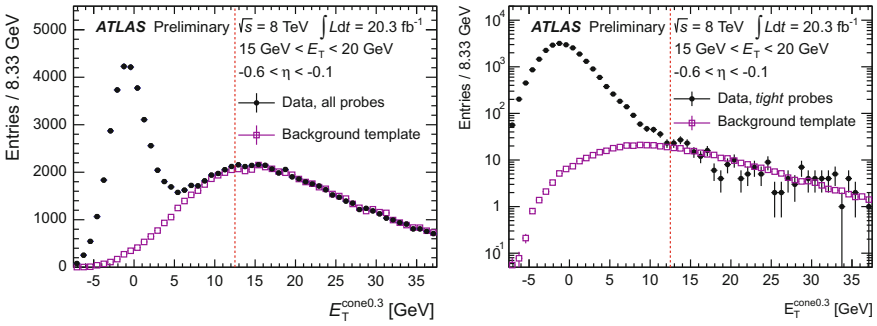

Fig. 6.11 Depiction of the Z_{Iso} method for measuring efficiencies. Left: background subtraction using templates in the denominator of the efficiency measurement. Right: the numerator of the efficiency measurement

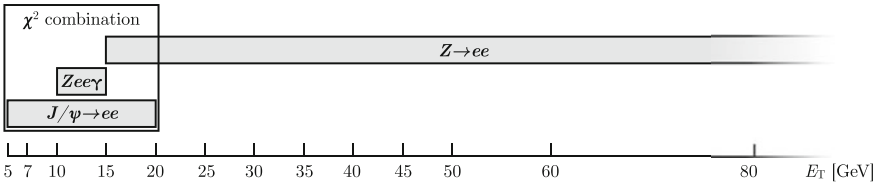

Fig. 6.12 Summary of the range of efficiency measurement methods, and the region in which measurements are combined using a χ^2 minimization

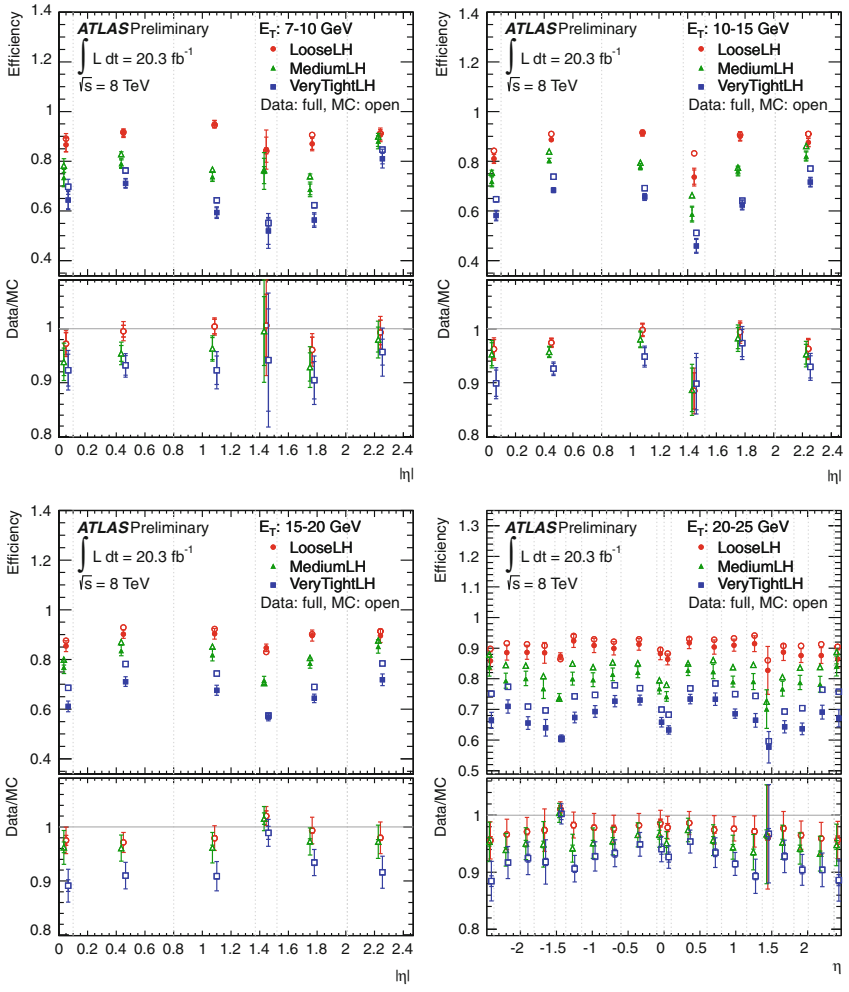

Fig. 6.13 Electron efficiency and scale factor measurements at $7 < E_T < 25$ GeV. Measurements at $E_T < 10$ GeV use $J/\psi \to ee$ measurements; $10 < E_T < 15$ GeV measurements are made using a χ^2 combination of $J/\psi \to ee$ and $Z \to ee\gamma$ measurements. Measurements between $15 < E_T < 20$ GeV are made using the combination of $J/\psi \to ee$ and $Z \to ee$ measurements. $E_T > 20$ GeV measurements use $Z \to ee$ methods

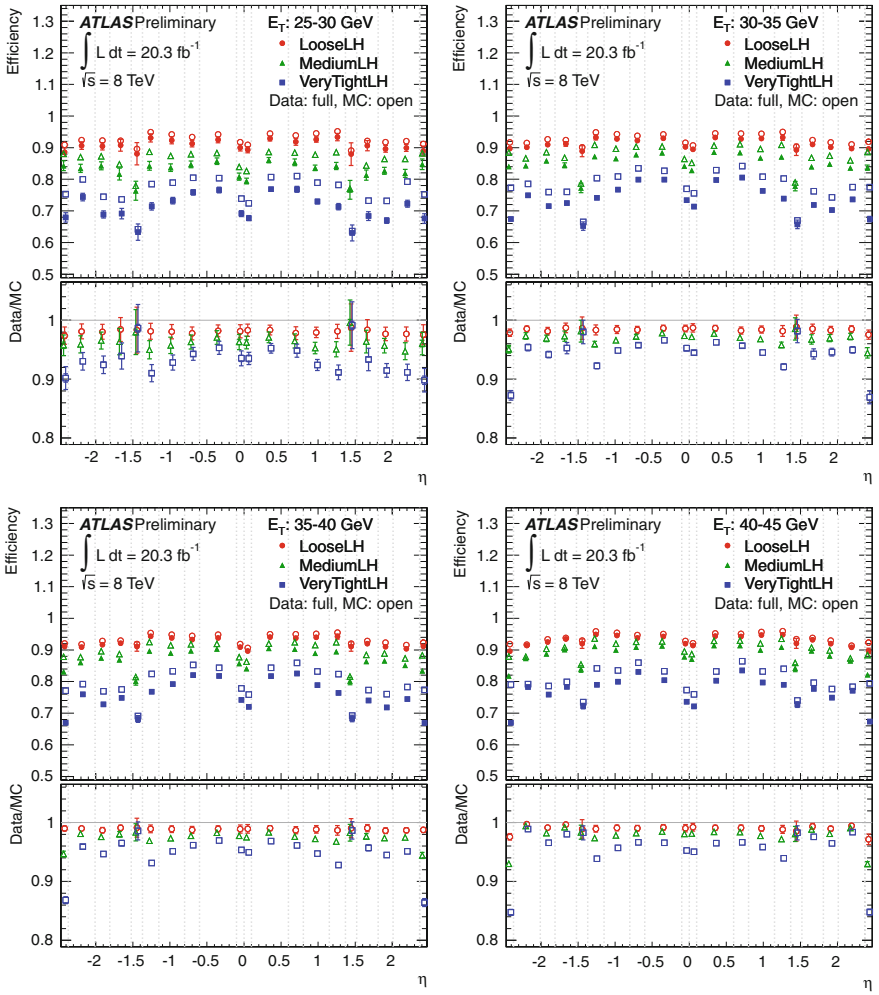

Fig. 6.14 Electron efficiency and scale factor measurements at $25 < E_{\mathrm{T}} < 45\,\mathrm{GeV}$. The $E_{\mathrm{T}} > 20\,\mathrm{GeV}$ measurements use $Z \to ee$ methods

In the range $10 < E_{\mathrm{T}} < 20\,\mathrm{GeV}$, electron efficiency measurements from $Z \to ee$, $Z \to ee\gamma$ and $J/\psi \to ee$ methods, in the ranges of validity shown in Fig. 6.12 are combined using a χ^2 minimization method [3]. All measurements in $E_{\mathrm{T}} \times \eta$ are rebinned to the coarser granularity of $J/\psi \to ee$, using $|\eta|$ instead of η:

$$|\eta| = [0.00,\ 0.10,\ 0.80,\ 1.37,\ 1.52,\ 2.01,\ 2.47\,]. \tag{6.19}$$

Within each method, systematic uncertainties are correlated across $E_{\mathrm{T}} \times \eta$ bins and treated as nuisance parameters in the χ^2 minimization. The combined measurement

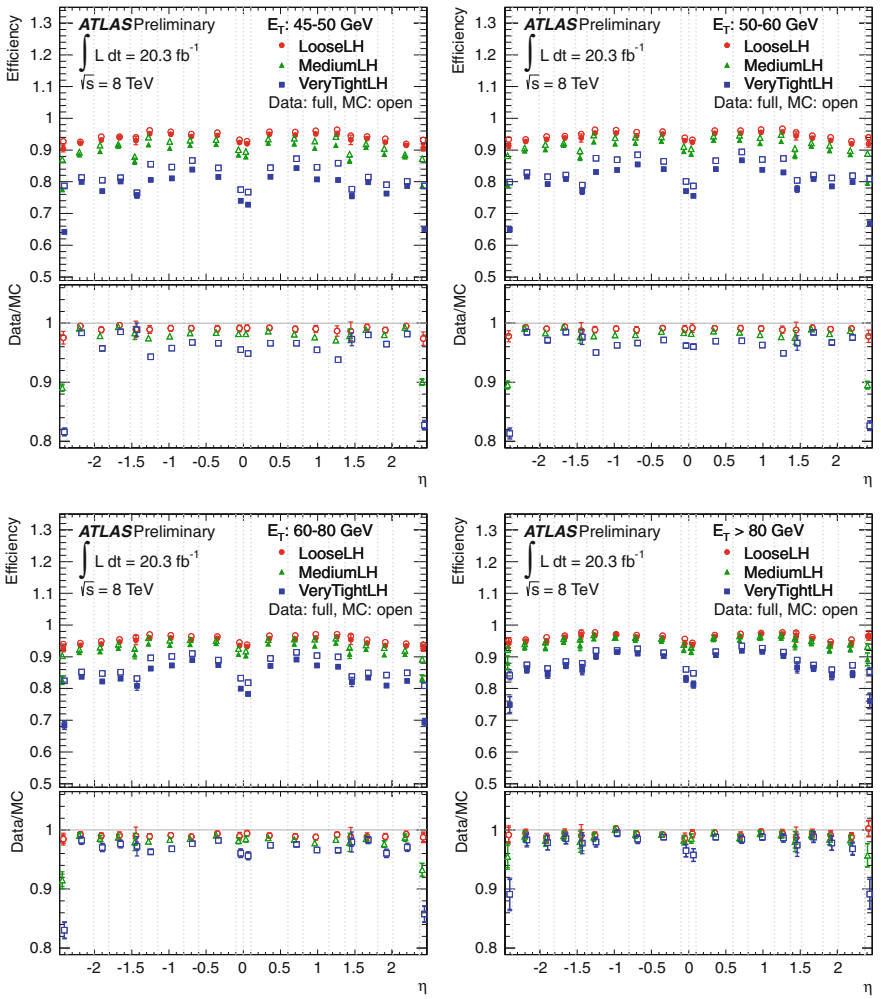

Fig. 6.15 Electron efficiency and scale factor measurements at $E_{\mathrm{T}} > 45\,\mathrm{GeV}$. The $E_{\mathrm{T}} > 20\,\mathrm{GeV}$ measurements use $Z \rightarrow ee$ methods

and uncertainty resulting from the minimization are are taken for $10 < E_{\mathrm{T}} < 20\,\mathrm{GeV}$, and the pulls of the systematic uncertainties are propagated to the $7 < E_{\mathrm{T}} < 10\,\mathrm{GeV}$ $J/\psi \rightarrow ee$ measurements.

The plots of all efficiency and scale factor measurements for 2012 likelihood menus are displayed in Figs. 6.13, 6.14 and 6.15.

6.9 Prospects for Electron Efficiency Improvements

In the future, two goals should be prioritized: ensuring that the central value of measurement is not systematically biased in one particular direction, and improving the treatment of systematic uncertainties. For the former, the normalization region systematic uncertainty at low-E_{T}, as described in Sect. 6.6, represents a major improvement. Experience has shown that simply using one normalization region, and two templates that have the same bias, does not suffice to envelope the true efficiency central value. This principle should be kept in the forefront, and perhaps applied to the Z_{Iso} method, which suffers similar uni-directional template biases; in the case of Z_{Iso}, however, only one normalization region is available (the isolation tail), so solving the issue in this case requires some cleverness.

The latter goal, the treatment of systematic uncertainties, should have a focus of choosing reasonable variations, particularly for low-E_{T} measurements. Figure 6.16 shows the estimated s/b ratio as the mass window is increased, with arrows indicating windows of 20, 30 and 40 GeV used in the analysis for systematic variations. The extreme variations increase the s/b by a factor of two in some bins; although the mass window variation is intended to probe effects of electron energy loss on efficiency results, that subtle effect is drowned out by the background increase. Furthermore, the average of all variations is used as the central value for the measurement, instead of taking the variation with the lowest s/b as the central measurement.

The typical analysis does not assess the uncertainty on its background estimate by increasing the background by a factor of two in its signal region; furthermore, measurements are made in a signal region with an optimized s/b. A similar approach is warranted for the $Z \rightarrow ee$ efficiency measurements, and most likely one that changes as a function of electron E_{T}, to account for the varying impact of background at low- and high-E_{T}.

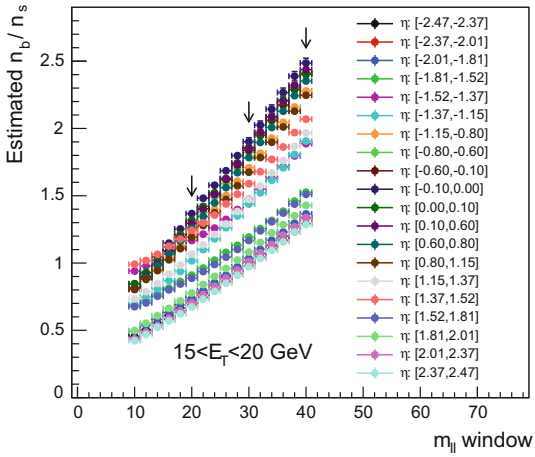

Fig. 6.16 The estimated s/b ratio for various choices of the Z mass window selection requirement

References

1. ATLAS Collaboration, Electron efficiency measurements with the ATLAS detector using the 2012 LHC proton–proton collision data, ATLAS-CONF-2014-032 (2014), http://cdsweb.cern.ch/record/1706245
2. C. Blocker, Uncertainties on efficiencies (2004), http://www-cdf.fnal.gov/physics/statistics/notes/cdf7168_eff_uncertainties.psCDF/MEMO/STATISTICS/PUBLIC/7168, (http://www-cdf.fnal.gov/physics/statistics/notes/cdf7168_eff_uncertainties.ps)
3. H1 Collaboration, F.D. Aaron et al., Measurement of the inclusive ep scattering cross section at low Q^2 and x at HERA. Eur. Phys. J. **C63**, 625–678 (2009), https://doi.org/10.1140/epjc/s10052-009-1128-6, arXiv:0904.0929 [hep-ex]

Chapter 7
Higgs Decaying to Four Leptons

This chapter presents the Higgs fiducial differential and inclusive cross section measurements in the $H \rightarrow ZZ^* \rightarrow 4\ell$ channel using $20.3\,\text{fb}^{-1}$ of $\sqrt{s} = 8\,\text{TeV}$ data collected in 2012. The differential measurements are the first of their kind in this channel; the measurements are statistically limited, but the analysis represents the beginning of a program to measure the Higgs boson properties to a high degree of precision as more data is collected by the ATLAS detector. The final section of this chapter is dedicated to the prospects of the differential measurements in Run 2.

The details presented in this chapter represent only those required to understand the ingredients of the fiducial differential and inclusive cross section measurements. Other measurements of the Higgs properties in the ZZ^* channel are omitted, including the Higgs mass, cross section measurements in different categories corresponding to different production modes, measurements of coupling parameters, and spin properties.

The $H \rightarrow ZZ^* \rightarrow 4\ell$ decay channel is particularly well-suited to study the properties of the Higgs boson because all of the decay products are visible, meaning the kinematics of the Higgs boson can be fully reconstructed. Six differential distributions are chosen for study due to their sensitivity to interesting physics, including potential sensitivity to physics outside the standard model. Any deviation from a theoretically accurate SM description of the Higgs p_{T} could be an indication of new physics; for instance, if the Higgs boson were produced in association with a dark matter particle, its p_{T} spectrum would be modified. As a result there has been intense theoretical effort to describe the transverse momentum of the Higgs boson. Other quantities of interest include the distribution of the angles between the various decay products of the Higgs boson. In particular, the magnitude of the angle between the beam axis and the leading Z boson decaying the Higgs rest frame, $|\cos\theta^*|$ is sensitive to the spin properties of the particle; this angle is illustrated in Fig. 7.1. The N_{jets} and $p_{\text{T},\,jet1}$ are sensitive to associated jet radiation, and to the relative cross section magnitude of different Higgs production modes. The Higgs rapidity $|y_H|$ is

K. Brendlinger, *Physics with Electrons in the ATLAS Detector*, Springer Theses,
https://doi.org/10.1007/978-3-319-73930-4_7

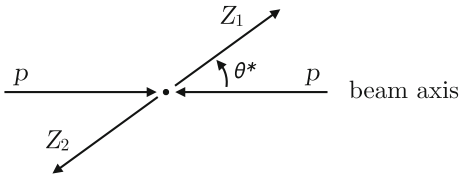

Fig. 7.1 The θ^* variable is the angle between the beam axis and the leading Z boson in the Higgs rest frame

affected by the parton distribution function. Finally, m_{34} is sensitive to the Lagrangian structure [1].

A fiducial cross section measurement (differential or inclusive) is organized in such a way that the data and theoretical predictions can be directly compared with one another with minimal dependence on any particular physics model. The cross section is measured in a phase space of accessible events called the fiducial volume. The selection requirements defining the fiducial volume can be geometric or kinematic: geometric requirements select events whose decay products fall inside the detector's instrumented region, and kinematic requirements are imposed to remove backgrounds that are difficult to determine with sufficient precision. Within this fiducial volume, the selection can be subdivided as a function of one or more kinematic properties—this is referred to as a "differential" measurement.

After selecting events satisfying the fiducial requirements and subtracting the estimated background, the data must be corrected to account for detector-level effects such as lepton identification inefficiencies and imperfect momentum resolution in a process called unfolding, which relates reconstructed quantities to their true underlying distributions. The unfolding step is ideally performed with as few assumptions as possible on the underlying physics model (referred to as "model-independent" unfolding). In an inclusive fiducial cross section measurement, the unfolding correction is a single number called the correction factor. For differential fiducial cross sections, the unfolding is complicated by the possibility of event migration between differential bins that can bias the measurement.

To compare with theory, theoretical calculations are often accompanied by a Monte Carlo generator for producing individual events, and the fiducial selection can be applied to the simulated ("truth") particles. The subsequent prediction after applying the fiducial selection can be directly compared to the unfolded data. Figure 7.2 summarizes each step of the fiducial differential and inclusive measurements described above.

The $H \to 4\ell$ channel has a small cross section times branching ratio compared to other Higgs boson decay channels, but it also has a high signal-to-background ratio. The main backgrounds in the analysis are continuum ZZ^* decaying to four prompt leptons, and Z+jet and $t\bar{t}$ backgrounds with two real leptons and two objects misidentified as leptons ("fake" leptons). The ZZ^* background is called "irreducible" because it has the same prompt lepton multiplicity as the Higgs signal; Z+jet and $t\bar{t}$ are "reducible" in the sense that stricter identification requirements applied to the leptons can reduce their abundance in the signal region. The yield, uncertainty

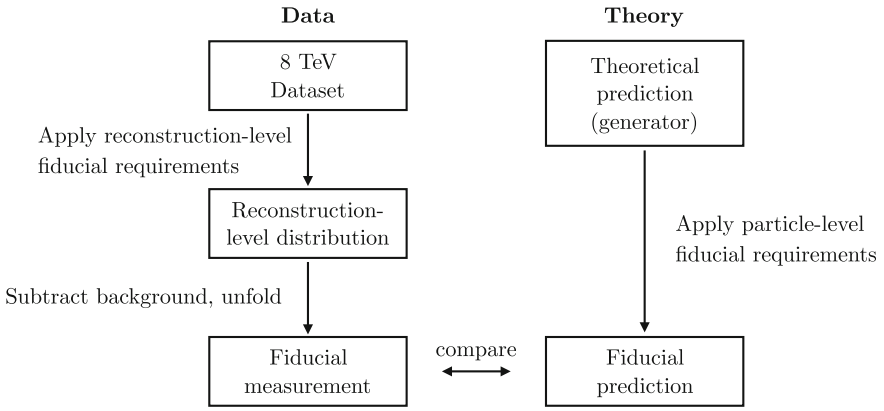

Fig. 7.2 Schematic of a fiducial differential (or inclusive) cross section measurement. On the left, fiducial requirements are applied to the reconstructed objects in data, resulting in a reconstruction-level distribution (or an inclusive yield). Background estimates are subtracted, and the data are unfolded to relate the reconstructed quantity to the true physical quantity comparable with the theoretical prediction. On the right, the fiducial requirements are applied to events generated using a theoretical prediction, resulting in a prediction of the fiducial cross section

and kinematic shapes of the ZZ^* background are predicted using simulation; the reducible backgrounds Z+jet and $t\bar{t}$ are estimated using data-driven methods.

The differential measurement procedure can be summarized as follows: events satisfying the fiducial selection requirements are used to populate the bins of each distribution. (The inclusive measurement can be considered a single-bin distribution containing the entire fiducial phase space.) The backgrounds are estimated in each bin of the distribution, and the data is unfolded using a simple correction factor procedure. The cross section is extracted using a profile likelihood ratio, allowing sources of systematic uncertainties to be correlated across bins; the result of maximizing the likelihood ratio produces an estimate of the signal yield in each bin of the fiducial differential cross section distribution. The differential measurement is compared with leading theoretical predictions, and the compatibility between theory and measurement is tested.

7.1 Fiducial Phase Space

The fiducial phase space, imposed on the truth-level decay products of the Higgs boson, is defined primarily to limit the kinematic range of the four leptons in the decay such that they fall inside the instrumented region of the detector. Other event-level criteria are imposed to match requirements imposed on the data to reduce sources of background. The fiducial selection is intended to be reproducible by theorists at the

Table 7.1 Definition of truth particles and the fiducial region for the fiducial and differential cross sections

Fiducial requirements for the $H \to ZZ^* \to 4\ell$ channel	
Particles	
▹ Muon kinematics	$p_{\mathrm{T},\mu} > 6\,\mathrm{GeV},\ \lvert\eta_\mu\rvert < 2.7$
▹ Electron kinematics	$p_{\mathrm{T},e} > 7\,\mathrm{GeV},\ \lvert\eta_e\rvert < 2.47$
(Jet definition for jet variable observables)	$p_{\mathrm{T},jet1} > 30$ GeV, $\lvert y_{\mathrm{jet}}\rvert < 4.4,\ \Delta R(j,\mu) > 0.2$
Event level	
▹ Lepton multiplicity	At least 4 leptons (electrons or muons)
▹ Lepton kinematics	$p_{\mathrm{T}}^{\ell 1} > 20\,\mathrm{GeV};\ p_{\mathrm{T}}^{\ell 2} > 15\,\mathrm{GeV};\ p_{\mathrm{T}}^{\ell 3} > 10\,\mathrm{GeV}$
▹ Lepton separation	$\Delta R(\ell,\ell') > 0.1\ (0.2)$, same (different) flavor leptons
▹ Z boson pairs	Require two same-flavor, opposite-charge (SFOC) lepton pair
(Lepton association with Z_{12} and Z_{34} bosons)	Associate remaining SFOC lepton pair with subleading Z boson (Z_{34})
	Associate SFOC lepton pair having smallest $\lvert m_{\ell\ell} - m_Z\rvert$ with leading Z boson (Z_{12})
▹ Z mass windows	$50 < m_{12} < 106\,\mathrm{GeV};\ 12 < m_{34} < 115\,\mathrm{GeV}$
▹ J/ψ veto	$m_{\ell\ell} > 5\,\mathrm{GeV}$ for all SFOC lepton pairs
▹ Higgs mass window	$118 < m_{4\ell} < 129\,\mathrm{GeV}$

generator level and to closely match the reconstruction-level requirements in order to minimize extrapolations.

At particle (truth generator object) level, electron and muon kinematics are determined at the Born level—at level of the matrix element, before any QED corrections are applied. Muons must have $p_{\mathrm{T}} > 6\,\mathrm{GeV}$ and $|\eta < 2.7|$, and electrons have $p_{\mathrm{T}} > 7\,\mathrm{GeV}$ and $|\eta < 2.47|$. The p_{T} requirements are imposed because backgrounds become larger at lower p_{T}. Particle-level jets are constructed from all stable particles, excluding muons and neutrinos, using the anti-$k_t$algorithm with distance parameter $R = 0.4$. Jets are defined as having $p_{\mathrm{T}} > 30\,\mathrm{GeV}$, $|y| < 4.4$, and must be a distance $\Delta R > 0.2$ from any truth electron. The Born-level electrons, muons and jets are collectively referred to as "truth" particles.

Table 7.1 summarizes the selection used to define the fiducial region, including the additional event-level requirements intended to match the reconstruction-level selection imposed on the data to reduce backgrounds. At the particle level, all Born final state leptons originating from a W or a Z, but not hadrons, are considered as possible Higgs boson decay products. They are paired to the Z bosons by finding same-flavor, opposite-charge pairs; the pair closest to the Z boson mass (PDG) is labeled Z_{12} with mass m_{12}, and the second pair is labeled Z_{34} with mass m_{34}. The mass windows imposed on the Z boson pairs and on $m_{4\ell}$ mirror the reconstruction-level requirements, as do the lepton ΔR and J/ψ veto requirements.

No explicit requirement is made on the parent boson of the particle-level leptons (from the generator truth record). As a result, leptons can be mispaired when forming Z_{12} and Z_{34} in the $4e$ and 4μ channel, and leptons that do not originate from the decay of the Higgs boson in the WH, ZH and $t\bar{t}H$ processes can be incorrectly assigned to the Higgs. Kinematic quantities including m_{12} and m_{34} are affected by mispairing or mis-assignment, affecting the number of events passing the fiducial selection.[1] These effects also affect the m_{34} and $|\cos\theta^*|$ differential distribution predictions. The choice not to make a parent boson requirement is motivated by the need to keep the definition of the particle-level fiducial selection applied to the generator prediction close to that applied to the data, in order to make them as comparable as possible. Since no such boson assignment is possible in the data, it is omitted at the particle level.

7.2 Data Set and Simulated Signal Samples

The cross section and differential distribution measurements are made using $20.3\,\text{fb}^{-1}$ of data collected from the ATLAS experiment in 2012, from LHC collisions with $\sqrt{s} = 8\,\text{TeV}$ c.o.m. energy. Cross sections and differential distributions change with the energy of the p–p collisions; therefore, the $\sqrt{s} = 7\,\text{TeV}$ data collected in 2011 are not included in this measurement.

The following simulated signal samples are used in the differential analysis to determine the correction factors used to extrapolate from the reconstruction-level to the particle-level differential distributions, as described in Sect. 7.3.5. The simulated events are propagated through a GEANT4 description of the ATLAS detector, with corrections applied to objects and event properties in order to more closely match the behavior of the data. The descriptions below do not apply to the theoretical predictions POWHEG, MINLO and HRES2 used to compare with unfolded data; Sect. 7.4 describes those samples.

ggF and VBF. The Higgs gluon-gluon fusion (ggF) and vector boson fusion (VBF) production processes are simulated using POWHEG with NLO matrix elements. For the calculation of the correction factors (see Sect. 7.3.5), events are re-weighted with a generator tune designed to match the Higgs transverse momentum distribution with that of a calculation performed with NNLL+NLO accuracy, including soft gluon resummation [2]. PYTHIA is used to simulate showering, hadronization and the underlying event of this sample [3].

***VH* and $t\bar{t}H$.** Higgs production in association with a W or Z boson (VH), or with two top quarks ($t\bar{t}H$), is simulated using PYTHIA.

[1] This will have an effect on the fiducial acceptance and correction factors discussed in Sect. 7.3.5.

7.3 Analysis Overview

The object and event selection is identical to an ATLAS paper published around the same time measuring the signal strength and couplings of the Higgs in the $H \to ZZ \to 4\ell$ decay channel [4]. A brief description of the object and event selection is presented in this section, with a focus on the lepton identification requirements used for the $\sqrt{s} = 8\,\text{TeV}$ data set.

7.3.1 Object Selection

Electrons are ID tracks matched to calorimeter clusters in the EM calorimeter, and identified using the likelihood identification technique described extensively in Chap. 5 using the LOOSE criteria. The identification criteria includes a nBlayerHits requirement on the ID track. Electrons must satisfy the impact parameter significance, track isolation, and calorimeter isolation requirements detailed in Table 7.2. Several improvements have been made to the reconstruction and identification of electrons compared to the previous measurement [5]. First, the track reconstruction of electron candidates has been modified to use a Gaussian Sum Filter to model bremsstrahlung losses in electrons [6], resulting in higher electron reconstruction efficiencies. The second improvement is the use of the Likelihood identification method mentioned above, which improves the rejection of backgrounds typical for this analysis by roughly a factor of 2. Figure 7.3 illustrates the effect of these improvements: higher electron efficiencies, and higher rejection power for sources of reducible background.

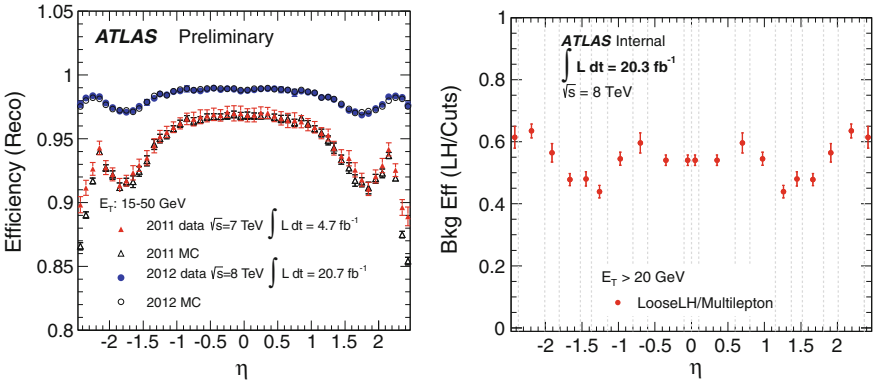

Fig. 7.3 Left: the electron reconstruction efficiencies measured in 2011 and 2012 data. The main difference between the two data sets is the improved track reconstruction using a Gaussian Sum Filter to model bremsstrahlung losses. Right: ratio of background efficiency using the LOOSE likelihood requirement (including a requirement on nBlayerHits) to that using the cut-based MULTILEPTON identification requirement on a sample of representative electron background sources [7]

Table 7.2 Highlights of the electron and muon selection for the $H \to 4\ell$ analysis

Electrons	Muons
$p_{\mathrm{T}} > 7\,\mathrm{GeV}$	$p_{\mathrm{T}} > 6\,\mathrm{GeV}$
$\lvert\eta\rvert < 2.47$	$\lvert\eta\rvert < 2.7$
LooseLH+BLayer identification	Loose quality tracking requirements
$\lvert d_0/\sigma(d_0)\rvert < 6.5$	$\lvert d_0/\sigma(d_0)\rvert < 3.5$
$p_{\mathrm{T}}^{\mathrm{cone20}}/p_{\mathrm{T}} < 0.15$	$p_{\mathrm{T}}^{\mathrm{cone20}}/p_{\mathrm{T}} < 0.15$ (stand-alone)
$E_{\mathrm{T}}^{\mathrm{cone20}}/E_{\mathrm{T}} < 0.20$	$p_{\mathrm{T}}^{\mathrm{cone20}}/p_{\mathrm{T}} < 0.30$ (all other types)

Muons are reconstructed and identified using the techniques described in Chap. 3, Sect. 3.2.4. The analysis uses all four types of reconstructed muon: combined, segment-tagged, standalone, and calorimeter-tagged. Because of their higher background rate, at most one segment-tagged muon or calorimeter-tagged muon can be used in each event. Muons must also satisfy the impact parameter significance and calorimeter isolation requirements listed in Table 7.2.

Jets used for the N_{jets} differential distributions are reconstructed using the anti-k_t algorithm [8] with distance parameter R = 0.4 using energy clusters in the hadronic and electromagnetic calorimeters. Jets are defined to have $p_{\mathrm{T}} > 30\,\mathrm{GeV}$ and $\lvert y\rvert < 4.4$, and must be $\Delta R > 0.2$ from signal electrons.

7.3.2 Event Selection

Events in 2012 data are collected using the lepton triggers summarized in Table 7.3. The efficiency of this collection of triggers with respect to events passing the final offline selection is between 97 and 100%.

The event selection applied to reconstructed objects in data matches the fiducial selection criteria listed in Table 7.1 of Sect. 7.1, including the lepton multiplicity, lepton p_{T} thresholds, lepton ΔR separation, and Z, $J\psi$ and Higgs mass window requirements. A few additional procedural details, related to which leptons are associated to the Higgs in the case of more than four leptons in an event, are discussed

Table 7.3 Triggers used for collecting candidate events in 2012 data. More details on the triggers are described in Chap. 3, Sect. 3.2.5

Single electron	e24vhi_medium1 || e60_medium1
Di-electron	2e12Tvh_loose1
Single muon	mu24i_tight || mu36_tight
Di-muon	2mu13 || mu18_tight_mu8_EFFS
Electron-muon	e12Tvh_medium1_mu8 || e24vhi_loose1_mu8

below. Finally, kinematic corrections are applied to the leading Z boson to improve the measurement of the Higgs observables; these are summarized below as well.

Events in data are categorized into "channels" according to the flavor of the leptons associated with the leading and subleading Z bosons. Events with four muons (four electrons) associated to the two Z bosons are called 4μ events ($4e$ events); events in which the leading Z boson is formed from muons (electrons) and the subleading from electrons (muons) are labeled $2\mu 2e$ ($2e2\mu$). Leptons are paired to leading and subleading Z bosons, forming a quadruplet, in the same way as in the fiducial definition. The leading SFOC pair is taken as the Z-pair closest to the PDG Z mass, and the subleading SFOC pair that is next-to-closest to the Z mass in the range $12 < m_{\ell\ell} < 115\,\text{GeV}$ is taken as the subleading Z-pair. If more than four leptons are identified in an event, the formation of lepton quadruplets proceeds on a channel-by-channel basis: first, a 4μ quadruplet satisfying the event selection is sought; if no such quadruplet exists, then the $2e2\mu$ channel is tested, followed by the $2\mu 2e$ and $4e$ channels. The first quadruplet found to satisfy the event selection is selected in the event.

After the selection of the quadruplet, a series of corrections on the kinematics of the four-lepton system is applied. To improve the measurement of the Higgs kinematics, photons from final-state radiation (FSR) off of the leading Z boson are recovered by searching for a reconstructed photon consistent with an FSR hypothesis and adding its four-momentum to the calculation of the invariant mass of the leading Z boson [9]. Reconstructed photons collinear with muons $\Delta R < 0.15$, $p_{\text{T}} > 1.5\,\text{GeV}$, consistent with a photon calorimeter signature are used for this correction. If no collinear photon is found, non-collinear photons ($\Delta R > 0.15$) with $p_{\text{T}} > 10\,\text{GeV}$ and satisfying strict photon identification requirements are considered for the correction: if $m_{\ell\ell} < 81$ GeV and $m_{\ell\ell\gamma} < 100\,\text{GeV}$, the FSR-corrected leading Z boson is used to define the Higgs kinematics.

Finally, the leading Z boson mass is recalculated using a fit combining the momentum resolution of the individual leptons with the Breit-Wigner shape hypothesis of the Z mass. The momentum resolution of each lepton is parameterized as a Gaussian distribution with a width equal to that measured in data; a likelihood combining the probability density functions of the lepton momenta and the Z mass shape hypothesis is maximized to find the constrained Z boson mass. The result is an improvement in the Z mass resolution of about 15%.

7.3.3 Backgrounds

The following section describes the methods used to describe the differential distributions (yield and shapes) of the ZZ^*, Z+jet and $t\bar{t}$ backgrounds. They are described only briefly here, and discussed more deeply in [4]. The ZZ^* continuum background is produced mainly through the $q\bar{q}$ annihilation process, with a small (<2% in the analysis $m_{4\ell}$ mass window) contribution from gluon fusion production. The former is simulated using POWHEG-BOX [10], and the latter using GG2ZZ [11]. The

reducible backgrounds from Z+jet and $t\bar{t}$ are estimated using data-driven methods. These backgrounds are split according to the flavor of the subleading Z-pair, either $\ell\ell + ee$ for a subleading electron pair, or $\ell\ell + \mu\mu$ for a subleading muon pair. These contributions are estimated separately as described below.

The $\ell\ell+\mu\mu$ is dominated by $Z+b\bar{b}$, $Z+2j$ with two light-flavor jets, and $t\bar{t}$ events in which both accompanying b-jets decay leptonically to muons. Their abundance near the signal region is estimated using a fit of four control regions, defined by the following:

- Removing the isolation requirement on the subleading muons, and requiring at least one of the subleading muons to fail the impact parameter significance requirement
- Requiring at least one of the subleading muons to fail the isolation requirement
- Choosing an $e\mu$ pair as the leading pair, instead of a same-flavor, opposite sign pair, enriching the sample in $t\bar{t}$
- Requiring two muons of the same charge for the subleading muon pair.

A simultaneous maximum likelihood fit of all four regions is used to obtain the yields of these backgrounds, which is expressed in terms of a yield estimate in a control region applying all signal selection criteria except for the isolation and impact parameter requirements of the subleading muons. This estimate is then extrapolated to the signal region by multiplying by the efficiency of the fake muons to satisfy the isolation and impact parameter criteria. That efficiency is calculated using simulation and validated in Z+jet events with a fake muon; the uncertainty due to the agreement between data and MC is very small. The shape of the $\ell\ell + \mu\mu$ background is taken from simulation.

The $\ell\ell + ee$ background events in the signal region are estimated by extrapolating from a $3\ell + X$ control region, where the three leading leptons are required to pass the signal selection and the fourth object is a reconstructed electron with most identification criteria relaxed. In addition, the subleading Z pair is formed using same-sign electrons, to reduce contamination from ZZ in the sample. The object X is enriched in fake electron backgrounds, composed of three sources: light-flavor hadrons, converted photons, and heavy-flavor hadrons. A $Z + X$ control sample is used to derive the efficiencies of each of these contributions, and to derive the shapes of two discriminating variables, F_{HT} (the TRT ratio of high-threshold to low-threshold hits) and nBlayerHits, for each background type. The shapes are used in a simultaneous fit of both variable distributions in the $3\ell + X$ control region to obtain the background composition in that sample, and the yield of each background is multiplied by the efficiencies derived in the $Z + X$ region to obtain the final reducible background estimate.

7.3.4 Summary of Event Yields and Estimated Background

A summary of the expected signal, irreducible ZZ^*, reducible Z+jet and $t\bar{t}$ backgrounds is presented in Table 7.4 for both 7 TeV data collected in 2011 and 8 TeV

Table 7.4 Summary of the expected signal and background event yields and the observed number of events in the region $120 < m_{4\ell} < 130\,\text{GeV}$ from the 2011 and 2012 data taking periods. The $\sqrt{s} = 7\,\text{TeV}$ data is presented as a means of drawing comparisons of the signal-to-background ratios in electron channels.

Final state	Signal	ZZ^*	Z+jet, $t\bar{t}$	Expected S/B	Expected yield	Observed yield
$\sqrt{s} = 7\,\text{TeV}$, $120 < m_{4\ell} < 130\,\text{GeV}$						
4μ	0.91 ± 0.09	0.46 ± 0.02	0.10 ± 0.04	1.7	1.47 ± 0.10	2
$2e2\mu$	0.58 ± 0.06	0.32 ± 0.02	0.09 ± 0.03	1.5	0.99 ± 0.07	2
$2\mu 2e$	0.44 ± 0.04	0.21 ± 0.01	0.36 ± 0.08	0.8	1.01 ± 0.09	1
$4e$	0.39 ± 0.04	0.19 ± 0.01	0.40 ± 0.09	0.7	0.98 ± 0.10	1
Total	2.32 ± 0.23	1.17 ± 0.06	0.96 ± 0.18	1.1	4.45 ± 0.30	6
$\sqrt{s} = 8\,\text{TeV}$, $120 < m_{4\ell} < 130\,\text{GeV}$						
4μ	5.28 ± 0.52	2.36 ± 0.12	0.69 ± 0.13	1.7	8.33 ± 0.6	12
$2e2\mu$	3.45 ± 0.34	1.67 ± 0.08	0.60 ± 0.10	1.5	5.72 ± 0.37	7
$2\mu 2e$	2.71 ± 0.28	1.17 ± 0.07	0.36 ± 0.08	1.8	4.23 ± 0.30	5
$4e$	2.38 ± 0.25	1.03 ± 0.07	0.35 ± 0.07	1.7	3.77 ± 0.27	7
Total	13.8 ± 1.4	6.24 ± 0.34	2.00 ± 0.28	1.7	22.1 ± 1.5	31

data collected in 2012. Only the latter is used for the differential and fiducial cross section measurements presented here, however a comparison between the two data sets is instructive to illustrate the improvements in electron identification presented in the text. In particular, electron reconstruction using the Gaussian Sum Filter and the electron likelihood identification were introduced in the 8 TeV data set, and are not present in the 7 TeV data set. The former improves the signal yields for channels with electrons in the final state, and the latter improves the S/B ratio for events with a subleading ee pair (in the $2\mu 2e$ and $4e$ channels), as can be seen by comparing the two data sets.[2]

The table quotes signal yields in the region $120 < m_{4\ell} < 130\,\text{GeV}$; the mass range used in the differential cross section measurements is $118 < m_{4\ell} < 129$ GeV, but the expected background yields there are similar: 6.7 irreducible ZZ^* and 2.2 reducible background events are expected in the 2012 data set. Figure 7.4 shows the $m_{4\ell}$ spectrum after all signal selection criteria are applied, combining data from $\sqrt{s} = 7\,\text{TeV}$ and $\sqrt{s} = 8\,\text{TeV}$ data sets.

[2]The Higgs cross section is expected to increase by about 7% in the ggF channel between $\sqrt{s} = 7$ and 8 TeV; however, the gains in signal yield are larger than this.

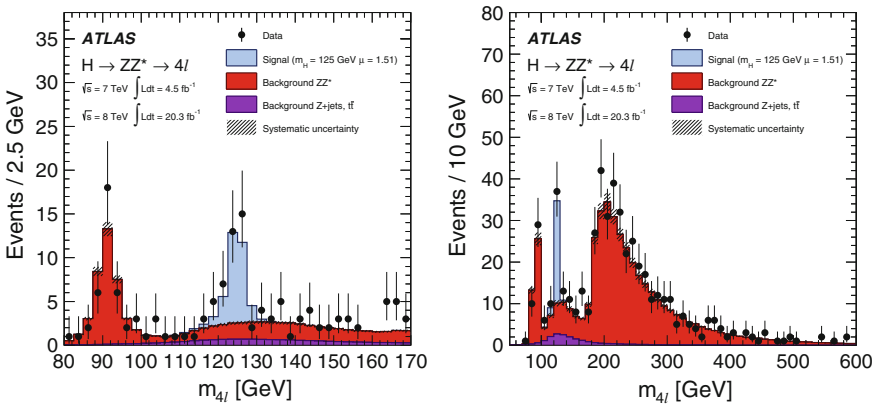

Fig. 7.4 The $m_{4\ell}$ spectrum after all signal selection criteria are applied, shown for all channels. The low-mass range is shown on the left, and the full mass range up to $m_{4\ell} = 600\,\text{GeV}$ is shown on the right. The ZZ^* background is estimated using simulation, and the reducible background from Z+jet and $t\bar{t}$ are estimated using the data-driven methods described in the text. The plot combines data from $\sqrt{s} = 7\,\text{TeV}$ and $\sqrt{s} = 8\,\text{TeV}$ data sets

7.3.5 *Unfolding Procedure*

Procedures to unfold the differential distributions without introducing bias are discussed in [12]. In this analysis, bin-by-bin correction factors are used to unfold the distributions to the truth level. The response matrices, relating the reconstructed to the true quantities for each distribution, are sufficiently diagonal that the simple correction factor procedure does not introduce large biases. The correction factor uncertainties are small compared to the statistical precision of the measurement. The Bayesian iterative unfolding method is used as a cross-check to the correction factor procedure.

A fiducial cross section is calculated in each bin of each differential distribution using a correction factor, defined as the number of reconstructed events passing the signal event selection divided by the number of events at the particle (Born) level passing the fiducial requirements of Table 7.1, as described by simulation:

$$C = \frac{N^{MC}_{\text{reco}}}{N^{MC}_{\text{true}}}. \tag{7.1}$$

The correction factor is calculated by combining the simulated samples for each Higgs production mode (ggF, VBF, WH, ZH and $t\bar{t}H$) according to the SM prediction of their relative production cross sections, and calculating the correction factor inclusively. The correction factors are similar for each production mode, except for $t\bar{t}H$, which is smaller because of the reconstruction-level isolation requirements

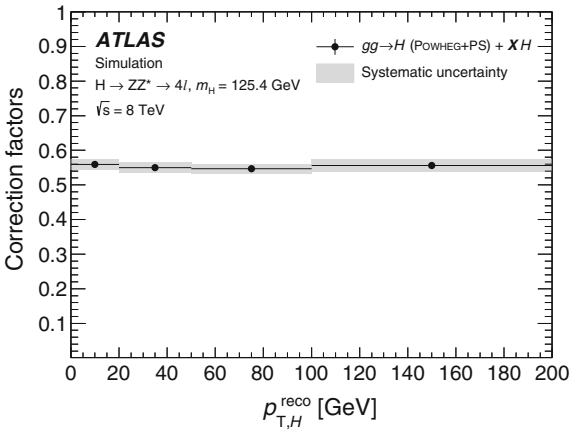

Fig. 7.5 Correction factors for each bin used in the $p_{\mathrm{T},H}$ differential cross section measurement

of the leptons. Figure 7.5 shows the correction factors for each bin in the $p_{\mathrm{T},H}$ distribution.

The fiducial cross section in each bin is:

$$\sigma_i^{\mathrm{fid}} = \frac{N_{\mathrm{data}} - N_{\mathrm{bkg}}}{\mathcal{L}_{\mathrm{int}} \cdot C_i}, \tag{7.2}$$

where σ_i^{fid} is the fiducial cross section, of Higgs decays to 4μ, $2e2\mu$, $2\mu2e$, and $4e$, in each bin i of a variable distribution. The differential fiducial cross section with respect to variable x in bin i is simply

$$\left(\frac{\mathrm{d}\sigma^{\mathrm{fid}}}{\mathrm{d}x}\right)_i = \frac{\sigma_i^{\mathrm{fid}}}{\Delta x_i}, \tag{7.3}$$

where Δx_i is the width of the bin.

7.3.6 Systematic Uncertainties

The systematic errors can be split into two types of sources: uncertainties arising from the estimation of the background processes, and uncertainties in the unfolding process, mainly associated with the correction factors used to unfold the reconstruction-level distributions to the corresponding truth quantities. Furthermore, many of the uncertainties associated with backgrounds are decomposed into *normalization* and *shape* uncertainties, where the total integral of the shape uncertainty variations are equal. The decomposition of uncertainties in this way allows for anti-correlations between bins of the differential measurements.

Uncertainties on lepton efficiency, energy scale and momentum scale are evaluated for their effect on both the background processes and the correction factor. Jet energy scale and resolution uncertainties, and an uncertainty on the jet vertex fraction selection requirement, are assessed for the jet variable measurements only.

The ZZ^* background predicted by simulation has PDF and scale uncertainties. One PDF uncertainty is evaluated using the eigenvectors of the CT10 PDF set, and another is assessed by taking the envelope of the differences between the CT10 PDF set and the NNPDF and MSTW sets. The two uncertainties are added in quadrature. The scale uncertainty is evaluated by varying μ_R and μ_F by factors of 0.5 and 2 around their nominal value m_Z, in all combinations satisfying $0.5 < \mu_R/\mu_F < 2$. The PDF and scale uncertainties are both factorized into normalization and shape uncertainties.

To validate both the yield and the shape of the ZZ^* kinematic distributions in the signal region of the Higgs at 125 GeV, the ZZ^* background distributions and data distributions are compared in the region $m_{4\ell} > 190$ GeV, where the ZZ^* process is dominant (at over 99%). The yields and most background shapes are found to be in good agreement. The N_{jets} distribution shows some disagreement, partially due to the low number of events in data, so an additional uncertainty is added to the ZZ^* N_{jets} and $p_{\text{T},jet1}$ shapes. These shape uncertainty are taken to be either the difference between the shape of the simulation and the data, or the statistical uncertainty in the data, whichever is larger in a given differential bin.

Uncertainties on the reducible background describing $t\bar{t}$ and Z+jet processes are assessed independently for the $\ell\ell + ee$ and $\ell\ell + \mu\mu$ estimates. For the $\ell\ell + \mu\mu$ estimate, the normalization uncertainty is dominated by the uncertainties of the fit and of the factors used to extrapolate to the signal region. The shape uncertainty is obtained by relaxing or tightening the isolation and impact parameter selections used in the method. For the $\ell\ell + ee$ estimate, the normalization systematic uncertainty is dominated by uncertainties on the efficiencies used to extrapolate from the $3\ell + X$ control region for each background type. Shape systematic uncertainties are assessed by varying the requirements on the $3\ell + X$ control region and taking the resulting shape difference of the variation. Another variation is assessed by comparing the shape estimate of a cross-check method used to estimate $\ell\ell + ee$ (the "reco-truth unfolding method" described in [4]) with that of the nominal method.

The correction factors are intended to be a model-independent means to extrapolate to truth-level differential distributions. However, the calculation of the correction factors is performed using an admixture of production modes of simulated Higgs samples, mixed according to the SM prediction of their relative cross sections. In order to quantify the dependence of the correction factors due to production mode cross sections, the relative cross sections are varied up and down within the experimental uncertainties from [13]: the VBF and VH fractions are scaled up and down by factors of 2 and 0.5, and $t\bar{t}H$ is varied by factors of 0 and 5, all independently. The largest of these variations in each differential bin is taken to be the systematic uncertainty due to signal production mode composition.

Model dependence can also arise from the choice of Higgs mass at which samples are simulated. The experimental uncertainty of Higgs boson mass, calculated in

Table 7.5 Summary of the systematic uncertainties

Systematic uncertainties (%)	
Background estimate	
Luminosity	1.4–2.3
Reducible background	1.6–34
Experimental, leptons	1.3–2.3
PDF/scale	3.0–24
Correction factors/conversion to σ	
Luminosity	2.8
Experimental, leptons	2.1–2.6
Experimental, jets	2.7–13
Production process	0.1–15
Higgs boson mass	0.4–2.7

[13], is 0.4 GeV. To assess the uncertainty in the correction factor due to incomplete knowledge of the exact Higgs mass, correction factors are calculated using Higgs samples simulated with a mass of 125 and 126 GeV. The difference in correction factors leads to systematic uncertainties between 0.4 and 2.7% on the different bins of the differential cross section measurement.

Table 7.5 summarizes the range of systematic uncertainties in each bin of the six differential cross section distributions.

7.3.7 Signal Extraction with Profile Likelihood

The number of signal events in each of the n bins of a distribution ($s_0, s_1, ...s_n = \boldsymbol{s}$) can be extracted simultaneously by maximizing a profile likelihood ratio based on [14, 15], and summarized in [16]. Given a list of nuisance parameters $\boldsymbol{\theta}$ from the systematic uncertainties, the likelihood is defined as:

$$\mathcal{L}(\boldsymbol{s}, \boldsymbol{\theta}) = \prod_{i=0}^{n} \text{Poisson}\left(n_i^{\text{obs}}; s_i + \sum b_i^{\text{exp}}\right) \cdot \prod_{i=0}^{N_{\text{syst}}} \text{Gaussian}(\theta_j; 0, 1), \tag{7.4}$$

where the background in each bin $\sum b_i$, consisting of ZZ and reducible backgrounds, is affected by the nuisance parameters according to

$$b_i^{\text{exp}} = b_i^{\text{nom}} \prod_{j=0}^{N_{\text{syst}}} (1 + \alpha_{i,j} \cdot \theta_j), \tag{7.5}$$

where b_i^{nom} is the nominal background estimate, and $\alpha_{i,j}$ is the relative effect that varying systematic j up or down by 1σ has on b in bin i. Note that the shape systematics described in Sect. 7.3.6 will have bins with positive and negative $\alpha_{i,j}$, encoding the anti-correlations between bins. The maximum likelihood estimate is obtained by maximizing $\mathcal{L}$ and denoted by $\mathcal{L}(\hat{\boldsymbol{s}}, \hat{\boldsymbol{\theta}})$, where $\hat{\boldsymbol{s}}$ and $\hat{\boldsymbol{\theta}}$ are the unconditional maximum likelihood estimators (one hat for "unconditional" estimator).

The profile likelihood ratio $\Lambda(\boldsymbol{s})$ for a fixed signal hypothesis $\boldsymbol{s}$ is defined as

$$\Lambda(\boldsymbol{s}) = \frac{\mathcal{L}(\boldsymbol{s}, \hat{\hat{\boldsymbol{\theta}}})}{\mathcal{L}(\hat{\boldsymbol{s}}, \hat{\boldsymbol{\theta}})}, \tag{7.6}$$

where $\mathcal{L}(\boldsymbol{s}, \hat{\hat{\boldsymbol{\theta}}})$ is the conditional maximum likelihood at fixed value $\boldsymbol{s}$, i.e. the $\boldsymbol{\theta}$ are chosen to maximize $\mathcal{L}$ for the given $\boldsymbol{s}$ (two hats for "conditional" estimator). To obtain statistical and systematic uncertainties, the quantity $-2\ln\Lambda(\boldsymbol{s})$ is used; in the asymptotic assumption, this test statistic follows a χ^2 distribution with n degrees of freedom [16]. The 68% confidence level limits are obtained by finding the values of $\boldsymbol{s}$ at which $-2\ln\Lambda(\boldsymbol{s}) = 1$.

Note that the above formulas are obtained for finding the central value and total uncertainty of $\boldsymbol{s}$; to find the total uncertainty of the differential measurements in each bin of a distribution, accounting for correlations between systematic uncertainties in the correction factor and luminosity, the likelihood from Eq. 7.4 is modified to test each bin of $(\mathrm{d}\sigma^{\text{fid}}/\mathrm{d}x)$ as the parameters of interest, using Eqs. 7.1, 7.2, and 7.3:

$$\begin{aligned} \mathcal{L}(\boldsymbol{s}, \boldsymbol{\theta}) \;&\rightarrow\; \mathcal{L}\left(\left(\frac{\mathrm{d}\sigma^{\text{fid}}}{\mathrm{d}x}\right)_0, \left(\frac{\mathrm{d}\sigma^{\text{fid}}}{\mathrm{d}x}\right)_1, \ldots \left(\frac{\mathrm{d}\sigma^{\text{fid}}}{\mathrm{d}x}\right)_n, \boldsymbol{\theta}\right) \\ s_i \;&\rightarrow\; \left(\frac{\mathrm{d}\sigma^{\text{fid}}}{\mathrm{d}x}\right)_i \cdot \mathcal{L}_{\text{int}} \cdot C_i \cdot \Delta x_i . \end{aligned} \tag{7.7}$$

Pseudo-experiments are performed to cross-check the results from the profile likelihood ratio. In each pseudo-experiment, a random number is drawn from a Poisson distribution with mean equal to the number of expected events for each bin of a given differential distribution. The results $(d\sigma/dx)_i$ are computed by minimizing the profile likelihood ratio, taking into account correlations between bins; this procedure is repeated $100k$ times and the 68% CL errors are compared to those obtained using $-2\Delta\ln\Lambda$ using the asymptotic assumption. In most cases, the differences between the two approaches are very similar, however they disagree in bins where the number of expected events is small, and thus the asymptotic assumption breaks down. In these cases, the 68% CL errors from pseudo-experiments are used in which a random number is drawn from a Poisson distribution with the observed cross section as its mean.

7.4 Theory Predictions

The unfolded fiducial differential distributions are compared to the shape of leading theoretical predictions in the fiducial region. The shapes of POWHEG, HRES2 [17, 18] and MINLO [19] predictions are compared with data; the total cross section of each prediction is normalized to the best NNLO total cross section times branching ratio prediction of a Higgs boson with mass 125.4 GeV [20], such that the differential shapes of three generators are truly compared. These calculations predict Higgs production via gluon fusion; the sub-dominant production modes are calculated using POWHEG (VBF) and PYTHIA 8 ($VH, t\bar{t}H$) and account for only about 13% of the total Higgs cross section. These additional processes are scaled to the best predictions of their cross section times branching ratios [20].

The three generators chosen for comparison with the data are chosen for distinct reasons. POWHEG is an NLO calculation of Higgs production interfaced to PYTHIA; similar implementations of Higgs and other processes are extensively used by the ATLAS collaboration to model physics at the LHC. The MINLO (Multi-scale improved NLO) prediction presented here is also interfaced to PYTHIA, and accurately describes observables of Higgs produced in association with a jet with NLO accuracy. The HRES2 prediction includes resummation of gluon emissions at small transverse momenta up to next-to-leading logarithmic accuracy (NNLL); this correction has a large impact on the prediction of the Higgs p_{T} spectrum. HRES2 was expanded to account for finite top and bottom quark masses up to NLO, which also impact the Higgs p_{T}.

Each of the three theoretical calculations consists of or is accompanied by a Monte Carlo generator for producing individual events, such that the fiducial requirements of Table 7.1 can be applied on an event-by-event basis to determine the fiducial acceptance of the sample and the Born-level kinematic differential distributions. For the POWHEG and MINLO predictions, jet showering, hadronization, and multiparton interactions are performed by interfacing to PYTHIA 8 [3, 21]. Jets are reconstructed from all stable particles, excluding muons and neutrinos, and clustered using FASTJET [22] with the anti-k_t algorithm with a distance parameter of 0.4. Born leptons from the truth particle record of PYTHIA 8 and originating from a W or Z are used to define the Higgs kinematics. For the HRES2 prediction, leptons are generated at the born level; parton showering and hadronization are not performed, and jet variables are therefore not available.

Uncertainties are assessed on each theoretical prediction, and consist of uncertainties due to choices of QCD scale in the calculation, and due to the description of the proton PDFs. The total uncertainty is the quadrature sum of scale and PDF uncertainties, described below. A complete account of scale and PDF uncertainties for each theoretical prediction is listed in Appendices C.1, C.3 and C.2.

7.4.1 Scale Uncertainties

The factorization scale μ_F is the cutoff scale under which gluon emissions are accounted for inside the parton distribution, and over which they are handled in the calculation of the hard scatter. The renormalization scale μ_R is a parameter used in the renormalization of the running α_s coupling; varying this scale gives indication of the magnitude of terms of higher order in α_s. Both scales are nominally set to m_H for all three theory predictions; for POWHEG and MINLO this is a fixed scale, and for HRES2 the scale is dynamic. The renormalization and factorization scale uncertainties are evaluated by varying μ_R and μ_F up ($\times 2$) and down ($\times 0.5$) from the nominal value in all six combinations satisfying $0.5 < \mu_R/\mu_F < 2$, and taking the envelope of the variations as the scale uncertainty. In all three predictions, the renormalization scale uncertainty dominates.

The HRES2 prediction has two additional scale parameters associated with the soft gluon resummation: Q_1 is nominally set to $m_H/2$, and Q_2 controls the bottom quark contribution and is nominally set to the mass of the bottom quark, $Q_2 = m_b$. To evaluate the HRES2 QCD scale uncertainty, first μ_R and μ_F are varied as in the description above, keeping Q_1 and Q_2 fixed to their nominal values; next, Q_1 and Q_2 are varied up and down ($\times 2$ and $\times 0.5$ for Q_1, $\times 4$ and $\times 0.5$ for Q_2) keeping μ_R and μ_F both fixed. The envelope of these 15 variations is taken as the QCD scale uncertainty. As in the POWHEG and MINLO cases, the renormalization variations dominate the uncertainty here as well.

Figure 7.6 illustrates the effect of QCD scale variations on the Higgs p_{T} differential distributions, for the POWHEG and HRES2 generators. Scale uncertainties for POWHEG and MINLO are typically on the order of 20%; for HRES2, scale uncertainties are about 10% at low-$p_{\mathrm{T},H}$, increasing to 20% at high-$p_{\mathrm{T},H}$.

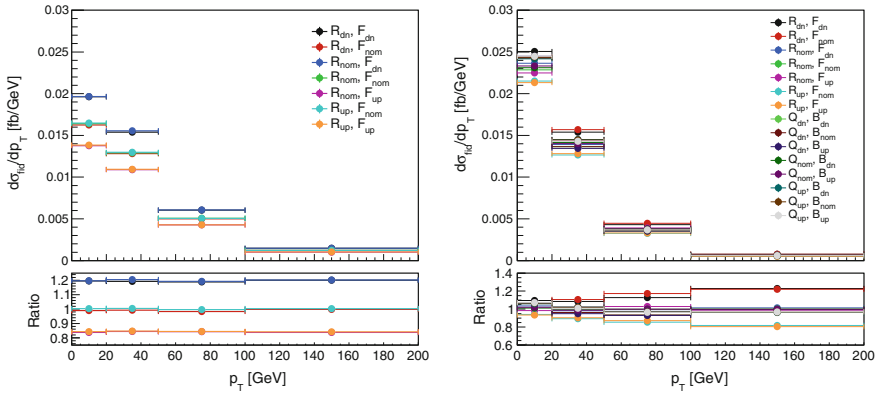

Fig. 7.6 Left: scale variations for the POWHEG NLO prediction. Right: scale variations for the HRES2 prediction

To evaluate the QCD scale uncertainty in the N_{jets} distribution for POWHEG and MINLO samples, the Stewart-Tackmann (ST) procedure is used to account for the additional perturbative uncertainty associated with a minimum jet p_{T} requirement [23]. The ST scale uncertainty is used in place of the QCD scale uncertainty, and added in quadrature with the other uncertainties.

7.4.2 PDF Uncertainties

The nominal PDFs used in the theoretical cross section predictions are CT10 [24] (POWHEG and MINLO) and MSTW2008 [25] (HRES2); NNPDF [26, 27] is also used to evaluate systematic uncertainties. The uncertainty on the PDF description is determined with two approaches. First, the differential cross sections are calculated using several available PDF sets (CT10, MSTW, and NNPDF), and an uncertainty band corresponding to the envelope of the three predictions is used to quantify the uncertainty due to the choice of PDF description. This uncertainty probes the effects of the different assumptions used to construct each PDF description.

The second uncertainty is the intrinsic uncertainty of the PDF, associated with the free parameters of the PDF description that are fit using data from deep inelastic scattering, Drell-Yan and jet production measurements. The CT10 set contains 26 such parameters, and MSTW2008 has 20. Since parameter uncertainties are typically correlated, the Hessian method is used to transform the parameters to an orthonormal eigenvector basis. The PDF collaboration provides a set of PDFs corresponding to the up and down (+ and −) variations of each uncorrelated error in this basis, allowing the differential cross section calculation to be repeated for each variation. It is not known a priori whether a given + or − variation will increase or decrease the cross section; thus, the variations (+ or −) that decrease the cross section are summed in quadrature to determine the lower error bound ΔX^-, and the variations that increase the cross section are summed in quadrature to determine the upper error bound ΔX^+, according to:

$$\begin{aligned} \Delta X^+ &= \sqrt{\sum_{i=1}^{n} \left[\max(X_i^+ - X_0,\ X_i^- - X_0, 0)^2 \right]}, \\ \Delta X^- &= \sqrt{\sum_{i=1}^{n} \left[\max(X_0 - X_i^+,\ X_0 - X_i^-, 0)^2 \right]}, \end{aligned} \tag{7.8}$$

where X_0 is the nominal PDF estimate and $X_i^{\pm}$ are the individual variations (26×2 for CT10 and 20×2 for MSTW) [28].

Figure 7.7 depicts the three PDFs used to determine the "PDF choice" uncertainty, and the CT10 eigenvector variations used to determine the "eigenvector"

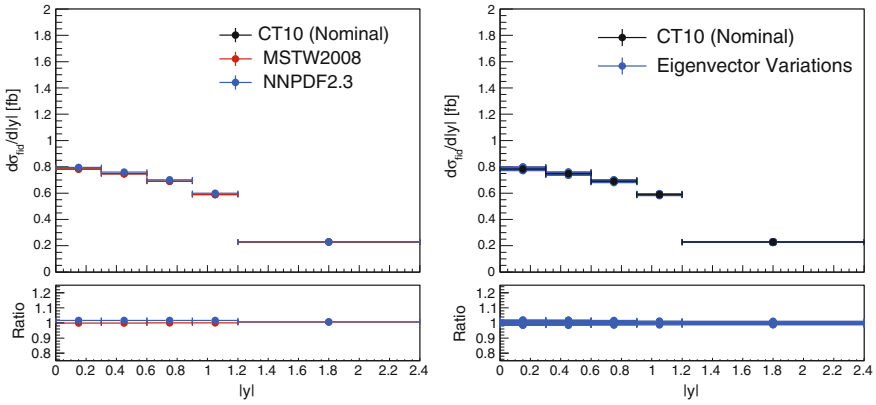

Fig. 7.7 Left: variations due to PDF choice for the POWHEG prediction. Right: each of the eigenvector variations for the POWHEG prediction, combined as described in the text

uncertainties for the POWHEG prediction. The eigenvector and PDF set choice uncertainties are added in quadrature.

7.5 Results

Figure 7.8 depicts the event yields in each bin used for the differential measurement, and Fig. 7.9 presents the differential cross section measurements in each of the six variables of interest, alongside the theoretical predictions.

There are visible differences between the data and predictions; to assess the degree of tension, a compatibility test equivalent to a χ^2 test is used. As described in Sect. 7.3.7, the statistical observable $-2\ln\Lambda$ follows a χ^2 distribution with n degrees of freedom [16]; the difference between $-2\ln\Lambda(\hat{\boldsymbol{s}})$ at the best-fit value obtained using data and the $-2\ln\Lambda(\boldsymbol{s})$ where $\boldsymbol{s}$ is set to the predicted theoretical values is used to obtain the p-value[3] between the data and the prediction. Table 7.6 shows the p-values comparing the unfolded data and the three different theoretical predictions, which range from 16–60%. If the fiducial cross section of the theoretical predictions is roughly normalized to the fiducial cross section observed in data, then the compatibility of the shapes improves, with p-values ranging from to 53–96%. In either case, the data and theoretical predictions are statistically compatible; more data is required to resolve their potential differences.

The inclusive fiducial cross section is calculated in two ways. In the first method, the number of data events in the range $118 < m_{4\ell} < 129\,\text{GeV}$ is counted, and a profile likelihood ratio is maximized as described in Sect. 7.3.7. The result of this

[3]The p-value is the probability that the agreement between the data and the prediction is worse than the observed agreement when the experiment is repeated.

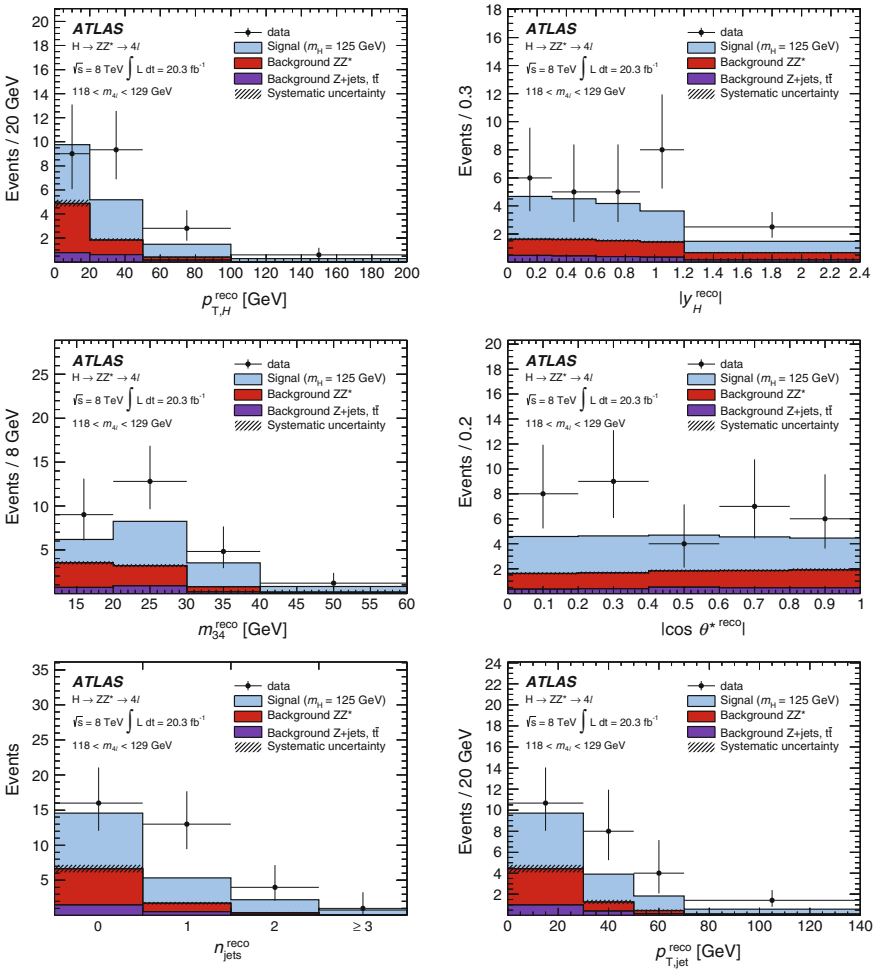

Fig. 7.8 Observed event yields, binned in each observable variable measured differentially. The background estimate and its systematic uncertainty are depicted, as is the signal estimate assuming a SM Higgs boson with $m_H = 125\,\text{GeV}$

method, called the "counting method," is:

$$\sigma^{\text{fid}} = 2.21^{+0.56}_{-0.48}\,(\text{stat})^{+0.14}_{-0.10}\,(\text{syst})\ \text{fb}. \tag{7.9}$$

A second method, referred to as the "fit method," takes a similar approach but fits the shapes of the signal and background in the $m_{4\ell}$ distribution; this result is compatible with the counting method result:

$$\sigma^{\text{fid}} = 2.11^{+0.53}_{-0.47}\,(\text{stat}) \pm 0.08\,(\text{syst})\ \text{fb}. \tag{7.10}$$

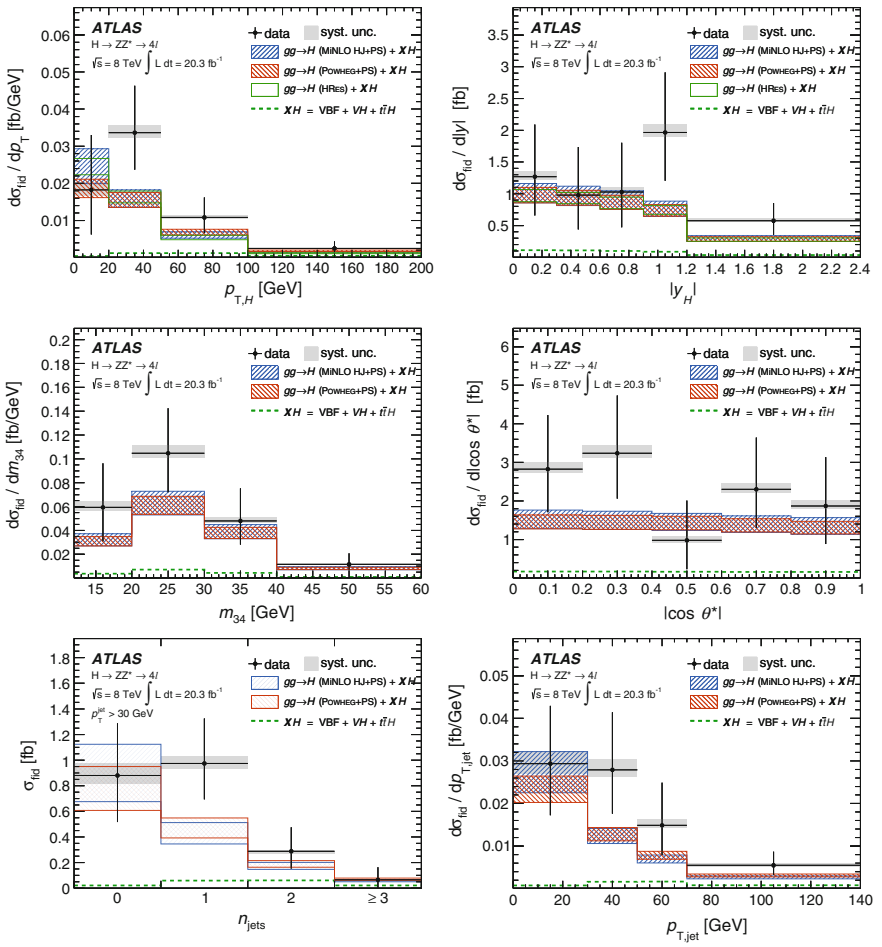

Fig. 7.9 Differential cross section measurements in $p_{\mathrm{T},H}$, $|y_H|$, $|\cos\theta^*|$, m_{34}, N_{jets} and $p_{\mathrm{T},jet1}$, and comparisons to the leading theoretical predictions from HRES2, POWHEG and MINLO

Table 7.6 Compatibility tests between the data and theoretical predictions

Variable	p-values		
	POWHEG	MINLO	HRES2
$p_{\mathrm{T},H}$	0.30	0.23	0.16
$\lvert y_H\rvert$	0.37	0.45	0.36
$\lvert\cos\theta^*\rvert$	0.48	0.60	–
m_{34}	0.35	0.45	–
N_{jets}	0.37	0.28	–
$p_{\mathrm{T},jet1}$	0.33	0.26	–

The NNLO theoretical prediction from [20] is 1.30 ± 0.13 fb; the measured fiducial cross section is roughly 1.5 times larger than the theoretical prediction.

7.6 Combination with $H \to \gamma\gamma$ Channel, and Future Prospects

A more precise measurement of the differential fiducial cross sections can be made by combining the differential measurements from two or more Higgs final states. In 2012, a combination of $H \to ZZ^* \to 4\ell$ and $H \to \gamma\gamma$ channels was performed [29]. For this combination, the fiducial differential cross sections of each channel must be extrapolated to a common total cross section using an acceptance factor $A_{H\to X}$ for each channel, derived using a simulated sample of SM Higgs production:

$$A_{H\to X} = \frac{N^{\mathrm{MC,H}\to X}_{\mathrm{total}}}{N^{\mathrm{MC},H\to X}_{\mathrm{fiducial}}} \,. \tag{7.11}$$

The total cross section in each channel is then the fiducial cross section corrected by the acceptance factor and the branching ratio:

$$\sigma^{\mathrm{tot.}}_{H\to X} = \frac{\sigma^{\mathrm{fid.}}_{H\to X}}{\mathcal{B}_{H\to X}\, A_{H\to X}} \,. \tag{7.12}$$

The two measurements are combined by maximizing a profile likelihood ratio similar to the one described in Sect. 7.3.7, to calculate both a total cross section and to calculate the differential measurements. The combined total cross section measurement at $\sqrt{s} = 8$ TeV is

$$\sigma_{\mathrm{tot}} = 33.0 \pm 5.3\ (\mathrm{stat}) \pm 1.6\ (\mathrm{sys})\ \mathrm{pb}. \tag{7.13}$$

Figure 7.10 presents the combined differential measurement of $p_{\mathrm{T},H}$ and a comparison with the NNLOPS generator [30, 31]. Even when the $H \to ZZ^* \to 4\ell$ and $H \to \gamma\gamma$ are combined, the statistical uncertainty of both measurements still dominates.

The prospects for this measurement improve beginning in 2015, when the LHC begins to collect a large data set with an increased center-of-mass energy at 13 TeV. To evaluate the prospects of $H \to ZZ^* \to 4\ell$ and $H \to \gamma\gamma$ differential measurements and their combination in the future, a study was performed to extrapolate the measurement to higher energy and integrated luminosity, using the Asimov data set—a simulated data set that has statistical properties similar to the expected data that can be used in place of pseudo-experiments [16]. Figure 7.11 reports the expected differential measurements with an integrated luminosity of $80\,\mathrm{fb}^{-1}$ of data collected at $\sqrt{s} = 13$ TeV. In the Asimov data, the Higgs cross section is set to be 1.5 times the SM predicted cross section. After combining the channels, a statistical uncertainty of

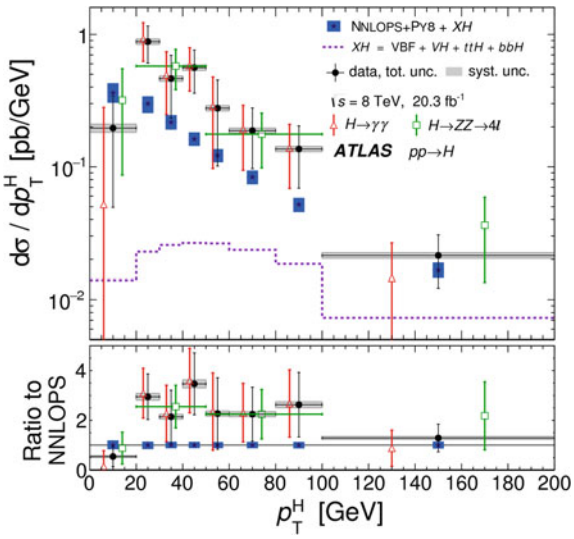

Fig. 7.10 Combination of differential cross section measurements in the $H \to ZZ^* \to 4\ell$ and $H \to \gamma\gamma$ channels at $\sqrt{s} = 8\,\text{TeV}$ [29]

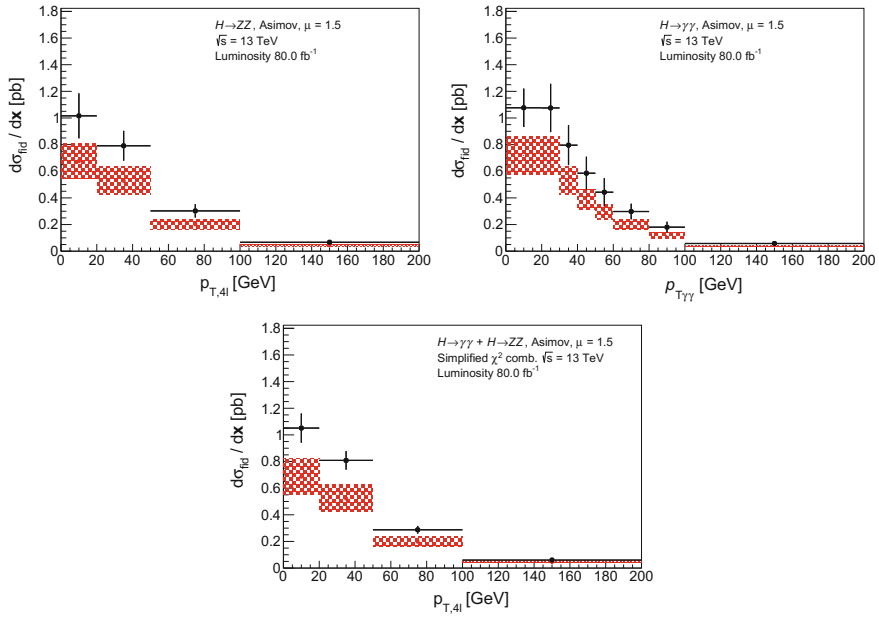

Fig. 7.11 Prospects for the fiducial differential cross section measurements in the $H \to ZZ^* \to 4\ell$ (top left) and $H \to \gamma\gamma$ (top right) channels, and their combination (bottom), assuming an integrated luminosity of $80\,\text{fb}^{-1}$ collected at collision energy $\sqrt{s} = 13\,\text{TeV}$

around 10% can be achieved, competitive with the current theoretical uncertainties. Differential cross section measurements of the Higgs boson will be very exciting in Run 2, allowing careful comparison with the SM prediction and potentially offering hints of new physics beyond the SM.

References

1. M. Gonzalez-Alonso, A. Greljo, G. Isidori, D. Marzocca, Electroweak bounds on Higgs pseudo-observables and $h \to 4\ell$ decays. Eur. Phys. J. C **75**, 341 (2015), arXiv:1504.04018 [hep-ph]
2. D. de Florian, G. Ferrera, M. Grazzini, D. Tommasini, Transverse-momentum resummation: Higgs boson production at the tevatron and the LHC. JHEP **11**, 064 (2011), arXiv:1109.2109 [hep-ph]
3. T. Sjostrand, S. Mrenna, P.Z. Skands, A brief introduction to PYTHIA 8.1. Comput. Phys. Commun. **178**, 852–867 (2008), https://doi.org/10.1016/j.cpc.2008.01.036, arXiv:0710.3820 [hep-ph]
4. ATLAS Collaboration, Measurements of Higgs boson production and couplings in the four-lepton channel in pp collisions at center-of-mass energies of 7 and 8 TeV with the ATLAS detector. Phys. Rev. D **91**, 012006 (2015), https://doi.org/10.1103/PhysRevD.91.012006, arXiv:1408.5191 [hep-ex]
5. ATLAS Collaboration, Measurements of Higgs boson production and couplings in diboson final states with the ATLAS detector at the LHC. Phys. Lett. B **88**, 726 (2013), https://doi.org/10.1016/j.physletb.2013.08.010, arXiv:1307.1427 [hep-ex]
6. ATLAS Collaboration, Improved electron reconstruction in ATLAS using the Gaussian Sum Filter-based model for bremsstrahlung, ATLAS-CONF-2012-047, (2012), http://cdsweb.cern.ch/record/1449796
7. ATLAS Collaboration, Electron efficiency measurements with the ATLAS detector using the 2012 LHC proton–proton collision data, ATLAS-CONF-2014-032, (2014), http://cdsweb.cern.ch/record/1706245
8. M. Cacciari, G.P. Salam, G. Soyez, The anti-k_t jet clustering algorithm. JHEP **04**, 063 (2008), arXiv:0802.1189 [hep-ph]
9. ATLAS Collaboration, Reconstruction of collinear final-state-radiation photons in Z decays to muons in $\sqrt{s} = 7\ TeV$ proton–proton collisions, ATLAS-CONF-2012-143 (2012), http://cdsweb.cern.ch/record/1491697
10. T. Melia, P. Nason, R. Rontsch, G. Zanderighi, W+W-, WZ and ZZ production in the POWHEG BOX. JHEP **11**, 078 (2011), https://doi.org/10.1007/JHEP11(2011)078, arXiv:1107.5051 [hep-ph]
11. T. Binoth, N. Kauer, P. Mertsch, Gluon-induced QCD corrections to pp –> ZZ –> l anti-l l-prime anti-l-prime, in *Proceedings, 16th International Workshop on Deep Inelastic Scattering and Related Subjects (DIS 2008)* (2008) p. 142, https://inspirehep.net/record/789541/files/arXiv:0807.0024.pdf, https://doi.org/10.3360/dis.2008.142, arXiv:0807.0024 [hep-ph]
12. G.D. Cowan, *Statistical Data Analysis* (Oxford University Press, Oxford, 1998), https://cds.cern.ch/record/358560
13. ATLAS Collaboration, *Measurement of the Higgs boson mass from the* $H \to \gamma\gamma$ *and* $H \to ZZ^* \to 4\ell$ *channels in pp collisions at center-of-mass energies of* 7 *and* 8 TeV *with the ATLAS detector*, Phys. Rev. D **90** (2014) 052004, https://doi.org/10.1103/PhysRevD.90.052004, arXiv:1406.3827 [hep-ex]
14. S.S. Wilks, The Large-Sample Distribution of the Likelihood Ratio for Testing Composite Hypotheses. Ann. Math. Stat. **9**(1), 60–62 (1938), https://doi.org/10.1214/aoms/1177732360
15. A. Wald, Tests of statistical hypotheses concerning several parameters when the number of observations is large. Trans. Am. Math. Soc. **54**, 426–482 (1943), https://doi.org/10.1090/S0002-9947-1943-0012401-3

16. G. Cowan, K. Cranmer, E. Gross, O. Vitells, Asymptotic formulae for likelihood-based tests of new physics. Eur. Phys. J. **C71**, 1554 (2011). https://doi.org/10.1140/epjc/s10052-011-1554-0, https://doi.org/10.1140/epjc/s10052-013-2501-z, arXiv:1007.1727 [physics.data-an]. [Erratum: Eur. Phys. J.C73,2501(2013)]
17. D. de Florian, G. Ferrera, M. Grazzini, D. Tommasini, Higgs boson production at the LHC: transverse momentum resummation effects in the $H \to \gamma\gamma$, $H \to WW \to l\nu l\nu$ and $H \to ZZ \to 4l$ decay modes. JHEP **06**, 132 (2012), https://doi.org/10.1007/JHEP06(2012)132, arXiv:1203.6321 [hep-ph]
18. M. Grazzini, H. Sargsyan, Heavy-quark mass effects in Higgs boson production at the LHC. JHEP **09**, 129 (2013), https://doi.org/10.1007/JHEP09(2013)129, arXiv:1306.4581 [hep-ph]
19. K. Hamilton, P. Nason, G. Zanderighi, MINLO: Multi-scale improved NLO. JHEP **10**, 155 (2012), https://doi.org/10.1007/JHEP10(2012)155, arXiv:1206.3572 [hep-ph]
20. LHC Higgs Cross Section Working Group Collaboration, J.R. Andersen et al., *Handbook of LHC Higgs Cross Sections: 3. Higgs Properties*, arXiv:1307.1347 [hep-ph]
21. T. Sjostrand, S. Mrenna, P. Skands, PYTHIA 6.4 physics and manual. JHEP **05**, 026 (2006), arXiv:0603175 [hep-ph]
22. M. Cacciari, G.P. Salam, G. Soyez, FastJet User Manual. Eur. Phys. J. **C72**, 1896 (2012), https://doi.org/10.1140/epjc/s10052-012-1896-2, arXiv:1111.6097 [hep-ph]
23. I.W. Stewart, F.J. Tackmann, Theory Uncertainties for Higgs and Other Searches Using Jet Bins. Phys. Rev. **D85**, 034011 (2012), https://doi.org/10.1103/PhysRevD.85.034011, arXiv:1107.2117 [hep-ph]
24. H.-L. Lai, M. Guzzi, J. Huston, Z. Li, P.M. Nadolsky, J. Pumplin, C.P. Yuan, New parton distributions for collider physics. Phys. Rev. **D82**, 074024 (2010), https://doi.org/10.1103/PhysRevD.82.074024, arXiv:1007.2241 [hep-ph]
25. A.D. Martin, W.J. Stirling, R.S. Thorne, G. Watt, Parton distributions for the LHC. Eur. Phys. J. **C63**, 189–285 (2009), https://doi.org/10.1140/epjc/s10052-009-1072-5, arXiv:0901.0002 [hep-ph]
26. R.D. Ball, V. Bertone, F. Cerutti, L. Del Debbio, S. Forte, A. Guffanti, J.J. Latorre, J. Rojo, M. Ubiali, Impact of heavy quark masses on parton distributions and LHC phenomenology. Nucl. Phys. **B849**, 296–363 (2011), arXiv:1101.1300 [hep-ph]
27. R.D. Ball et al., Parton distributions with LHC data. Nucl. Phys. **B867**, 244–289 (2013), https://doi.org/10.1016/j.nuclphysb.2012.10.003, arXiv:1207.1303 [hep-ph]
28. J.M. Campbell, J.W. Huston, W.J. Stirling, Hard interactions of quarks and gluons: a primer for LHC physics. Reports on Progress in Physics **70**(1), 89 (2007), http://stacks.iop.org/0034-4885/70/i=1/a=R02
29. ATLAS Collaboration, Measurements of the total and differential higgs boson production cross sections combining the $H \to \gamma\gamma$ and $H \to ZZ^* \to 4\ell$ decay channels at $\sqrt{s} = 8\ TeV$ with the ATLAS detector. Phys. Rev. Lett. **115**, 091801 (2015), https://doi.org/10.1103/PhysRevLett.115.091801, arXiv:1504.05833 [hep-ex]
30. S. Catani, An NNLO subtraction formalism in hadron collisions and its application to Higgs boson production at the LHC. Phys. Rev. Lett. **98**, 222002 (2007), https://doi.org/10.1103/PhysRevLett.98.222002, arXiv:hep-ph/0703012 [hep-ph]
31. K. Hamilton, P. Nason, E. Re, G. Zanderighi, NNLOPS simulation of Higgs boson production. JHEP **10**, 222 (2013), https://doi.org/10.1007/JHEP10(2013)222, arXiv:1309.0017 [hep-ph]

Chapter 8
Measurement of WZ Boson Pair Production at $\sqrt{s} = 13$ TeV

Diboson production processes offer a powerful means to measure the triple and quartic gauge couplings in the electroweak sector, an important test of the Standard Model theory. Any deviation from the predicted couplings could give an indication of physics beyond the Standard Model.

The WZ process is a particularly useful probe of diboson physics. Figure 8.1 shows the leading-order diagrams for WZ production at the LHC. Both WW and WZ receive contributions from leading-order triple gauge coupling vertices, however WZ is an experimentally cleaner signature than WW with fewer backgrounds. The WW process must cope with a large $t\bar{t}$ background, which can require imposing a jet veto leading to large experimental uncertainties. In addition, WZ has only one invisible particle (rather than two in the WW case) which makes physical observables easier to reconstruct. Finally, its cross section times branching ratio is larger than the ZZ production process. Theoretical predictions for WW, WZ and ZZ diboson processes have been calculated to NNLO precision in QCD [1–3], allowing for a precise comparison with the SM prediction. Previous measurements of WZ production and decay via leptons have been made at the Tevatron collider [4, 5] and at the LHC by the ATLAS collaboration in 7 and 8 TeV p–p collisions [6, 7], as well as by CMS at 7, 8 and 13 TeV [8, 9] (preliminary).

The analysis presented in this chapter measures the fiducial cross section[1] of the WZ diboson process decaying to three leptons in the eee, $e\mu\mu$, μee and $\mu\mu\mu$ decay channels using 3.2 fb^{-1} of ATLAS data collected at $\sqrt{s} = 13$ TeV c.o.m. energy. The measurements from all four channels are combined using a χ^2 minimization technique to obtain a fiducial cross section measurement. Finally, the measurement is extrapolated to obtain the total cross section. The paper on which these results are based also presents a jet multiplicity differential cross section measurement [10].

The three-lepton channels composed of electrons and muons are used to measure the WZ cross section because their backgrounds are small compared to other final

[1] The fiducial cross section of a process is defined in the introduction to Chap. 7.

K. Brendlinger, *Physics with Electrons in the ATLAS Detector*, Springer Theses,
https://doi.org/10.1007/978-3-319-73930-4_8

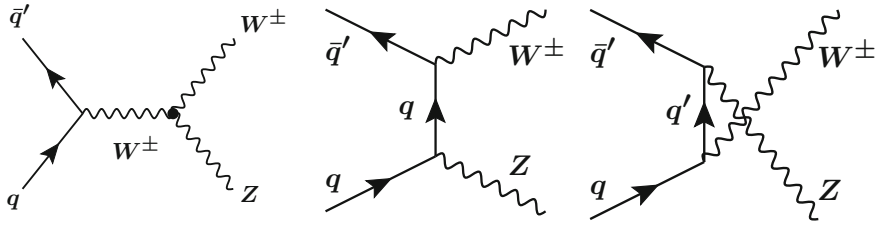

Fig. 8.1 Leading-order diagrams for WZ production in p–p collisions

states. Final states with the W and/or Z decaying to hadrons have larger branching ratios, but much larger backgrounds from a wide array of processes, including multijet, $t\bar{t}$, Z + jet and W + jet production.

Final states including taus are not measured directly either; the tau decays primarily to hadronic final states (about 65%) which are not easily separated from jet backgrounds. The remaining taus decay to $e\,\bar{\nu}_e\nu_\tau$ or $\mu\,\bar{\nu}_\mu\nu_\tau$, with a lifetime $c\tau = 87\,\mu$m, and are nearly indistinguishable from prompt leptons from the collision vertex (apart from having lost energy to the neutrinos). Thus, events with one or more leptonically decaying taus in the final state contribute to the signal regions of the four measured channels. Their fractional contribution to each channel is estimated using simulation and accounted for using a special correction during the calculation of the fiducial cross section, in a way that does not assume a priori the WZ cross section.

8.1 Overview of Backgrounds

The backgrounds to WZ in this analysis can be categorized into two broad types: irreducible and reducible background. Irreducible backgrounds feature exactly three prompt leptons in the fiducial detector volume; they include certain ZZ event topologies, as well as the rare processes $t\bar{t}+V$, tZ, and VVV. These processes are estimated using simulation.

Reducible backgrounds include those in which one or more particles reconstructed by the ATLAS software is incorrectly identified as a prompt, isolated signal lepton. Objects that are misclassified as leptons are alternately referred to as "fake" or "misidentified" leptons. The main backgrounds with a fake lepton in this measurement are the Z+jet, $Z\gamma$, and $t\bar{t}$ processes, depicted in Fig. 8.2. In the Z+jet process, a jet can be misidentified as an electron or a muon, or a b- or c-quark decaying weakly to a lepton can be misidentified as a prompt lepton from the hard scatter. The $Z\gamma$ process can have its photon convert to an e^+e^- pair inside the detector volume, and one of the electrons can be misidentified as prompt.[2] In the $t\bar{t}$ decay $t\bar{t} \to \ell\nu\ell'\nu' + b\bar{b}$ one of the two b-jets decays weakly and its lepton is misidentified as prompt. These

[2]Typically the $Z\gamma$ background in this analysis features an initial-state radiation photon (ISR photon) instead of a final-state radiation photon (FSR). The signal selection requires a lepton pair with a

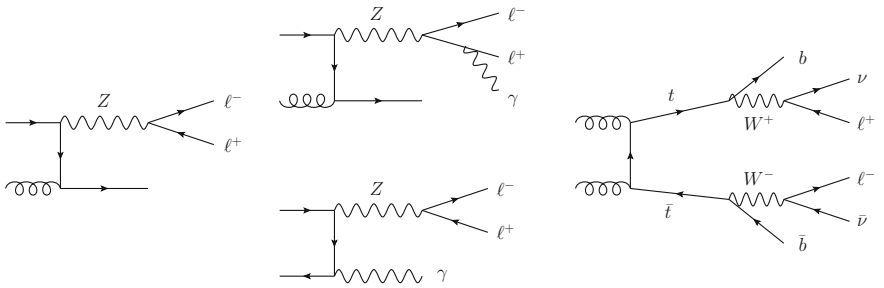

Fig. 8.2 Reducible backgrounds to the WZ process: Z + jet, $Z\gamma$ (including FSR, top, and ISR, bottom) and $t\bar{t}$, respectively. Each process has one object that fakes a lepton

backgrounds are called "reducible" in the sense that applying stricter lepton identification criteria can reduce the size of the background relative to signal in the signal region, thus increasing the signal-to-background ratio.

While the detector response to jets is typically modeled quite well by simulation, the response to the small subset of jets satisfying lepton criteria, about 1 in every 100,000 jets, is understandably imperfect; the situation is similar for photons. As a result, the MC prediction of backgrounds with jets and photons faking leptons is unreliable. Thus, these processes are estimated using data-driven techniques. To reduce the impact of these backgrounds in the signal region, strict lepton identification criteria are applied to remove most events with a fake lepton. The remaining contribution is estimated using a specific control region for the $t\bar{t}$ background and a technique known in ATLAS as the "Fake Factor Method" for estimating Z + jet and $Z\gamma$ backgrounds.

Other sources of background that can be reduced by means of lepton selection criteria are processes whose decay chains result in four leptons, all of which enter the fiducial detector volume, but with one that fails lepton identification requirements. In the WZ analysis this is dominantly the $ZZ \to 4\ell$ background; a dedicated four-lepton veto constructed using relaxed lepton identification criteria is used to reduce this background. The remaining background is estimated using simulation, with a special correction for the MC modeling of prompt leptons that fail identification.

The signal selection is designed to efficiently remove background events. A tight $m_{\ell\ell}$ window on the leptons associated with the Z boson is enforced to suppress $t\bar{t}$ background. Lepton identification criteria are made restrictive, particularly on the lepton associated in the event selection with the W boson, to reduce the contribution from Z + jet and $Z\gamma$. A requirement on m_{T}^{W} reduces backgrounds with low amounts of real $E_{\mathrm{T}}^{\mathrm{miss}}$; however, no explicit requirement is placed on $E_{\mathrm{T}}^{\mathrm{miss}}$, in keeping with the fiducial region definition in the ATLAS 8 TeVmeasurement.

---

mass close to the Z boson mass. In the ISR scenario the invariant mass of the lepton pair is close to the Z mass, but in the FSR scenario the $\ell\ell\gamma$ system reconstructs the Z mass, and typically the $\ell\ell$ system has a mass that falls below the selection requirement.

Table 8.1 Summary of the fiducial and total phase spaces. Quantities are constructed using dressed lepton kinematics

Fiducial phase space $WZ \to \ell'\nu\ell\ell$	Total phase space WZ Production
$81.188 < m_{\ell\ell} < 101.188\,\text{GeV}$	$66 < m_{\ell\ell} < 116\,\text{GeV}$
Z leptons: $p_{\text{T}} > 15\,\text{GeV}$, $\lvert\eta\rvert < 2.5$	
W lepton: $p_{\text{T}} > 20\,\text{GeV}$, $\lvert\eta\rvert < 2.5$	
$\Delta R(\ell_Z, \ell_W) > 0.3$	
$\Delta R(\ell_Z^{\text{lead}}, \ell_Z^{\text{sublead}}) > 0.2$ $m_{\text{T}}^W < 30\,\text{GeV}$	

8.2 Total and Fiducial Phase Space

The cross section is measured in a fiducial phase space defined to ensure that WZ decay products fall within the fiducial volume and to reject backgrounds whose magnitude is difficult to measure accurately. The fiducial selection is applied both to events in data and to the POWHEG and SHERPA event generator predictions in order to directly compare them. The fiducial definition, described below, is identical to the one used in the ATLAS WZ measurement using 8 TeVdata collected in 2012 [7].

In defining the total phase space of WZ at the particle level, kinematic quantities from so-called "dressed" leptons (e or μ) are used to determine event-level properties. Leptons are dressed by adding nearby four-vector collinear FSR photons within a cone $\Delta R \equiv \sqrt{\Delta\phi^2 + \Delta\eta^2} < 0.1$. Neutrinos that do not originate from hadronic or tau decays are also considered at particle level. The neutrinos and dressed leptons are assigned to their parent bosons before applying the fiducial selection, whose selection requirements depend on the assignment. A procedure called the Resonant Shape algorithm makes this assignment based on the kinematic quantities of the leptons by minimizing the following estimator among all allowed pairing combinations:

$$p_k = \left(\frac{1}{m^2_{\ell\ell,k} - m_Z^2 + i\Gamma_Z m_Z}\right) \times \left(\frac{1}{m^2_{\ell'\nu,k} - m_W^2 + i\Gamma_W m_W}\right). \tag{8.1}$$

This boson assignment is used when applying the fiducial selection on events from any generator, in order to ensure a uniform treatment across generators.[3]

Table 8.1 summarizes the fiducial and total phase space definitions. To define the total fiducial phase space after boson assignment, a requirement on the Z mass, $66 < m_{\ell\ell} < 116\,\text{GeV}$, is used to distinguish resonant WZ from continuum $W\gamma^*$. The fiducial phase space requirements, which are designed to closely match the

[3]Some generators have a built-in boson assignment algorithm, but the procedure differs across generators. The SHERPA generator does not explicitly assign leptons to either the W or Z due to the quantum-mechanical ambiguity of events with three leptons of identical lepton flavor and the associated interference effects. A uniform treatment ensures that differences in fiducial cross section predictions are not caused by unphysical boson assignment effects.

signal selection to be described in Sect. 8.4, include a stricter Z-mass requirement, lepton p_{T} and η restrictions, minimum ΔR requirements between leptons, and an m_{T}^{W} requirement on the $W \to \ell\nu$ pair.

8.3 Data Set and MC Samples

The measurement is made using $3.2\,\mathrm{fb}^{-1}$ of data collected from the ATLAS experiment in 2015, from LHC collisions with $\sqrt{s} = 13\,\mathrm{TeV}$ c.o.m. energy.

Signal WZ and several background processes are predicted using Monte Carlo generators, whose events are propagated through the ATLAS detector using a Geant4 description, digitized, and reconstructed. Table 8.2 summarizes the generators used to obtain each prediction; the table indicates where data-driven methods are used to estimate the backgrounds. In these cases, simulation is used as a reference to corroborate the data-driven measurements.

Table 8.2 The background processes in the WZ analysis and the methods used to estimate them, either data-driven or using MC simulation. Each associated sub-process considered is listed with its cross section times branching ratio (including k-factors). The first entry in the table lists for comparison the NLO WZ cross section prediction in the total phase space defined in Table 8.1. MC samples for data-driven processes are used for validation purposes only. All cross section times branching ratios are listed for final states with all allowed combinations of $\ell = e, \mu, \tau$, except the cross section of the $t\bar{t}+W$ process, which includes decays to all (including hadronic) final states

Processes	Method	Sub-processes	Generator	$\sigma \times$BR (pb)
WZ	–	$WZ \to \ell'\nu\ell\ell$	Powheg + PYTHIA8 SHERPA	169.6
ZZ	MC	$q\bar{q} \to ZZ \to 4\ell$ $gg \to ZZ \to 4\ell$	Powheg + PYTHIA8 SHERPA	1.37 31.8×10^{-3}
$t\bar{t}+V$	MC	$t\bar{t}+W$ $t\bar{t}+Z,\ Z \to \ell\ell$	MadGraph + PYTHIA8 MadGraph + PYTHIA8	0.567 0.110
tZ	MC	$tZ \to 3\ell$	MadGraph + PYTHIA6	9.06×10^{-3}
VVV	MC	$VVV \to 3\ell3\nu,\ 4\ell2\nu,$ $2\ell4\nu,\ 5\ell1\nu,\ 6\ell$	SHERPA	21.0×10^{-3}
Data-driven				
$Z+j,\ Z\gamma$	Fake Factor	$Z \to \ell\ell$ $Z \to \ell\ell\gamma$	Powheg + PYTHIA8 SHERPA	5850. 175.2
$t\bar{t},\ Wt,\ WW+j$	MC kinematics with data-driven norm.	$t\bar{t}\ (\geq 1\ell)$ $q\bar{q} \to WW \to \ell\nu\ell\nu$ $Wt\ (\geq 2\ell)$	Powheg + PYTHIA6 Powheg + PYTHIA8 Powheg + PYTHIA6	832. 10.6 7.5

8.4 Object and Event Selection

8.4.1 Object Selection

Electrons and muons are identified using a combination of isolation, tracking and other identification criteria. (These criteria are described in more detail in Chap. 3, Sect. 3.2.4.) Three levels of lepton identification are used in the analysis, described in Table 8.3. Each level, "baseline," "Z", and "W," applies the selection of the previous levels, along with new or stricter criteria. The baseline selection features leptons with relaxed identification criteria and low p_{T} thresholds; it is defined to have high efficiency in order to identify and remove processes decaying to four prompt leptons (the four-lepton veto requirement). Leptons associated with the Z and W bosons must satisfy a stricter selection. The selection on the lepton associated with the W

Table 8.3 The three levels of lepton object selection used in the analysis. The reference name used in the text is on the left, where applicable. The ">" symbol in the overlap removal criteria indicates which object is kept (left-hand side) and which object is removed (right-hand side)

Requirement name	Electrons	Muons
Baseline selection		
–	$p_{\mathrm{T}} > 7\,\mathrm{GeV}$	$p_{\mathrm{T}} > 7\,\mathrm{GeV}$
–	$\lvert\eta^{\mathrm{cluster}}\rvert < 2.47, \lvert\eta\rvert < 2.5$	$\lvert\eta\rvert < 2.5$
–	Detector data-quality criteria	
Identification (id)	LooseLH +nBlayerHits identification	Loose quality
d_0 cut	$\lvert d_0^{\mathrm{BL}}/\sigma(d_0^{\mathrm{BL}})\rvert < 5$	$\lvert d_0^{\mathrm{BL}}/\sigma(d_0^{\mathrm{BL}})\rvert < 3$
z_0 cut	$\lvert\Delta z_0^{\mathrm{BL}} \sin\theta\rvert < 0.5\,\mathrm{mm}$	$\lvert\Delta z_0^{\mathrm{BL}} \sin\theta\rvert < 0.5$ mm
Isolation (iso)	LooseTrackOnly isolation	LooseTrackOnly isolation
–	Survive $\mu > e$ overlap removal	
Z Selection adds...		
–	survive jet $> e$ overlap removal	Survive jet $> \mu$ overlap removal
–	$p_{\mathrm{T}} > 15\,\mathrm{GeV}$	$p_{\mathrm{T}} > 15\,\mathrm{GeV}$
crack veto	Exclude $1.37 < \lvert\eta^{\mathrm{cluster}}\rvert < 1.52$	
–	MediumLH identification	Medium quality
–	Gradient loose isolation	Gradient loose isolation
W Selection adds...		
–	$p_{\mathrm{T}} > 20\,\mathrm{GeV}$	$p_{\mathrm{T}} > 20\,\mathrm{GeV}$
–	TightLH identification	
–	Gradient isolation	

boson is the most stringent in order to suppress the largest reducible backgrounds, Z + jet and $Z\gamma$, whose fake lepton is generally associated with the W.

Electrons at the Baseline level must have $p_{\mathrm{T}} > 7\,\mathrm{GeV}$, and must fall inside the instrumented region of the inner detector ($|\eta| < 2.5$) and the electromagnetic calorimeter (meaning the associated EM cluster must have $|\eta^{\mathrm{cluster}}| < 2.47$). In addition, the electrons must satisfy the LooseLH identification criteria described in Chap. 5, including the requirement of at least one hit in the first layer of the pixel detector (B-Layer), and fulfill requirements on the transverse and longitudinal impact parameter variables described in Chap. 3, Sect. 3.2.4. Finally, the electrons must satisfy a track isolation requirement (LooseTrackOnly) designed to be 99% efficient for prompt electrons [11].

Electrons satisfying the Z selection criteria must additionally fulfill a higher p_{T} threshold ($p_{\mathrm{T}} > 15\,\mathrm{GeV}$), a tighter identification menu (MediumLH), and track and calorimeter isolation requirements whose combined efficiency is designed to be between 95 and 99% for electrons between 25 and 60 GeV. In addition, electrons inside the electromagnetic calorimeter transition region ("crack") are vetoed at this level. Electrons meeting the W selection requirements must additionally satisfy $p_{\mathrm{T}} > 20\,\mathrm{GeV}$, even tighter identification criteria (TightLH), and track/calorimeter isolation requirements with a combined efficiency between 90 and 99% for electrons between 25 and 60 GeV.

Muons at the Baseline level must satisfy $p_{\mathrm{T}} > 7\,\mathrm{GeV}$ and $|\eta| < 2.5$, a "Loose" selection criteria based on a set of discriminating variables, requirements on the track transverse and longitudinal impact parameters, and the 99% efficient LooseTrackOnly isolation requirement [12]. Muons meeting the Z selection requirements must also satisfy $p_{\mathrm{T}} > 15\,\mathrm{GeV}$, "Medium" quality identification requirements, and the GradientLoose track and calorimeter isolation requirement (95−99% for muons between 25 and 60 GeV). Muons satisfying the W selection criteria must additionally have $p_{\mathrm{T}} > 20\,\mathrm{GeV}$.

Jets are required to construct the $E_{\mathrm{T}}^{\mathrm{miss}}$ and for a measurement of the unfolded jet multiplicity distribution in the analysis. Jets are reconstructed from topological clusters using the Anti-k_t algorithm [13] with a radius parameter $R = 0.4$. Jets used for the construction of the $E_{\mathrm{T}}^{\mathrm{miss}}$ are required to have $p_{\mathrm{T}} > 20\,\mathrm{GeV}$ and $|\eta| > 4.5$; jets used for the jet multiplicity measurement must satisfy a higher transverse momentum requirement, $p_{\mathrm{T}} > 25\,\mathrm{GeV}$. Jets that satisfy the requirements $|\eta| > 2.4$ and $20 < p_{\mathrm{T}} < 50\,\mathrm{GeV}$ must pass a selection designed to suppress jets from pile-up events [14].

Separate algorithms are run in parallel to reconstruct and identify electrons, muons and jets. Because a single particle can be reconstructed by more than one object reconstruction algorithm resulting in more than one particle hypothesis, the collections of electrons, muons and jets are put through a procedure designed to resolve ambiguities. First, an electron is removed and a muon kept if the two objects share an ID track (referred to here as the $\mu > e$ overlap removal step, where the ">" symbol indicates that the muon is kept and the electron is removed). Next, jets are removed if within $\Delta R < 0.2$ of an electron, the electron is removed if it is within $0.2 < \Delta R < 0.4$ of the jet. Finally, muons are removed if within $\Delta R < 0.4$ of a jet with ≥ 3 tracks; the

jet is removed if the track has fewer than three tracks. As indicated in Table 8.3, the overlap removal between electrons and muons is performed as part of the electron baseline definition, while the overlap removal with jets is performed with leptons surviving the W and Z lepton identification levels.

The missing transverse momentum ($E_{\mathrm{T}}^{\mathrm{miss}}$) of an event is defined as the negative vector sum of the transverse momenta of the calibrated selected leptons and jets and the sum of transverse momenta of additional soft objects in the event, which is determined using ID tracks.

8.4.2 Event Selection

The event selection, summarized in Table 8.4, is as follows: after applying basic quality criteria based on the performance of the detector systems, events are selected with single-lepton triggers, and with a reconstructed primary vertex with ≥ 2 tracks. Exactly three leptons of "baseline" quality are required; this vetoes events with four leptons identified with high-efficiency selection criteria.[4] To ensure that the leading lepton p_{T} threshold is higher than the lepton trigger thresholds, a minimum p_{T} requirement of 25 GeV is applied.

Next, a same-flavor, opposite-charge (SFOC) lepton pair is required, to be consistent with a Z boson. At this step, three leptons are assigned to candidate parent bosons using criteria that are slightly different from the particle-level algorithm described in Sect. 8.2: if a single SFOC pair exists, it is assigned to the Z boson; if two pairs exist, the pair with the smallest $\Delta m = |m_{\ell\ell} - m_Z|$ is associated with the Z boson. The remaining lepton is assigned to the W boson. The leptons assigned to the Z boson are referred to as ℓ_Z^{lead} and $\ell_Z^{\mathrm{sublead}}$ where the leading Z-lepton is the one with higher p_{T}. The lepton assigned to the W boson is labeled ℓ_W. After assignment, the Z and W identification requirements are applied to their respective leptons.

To suppress non-resonant backgrounds such as $t\bar{t}$, a window $|m_{\ell\ell} - m_Z| < 10$ GeV around the Z mass is imposed. Finally, a requirement on the transverse mass of the ℓ_W–$E_{\mathrm{T}}^{\mathrm{miss}}$ system is applied to select W bosons, similarly to how the $m_{\ell\ell}$ requirement is designed to select the Z boson. The transverse mass is defined as:

$$m_{\mathrm{T}}^{W} = \sqrt{2 p_{\mathrm{T}}^{\ell} E_{\mathrm{T}}^{\mathrm{miss}} \left(1 - \cos \Delta\phi(\ell, \nu)\right)} \tag{8.2}$$

where $\Delta\phi(\ell, \nu)$ is the angle between the lepton and neutrino in the transverse plane. The requirement $m_{\mathrm{T}}^{W} > 30$ GeV is applied. This requirement suppresses events with low $E_{\mathrm{T}}^{\mathrm{miss}}$, such as Z+jet, $Z\gamma$ and ZZ backgrounds. A requirement on m_{T}^{W} is preferred to a direct requirement on $E_{\mathrm{T}}^{\mathrm{miss}}$ because the latter was found to negatively impact searches for anomalous triple gauge couplings (aTGC). Although aTGC limits are

[4] Events are required to have exactly three leptons after $\mu > e$ overlap removal, as well as exactly three leptons after the overlap removal steps between jets and leptons.

Table 8.4 Signal event selection. In case more than one same-flavor, opposite sign lepton pairs exist, the pair whose $m_{\ell\ell}$ is closest to PDG Z mass is associated with the Z boson. Below it, the triggers used for the trigger requirement are listed. A discrepancy in one electron trigger between the L1 trigger emulated in the MC and the L1 trigger used to collect data is indicated with a subscript and superscript. More details on the triggers are described in Chap. 3, Sect. 3.2.5

Event Selection	
▷ Event cleaning	Reject LAr, Tile and SCT corrupted events and incomplete events
▷ Trigger	eee case: Electron trigger fires. $\mu\mu\mu$ case: Muon trigger fires $e\mu\mu/\mu ee$ case: Electron or muon trigger fires
▷ Primary vertex	Reconstructed vertex with ≥ 2 tracks
▷ Lepton multiplicity	Exactly 3 baseline leptons
▷ Leading lepton p_{T}	$p_{\mathrm{T}}^{\ell 1} > 25\,\mathrm{GeV}$
▷ Z leptons	Require two same-flavor, opposite-charge (SFOC) leptons
(Lepton association with Z, W bosons)	Associate SFOS lepton pair with Z boson (use pair with smallest $\lvert m_{\ell\ell} - m_Z \rvert$)
	Associate remaining lepton with W boson
▷ Z lepton quality	Leptons associated with Z boson pass Z lepton selection
▷ W lepton quality	Lepton associated with W boson passes W lepton selection
▷ Z mass window	$\lvert m_{\ell\ell} - m_Z \rvert < 10\,\mathrm{GeV}$
▷ W transverse mass	$m_{\mathrm{T}}^{W} > 30\,\mathrm{GeV}$
Lepton Triggers	
Electron trigger $^{\mathrm{data}}_{[\mathrm{MC}]}$	e24_lhmedium_L1EM$^{20}_{[18]}$VH || e60_lhmedium || e120_lhloose
Muon trigger	mu20_iloose_L1MU15 || mu50

not presented in this paper, the selection is designed to maintain consistency with the fiducial requirements of previous WZ measurements [7].

8.4.3 Notation Conventions

In the following, leptons associated to the Z and W bosons are referred to in the text as ℓ_Z^{lead}, $\ell_Z^{\mathrm{sublead}}$, and ℓ_W. Events passing the signal selection, or a selection in which leptons are assigned to parent bosons, are given a channel label according to the flavor of the constituent leptons. The channel label reports the flavor of the candidates according to following order: the flavor of the lepton associated to the

W boson, followed by the flavor of the leading Z lepton, and finally the flavor of the subleading Z lepton, e.g. $\ell_W \ell_Z^{\text{lead}} \ell_Z^{\text{sublead}}$. As an example, the WZ decaying via $W \to e\nu$, $Z \to \mu\mu$ is labeled "$e\mu\mu$."

8.5 Backgrounds

The background section is focused on the description of the data-driven reducible background estimates, as well as the corrections applied to the ZZ simulated samples to account for lepton identification mismodeling effects. All other processes—$t\bar{t}+V$, tZ, and VVV—are estimated using simulation.

The $t\bar{t}$, Wt, and WW processes all have similar event features, and can thus be estimated simultaneously. These three backgrounds are collectively referred to as the "top-like" backgrounds (of the three, $t\bar{t}$ will be the main contribution to the signal region). We measure the top-like processes in a control region close to the analysis signal region, distinguished by its different-flavor, opposite-charge pair and a veto of events with any same-flavor, opposite-charge pairs. The control region is used to derive a data-MC normalization factor, which is then applied to MC passing the signal selection to estimate the number of top-like events in the signal region, covering $t\bar{t}$, Wt, and WW.

The $Z+$jet and $Z\gamma$ backgrounds feature two real leptons and one object misidentified as a lepton (a "fake" lepton); this is typically a non-prompt lepton from a b-jet decay ($Z+$jet), a light-flavor particle mimicking an isolated lepton signature ($Z+$jet), or a converted photon reconstructed as an electron ($Z\gamma$). These two processes are estimated using the Fake Factor method adapted for three lepton events. An extrapolation factor (the fake factor) between leptons passing the signal selection and leptons passing an inverted selection is measured in a control region enriched in $Z+$jet and $Z\gamma$ events. To estimate the $Z+$jet and $Z\gamma$ in the signal region, the fake factor is then applied to a region identical to the signal region except for the quality of leptons: two signal leptons, and one passing the inverted selection. The method is described in detail in the following sections.

It is worth noting that the approaches taken here is different from the approach to $Z+$jet, $Z\gamma$ and top-like backgrounds in the WZ measurement at 8 TeV [7]. In that paper, all three backgrounds are treated simultaneously using the "Matrix Method," which is functionally identical to the Fake Factor method described here. The justification for using the present approach is discussed in Sect. 8.5.2.

8.5.1 Top-Like Backgrounds

To estimate the top-like ($t\bar{t}$, Wt and WW) backgrounds in the signal region, the prediction from MC simulation is normalized to a control region enriched in these events. Events in the region must pass all signal region requirements, with the exception that

Table 8.5 Top-like control regions for the WZ analysis. The rows represent the flavor of the leptons associated with a Z boson, allowing for different-flavor, opposite-sign pairs to be associated with the Z. The columns show the possible flavor and charge of the lepton associated with the W boson. Channels with a "-" contain $\ell^+\ell^-$ pairs, and thus they are excluded from the top-CRs to avoid Z/γ^* contamination

	$e^{\pm}$	$e^{\mp}$	$\mu^{\pm}$	$\mu^{\mp}$
$e^{\pm}e^{\mp}$	SR	SR	SR	SR
$e^{\pm}\mu^{\mp}$	top-CR (e)	–	–	top-CR (μ)
$\mu^{\pm}e^{\mp}$	–	top-CR (e)	top-CR (μ)	–
$\mu^{\pm}\mu^{\mp}$	SR	SR	SR	SR

a different-flavor, opposite-charge (DFOC) pair is required instead of a SFOC pair. In the ensuing boson assignment step, by analogy with the signal selection, the DFOC pair is labeled the Z boson pair; if two DFOC pairs exist, then the pair with the smallest $\Delta m = |m_{\ell\ell} - m_Z|$ is associated with the Z. To remove any contribution from Z + jet and $Z\gamma$, no events are considered in which a same-flavor, opposite-charge pair can be formed. Thus, events in this region are limited to $\ell^{\pm}\ell'^{\mp}\ell^{\pm}$ channels—more explicitly, $\mu^{\pm}e^{\mp}\mu^{\pm}$, $\mu^{\pm}\mu^{\pm}e^{\mp}$, $e^{\pm}e^{\pm}\mu^{\mp}$ and $e^{\pm}\mu^{\mp}e^{\pm}$. To increase the size of the control region, the requirement $|m_{\ell\ell} - m_Z| < 10\,\text{GeV}$ on the leptons associated with the Z boson is removed. The top-like control regions, and their relation to the signal regions are summarized in Table 8.5. This set of regions is collectively referred to as the top control region parallel to the signal region, or top-CR||SR.

Two global data-MC scale factors are derived from this region: one associated to events with a fake muon, and one to events with a fake electron. Events are assigned to one of the two categories using the following logic: each $t\bar{t}$ (or WW or Wt) event must contain a pair of real, opposite-charge leptons, and one fake lepton. In e.g. an $\mu^{\pm}e^{\mp}\mu^{\pm}$ event topology, the e must participate in the opposite-charge pair, and therefore must be a real lepton; thus, the fake lepton must be one of the other two leptons, and must have flavor μ. (The logic is identical for the other flavor combinations in this region.) The region with a fake muon (electron) is referred to as the "μ-fake" ("e-fake") region.

The data-MC scale factor in each region (μ-fake and e-fake) is given by:

$$SF_{t\bar{t}} = \frac{N_{\text{data}} - N_{\text{other}}^{\text{MC}}}{N_{t\bar{t}}^{MC}} \tag{8.3}$$

where $N_{\text{other}}^{\text{MC}}$ represents the MC prediction of all other processes in the $t\bar{t}$ CR (mainly WZ and $t\bar{t}+V$). The WZ yield in these regions is scaled up by 1.15 to reflect the Run 1 cross section measurement. Table 8.6 shows the MC prediction, data yields, and scale factor $SF_{t\bar{t}}$ for the top-CR, separately for e-fake and μ-fake channels. The $m_{\ell\ell}$ spectrum of these control regions is shown in Fig. 8.3.

The final top-like prediction is given by the MC prediction for the $t\bar{t}+Wt+WW$ yield in the signal region, normalized by the e-fake or μ-fake scale factor (chosen

Table 8.6 Expected and observed number of events in the $t\bar{t}$ control region parallel to the signal region, removing the Z window cut for the DFOC pairs. Channels are split into those with a fake muon (top row) and those with a fake electron. The $t\bar{t}$ MC is normalized by these scale factors in the signal region. The scale factor errors include statistical error on the data (first) and statistical error on the MC (last)

Channel	Top-like MC	Other MC	Total MC	Data	Top-like scale factor
$\mu^{\pm}e^{\mp}\mu^{\pm} + \mu^{\pm}\mu^{\pm}e^{\mp}$	7.07 ± 0.83	2.00 ± 0.09	9.07 ± 0.83	12.00 ± 3.46	$1.41 \pm 0.49 \pm 0.17$
$e^{\pm}e^{\pm}\mu^{\mp} + e^{\pm}\mu^{\mp}e^{\pm}$	8.14 ± 0.83	2.62 ± 0.10	10.76 ± 0.84	7.00 ± 2.65	$0.54 \pm 0.32 \pm 0.05$

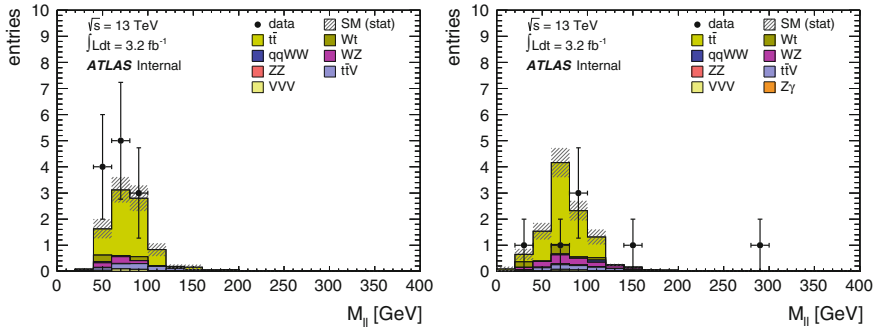

Fig. 8.3 Control plots for the top-CR parallel to the signal region, where the data-MC transfer factor is derived, in the $m_{\ell\ell}$ variable. Left: the $\mu^{\pm}e^{\mp}\mu^{\pm}$+$\mu^{\pm}\mu^{\pm}e^{\mp}$ (μ-fake) region. Right: the $e^{\pm}e^{\pm}\mu^{\mp}$+$e^{\pm}\mu^{\mp}e^{\pm}$ (e-fake) region

Table 8.7 Summary of the top-like estimate in the signal region. The first and second rows show the number of events predicted by MC having a muon or electron fake, according to the truth record. The total MC is shown after the scale factor from Table 8.6 is applied. The data and MC statistical uncertainty from the μ-fake and e-fake scale factors are also shown, propagated through the estimate. The procedure predicts 9.16 ± 3.05 top-like events

Channels	eee	$e\mu\mu$	μee	$\mu\mu\mu$	Total
Top-like MC×SF, μ-fake	–	1.83 ± 0.46	0.82 ± 0.33	3.58 ± 0.71	6.23 ± 0.91
Top-like MC×SF, e-fake	1.23 ± 0.24	0.55 ± 0.17	1.15 ± 0.24	–	2.93 ± 0.38
Top-like MC×SF, total	1.23 ± 0.24	2.38 ± 0.49	1.97 ± 0.41	3.58 ± 0.71	9.16 ± 0.98
μ-fake uncertainty	–	0.67	0.30	1.32	2.29
e-fake uncertainty	0.74	0.33	0.69	–	1.76

according to the flavor of the signal lepton identified as being fake by the truth record). Table 8.7 shows the MC yields and final top-like estimate in the signal region.

Combining all channels, the final top-like ($t\bar{t} + Wt + WW$) estimate in the signal region is estimated as 9.16 ± 3.05 where the error represents the statistical error of the data and MC in the top-CR||SR, and the statistical error of the top-like MC in the SR.

The estimate described above is used to determine both the event yields and the kinematic distributions of top-like backgrounds in the signal region. Thus, the kinematic shapes used for reconstruction-level signal region distributions and the measurement of the unfolded jet multiplicity distribution are described by simulation.

Systematic errors on the method are postponed to Sect. 8.5.3, after the discussion of the $Z + \text{jet}/Z\gamma$ estimate.

8.5.2 $Z + \text{jet}/Z\gamma$ Background

The following describes the estimate of the $Z +$ jet and $Z\gamma$ backgrounds using the Fake Factor method.

8.5.2.1 Fake Factor Methodology

The Fake Factor method is a data-driven technique used to estimate the magnitude and shape of background processes in which one or more non-lepton objects is misidentified as a signal lepton (called a "fake lepton"), causing the event to enter into the signal region. Fake lepton misidentification rates are difficult to model correctly in simulation; thus it is desirable to measure the misidentification rate in a region enriched in fake leptons, and apply it to a control region to estimate the amount of reducible background in the signal region.

The procedure is as follows: for the lepton in question, an anti-id selection is created by relaxing and inverting the electron and muon identification variables. The anti-id selection (also referred to as the "denominator" or "Loose" selection) is enriched in fake leptons and orthogonal to the signal lepton selection (also called the "id," "numerator" or "Tight" selection). Using these anti-id and signal lepton selections, a fake factor F is calculated in a kinematic region enriched in a process that features fake leptons with a similar type and composition to that of the target reducible background. This region is referred to as the "Fake Factor Region," and the fake factor measured there is defined as:

$$F = \frac{N_{\text{id}}}{N_{\text{anti-id}}}. \tag{8.4}$$

In the implementation used here, the fake factor is calculated as a function of the p_{T} of the fake lepton:

$$F(i) = \frac{N_{\text{id}}(i)}{N_{\text{anti-id}}(i)}, \tag{8.5}$$

where i refers to the ith p_{T} bin. Given the small dataset used in the present analysis, the fake factor is calculated in bins of fake lepton p_{T}. With more data, fake factor can be characterized in bins of $p_{\text{T}} \times \eta$.

The fake factor is then applied to a control region with a selection identical to the signal region, except that the signal lepton identification is replaced by the anti-id selection to select the lepton. The number of reducible events in the signal region is then:

$$N_{\mathrm{SR}}^{\mathrm{red}} = \sum_i N_{\mathrm{CR}}^i \cdot F(i), \tag{8.6}$$

where the sum is over i p_{T} bins of the fake factor.

The fake factor procedure is used to estimate only the Z + jet and $Z\gamma$ reducible background, which features two real leptons and one fake lepton. (Z + jet and $Z\gamma$ will hereafter be referred to as simply "Z + jet/$Z\gamma$" for brevity, unless otherwise noted.) The $t\bar{t}$ process also has two real and one fake lepton, however this procedure is not used to estimate $t\bar{t}$ in the SR. To deal with contamination from $t\bar{t}$ events in the Z + jet/$Z\gamma$ control region, a $t\bar{t}$ control region, similar to the one described in Sect. 8.5.1, is used to estimate and remove the contamination. In this way, the fake factor procedure is used to estimate the Z + jet/$Z\gamma$ processes only. The justification for such a treatment is deferred until later in this section. The control region used to obtain the estimate of $t\bar{t}$ and top-like events in the signal region is described in Sect. 8.5.1.

To develop the Fake Factor method for Z + jet/$Z\gamma$ events, the fake factor method must be extended to accommodate a three-lepton decay topology. Each identified lepton is assigned a parent boson in the event selection.[5] The fake lepton in the Z + jet/$Z\gamma$ event is typically assigned to the W boson, because the two real leptons are likely to form a same-flavor opposite-sign pair whose mass is very close to the PDG Z mass. However, all boson association combinations are considered, to account for events in which the fake lepton is mispaired with one of the real leptons and associated with the Z boson. (It will be confirmed later that this misassignment effect is indeed present.)

To illustrate the three-lepton case, it is constructive to write the entire matrix of possible boson association and lepton identification outcomes for the Z + jet or $Z\gamma$ process, plus those of the signal WZ process (and other processes with three real leptons). In the following, indices refer to leptons and are distinguished according to the boson to which the lepton was assigned during event selection: the W lepton, leading Z lepton, or subleading Z lepton (indices 1, 2 and 3, respectively).

Leptons are categorized according to their true content, and according to reconstructed categories. Events with three real leptons are labeled RRR; a Z + jet event where the two real leptons are correctly assigned to the Z boson, and the fake lepton is associated with the W, is labeled FRR. Misassigned Z + jet events are labeled RFR (leading Z lepton is fake) or RRF (subleading Z lepton is fake).

At reconstruction level, leptons (real or fake) are categorized according to whether they pass Loose ("L") or Tight ("T") identification criteria.[6] The identification efficiency of a real lepton is denoted e; the fake id efficiency is f. Finally, $\bar{e} = (1 - e)$ is the efficiency of real leptons passing the anti-id criteria; $\bar{f} = (1 - f)$ is the fake

[5] It is important to note that the procedure that associates leptons with parent bosons does not consider whether the leptons are classified as Loose or Tight, i.e. it is completely independently of lepton identification. In other words, the lepton is assigned a parent before its quality is known.

[6] Note that Loose and Tight need not be adjoined in the phase space of identification variables for this formalism to hold. Thus "efficiency" here refers really to the number of Tight leptons divided by the sum of Loose and Tight leptons.

efficiency for the anti-id selection. Note that the fake factor described previously can be rewritten as $F = f/\bar{f}$. Then each WZ/ZZ and $Z+\text{jet}/Z\gamma$ event can be described by the following matrix, relating truth classification to reconstructed regions:

$$\begin{pmatrix} N_{TTT} \\ N_{LTT} \\ N_{TLT} \\ N_{TTL} \\ N_{LLT} \\ N_{LTL} \\ N_{TLL} \\ N_{LLL} \end{pmatrix} = \begin{pmatrix} e_1e_2e_3 & f_1e_2e_3 & e_1f_2e_3 & e_1e_2f_3 \\ \bar{e}_1e_2e_3 & \bar{f}_1e_2e_3 & \bar{e}_1f_2e_3 & \bar{e}_1e_2f_3 \\ e_1\bar{e}_2e_3 & f_1\bar{e}_2e_3 & e_1\bar{f}_2e_3 & e_1\bar{e}_2f_3 \\ e_1e_2\bar{e}_3 & f_1e_2\bar{e}_3 & e_1f_2\bar{e}_3 & e_1e_2\bar{f}_3 \\ \bar{e}_1\bar{e}_2e_3 & \bar{f}_1\bar{e}_2e_3 & \bar{e}_1\bar{f}_2e_3 & \bar{e}_1\bar{e}_2f_3 \\ \bar{e}_1e_2\bar{e}_3 & \bar{f}_1e_2\bar{e}_3 & \bar{e}_1f_2\bar{e}_3 & \bar{e}_1e_2\bar{f}_3 \\ e_1\bar{e}_2\bar{e}_3 & f_1\bar{e}_2\bar{e}_3 & e_1\bar{f}_2\bar{e}_3 & e_1\bar{e}_2\bar{f}_3 \\ \bar{e}_1\bar{e}_2\bar{e}_3 & \bar{f}_1\bar{e}_2\bar{e}_3 & \bar{e}_1\bar{f}_2\bar{e}_3 & \bar{e}_1\bar{e}_2\bar{f}_3 \end{pmatrix} \begin{pmatrix} N_{RRR} \\ N_{FRR} \\ N_{RFR} \\ N_{RRF} \end{pmatrix} \tag{8.7}$$

The reducible background term, $N_{TTT}^{Red} = N_{TTT} - N_{RRR}$, can be rewritten in terms of only reconstructed categories. To achieve this, each side of the equation is multiplied by the column vector

$$\left(1 \quad -\frac{f_1}{\bar{f}_1} \quad -\frac{f_2}{\bar{f}_2} \quad -\frac{f_3}{\bar{f}_3} \quad \frac{f_1f_2}{\bar{f}_1\bar{f}_2} \quad \frac{f_1f_3}{\bar{f}_1\bar{f}_3} \quad \frac{f_2f_3}{\bar{f}_2\bar{f}_3} \quad -\frac{f_1f_2f_3}{\bar{f}_1\bar{f}_2\bar{f}_3} \right). \tag{8.8}$$

All terms in the RHS matrix cancel exactly, except for the first column with three real leptons, originating mostly from WZ and ZZ. These terms are labeled e.g. $\bar{e}_1e_2e_3 \equiv N_{LTT}^{RRR}$, and are estimated using MC corrected using lepton identification scale factors. Canceling terms and making substitutions leads to

$$\begin{aligned} N_{TTT} - N_{LTT}\frac{f_1}{\bar{f}_1} - N_{TLT}\frac{f_2}{\bar{f}_2} - N_{TTL}\frac{f_3}{\bar{f}_3} + N_{LLT}\frac{f_1}{\bar{f}_1}\frac{f_2}{\bar{f}_2} + N_{LTL}\frac{f_1}{\bar{f}_1}\frac{f_3}{\bar{f}_3} + N_{TLL}\frac{f_2}{\bar{f}_2}\frac{f_3}{\bar{f}_3} \\ - N_{LLL}\frac{f_1}{\bar{f}_1}\frac{f_2}{\bar{f}_2}\frac{f_3}{\bar{f}_3} = N_{TTT}^{RRR} - N_{LTT}^{RRR}\frac{f_1}{\bar{f}_1} - N_{TLT}^{RRR}\frac{f_2}{\bar{f}_2} - N_{TTL}^{RRR}\frac{f_3}{\bar{f}_3} \\ + N_{LLT}^{RRR}\frac{f_1}{\bar{f}_1}\frac{f_2}{\bar{f}_2} + N_{LTL}^{RRR}\frac{f_1}{\bar{f}_1}\frac{f_3}{\bar{f}_3} + N_{TLL}^{RRR}\frac{f_2}{\bar{f}_2}\frac{f_3}{\bar{f}_3} - N_{LLL}^{RRR}\frac{f_1}{\bar{f}_1}\frac{f_2}{\bar{f}_2}\frac{f_3}{\bar{f}_3} \end{aligned} \tag{8.9}$$

Rearranging terms and substituting $F = f/\bar{f}$, the final expression is:

$$\begin{aligned} N_{TTT} - N_{TTT}^{RRR} = \left[N_{LTT} - N_{LTT}^{RRR}\right]F_1 + \left[N_{TLT} - N_{TLT}^{RRR}\right]F_2 + \left[N_{TTL} - N_{TTL}^{RRR}\right]F_3 \\ - \left[N_{LLT} - N_{LLT}^{RRR}\right]F_1F_2 - \left[N_{LTL} - N_{LTL}^{RRR}\right]F_1F_3 \\ - \left[N_{TLL} - N_{TLL}^{RRR}\right]F_2F_3 + \left[N_{LLL} - N_{LLL}^{RRR}\right]F_1F_2F_3. \end{aligned} \tag{8.10}$$

Assuming that F and $\bar{e}/e$ are both small, terms with more than one fake factor in them can be neglected (these are also the terms with 2 Loose leptons). To understand this, it is instructive to consider the relative scale of a few exemplary terms. Restricting

ourselves to the N_{FRR} true events (the common Z+jet/$Z\gamma$ lepton-boson assignment), we consider the largest 1-Loose lepton term ($\bar{f}_1 e_2 e_3 N_{FRR}$) against the two largest 2-Loose terms (($\bar{f}_1 \bar{e}_2 e_3 + \bar{f}_1 e_2 \bar{e}_3) N_{FRR}$). It will be shown that the measured fake factors in this method are < 0.1 everywhere; if the real lepton ID efficiency is 0.85 (conservatively low), then the relative contributions of the 1-Loose (1L) term is

$$\bar{f}_1 e_2 e_3 \cdot F_1 \cdot N_{FRR} \sim 0.065. \tag{8.11}$$

The 2-Loose (2L) term is:

$$(\bar{f}_1 \bar{e}_2 e_3 + \bar{f}_1 e_2 \bar{e}_3) \cdot F_1 F_2 \cdot N_{FRR} \sim 0.0023 \tag{8.12}$$

Thus, the 2 L terms are at most 3.5% the size of the analogous 1 L terms, and 2L (or 3L) terms can be safely neglected in this regime.

We can rewrite the fake factor equation, now featuring only the 1 L term, to accommodate multiple fake factor bins:

$$N_{TTT} - N_{TTT}^{RRR} = \sum_i \left[N_{LTT}(i) - N_{LTT}^{RRR}(i) \right] F_1(i) + \sum_i \left[N_{TLT}(i) - N_{TLT}^{RRR}(i) \right] F_2(i) + \sum_i \left[N_{TTL}(i) - N_{TTL}^{RRR}(i) \right] F_3(i) \tag{8.13}$$

where $F_1 \equiv F_W$ is the fake factor for the W identification selection, and $F_2 \equiv F_3 \equiv F_Z$ is the fake factor for the Z identification selection.

Note that processes involving two fake leptons (W + 2j or semi-leptonic $t\bar{t}$ + 2j) are omitted in the above equation. However, if the exercise were repeated with these terms (N_{RFF}, N_{FRF}, N_{FFR}), multiplying by the same column vector and with the same algebra, the result is Eq. 8.10. In fact, Eq. 8.10 has the property that it can simultaneously treat processes with 1, 2 and 3 fake leptons, provided their fake factors are identical (Eq. 8.13 has assumptions that only apply to the 1-fake case).

The formalism above is based on a few assumptions, which will be shown to hold true in the following implementation of the fake factor method. First, the procedure requires that processes with three real leptons (WZ, ZZ, and other processes) must be subtracted using MC in the regions with one Loose lepton. It will be confirmed that the impact of this component of the fake factor method is small. Finally, it should be checked that the terms involving two and three Loose leptons are small. This would also address the question of whether the contribution from reducible processes involving two or three fake leptons is small.

8.5.2.2 Application of the Fake Factor Method to Z + jet/$Z\gamma$

The Z + jet/$Z\gamma$ fake factor is derived in a three-lepton region orthogonal to the WZ signal selection and enriched in Z + jet/$Z\gamma$ events: $m_{\mathrm{T}}^{W} < 30\,\mathrm{GeV}$ and

Table 8.8 Definition of the electron and muon baseline identification for the $Z + \text{jet}/Z\gamma$ Fake Factor Region. Events entering into the fake factor calculation must have exactly 3 leptons passing this baseline selection

Electrons	Muons
$p_{\text{T}} > 7\,\text{GeV}$	$p_{\text{T}} > 7\,\text{GeV}$
VeryLooseLH identification	Loose identification
$\lvert\eta\rvert < 2.47$ && $!(1.37 < \lvert\eta\rvert < 1.52)$	$\lvert\eta\rvert < 2.47$

Table 8.9 Definition of the electron and muon denominator (also called anti-id or Loose) selection criteria

Electrons	Muons
Pass OR against muons and jets	No OR requirement
VeryLooseLH identification	Medium identification
(!MediumLH identification || $\lvert d_0^{\text{BL}}$ significance$\rvert > 5$ || !GradientLoose isolation)	($\lvert\Delta z_0^{\text{BL}} \sin\theta\rvert > 0.5$ || $\lvert d_0^{\text{BL}}$ significance$\rvert > 3$ || !GradientLoose isolation)

$E_{\text{T}}^{\text{miss}} < 40\,\text{GeV}$ (hereafter referred to as the Fake Factor Region). The events populating the numerator of the fake factor must satisfy all signal selection criteria (see Sect. 8.4), excluding the modified m_{T}^{W} and $E_{\text{T}}^{\text{miss}}$ cuts. The denominator selection is as follows: a loosened baseline object definition designed specifically for the fake factor procedure is described in Table 8.8; the looser definition is necessary to increase the number of fake leptons in the denominator. To mimic the signal region selection, events with ≥ 4 baseline leptons are vetoed, following the same procedure. Denominator events must also satisfy all other selection criteria defining signal events, except that the lepton associated with the W boson must satisfy the denominator-level (anti-id) identification criteria listed in Table 8.9.[7] For the muon-jet overlap removal at denominator level, all muon objects are kept and jets removed for pairs with $\Delta R(\mu, j) < 0.4$. Trigger matching is applied by checking that one of the Tight leptons is matched to a lepton trigger.

The fake factor is calculated using the numerator (Tight) and denominator (Loose) events, and binned as a function of the p_{T} of the lepton associated to the W boson (assumed to be the fake lepton). Figure 8.4 shows the p_{T} distributions of the lepton associated with the W boson for the numerator and denominator selection. For each lepton flavor, two fake factors are computed: one for the W identification selection criteria, and one for the Z identification selection. For calculating the Z identification fake factor, the selection of the W lepton is modified to match the Z identification criteria, and the fake factor measurement is repeated. Because leptons passing the W identification criteria are a subset of the leptons passing the Z identification criteria, the statistical uncertainties of these two fake factors are treated as 100% correlated.

[7] The leptons associated with the Z boson must both pass Tight (Z identification) selection as before.

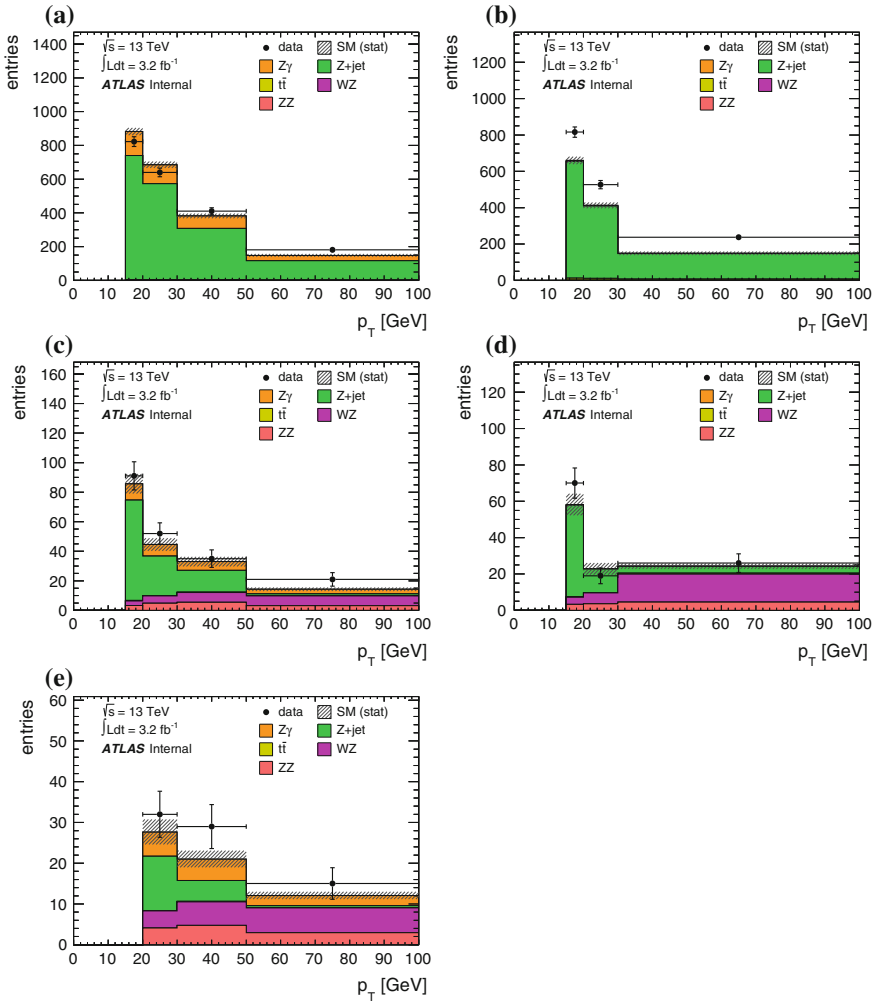

Fig. 8.4 Control distributions for the $Z+\text{jet}/Z\gamma$ Fake Factor Region, showing the p_{T} of the lepton associated with the W boson. This lepton is assumed to be the faking object for the purposes of calculating the fake factors. The p_{T} is shown for the electron anti-id selection (**a**), muon anti-id selection (**b**), electron Z-id selection (**c**), muon W-id and Z-id selection (**d**), and electron W-id selection (**e**). The eee and $e\mu\mu$ channels are used for the electron-id plots, and the μee and $\mu\mu\mu$ channels are used for the muon-id plots. The WZ cross section is scaled up by 1.15 to reflect the Run 1 cross section measurement. Errors are statistical only. The overlap between the Z+jets and $Z\gamma$ simulated samples has been removed

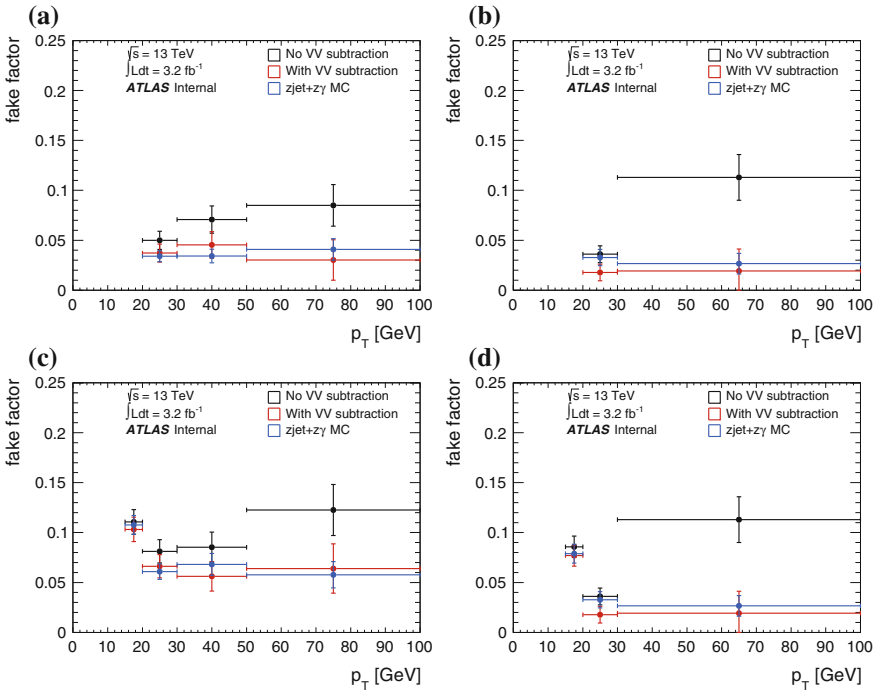

Fig. 8.5 Fake Factors for the electron W selection (**a**), muon W selection (**b**), electron Z selection (**c**), and muon Z selection (**d**), obtained in the $Z + \text{jet}/Z\gamma$ Fake Factor Region. Fake Factors are obtained using the lepton associated with the W boson in this control region. The black entries are the data-driven fake factors before subtracting contamination from WZ and ZZ processes; red entries are the fake factors after subtracting WZ (scaled by 1.15) and ZZ using MC. Blue points show the MC prediction for the fake factor

(It will be shown that this treatment leads to only a small increase in the final fake factor uncertainty.) In the fake factor calculation, events with three real leptons from WZ and ZZ processes are subtracted using MC; for the subtraction, the WZ cross section is scaled up by 1.15 to reflect the Run 1 cross section measurement. Figure 8.5 shows the fake factors plotted as a function of p_{T}, for the W and Z selections of muons and electrons.

A small bias exists in the fake factor calculation for eee and $\mu\mu\mu$ channels. In these events, since two same-flavor, opposite-charge pairs can be formed, the fake lepton assumed to be assigned to the W boson can in fact be assigned to the Z boson. The fake factor is usually binned in the p_{T} of the lepton associated to the W boson, which is assumed to be the fake in this procedure. But due to this mis-assignment, the p_{T} from the real lepton in the event will be used. Furthermore, only LTT events are used in the denominator for the computation of the fake factor, so there are no corresponding mis-assigned events in the denominator. In MC this effect is shown to be small: less than 5% of events that enter into the numerator of the fake factor

calculation have a fake mis-assigned to a Z boson. The effect can thus be safely ignored.

To increase the sample size in the determination of the muon fake factor, the identification of electrons associated to the Z boson in the μee channel is loosened to the LooseLH + BLayer identification criteria, with LooseTrackOnly isolation criteria.

Though the samples are too small to calculate fake factors in bins of $p_{\mathrm{T}} \times \eta$, the η distributions of the fake lepton in the numerator and denominator are compared. Figure 8.6 shows the η distribution of the fake lepton in the denominator and numerator, for electron and muon fakes. In both the electron and muon case, the denominator is slightly more central and the numerator flatter in η. This suggests that the fake factor is larger at high values of $|\eta|$ than at low $|\eta|$. In Sect. 8.5.2.5, it is confirmed that the η distribution where the fake factor is applied is roughly similar to the η distribution of the Z Fake Factor region where it is derived.

To obtain an estimate for the number of $Z + \mathrm{jet}/Z\gamma$ events in the signal region, the fake factor is applied to events in a control region (the "$Z + \mathrm{jet}/Z\gamma$ CR", or ZCR) close to the signal region. Events in the ZCR must satisfy all kinematic event selection and lepton identification criteria, except for one of the three leptons, which must pass the fake factor denominator selection described above. Again, trigger matching is applied by checking that one of the Tight leptons is matched to a trigger lepton. The ZCR consists of three sub-regions: one in which the anti-id lepton is associated with the W boson (LTT), and two in which a misassignment causes the anti-id lepton to be associated with the leading (or subleading) Z lepton (TLT and TTL). Each event can only be counted in one of these regions, because the boson association step is blind to the identification quality of the leptons. All $e\mu\mu$- and μee-channel events falling in the TLT and TTL regions are not considered, because a misassignment in these channels would require the presence of an additional fake object, the odds of which are low. (The events that do show up in the TLT and TTL channels are mainly $t\bar{t}$ events, which are estimated elsewhere.)

The fake factor is applied to events in the ZCR following Eq. 8.13. As implied by Eq. 8.13, WZ and ZZ contamination in the ZCR is subtracted using MC: MC events are collected in the ZCR, and the appropriate fake factor is applied to the MC to get an estimate of the magnitude of the WZ/ZZ component of the fake factor procedure and the shapes of its distributions. This component is subtracted from the nominal fake factor estimate. Similarly, we allude to a procedure to estimate and remove the $t\bar{t}$ and top-like contribution from the estimate. The details of this estimate are described in Sect. 8.5.2.4; for now we refer to this term as $N_{t\bar{t}}$. Then Eq. 8.13 can be rewritten as:

$$N_{SR}^{Z+\mathrm{jet}/Z\gamma} = \sum_{Cat} \sum_{\text{bin } i} \left[N_{ZCR}^{Cat}(i) - N_{t\bar{t}}^{Cat}(i) - N_{MC,WZ/ZZ}^{Cat}(i) \right] \cdot F^{Cat}(i) \qquad (8.14)$$

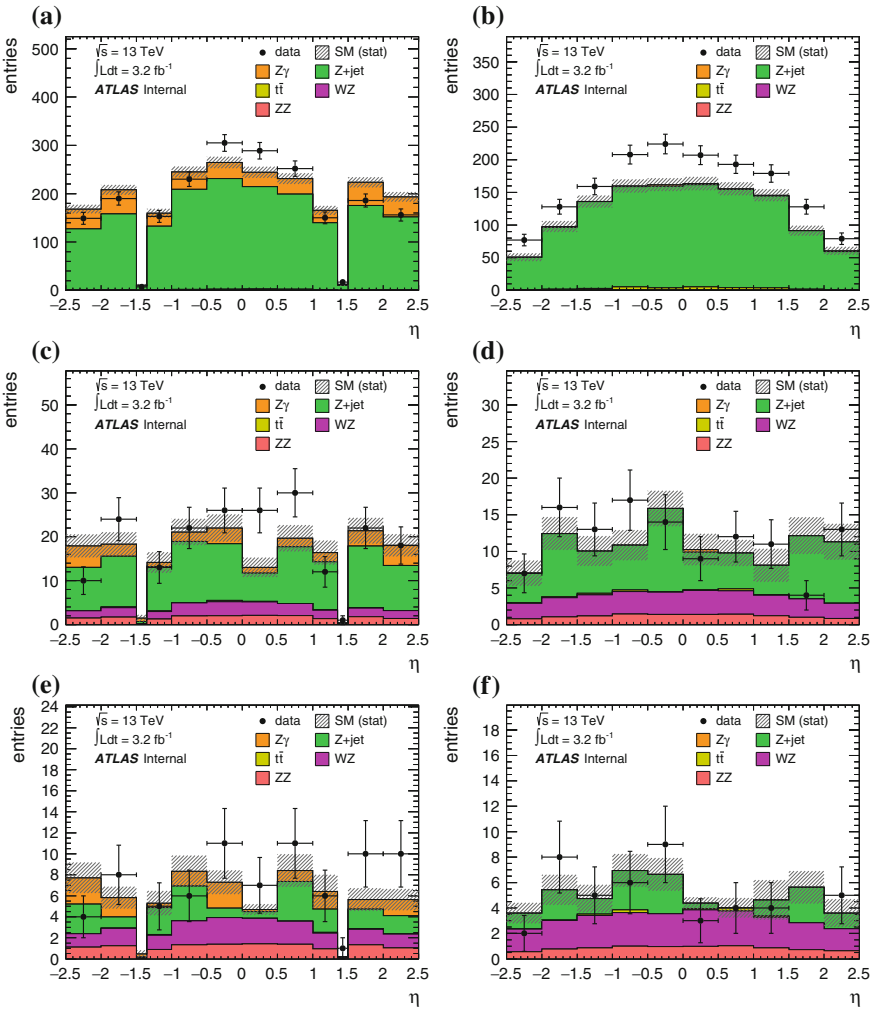

Fig. 8.6 The η distribution of leptons associated with the W boson (the presumed fake lepton) in the Z Fake Factor region. On top is the η distribution of the electron (**a**) and muon (**b**) Loose region, followed by the distribution of Tight electrons passing Z identification criteria (**c**), Tight muons passing Z identification criteria (**d**), Tight electrons passing W identification criteria (**e**), and Tight muons passing W identification criteria (**f**) in the determination of the fake factors

where the sum is taken over i bins of the Loose lepton p_{T}, and the reconstruction categories LTT, TLT, and TTL. The fake factors F^{Cat} are F_W for the LTT region, and F_Z for the TLT and TTL regions.

We can now return to the question of how we justify measuring both Z + jet and $Z\gamma$ reducible backgrounds using the Fake Factor method, and why we choose to exclude $t\bar{t}$ from the method, despite it having two real and one fake lepton as well. Z + jet and $Z\gamma$ processes have different fake compositions (one is enriched in jet-fakes and the other in fakes from photon conversions); however, both should be well represented in the Z Fake Factor Region. Furthermore, as is shown in the following section, the proportion of jet-fakes and photon conversion fakes in the Z Fake Factor Region is similar to that of the signal region, as might be expected, since both Z + jet and $Z\gamma$ should have broadly similar kinematic properties.

By contrast, $t\bar{t}$ events are not represented in the Z Fake Factor region. Furthermore, the fake lepton in a $t\bar{t}$ event typically originates from a leptonically-decaying b-jet from the $t\bar{t}$ decay. Though heavy-flavor fakes are represented in the Z Fake Factor region, the p_{T} of the underlying b-jet in $t\bar{t}$ events is likely much larger than in Z + jet events, which could lead to differences in the true fake factor. Though it is possible to carefully choose an anti-id lepton definition, guided by MC, such that the $t\bar{t}$ and Z + jet/$Z\gamma$ fake factors are similar in all bins of p_{T}, we instead choose to measure the Z + jet/$Z\gamma$ fake factor only, and apply it to a control region enriched in Z + jet/$Z\gamma$ events to obtain our signal region estimate.

8.5.2.3 Closure Test Using MC

The fake factor method is valid only if the fake factor, derived in a fakes-enriched region, accurately describes the behavior of the reducible background events in the ZCR and the signal region. If the composition of the fake leptons in the Fake Factor Region is different from that of the ZCR, or if there are unaccounted-for kinematic differences between the two regions, then the method can lead to an incorrect result.

To test for these effects, an MC closure test is used to evaluate the intrinsic accuracy of the method. The Fake Factor procedure is run on Z + jet and $Z\gamma$ MC samples: a fake factor is calculated in the low-m_{T}^{W}, low-$E_{\mathrm{T}}^{\mathrm{miss}}$ fake factor region. The fake factor then is applied to events in the ZCR to obtain a Z + jet/$Z\gamma$ estimate in the signal region from the method. The estimate is compared to the out-of-the-box MC signal region prediction, as shown in Table 8.10. The fake factor prediction and the raw MC agree within statistical uncertainty in each channel, and the agreement between reconstruction-level categories and their corresponding truth-level categories is good as well.

The closure test lends support to the assertion that a fake factor derived in the Fake Factor region is applicable to Z + jet/$Z\gamma$ events in the SR. Effects due to composition that cause a difference between the true fake factor and the one measured in the Fake Factor Region are handled using a systematic uncertainty procedure described in Sect. 8.5.2.6.

Table 8.10 $Z + \text{jet}/Z\gamma$ closure test showing the estimate given by performing the full fake factor method using an all-MC procedure (top), compared to the out-of-the-box estimate from MC in the signal region (bottom). The first uncertainty is the statistical uncertainty from the ZCR; the second error term is the statistical uncertainty propagated from the fake factors F. The truth categorization does not add up in the eee channel due to a failure to classify all three leptons during truth classification

Channels	eee	$e\mu\mu$	μee	$\mu\mu\mu$	All
$N_{LTT} \cdot F$	$8.37 \pm 0.33 \pm 1.00$	$11.53 \pm 0.44 \pm 1.37$	$4.80 \pm 0.28 \pm 1.01$	$6.40 \pm 0.37 \pm 1.36$	$31.10 \pm 0.72 \pm 3.36$
$N_{TLT} \cdot F$	$0.53 \pm 0.10 \pm 0.08$	–	–	$0.17 \pm 0.06 \pm 0.04$	$0.70 \pm 0.12 \pm 0.09$
$N_{TTL} \cdot F$	$2.42 \pm 0.29 \pm 0.17$	–	–	$1.97 \pm 0.30 \pm 0.22$	$4.38 \pm 0.41 \pm 0.28$
Total	$11.32 \pm 0.45 \pm 1.20$	$11.53 \pm 0.44 \pm 1.37$	$4.80 \pm 0.28 \pm 1.01$	$8.54 \pm 0.48 \pm 1.55$	$36.19 \pm 0.84 \pm 3.63$
N_{FRR}	9.42 ± 1.71	10.46 ± 1.98	4.16 ± 1.52	6.75 ± 2.22	30.79 ± 3.75
N_{RFR}	0.27 ± 0.16	0	0	0	0.27 ± 0.16
N_{RRF}	2.02 ± 0.91	0	0	0.90 ± 0.61	2.93 ± 1.09
MC (Z + jet +$Z\gamma$)	11.57 ± 1.96	10.46 ± 1.98	4.16 ± 1.52	7.65 ± 2.30	33.84 ± 3.92

Table 8.11 $t\bar{t}$ control regions, parallel to the ZCR, for subtracting the $t\bar{t}$ contribution in the Z + jet/$Z\gamma$ control region. The rows represent the flavor of the leptons associated with a Z boson, allowing for different-flavor, opposite-sign pairs to be associated with the Z. The columns show the possible flavor and charge of the lepton associated with the W boson. Channels with a "-" contain $\ell^+\ell^-$ pairs, and thus they are excluded from the top-CRs to avoid Z/γ^* contamination

	$e^{\pm}$	$e^{\mp}$	$\mu^{\pm}$	$\mu^{\mp}$
$e^{\pm}e^{\mp}$	ZCR	ZCR	ZCR	ZCR
$e^{\pm}\mu^{\mp}$	$t\bar{t}$ CR (e)	–	–	$t\bar{t}$ CR (μ)
$\mu^{\pm}e^{\mp}$	-	$t\bar{t}$ CR (e)	$t\bar{t}$ CR (μ)	–
$\mu^{\pm}\mu^{\mp}$	ZCR	ZCR	ZCR	ZCR

8.5.2.4 Calculating and Subtracting the $t\bar{t}$ Contribution in the ZCR

Because the fake factor is derived in a region enriched in Z + jet/$Z\gamma$ events, and because it has not been shown that that this fake factor is applicable to $t\bar{t}$ and top-like (Wt and WW) events, the contribution to the total fake factor estimate due to top-like events in the ZCR must be removed, such that the fake factor procedure estimates only the Z + jet/$Z\gamma$ contribution in the signal region. The estimate of $t\bar{t}$ and top-like events in the SR is described earlier in Sect. 8.5.1.

Equation 8.14 depicts how the top-like component is removed in the fake factor procedure. MC simulation is used to predict the shape of top-like backgrounds in the ZCR; however, to avoid relying on the MC to faithfully predict the fake rates of objects faking leptons, we normalize the top-like MC to data in a control region similar to the ZCR, but enriched in $t\bar{t}$ events. The control region's construction is nearly identical to the one used to estimate top-like backgrounds in the signal region, described in Sect. 8.5.1. For this control region, all ZCR requirements are imposed (including the requirement of one Loose and two Tight leptons, and considering LTT, TLT and TTL event topologies), except that a different-flavor, opposite-charge pair is required in place of a SFOC pair. As before, the DFOS pair with the smallest $\Delta m = |m_{\ell\ell} - m_Z|$ is associated with the Z boson, and events are excluded if they include any same-flavor, opposite-charge pair to avoid contamination from Z/γ^* events. Four channels remain: $\mu^{\pm}e^{\mp}\mu^{\pm}$, $\mu^{\pm}\mu^{\pm}e^{\mp}$, $e^{\pm}e^{\pm}\mu^{\mp}$, and $e^{\pm}\mu^{\mp}e^{\pm}$. This region is referred to as the top-CR parallel to the ZCR, or top-CR||ZCR. As with the top-CR||SR, the top-CR||ZCR is split into two sub-regions, for e-fake and μ-fake events. Table 8.11 summarizes the ZCR and parallel top-like control regions used.

From the events in the top-CR||ZCR we then derive two global data-MC scale factors: one for events with a fake electron ($SF^{e}_{t\bar{t}}$) and one for fake muon events ($SF^{\mu}_{t\bar{t}}$). We use events in the top-CR||ZCR from LTT, TLT and TTL regions added together. The scale factor in this region is:

$$SF_{t\bar{t}} = \frac{N_{\text{data}} - N^{\text{MC}}_{\text{other}}}{N^{MC}_{t\bar{t}}} \tag{8.15}$$

The top component that we subtract from the fake factor procedure is estimated using top-like ($t\bar{t} + Wt + WW$) MC, multiplied by this scale factor (individually for

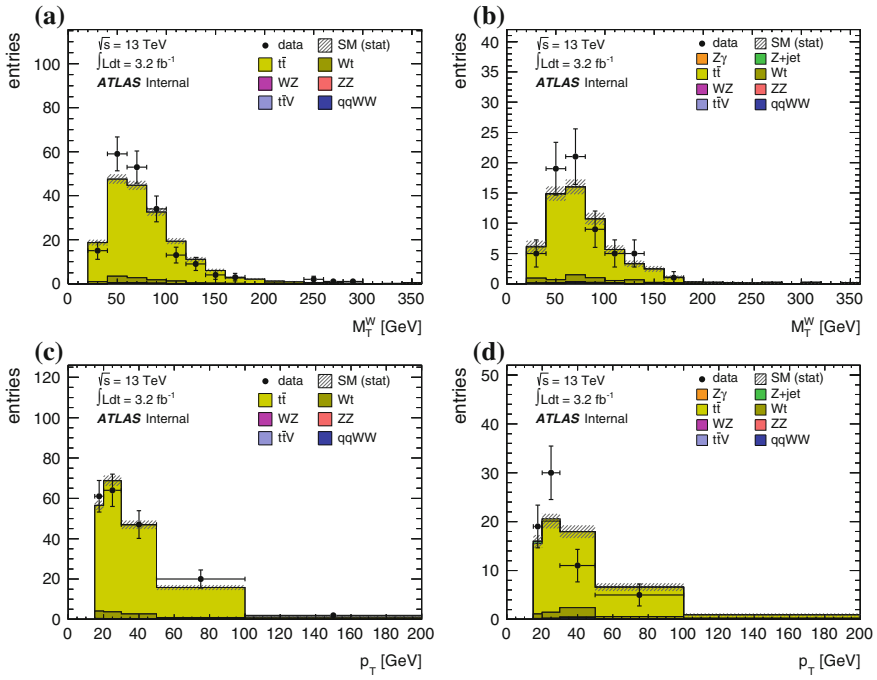

Fig. 8.7 Data-MC agreement in the top control region parallel to the ZCR, combining the LTT, TLT and TTL regions of the top-CR||ZCR. The m_{T}^{W} distribution (**a**) and the p_{T} of the fake lepton (**c**) are shown for the $\mu^{\pm}e^{\mp}\mu^{\pm} + \mu^{\pm}\mu^{\pm}e^{\mp}$ channels, while (**b**) and (**d**) show the same distributions for the $e^{\pm}e^{\pm}\mu^{\mp} + e^{\pm}\mu^{\mp}e^{\pm}$ channels

the μ-fake and e-fake terms). Equation 8.14 can be updated to include this scale factor:

$$N_{SR}^{Z+\mathrm{jet}/Z\gamma} = \sum_{Cat} \sum_{\mathrm{bin}\ i} \left[N_{ZCR}^{Cat}(i) - SF_{t\bar{t}}^{e} \cdot N_{MC,t\bar{t}}^{Cat,e-fake}(i) - SF_{t\bar{t}}^{\mu} \cdot N_{MC,t\bar{t}}^{Cat,\mu-fake}(i) - N_{MC,WZ/ZZ}^{Cat}(i) \right] \cdot F^{Cat}(i) \tag{8.16}$$

In the ZCR, eee events and LTT $e\mu\mu$ events are identified as having an electron fake, and $\mu\mu\mu$ and LTT μee events are identified as having a muon fake.

Figure 8.7 shows the data-MC comparison in the top-CR||ZCR (where the scale factors are derived), in each of the LTT, TLT, and TTL regions, combining e-fake and μ-fake regions. Table 8.12 shows the data and top-like MC yields in this control region—less than one event is predicted by MC for all other processes. The good agreement between data and $t\bar{t}$ $(+Wt)$ MC in both the total yield and the kinematic shapes suggests that fake lepton rates and kinematics in top-like events are well-modeled by MC.

The scale factor for μ-fake channels is estimated to be 1.03 ± 0.08; the e-fake channel scale factor is 1.05 ± 0.14; the errors represent the statistical error of both the data and the top-like MC. These scale factors are applied to top-like MC in the

Table 8.12 MC prediction and data in the top-like ($t\bar{t} + Wt + WW$) control regions parallel to the ZCR ($\mu^{\pm}e^{\mp}\mu^{\pm} + \mu^{\pm}\mu^{\pm}e^{\mp}$ and $e^{\pm}e^{\pm}\mu^{\mp} + e^{\pm}\mu^{\mp}e^{\pm}$). Less than one event is predicted by MC for all other processes, so they are ignored here. The data-MC scale factors for this region are shown in the last row

Channels	$\mu^{\pm}e^{\mp}\mu^{\pm} + \mu^{\pm}\mu^{\pm}e^{\mp}$	$e^{\pm}e^{\pm}\mu^{\mp} + e^{\pm}\mu^{\mp}e^{\pm}$	All
N_{LTT}, data	124.00 ± 11.14	32.00 ± 5.66	156.00 ± 12.49
N_{TLT}, data	14.00 ± 3.74	7.00 ± 2.65	21.00 ± 4.58
N_{TTL}, data	56.00 ± 7.48	26.00 ± 5.10	82.00 ± 9.06
Total, data	194.00 ± 13.93	65.00 ± 8.06	259.00 ± 16.09
N_{LTT}, top-like MC	113.73 ± 3.28	32.66 ± 1.77	146.39 ± 3.72
N_{TLT}, top-like MC	12.57 ± 1.10	5.23 ± 0.69	17.79 ± 1.30
N_{TTL}, top-like MC	62.26 ± 2.43	22.97 ± 1.45	85.23 ± 2.83
Total, top-like MC	188.56 ± 4.22	60.85 ± 2.39	249.41 ± 4.85
Total, other MC	0.57 ± 0.05	0.82 ± 0.12	1.38 ± 0.13
Data/MC scale factor	1.03 ± 0.08	1.05 ± 0.14	–

ZCR, along with the fake factor, to estimate and subtract the undesirable top-like component of the fake factor procedure.

8.5.2.5 Results of the $Z + \text{jet}/Z\gamma$ Fake Factor Estimate

The following section summarizes the $Z + \text{jet}/Z\gamma$ fake factor estimate in the signal region. The event yields in the ZCR ($m_{\text{T}}^{W} > 30\,\text{GeV}$, with one anti-id lepton and two ID leptons) are presented in the following figures: Fig. 8.8 shows the m_{T}^{W} distribution of events in the ZCR, in the LTT region only. Figures 8.9 and 8.10 show the ZCR events in the TLT and TTL regions, respectively. The p_{T} of the fake lepton is shown for the LTT, TLT and TTL regions in Figs. 8.11, 8.12, and 8.13, respectively. Events in these regions (excluding TLT and TTL events from the $e\mu\mu$ and μee channels) will be multiplied by the $Z + \text{jet}/Z\gamma$ fake factor to obtain the raw fake estimate, before WZ/ZZ or $t\bar{t}$ subtraction.

We can now address the question of how $Z + \text{jet}/Z\gamma$ events can enter into the TLT and TTL regions of the ZCR. This can happen in one of two ways. In the first case the boson association in the event selection successfully pairs the leptons with their parent W and Z bosons; in this scenario, the fake lepton passes the Tight identification selection and a real lepton fails Tight (and is classified as Loose). The chance of a fake lepton passing tight and a real one failing Tight is $fe\bar{e}$, roughly two orders of magnitude lower than the chances of the fake being Loose and the real passing Tight ($\bar{f}ee$, the main contributor to the ZCR). (The conclusions drawn are contingent on the fact that f and $\bar{e}$ are both small.)

The second scenario in which a $Z + \text{jet}/Z\gamma$ event falls into the TLT or TTL region is one in which the fake lepton is Loose, the real leptons pass Tight, but the fake

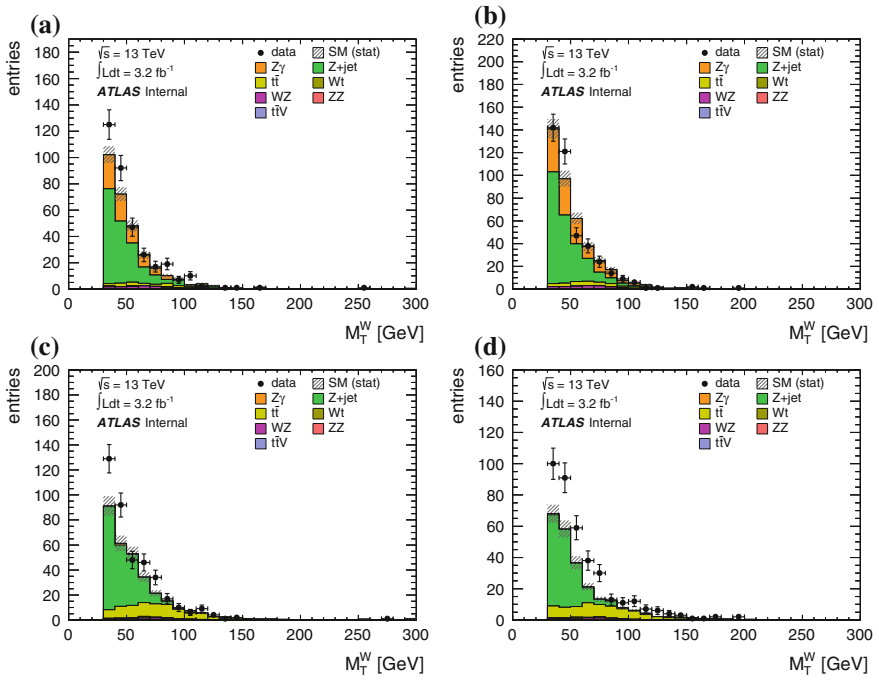

Fig. 8.8 Data-MC agreement in the ZCR LTT control region, in the m_{T}^{W} variable. The eee (**a**), $e\mu\mu$ (**b**), $\mu\mu\mu$ (**c**) and μee (**d**) channels are depicted

lepton is mistakenly paired with one of the real leptons and associated with the Z boson. The probability of this lepton classification is $\bar{f}ee$ (like the LTT region), but the misassignment probability is unknown. (There is another scenario in which a real lepton in the $Z + \mathrm{jet}/Z\gamma$ event is lost, and two fake leptons are identified, but the chances of this are even more remote.)

However, we can plot the $m_{\ell\ell}$ spectrum of the alternate pair (the same-flavor opposite-sign pair that was not picked by event selection) to understand this effect. Figure 8.14 shows the alternate $m_{\ell\ell}$ spectrum in the TLT+TTL region (and in the LTT region, for comparison).

In the LTT region, this quantity is spread over a range of around [0,250] GeV. In the TLT+TTL region, an otherwise diffuse spectrum is punctuated by a peak near the PDG Z mass. The MC supports the hypothesis that these are $Z + \mathrm{jet}/Z\gamma$ events, and the diffuse spectrum below are from $t\bar{t}$ and WZ. These plots support the conclusion that most $Z + \mathrm{jet}/Z\gamma$ events in the TLT and TTL regions originate from a misassignment in the boson association algorithm, rather than the scenario in which the fake lepton is classified as Tight and a real lepton is Loose. Note that this knowledge does not change how we treat these events in the fake factor procedure; rather, it is simply an exercise to understand how these events are classified, and to

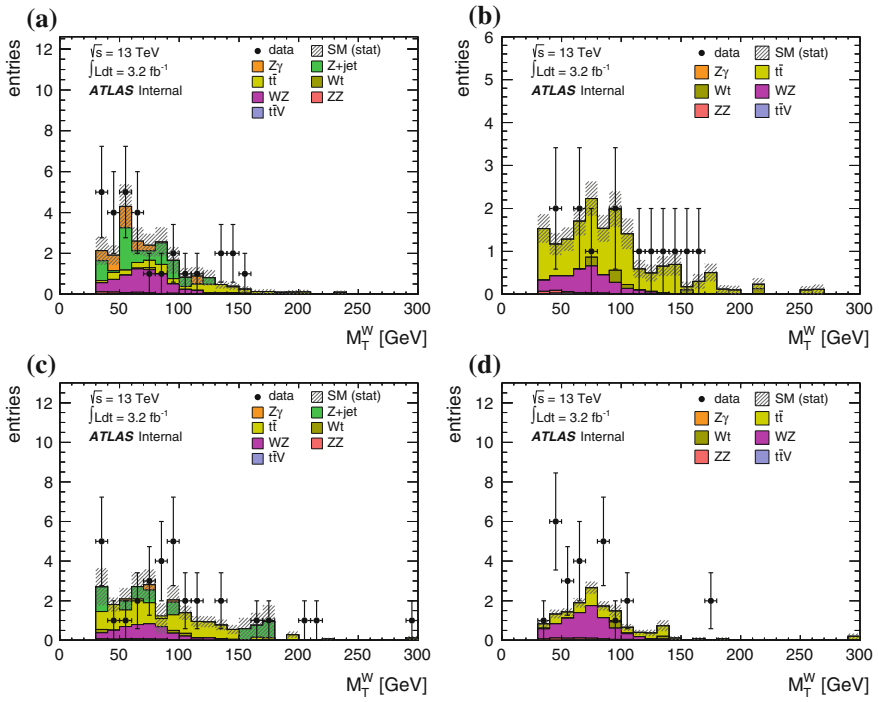

Fig. 8.9 Data-MC agreement in the ZCR TLT control region, in the m_T^W variable. The eee (**a**), $e\mu\mu$ (**b**), $\mu\mu\mu$ (**c**) and μee (**d**) channels are depicted. Only eee and $\mu\mu\mu$ channels are used in the $Z + \text{jet}/Z\gamma$ estimate; $e\mu\mu$ and μee, which have have no $Z + \text{jet}$ or $Z\gamma$ contribution, are shown for completeness

emphasize the importance of considering boson misassignment in the $Z + \text{jet}/Z\gamma$ background.

To check for potential effects in the η distributions of leptons, we plot in Fig. 8.15 the η of loose electrons and muons in all channels. The η spectra can be compared with η control distributions from the Z Fake Factor Region of Fig. 8.6; the η shapes of loose electrons in the ZCR look compatible with loose (denominator) electrons in the Fake Factor Region, and the loose muons look compatible (if slightly more central). Because the η distributions do not vary significantly from the Fake Factor Region to the ZCR, the η dependence of the fake factors is neglected.

Table 8.13 shows the result of multiplying the events in the ZCR by the p_T-binned fake factor. In this table, corrections from signal WZ, $t\bar{t}$ and top-like contamination are not yet subtracted.

Table 8.14 shows the magnitude of the WZ/ZZ subtraction in each channel: WZ/ZZ MC in the ZCR (with WZ scaled up by 1.15 to match the Run 1 result) is multiplied by the p_T-dependent fake factor to estimate this contribution, to be subtracted from the result of Table 8.13. A 15% systematic uncertainty is assigned

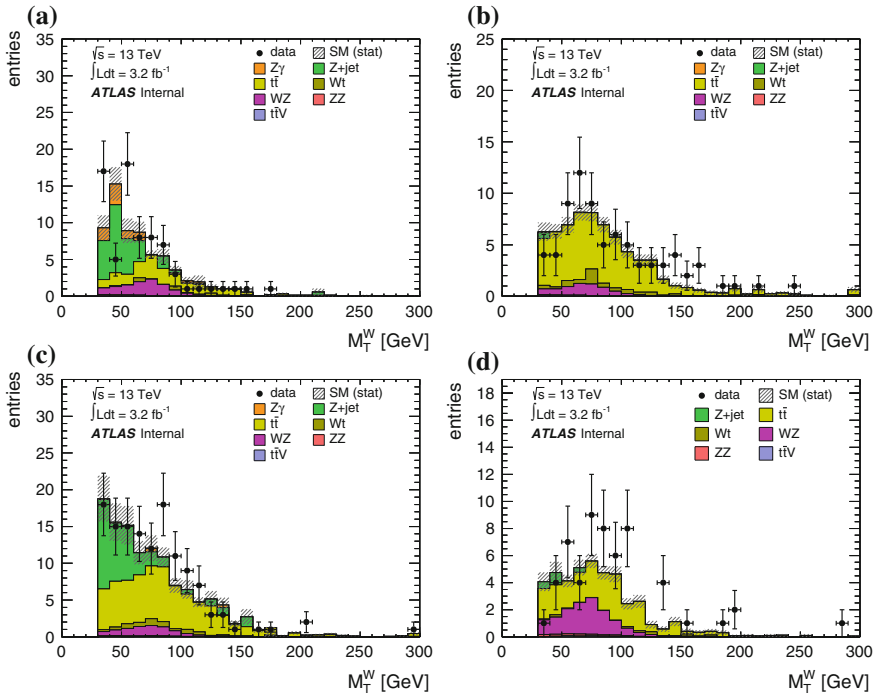

Fig. 8.10 Data-MC agreement in the ZCR TTL control region, in the m_{T}^{W} variable. The eee (**a**), $e\mu\mu$ (**b**), $\mu\mu\mu$ (**c**) and μee (**d**) channels are depicted. Only eee and $\mu\mu\mu$ channels are used in the $Z + \text{jet}/Z\gamma$ estimate; $e\mu\mu$ and μee, which have have no $Z + \text{jet}$ or $Z\gamma$ contribution, are shown for completeness

on the subtracted WZ/ZZ fake factor component (hereafter referred to as the "ZCR WZ Subtraction" uncertainty).

Table 8.15 shows the magnitude of the top-like correction in each channel. Top-like ($t\bar{t} + Wt + WW$) MC, corrected by the scale factors derived in Sect. 8.5.2.4, are multiplied by the fake factor to estimate the magnitude of $t\bar{t}$ and top-like component of the fakes estimate. The top-like contamination in the $Z + \text{jet}/Z\gamma$ estimate, after applying fake factors, is 14, 7, 19 and 35% in the eee, $e\mu\mu$, μee, and $\mu\mu\mu$ channels, respectively, and 18% overall.

Table 8.16 shows the final $Z + \text{jet}/Z\gamma$ reducible background estimate, with components from top-like and residual WZ/ZZ contamination subtracted. The final estimate for the $Z + \text{jet}/Z\gamma$ background is $45.12 \pm 1.54 \pm 9.59$ events. The first uncertainty is the statistical uncertainty from data and MC in the ZCR; the second error term is the statistical uncertainty propagated from the fake factors $F(i)$, and evaluated as described in Sect. 8.5.2.6. Systematic uncertainties on the $Z + \text{jet}/Z\gamma$ fake factor method are summarized in the following section.

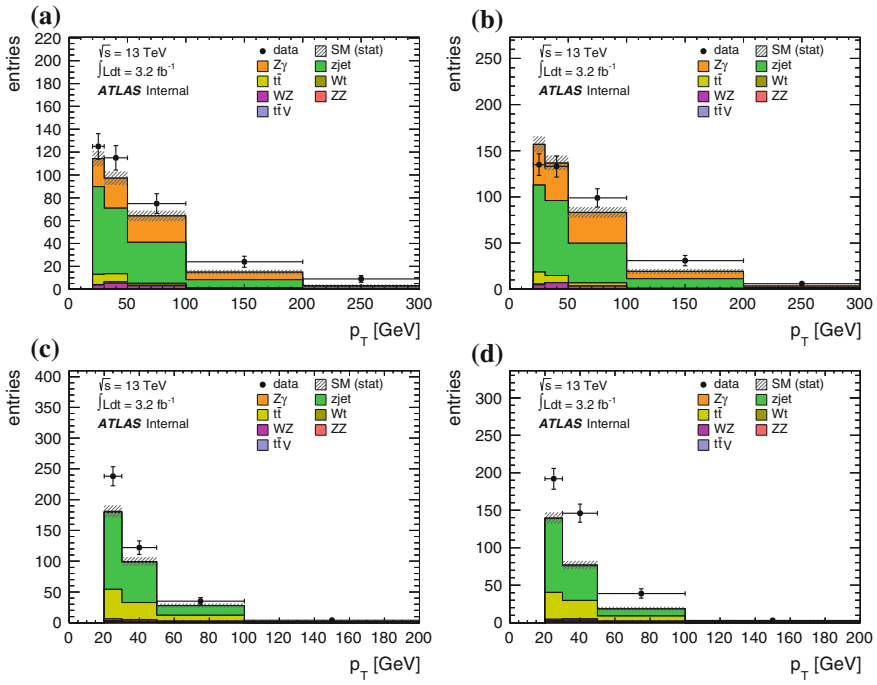

Fig. 8.11 Data-MC agreement in the ZCR LTT control region, binned in the p_{T} of the Loose lepton. The *eee* (**a**), $e\mu\mu$ (**b**), $\mu\mu\mu$ (**c**) and μee (**d**) channels are depicted

8.5.2.6 Uncertainties on the Fake Factor Method

This section provides a summary of the statistical and systematic uncertainties on the $Z + \text{jet}/Z\gamma$ fake factor estimate. First, the calculation of the fake factor has a fairly large statistical uncertainty coming from data events. This uncertainty (the "Z muon/electron FF stat" uncertainty) is propagated to the final $Z + \text{jet}/Z\gamma$ estimate when the fake factor is applied to the ZCR: each fake factor bin (of four electron and three muon bin, making seven variations) is varied independently by its statistical uncertainty. (Bins of Z-identification fake factors F_Z and W-identification fake factors F_W are taken to be 100% correlated.) The effect on the final $Z + \text{jet}/Z\gamma$ SR estimate is calculated for each variation, and the resulting seven statistical uncertainties are added in quadrature. The effect of treating the F_Z and F_W as 100% correlated can be seen in Table 8.16: in the *eee* channel, this amounts to the difference between adding the 2.79, 0.25 and 0.31 event uncertainties in quadrature (totaling 2.82 uncertainty on the number of events) and taking them as 100% correlated (a 3.35 event uncertainty). Similarly, the difference in the $\mu\mu\mu$ channel is a 2.97 (quadrature) versus a 3.59 event uncertainty. The difference is small and the most conservative approach (fully correlated) is chosen.

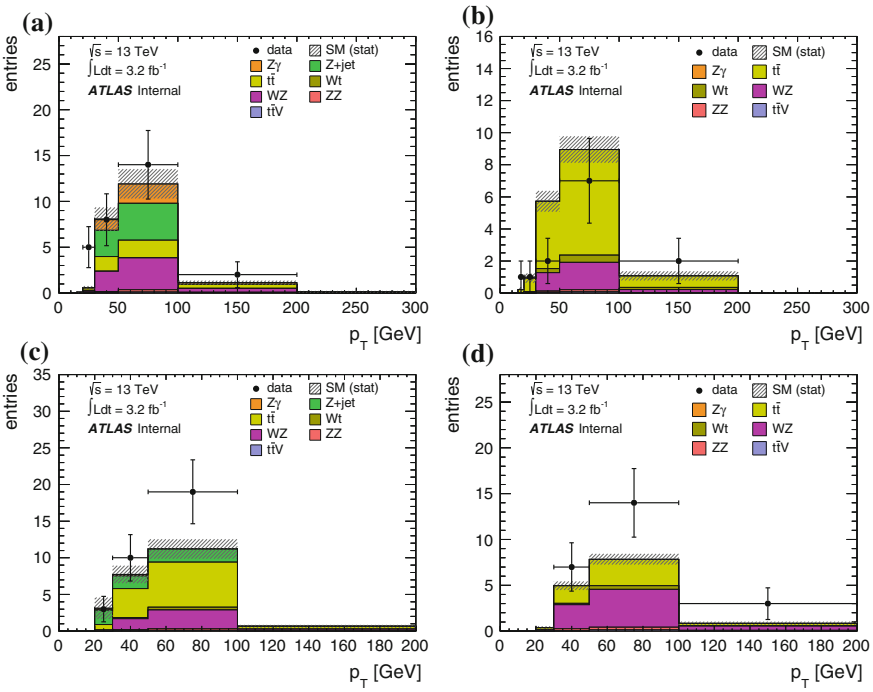

Fig. 8.12 Data-MC agreement in the ZCR TLT control region, binned in the p_T of the Loose lepton. The eee (**a**), $e\mu\mu$ (**b**), $\mu\mu\mu$ (**c**) and μee (**d**) channels are depicted. Only eee and $\mu\mu\mu$ channels are used in the $Z+\text{jet}/Z\gamma$ estimate; $e\mu\mu$ and μee, which have have no $Z+\text{jet}$ or $Z\gamma$ contribution, are shown for completeness

The fake factors also have an uncertainty associated with the subtraction of the WZ and ZZ contamination in the Fake Factor Region and the ZCR. This is assessed by varying the MC WZ and ZZ global yield estimate by 15% in the fake factor numerator, and in the ZCR (assuming 100% correlation among channels), and calculating the overall effect on the fake factor estimate. Table 8.17 shows the breakdown of this systematic uncertainty in the Z FF region. The ZCR WZ/ZZ systematic is assessed independently; it is much smaller, and is summarized in the final summary table.

The fake factor procedure has uncertainties associated with the subtraction of the top-like component in the ZCR. The statistical uncertainty on the data-MC scale factor derived in the top-CR parallel to the ZCR is propagated to the final estimate. The statistical uncertainties of the data and MC in the top-CR||ZCR, and the statistical uncertainty of the MC in the ZCR, are propagated through the fake factor method to the final result. There is also an uncertainty related to the use of MC to extrapolate from the top-CR||ZCR to the ZCR; this uncertainty is described in its own dedicated section, Sect. 8.5.3.

Finally, a systematic on the closure of the $Z+\text{jet}/Z\gamma$ fake factor method is assessed. This systematic concerns issues of composition, kinematics, or any effect

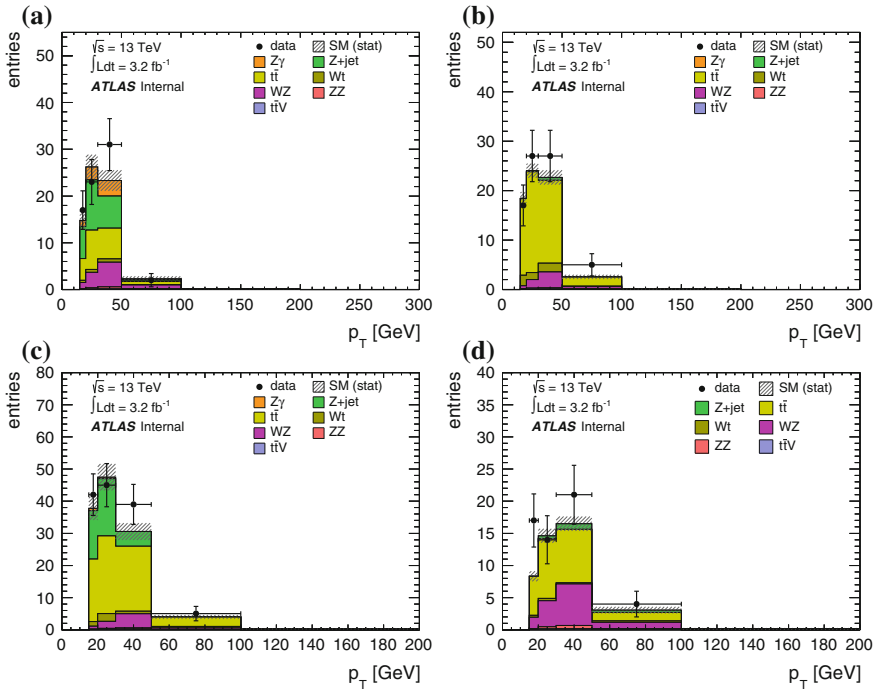

Fig. 8.13 Data-MC agreement in the ZCR TTL control region, binned in the p_{T} of the Loose lepton. The eee (**a**), $e\mu\mu$ (**b**), $\mu\mu\mu$ (**c**) and μee (**d**) channels are depicted. Only eee and $\mu\mu\mu$ channels are used in the $Z+\text{jet}/Z\gamma$ estimate; $e\mu\mu$ and μee, which have have no $Z+\text{jet}$ or $Z\gamma$ contribution, are shown for completeness

that would cause the fake factor measured in the Z Fake Factor Region to differ from the "true" fake factor in the signal region. To assess this uncertainty, the "true" fake factor is calculated using MC: a MC fake factor is calculated in the signal region, instead of the Z Fake Factor Region, and the full difference between this fake factor and the MC fake factor in the Z Fake Factor Region is taken as the systematic uncertainty.

The closure/composition systematic is assessed separately for W and Z identification criteria. For the W identification, a signal region fake factor is developed using LTT events in the ZCR as the denominator, binned according to the p_{T} of the W-associated lepton, and TTT events in the SR in which the W-matched lepton is labeled as fake by the truth record (also binned in the p_{T} of the W-associated lepton). For the true fake factor of the Z identification, ideally TLT and TTL events would comprise the denominator, and only TTT events in which one of the Z-matched leptons is the fake would enter the numerator; however, due to poor MC statistics, all three regions are used for the denominator (LTT, TLT, TTL) and numerator (FRR, RFR, RRF), and binned by the loose (denominator) or fake (numerator) lepton p_{T}.

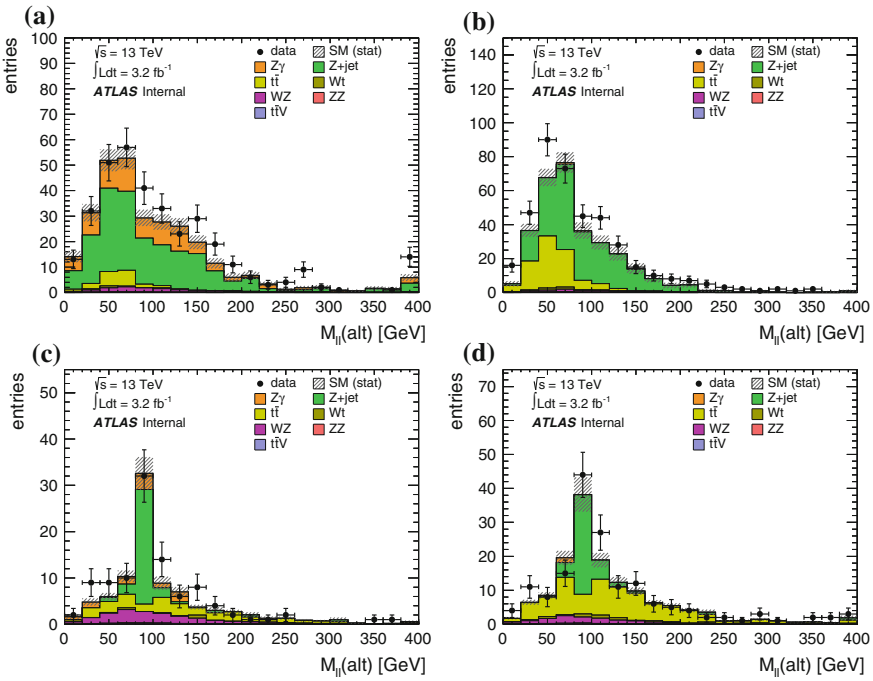

Fig. 8.14 The invariant mass of the same-flavor, opposite-sign dilepton pair that was not the pair associated with the Z boson during event selection. This variable is referred to as the alternate $m_{\ell\ell}$ pair (or $m_{\ell\ell}$(alt) in the plots), and does not exist for μee or $e\mu\mu$ events. The plots depict the alternate $m_{\ell\ell}$ in the ZCR: the LTT region in the eee channel (**a**), the LTT region in the $\mu\mu\mu$ channel (**b**), the TLT and TTL regions (added) in the eee channel (**c**), and the TLT and TTL (added) regions in the $\mu\mu\mu$ channel

Figure 8.16 shows the comparison between the nominal and signal region fake factors, both using MC simulation of $Z+$jet and $Z\gamma$ events. The difference between the two is taken as the systematic uncertainty due to composition and non-closure; the uncertainties range from 20–65%, depending on the p_{T} bin of the fake lepton. The uncertainties, propagated through the fake factor procedure, are summarized in Table 8.18.

Finally, the systematic uncertainty treatment of the extrapolation between the top-CR and the ZCR for the estimate of the top-like component is discussed in the next section. All $Z+$ jet/$Z\gamma$ estimate uncertainties are summarized together with the top-like signal region estimate uncertainties in Sect. 8.5.4.

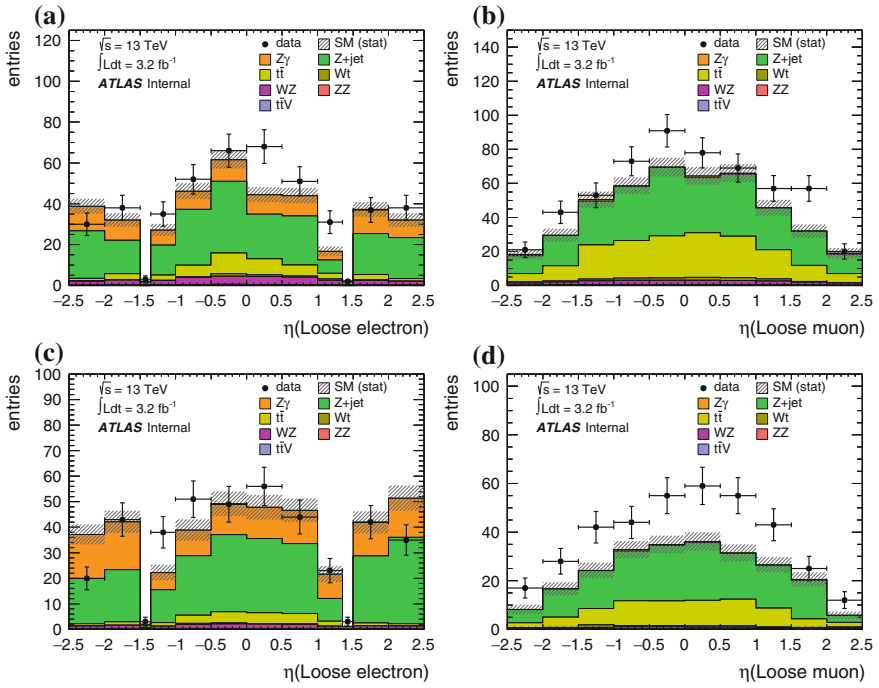

Fig. 8.15 η distributions of Loose leptons in the ZCR. Distributions include the Loose electrons in the LTT+TLT+TTL regions of the *eee* channel (**a**), the Loose muons in the LTT+TLT+TTL regions of the $\mu\mu\mu$ channel (**b**), Loose electrons in the LTT region of the $e\mu\mu$ channel (**c**), and Loose muons in the LTT region of the μee channel (**d**)

8.5.2.7 Comparison of $t\bar{t}$ Components in the SR Estimate and the Fake Factor Method

As part of the $Z + \text{jet}/Z\gamma$ fake factor estimate, top-like contamination in the ZCR must be subtracted using a dedicated procedure. Recall also that an estimate of $t\bar{t}$ and top-like events in the signal region, in a dedicated CR enriched in $t\bar{t}$ events, was presented in Sect. 8.5.1. It is natural to compare the two top estimates, and reflect on the reasons for developing separate $Z + \text{jet}/Z\gamma$ and top-like CRs, instead of using an inclusive ($Z + \text{jet}/Z\gamma$ and $t\bar{t}$) fake factor estimate using the ZCR, like the one presented in the 8 TeV ATLAS result [7].

Table 8.19 shows the estimate of the top-like component estimated in the ZCR, multiplied by the fake factor and by the scale factors derived in the top-CR||ZCR. The $e\mu\mu$- and μee-channel events in TLT and TTL regions have been restored, because an inclusive fake factor estimate would include these regions in order to capture all of the top-like background. The total, 15.61, can be considered a reasonable proxy for a $t\bar{t}$ Fake Factor estimate. The prediction is 70% larger than the 9.16 estimate from the top-CR signal region estimate, but both have fairly large statistical uncertainties.

Table 8.13 Fake factor results, without top-like or WZ/ZZ subtraction terms. Events in the ZCR are multiplied by the p_{T}-dependent fake factor to obtain the reported estimate in the signal region. The first uncertainty is the statistical uncertainty from the ZCR; the second error term is the statistical uncertainty propagated from the fake factors $F(i)$, and evaluated as described in Sect. 8.5.2.6

Channels	eee	$e\mu\mu$	μee	$\mu\mu\mu$	All
$N_{LTT} \cdot F$	$13.47 \pm 0.73 \pm 3.04$	$15.65 \pm 0.78 \pm 3.71$	$8.25 \pm 0.43 \pm 4.39$	$8.38 \pm 0.43 \pm 4.02$	$45.76 \pm 1.23 \pm 10.76$
$N_{TLT} \cdot F$	$1.78 \pm 0.33 \pm 0.44$	–	–	$0.80 \pm 0.14 \pm 0.63$	$2.58 \pm 0.36 \pm 0.77$
$N_{TTL} \cdot F$	$5.15 \pm 0.62 \pm 0.57$	–	–	$5.17 \pm 0.54 \pm 1.12$	$10.32 \pm 0.82 \pm 1.26$
Total	$20.39 \pm 1.01 \pm 3.83$	$15.65 \pm 0.78 \pm 3.71$	$8.25 \pm 0.43 \pm 4.39$	$14.35 \pm 0.70 \pm 5.63$	$58.65 \pm 1.52 \pm 12.52$

Table 8.14 WZ/ZZ correction in the ZCR: MC WZ/ZZ events in the ZCR regions, multiplied by the corresponding p_{T}-dependent fake factor. The first uncertainty is the statistical uncertainty from the WZ/ZZ MC in the ZCR; the second error term is the statistical uncertainty propagated from the fake factors $F(i)$, and evaluated as described in Sect. 8.5.2.6

Channels	eee	$e\mu\mu$	μee	$\mu\mu\mu$	All
$N_{LTT} \cdot F$	$0.48 \pm 0.01 \pm 0.11$	$0.61 \pm 0.01 \pm 0.13$	$0.16 \pm 0.00 \pm 0.10$	$0.21 \pm 0.00 \pm 0.13$	$1.46 \pm 0.01 \pm 0.34$
$N_{TLT} \cdot F$	$0.41 \pm 0.01 \pm 0.12$	–	–	$0.12 \pm 0.00 \pm 0.10$	$0.53 \pm 0.01 \pm 0.15$
$N_{TTL} \cdot F$	$0.75 \pm 0.01 \pm 0.10$	–	–	$0.25 \pm 0.01 \pm 0.12$	$1.01 \pm 0.02 \pm 0.15$
Total	$1.64 \pm 0.02 \pm 0.29$	$0.61 \pm 0.01 \pm 0.13$	$0.16 \pm 0.00 \pm 0.10$	$0.58 \pm 0.01 \pm 0.35$	$2.99 \pm 0.02 \pm 0.62$

Table 8.15 The $t\bar{t}$ correction component for the ZCR. The corrected total refers to the MC prediction multiplied by the scale factors shown in Table 8.12, and also multiplied by the fake factor. The first uncertainty is the statistical uncertainty from the $t\bar{t}$ MC in the ZCR; the second error term is the statistical uncertainty propagated from the fake factors $F(i)$, and evaluated as described in Sect. 8.5.2.6. The scale factor uncertainty below is the statistical error on the μ-fake and e-fake $t\bar{t}$ data-MC scale factors, propagated to the fake factor result

Channels	eee	$e\mu\mu$	μee	$\mu\mu\mu$	Total
$N_{LTT} \cdot F$	$0.86 \pm 0.06 \pm 0.16$	$1.05 \pm 0.06 \pm 0.19$	$1.60 \pm 0.06 \pm 0.83$	$1.96 \pm 0.07 \pm 0.97$	$5.46 \pm 0.12 \pm 1.83$
$N_{TLT} \cdot F$	$0.29 \pm 0.04 \pm 0.07$	–	–	$0.30 \pm 0.03 \pm 0.25$	$0.60 \pm 0.05 \pm 0.26$
$N_{TTL} \cdot F$	$1.67 \pm 0.11 \pm 0.17$	–	–	$2.81 \pm 0.12 \pm 0.64$	$4.47 \pm 0.17 \pm 0.66$
Total	$2.82 \pm 0.13 \pm 0.37$	$1.05 \pm 0.06 \pm 0.19$	$1.60 \pm 0.06 \pm 0.83$	$5.07 \pm 0.14 \pm 1.81$	$10.54 \pm 0.21 \pm 2.69$

Table 8.16 Final estimate of the number of events in the signal region predicted by the $Z + \text{jet}/Z\gamma$ fake factor method. The estimate includes corrections for $t\bar{t}$ and residual WZ/ZZ described in the text. The first uncertainty is the statistical uncertainty from the $t\bar{t}$ MC, WZ/ZZ MC, and data in the ZCR; the second error term is the statistical uncertainty propagated from the fake factors $F(i)$, and evaluated as described in Sect. 8.5.2.6

Channels	eee	$e\mu\mu$	μee	$\mu\mu\mu$	All
$N_{LTT} \cdot F$	$12.13 \pm 0.73 \pm 2.79$	$13.99 \pm 0.79 \pm 3.41$	$6.50 \pm 0.43 \pm 3.46$	$6.22 \pm 0.43 \pm 2.93$	$38.84 \pm 1.23 \pm 8.88$
$N_{TLT} \cdot F$	$1.08 \pm 0.33 \pm 0.25$	–	–	$0.37 \pm 0.14 \pm 0.28$	$1.45 \pm 0.36 \pm 0.38$
$N_{TTL} \cdot F$	$2.72 \pm 0.63 \pm 0.31$	–	–	$2.11 \pm 0.55 \pm 0.38$	$4.83 \pm 0.84 \pm 0.49$
Total	$15.93 \pm 1.02 \pm 3.21$	$13.99 \pm 0.79 \pm 3.41$	$6.50 \pm 0.43 \pm 3.46$	$8.70 \pm 0.72 \pm 3.50$	$45.12 \pm 1.54 \pm 9.59$

Table 8.17 The WZ/ZZ subtraction systematic in the Z FF region. Numbers represent the uncertainty on the final $Z+\text{jet}/Z\gamma$ estimate, in number of events. The WZ and ZZ yield in the FF region is varied up by 15% and the change in the fake factor result is taken as the systematic

Channels	eee	$e\mu\mu$	μee	$\mu\mu\mu$	All
$N_{LTT} \cdot F$	1.37	1.66	2.29	1.96	7.28
$N_{TLT} \cdot F$	0.10	–	–	0.17	0.27
$N_{TTL} \cdot F$	0.11	–	–	0.24	0.35
Total	1.59	1.66	2.29	2.36	7.90

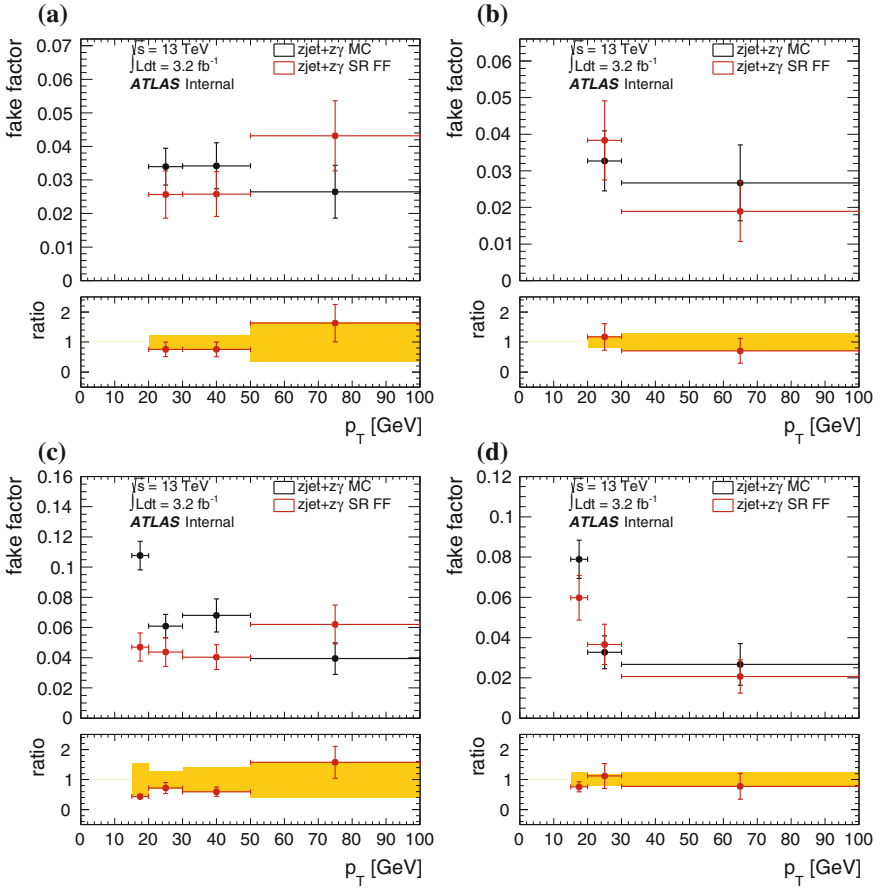

Fig. 8.16 Comparison between the nominal MC fake factor (black) and the signal region MC fake factor, for the systematic uncertainty test. Fake factors for electron W identification (**a**), muon W identification (**b**), electron W identification (**c**), and muon W identification (**d**) are shown. See the text for the description of the true signal region fake factor. The difference between the two fake factors is used for the systematic uncertainty due to non-closure and composition

Table 8.18 The non-closure and composition systematic uncertainty (in number of events) on the $Z+\text{jet}/Z\gamma$ fake factor, propagated through the full fake factor result. See the text for the description of the systematic uncertainty

Channels	eee	$e\mu\mu$	μee	$\mu\mu\mu$	All
$N_{LTT} \cdot F$	4.40	5.23	1.68	1.54	10.15
$N_{TLT} \cdot F$	0.52	–	–	0.09	0.52
$N_{TTL} \cdot F$	1.19	–	–	0.52	1.29
Total	6.10	5.23	1.68	2.14	11.96

As hinted earlier, there are advantages to measuring $t\bar{t}$ and $Z+\text{jet}/Z\gamma$ separately. First, the set of statistical and systematic uncertainties of each method are (effectively) distinct and uncorrelated. This means that the 30% statistical uncertainty in the $t\bar{t}$ SR estimate that applies to the 9.16 $t\bar{t}$ events does not apply to the 45.1 $Z+\text{jet}/Z\gamma$ events from the Fake Factor method. Likewise, the roughly 20% uncertainty due to the subtraction of WZ and ZZ in the Z Fake Factor Region is applied only to the 45.1 $Z+\text{jet}/Z\gamma$ events, instead of roughly 60 events from an inclusive Fake Factor estimate. Because the $Z+\text{jet}/Z\gamma$ Fake Factor and $t\bar{t}$ signal region estimates have completely separate uncertainties, the total fractional uncertainty of the combined result is smaller than that of an inclusive Fake Factor result. (The exception is the $t\bar{t}$ extrapolation uncertainty, which is present in both procedures but whose impact is small.)

The other advantage to estimating $t\bar{t}$ in a separate procedure is that the fake factors derived in the Z Fake Factor region are effectively applied only to $Z+\text{jet}/Z\gamma$ events. Measuring a fake factor in one region and applying it to the same process in another region should be more robust than trying to use a different process to model the fake factors, or trying to use one process to model the fakes of a mixture of processes. The composition, shapes and behavior of fakes is difficult to control across processes, and one would expect the composition uncertainties to increase, unless the fake factor denominator is very carefully chosen. Currently the composition systematics range from 20 to 65%, depending on the p_{T} bin; these composition uncertainties are kept low by using a $Z+\text{jet}/Z\gamma$ region to model fakes in only $Z+\text{jet}/Z\gamma$ events.

8.5.3 *Uncertainty on Extrapolation from Top-Like Control Regions*

The procedure to derive a data-MC scale factor in regions enriched in top-like events parallel to the signal region, and apply it to MC in the signal region, is subject to uncertainties introduced by using simulation to predict the ratio between events in the top-CR||SR and events in the signal region. The same applies to the procedure to estimate top-like contributions to the fake factor estimate by deriving a scale factor in

Table 8.19 The top-like correction component of the Fake Factor method in the ZCR, combining all regions, including the $e\mu\mu$- and μee-channel events falling in the TLT and TTL regions. All results are shown multiplied by the scale factors from Table 8.12, and also multiplied by the fake factors $F(i)$. The first uncertainty is the statistical uncertainty from the top-like MC in the ZCR; the second error term is the statistical uncertainty propagated from the fake factors $F(i)$, and evaluated as described in Sect. 8.5.2.6

Channels	eee	$e\mu\mu$	μee	$\mu\mu\mu$	Total
$N_{LTT} \cdot F$	$0.86 \pm 0.06 \pm 0.16$	$1.05 \pm 0.06 \pm 0.19$	$1.60 \pm 0.06 \pm 0.83$	$1.96 \pm 0.07 \pm 0.97$	$5.46 \pm 0.12 \pm 1.83$
$N_{TLT} \cdot F$	$0.29 \pm 0.04 \pm 0.07$	$0.36 \pm 0.03 \pm 0.28$	$0.38 \pm 0.05 \pm 0.10$	$0.30 \pm 0.03 \pm 0.25$	$1.34 \pm 0.08 \pm 0.55$
$N_{TTL} \cdot F$	$1.67 \pm 0.11 \pm 0.17$	$2.36 \pm 0.11 \pm 0.53$	$1.98 \pm 0.12 \pm 0.20$	$2.81 \pm 0.12 \pm 0.64$	$8.81 \pm 0.24 \pm 1.23$
Total	$2.82 \pm 0.13 \pm 0.37$	$3.76 \pm 0.13 \pm 0.81$	$3.94 \pm 0.14 \pm 0.87$	$5.07 \pm 0.14 \pm 1.81$	$15.61 \pm 0.28 \pm 3.51$

a region parallel to the ZCR. The MC must adequately model the event kinematics, as well as the kinematics of the two real leptons and one fake lepton in the event. These effects are assumed to be small; when the data and MC are compared in the top-CR parallel to the ZCR in Sect. 8.5.2.4, kinematic shapes are found to have reasonable agreement.

Instead, we focus on another potential source of uncertainty, caused by the real leptons, during the extrapolation: the MC, which is corrected using data-driven lepton scale factors, propagates differences in reconstruction and identification efficiencies between real leptons of different flavors when moving from the top-CR to the signal region (or ZCR). The uncertainty on these data-driven scale factors could have an impact on the procedure, and their effect must be tested. This is the main uncertainty discussed below.

It is important to note that, since events with an electron (muon) fake in the signal region are scaled using e-fake (μ-fake) events in the parallel top-CR, using MC to extrapolate between these two regions should not introduce uncertainties related to the fake object. Instead, uncertainties should be dominated by the consequences of exchanging real leptons of different flavors when extrapolating between the top-CR and the signal region (or ZCR), which have different real-lepton flavor compositions.

The uncertainties introduced by using corrected MC to extrapolate between regions of a different flavor channel consist of data-driven identification efficiency uncertainties, energy scale uncertainties and resolution uncertainties on the electron and muon. These uncertainties are calculated in [11], and can be propagated through the method here to measure the effect of each uncertainty on the top-like signal region estimate.

To understand how to propagate these uncertainties, start with the equation to estimate the number of top-like events in the signal region:

$$N_{\mathrm{SR}}^{\mathrm{top}} = \frac{N_{\mathrm{data}}^{\mathrm{CR}} - N_{\mathrm{other}}^{\mathrm{MC,CR}}}{N_{\mathrm{top}}^{\mathrm{MC,CR}}} \cdot N_{\mathrm{top}}^{\mathrm{MC,SR}}. \tag{8.17}$$

Varying a given lepton measurement θ_j up or down by $\pm\sigma_{\theta_j}$ can probe the effect of the signal region yield, as a fraction of the original yield:

$$\begin{aligned} 1 \pm \Delta N_{\mathrm{SR}}^{\mathrm{top}}(\%) &= \frac{N_{\mathrm{SR}}^{\mathrm{top}}(\theta_j) - N_{\mathrm{SR}}^{\mathrm{top}}(\theta_j \pm \sigma_{\theta_j})}{N_{\mathrm{SR}}^{\mathrm{top}}(\theta_j)} \\ &= \frac{\frac{N_{\mathrm{data}}^{\mathrm{CR}} - N_{\mathrm{other}}^{\mathrm{MC,CR}}}{N_{\mathrm{top}}^{\mathrm{MC,CR}}(\theta_j)} \cdot N_{\mathrm{top}}^{\mathrm{MC,SR}}(\theta_j) \pm \frac{N_{\mathrm{data}}^{\mathrm{CR}} - N_{\mathrm{other}}^{\mathrm{MC,CR}}}{N_{\mathrm{top}}^{\mathrm{MC,CR}}(\theta_j \pm \sigma_{\theta_j})} \cdot N_{\mathrm{top}}^{\mathrm{MC,SR}}(\theta_j \pm \sigma_{\theta_j})}{\frac{N_{\mathrm{data}}^{\mathrm{CR}} - N_{\mathrm{other}}^{\mathrm{MC,CR}}}{N_{\mathrm{top}}^{\mathrm{MC,CR}}(\theta_j)} \cdot N_{\mathrm{top}}^{\mathrm{MC,SR}}(\theta_j)} \end{aligned} \tag{8.18}$$

The effect of the $N_{\mathrm{other}}^{\mathrm{MC,CR}}$ term on the systematic is ignored, since variations in these terms will have a small effect on the outcome. The equation can then be simplified, leading to the following result:

$$1 \pm \Delta N_{\text{SR}}^{\text{top}}(\%) = 1 \pm \frac{N_{\text{top}}^{\text{MC,CR}}(\theta_j) \cdot N_{\text{top}}^{\text{MC,SR}}(\theta_j \pm \sigma_{\theta_j})}{N_{\text{top}}^{\text{MC,SR}}(\theta_j) \cdot N_{\text{top}}^{\text{MC,CR}}(\theta_j \pm \sigma_{\theta_j})} \tag{8.19}$$

This is a double-ratio: the ratio between events in the signal region and the top-CR is compared as a ratio between the nominal and up/down variation. This can be interpreted by taking an example case: comparing $\mu^{\pm}e^{\mp}\mu^{\pm}$ event with $\mu^{\pm}\mu^{+}\mu^{-}$ events, both have a fake muon and a real muon, and the $t\bar{t}$ CR event has a real electron where the $\mu\mu\mu$ topology has a second real muon. Varying an electron systematic will affect the top CR event and not the SR event; varying a muon systematic will affect the real muon in the top CR and two real muons in the $\mu\mu\mu$ event, so the difference when taking the double-ratio, on average and roughly speaking, is one real muon. Effectively this means that the uncertainty is driven by electron uncertainties assessed on one electron and muon uncertainties assessed on one muon, added in quadrature. Thus, this type of effect can be described as the uncertainty due to "replacing an electron with a muon" or vice-versa.

Equation 8.19 can be rewritten for assessing the uncertainty on the $t\bar{t}$ subtraction estimate in the ZCR. The only difference is that the events are weighted by the fake factor in a given bin i, and summed across LTT, TLT and TTL reconstruction categories:

$$1 \pm \Delta N_{\text{ZCR}}^{\text{top}}(\%) = 1 \pm \frac{N_{\text{top}}^{\text{MC,CR,Cat}}(\theta_j) \cdot \left(\sum_{Cat} \sum_{\text{bin } i} N_{\text{top}}^{\text{MC,ZCR,Cat}}(\theta_j \pm \sigma_{\theta_j}) \cdot F(i) \right)}{\left(\sum_{Cat} \sum_{\text{bin } i} N_{\text{top}}^{\text{MC,ZCR,Cat}}(\theta_j) \cdot F(i) \right) \cdot N_{\text{top}}^{\text{MC,CR}}(\theta_j \pm \sigma_{\theta_j})} \tag{8.20}$$

The correlation among flavor channels of these uncertainties is not straightforward, since the channels are affected by electron and muon uncertainties to a varying degree. Therefore the extrapolation uncertainties are considered fully correlated among channels; since the magnitude of the uncertainty is small this decision will have little impact on the final result. As a further simplification, the uncertainty is symmetrized by taking the larger of the up and down variations.

Uncertainty on Extrapolation from the Top Control Region Parallel to the ZCR

Table 8.20 shows the effect of electron and muon efficiency, scale and resolution systematics on the subtraction of top-like backgrounds in the ZCR, using Eq. 8.20. The total effect of these systematics on the $t\bar{t}$ estimate in the ZCR is less than 4% in all channels, and about 2% adding all channels.

Uncertainty on Extrapolation from the Top Control Region Parallel to the Signal Region

For evaluating the corresponding systematics on the $t\bar{t}$ estimate in the SR, the $t\bar{t}$ MC statistics of the top-CR||SR and the SR are too poor to evaluate such small effects (the systematic uncertainty would be lost under the statistical noise of the top-like MC samples). Instead, because the top subtraction component provided by the Fake

Table 8.20 Effect of the electron and muon efficiency, scale and resolution systematics on the $t\bar{t}$ subtraction in the ZCR. Equation 8.20 describes how the systematics are derived. Total up/down uncertainties are calculated by summing the up/down uncertainties above in quadrature

Systematic (%)	eee	$e\mu\mu$	μee	$\mu\mu\mu$
Electron resolution (down)	−0.05	0.35	−1.56	−0.38
Electron resolution (up)	3.23	1.55	0.19	−0.20
Electron energy scale (down)	−0.09	0.03	−1.28	−0.62
Electron energy scale (up)	0.64	0.60	1.14	0.53
Electron identification efficiency	0.86	0.91	0.84	0.83
Electron isolation efficiency	0.25	0.28	0.19	0.26
Electron reconstruction efficiency	0.43	0.44	0.43	0.42
Muon identification efficiency, stat.	0.16	0.15	0.18	0.16
Muon identification efficiency, sys.	0.32	0.27	0.34	0.32
Muon isolation efficiency, stat.	0.04	0.04	0.04	0.04
Muon isolation efficiency, sys.	0.20	0.22	0.21	0.21
Muon reconstruction, ID (down)	0.07	0.99	0.02	0.18
Muon reconstruction, ID (up)	1.21	0.41	−0.59	−0.57
Muon reconstruction, MS (down)	0.22	0.22	−0.03	0.06
Muon reconstruction, MS (up)	0.00	0.00	−0.22	−0.01
Muon energy scale (down)	0.00	0.00	0.12	−0.04
Muon energy scale (up)	0.09	0.09	−0.18	0.16
Total down	1.10	1.55	2.29	1.30
Total up	3.67	2.04	1.70	1.33

Factor method is a reasonable proxy for the top-like signal region estimate itself, we repeat the procedure using the top-like subtraction component in the Fake Factor method to evaluate the magnitude of the uncertainties. The only difference from the ZCR treatment is that the TLT and TTL regions of the $e\mu\mu$ and μee channels are included in the signal region case. Table 8.21 shows this result—the fractional uncertainty is then multiplied by the expected signal region yield in each channel to obtain the uncertainty in number of events due to extrapolation.

8.5.4 Reducible Background Summary

A schematic representation of the kinematic regions used for the Fake Factor method, and the top-like CRs used in both the top signal region estimate and the top contamination in the $Z + \text{jet}/Z\gamma$ estimate, is shown in Fig. 8.17.

Table 8.22 shows a complete summary of the $Z + \text{jet}/Z\gamma$ and top-like estimates, along with each source of systematic uncertainty. The total estimate of both reducible backgrounds is 54.28 ± 17.59. Separate estimates for these backgrounds in the W^+Z and W^-Z regions are detailed in Appendix D.1.

The reducible background has also been assessed with a matrix method procedure, similar to the one used in the measurement of $W^\pm Z$ production at $\sqrt{s} = 8$ TeV[7]. The matrix method estimates $Z + \text{jet}$, $Z\gamma$ and top-like backgrounds simultaneously. The method predicts $51.6 \pm 5.9 \pm 17.5$ reducible background events, where the first error is statistical, and the second is the systematic error. The two methods give compatible results.

8.5.5 ZZ Background

Typically the $ZZ \to 4\ell$ topology can enter into the 3ℓ WZ signal region in one of two ways: one of the four leptons falls outside the kinematic acceptance of the detector ($p_{\text{T}} < 7$ GeV or $|\eta| < \eta_{\text{max}}$), or all four leptons fall inside this acceptance but one lepton fails the identification criteria. The former is an irreducible source of background; the latter is reducible by means of the four-lepton veto described in Sect. 8.4.

Both irreducible and reducible ZZ backgrounds are estimated using simulation. In addition to the typical corrections applied to account for known data-MC differences, a correction is applied due to MC mismodeling of leptons that fall inside the detector acceptance but fail identification criteria (called anti-id leptons). Furthermore, a validation region containing four identified leptons is used to check the agreement between data and simulation with regard to the theory cross section and luminosity measurement.

An 8% theoretical uncertainty is assigned to the ZZ background (for the combination of qq and gg contributions). The additional anti-id scale factor correction is about 4%.

Table 8.21 Effect of the electron and muon efficiency, scale and resolution systematics on the $t\bar{t}$ estimate in the SR. Equation 8.20 describes how the systematics are derived. The SR uncertainties are estimated by taking the $t\bar{t}$ component subtracted from the Fake Factor result, including TLT and TTL regions of the $e\mu\mu$ and μee channels. Total up/down uncertainties are calculated by summing the up/down uncertainties above in quadrature

Systematic (%)	eee	$e\mu\mu$	μee	$\mu\mu\mu$
Electron resolution (down)	−0.05	−0.22	−1.10	−0.38
Electron resolution (up)	3.23	1.58	−0.14	−0.20
Electron energy scale (down)	−0.09	−0.25	−0.23	−0.62
Electron energy scale (up)	0.64	0.85	−0.12	0.53
Electron identification efficiency	0.86	0.28	0.60	0.83
Electron isolation efficiency	0.25	0.09	0.16	0.26
Electron reconstruction efficiency	0.43	0.18	0.30	0.42
Muon identification efficiency, stat.	0.16	0.05	0.13	0.16
Muon identification efficiency, sys.	0.32	0.12	0.23	0.32
Muon isolation efficiency, stat.	0.04	0.01	0.03	0.04
Muon isolation efficiency, sys.	0.20	0.07	0.15	0.21
Muon reconstruction, ID (down)	0.07	0.37	−0.02	0.18
Muon reconstruction, ID (up)	1.21	1.11	−0.72	−0.57
Muon reconstruction, MS (down)	0.22	0.39	−0.03	0.06
Muon reconstruction, MS (up)	0.00	−0.16	−0.18	−0.01
Muon energy scale (down)	0.00	−0.33	0.12	−0.04

(continued)

Table 8.21 (continued)

Systematic (%)	eee	$e\mu\mu$	μee	$\mu\mu\mu$
Muon energy scale (up)	0.09	0.05	−0.18	0.16
Total down	1.10	0.81	1.36	1.30
Total up	3.67	2.15	1.08	1.33

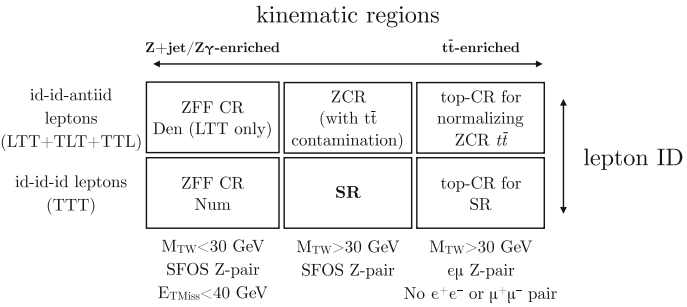

Fig. 8.17 Schematic representation of the regions used in the Fake Factor method, and in the estimation of top-like events in the ZCR and the signal region. In addition to the signal region, three orthogonal regions are defined by sequential cuts on kinematic and lepton identification variables. The fake factor F is derived from the numerator (TTT) and denominator (LTT) regions denoted by "Z Fake Factor Region," or ZFF CR, and it is applied to events in the ZCR, with one Loose lepton (LTT, TLT, and TTL). A top control region parallel to the ZCR, with Loose leptons, is used to estimate the top-like contamination in the $Z + \text{jet}/Z\gamma$ Fake Factor estimate. The top-CR with three Tight leptons is used for the estimate of top-like yields in the signal region

8.5.5.1 Anti-identification Scale Factors

Scale factors are derived for identified leptons using sources of unbiased leptons from $Z \to ee$ and $J/\psi \to ee$ decays, with uncertainties on the order of 1–10%. In contrast, scale factors for anti-identified leptons must be derived using the efficiencies of identified leptons in MC and data, instead of the efficiencies of the anti-id leptons themselves using the following formula:

$$\text{SF}^{\text{anti-id}} = \frac{1 - \varepsilon^{\text{data}}}{1 - \varepsilon^{\text{MC}}} = \frac{1 - \text{SF}^{\text{id}} \cdot \varepsilon^{\text{data}}}{1 - \varepsilon^{\text{MC}}} \tag{8.21}$$

where the substitution $\varepsilon^{\text{data}} = \text{SF}^{\text{id}} \cdot \varepsilon^{\text{data}}$ is used in part because a detailed efficiency measurement for lepton efficiencies in ZZ events is not possible.[8]

[8]Lepton efficiencies measured in e.g. $Z \to \ell\ell$ events are not trusted to apply to leptons in other processes, because of the effects of other objects in the event that may affect lepton efficiency; however, scale factors measured in $Z \to \ell\ell$ events are trusted to apply to leptons in other processes, with the assumption that the effects affect MC and data roughly equally, and thus cancel to first order.

Table 8.22 Summary of systematics. The labels in the "Correlation" column detail the correlation assumption among flavor channels: "none": no correlation between channels; "all": 100% correlation between channels; "W_e / W_μ": 100% correlation among channels with an electron (muon) associated to the W-boson, e.g. eee and $e\mu\mu$ (μee and $\mu\mu\mu$), and 0% correlation between these two categories; μ-fake (e-fake): 100% correlation among events where the truth-matched fake is a muon (electron)

Channels	eee	$e\mu\mu$	μee	$\mu\mu\mu$	All	Correlation
$Z + \text{jet}/Z\gamma$	15.93	13.99	6.50	8.70	45.12	–
$t\bar{t}$	1.23	2.38	1.97	3.58	9.16	–
Total yield	17.16	16.37	8.47	12.28	54.28	–
ZCR stat (data, MC)	1.02	0.79	0.43	0.72	1.54	None
Z FF WZ/ZZ Subtraction	1.59	1.66	2.29	2.36	7.90	All
ZCR WZ/ZZ Subtraction	0.25	0.09	0.02	0.09	0.45	All
Z muon FF stat	–	–	3.46	3.50	6.94	W_μ
Z electron FF stat	3.21	3.41	–	–	6.61	W_e
Composition/closure (μ)	–	–	1.68	2.14	3.82	W_μ
Composition/closure (ele)	6.09	5.23	–	–	11.32	W_e
Z FF $t\bar{t}$ μ SF MC+data stat	–	–	0.12	0.39	0.51	W_μ
Z FF $t\bar{t}$ ele SF MC+data stat	0.38	0.14	–	–	0.52	W_e
ZCR $t\bar{t}$ region Extrapolation	0.10	0.02	0.04	0.07	0.23	All
$t\bar{t}$ MC stat in SR	0.24	0.49	0.41	0.71	0.98	None

(continued)

Table 8.22 (continued)

Channels	eee	$e\mu\mu$	μee	$\mu\mu\mu$	All	Correlation
$t\bar{t}$ CR||SR mu SF MC+data stat	–	0.67	0.30	1.32	2.29	μ-fake
$t\bar{t}$ CR||SR ele SF MC+data stat	0.74	0.33	0.69	–	1.76	e-fake
$t\bar{t}$ CR||SR Extrapolation	0.05	0.05	0.03	0.05	0.18	All
Total uncertainty	7.20	6.57	4.58	5.03	17.59	All
Total uncertainty (%)	41.9	40.2	54.1	41.0	32.4	–

Table 8.23 Predicted ZZ yields after the full WZ selection, with and without anti-ID scale factors applied to unidentified fourth leptons within the acceptance. Only statistical uncertainties are shown

ZZ prediction	eee	$ee\mu$	$\mu\mu e$	$\mu\mu\mu$	All
No anti-ID SFs	6.35 ± 0.09	8.36 ± 0.11	8.12 ± 0.11	11.44 ± 0.13	34.27 ± 0.22
With anti-ID SFs	6.71 ± 0.10	8.55 ± 0.12	8.60 ± 0.12	11.73 ± 0.14	35.59 ± 0.24
Relative difference [%]	+5.7	+2.3	+5.9	+2.5	+3.9

The anti-id scale factors are applied only to ZZ events in the signal region in which a lepton candidate is reconstructed, but fails some identification criteria. Ideally, anti-id scale factors for the full anti-baseline criteria would be derived. However, for the publication only anti-loose (muon) scale factors are derived, and applied only to muons failing loose identification (thus not correcting muons that pass id but fail d_0, z_0, or isolation cuts). For electrons, anti-[id && d_0 && z_0] scale factors are derived, and applied to electrons failing one of those three criteria. Corrections for all cuts, and thus a full treatment of anti-id objects, can be made in a later publication.

The ZZ yields before and after the anti-id scale factor correction are shown in Table 8.23. Overall, the effect is about 4% on the total ZZ yield. The corrected yields are used in the analysis as the ZZ prediction, and an uncertainty uncertainty equal to 100% of the magnitude of the correction is applied to account for the effect and errors in the procedure.

8.5.5.2 ZZ Validation Region

A dedicated validation region is used to test the agreement of the ZZ prediction with data. (A "validation region" is a region used to compare the prediction to the data that is background-enriched, and in which the data is not used to constrain the final result.) As in the signal region, two same-flavor, oppositely-charged leptons with $|m_{\ell\ell} - m_Z| < 10\,\text{GeV}$ are required; if more than one pair exists then the pair closest to the PDG Z mass is associated with the Z boson. These leptons must satisfy the Z-lepton criteria. Two additional leptons must satisfy the baseline lepton criteria, and the one with higher p_{T} must satisfy the W-lepton criteria. Finally, the m_{T}^W cut ($m_{\text{T}}^W > 30\,\text{GeV}$) of the signal region is removed to increase the size of the validation region.

Data events passing this selection are compared to the MC prediction; MC is used to predict $Z + \text{jet}/Z\gamma$ and $t\bar{t}$ backgrounds in this region. This region is used to validate the theoretical ZZ cross section prediction and the luminosity measurement; it does not provide information on the data-MC agreement with regard to events in the signal region with an anti-identified or out-of-acceptance lepton.

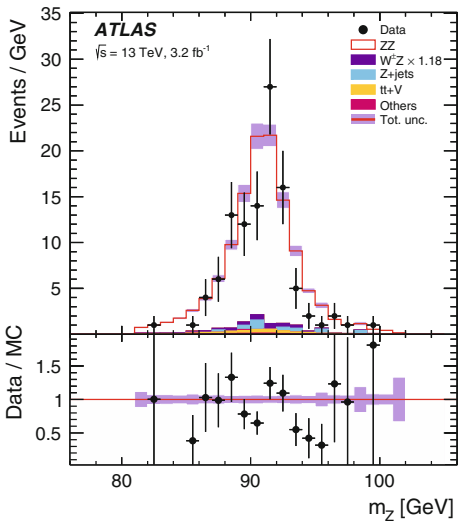

Fig. 8.18 The ZZ validation region

The mass of the Z boson pair closest to the PDG Z mass (if a second one exists) is plotted in Fig. 8.18. The validation region has 91.8 ± 0.4 ZZ events, 11.6 ± 1.1 other background (mostly WZ, $Z+$jet and $t\bar{t}+V$), totaling 103.4 ± 1.2 MC events, compared to 106 events in data. Currently, this region is not used to constrain the ZZ background in the signal region; this is because the current theoretical uncertainty on the ZZ background is 8%, with an additional 5% luminosity uncertainty. This 9.4% uncertainty can be compared to the roughly 11% uncertainty in the ZZ validation region due to statistics alone. However, using this region as a control region to constrain the ZZ background can beat the theory + luminosity uncertainty when around 150 events populate the validation region, corresponding to about 4.5 fb^{-1} of data collected.

8.6 Corrections for Acceptance and Detector Effects

The fiducial cross section is calculated in each channel using a correction factor to extrapolate from the number of reconstructed events to the number of true WZ events in the fiducial region:

$$C_{WZ} = \frac{N_{\text{reco}}^{\text{MC}}}{N_{\text{true}}^{\text{MC}}}. \tag{8.22}$$

C_{WZ} is calculated using simulated Powheg + PYTHIA8 events, with particles propagated through a GEANT4 4 description of the ATLAS detector. The kinematics of the particle-level (true) events are constructed using dressed leptons, and the boson association required for applying the fiducial selection cuts is performed using the

Resonant Shape algorithm discussed in Sect. 8.2. Reconstruction-level event selection proceeds according to the signal selection of Sect. 8.4. C_{WZ} factors are calculated separately in each flavor channel; Table 8.24 summarizes the C_{WZ} factors used in the analysis.

The fiducial cross section is calculated in each flavor channel according to the following formula:

$$\sigma^{\text{fid.}}_{W^{\pm}Z\to\ell'\nu\ell\ell} = \frac{N_{\text{data}} - N_{\text{bkg}}}{\mathcal{L}_{\text{int}} \cdot C_{WZ}} \times \left(\frac{N_{\text{all}} - N_{\tau}}{N_{\text{all}}}\right), \tag{8.23}$$

where $\mathcal{L}$ is the integrated luminosity of the collected data, N_{data} is the number of events observed in the channel, and N_{bkg} is the estimated number of expected background events. The term in parentheses corrects for the fraction of $WZ \to \ell'\nu\ell\ell$ events in the signal region with at least one $\tau \to \ell\nu$ in the final state, as predicted by POWHEG simulation. (N_{all} counts WZ contributions to the signal region from all final states, including those with a tau, but the fiducial cross section is reported for a single final state; the correction in parentheses transforms the reporting of the measurement from the former to the latter, using the fractional contribution from tau final states.) The tau fraction is calculated in each channel, and reported in Table 8.24; it is roughly 4% in all channels.

Once the fiducial cross sections are calculated in individual channels, a χ^2 minimization is used to combine the results from each channel into a single fiducial cross section measurement [15]. The combined fiducial cross section is then extrapolated to the total phase space described in Sect. 8.2 according to the following formula:

$$\sigma^{\text{tot.}}_{W^{\pm}Z} = \frac{\sigma^{\text{fid.}}_{W^{\pm}Z\to\ell'\nu\ell\ell}}{\mathcal{B}_W\, \mathcal{B}_Z\, A_{WZ}}, \tag{8.24}$$

where $\mathcal{B}_W$ and $\mathcal{B}_Z$ are the $W \to \ell\nu$ and $Z \to \ell\ell$ branching fractions, respectively [16], and A_{WZ} is the acceptance factor, defined as

$$A_{WZ} = \frac{N^{\text{MC}}_{\text{total}}}{N^{\text{MC}}_{\text{fiducial}}} \tag{8.25}$$

Table 8.24 C_{WZ} factors and τ fractions in each channel of the $W^{\pm}Z$ analysis. Errors are statistical only

	eee	μee	$e\mu\mu$	$\mu\mu\mu$
C_{WZ}	0.421 ± 0.003	0.553 ± 0.004	0.552 ± 0.004	0.732 ± 0.005
N_{τ}/N_{all}	0.040 ± 0.001	0.038 ± 0.001	0.036 ± 0.001	0.040 ± 0.001

and estimated using POWHEG simulation. A single acceptance factor of $A_{WZ} = 0.343 \pm 0.002$ (stat.) is used—calculated using the $e\mu\mu$ and μee channels to avoid a boson assignment ambiguity.

8.7 Statistical Combination

The fiducial cross sections calculated in each flavor channel are statistically combined using a χ^2 minimization method [15]. The method takes into account the systematic uncertainties and their correlations across eee, $e\mu\mu$, μee and $\mu\mu\mu$ channels. The χ^2 for the combined measurement of quantity m ($= \sigma^{\text{fid.}}_{W^{\pm}Z\to\ell'\nu\ell\ell}$), across i channels, given a list of nuisance parameters $\boldsymbol{b}$ from the correlated systematic uncertainties, is defined as

$$\chi^2\,(m, \boldsymbol{b}) = \sum_{\text{ch. } i} \frac{\left[m - \sum_j \gamma_{j,i}\, m\, b_j \; - \mu_i\right]^2}{\delta^2_{i,\text{stat}} \cdot \mu_i \cdot \left(m - \sum_j \gamma_{j,i}\, m\, b_j\right) + \left(\delta_{i,\text{uncor}} \cdot m\right)^2} + \sum_j b_j^2\,, \tag{8.26}$$

where μ_i is the measured cross section in channel i, $\delta_{i,\text{uncor}}$ is the total relative uncorrelated systematic uncertainty, $\gamma_{j,i}$ are the relative systematic uncertainties that are correlated across channels, and $\delta_{i,\text{stat}}$ is the relative statistical uncertainty. Nuisance parameters are centered at zero and have a standard deviation of one; the term $\sum_j b_j^2$ is the nuisance parameter penalty term.

In the 8 TeV WZ cross section measurement [7], combination results using the χ^2 minimization described above are compared to results from a profile likelihood ratio method; the two approaches yield nearly identical results.

8.8 Systematic Uncertainties

Systematic uncertainties affecting the measurement include experimental uncertainties on detector effects, uncertainties in the background estimation, and theoretical uncertainties affecting the fiducial measurement and extrapolation to the total cross section.

Experimental systematic uncertainties are obtained by repeating the analysis after applying variations for each systematic source. The systematic uncertainties on the measurement are summarized in Table 8.25. The largest uncertainty is from the $Z+\text{jet}/Z\gamma$ background; these uncertainties are summarized in Sect. 8.5.4. Jet uncertainties enter into the calculation of the $E_{\text{T}}^{\text{miss}}$, as well as the measurement of the jet multiplicity distribution [17]. The uncertainty on the ZZ background includes the 8% theoretical uncertainty, as well as the uncertainty associated with the correction of lepton that fail identification criteria, discussed in Sect. 8.5.5. The uncertainties

Table 8.25 Summary of experimental systematic uncertainties, presented relative to the cross section measurement in each channel

	eee	μee	$e\mu\mu$	$\mu\mu\mu$	Combined
Relative uncertainties [%]					
Z + jet/$Z\gamma$ background	10.1	4.5	4.7	3.1	3.6
Pile-up	0.7	1.1	1.0	0.7	0.9
ZZ background	1.0	0.7	0.6	0.7	0.7
μ id. efficiency	–	0.6	1.0	1.4	0.7
e id. efficiency	1.4	1.1	0.6	–	0.7
top-like background	1.1	0.8	0.5	0.9	0.6
$E_{\mathrm{T}}^{\mathrm{miss}}$ and jets	0.3	0.4	0.8	0.7	0.6
Other backgrounds	0.5	0.5	0.3	0.3	0.4
e energy scale	0.5	0.2	0.3	<0.1	0.2
Trigger	<0.1	0.1	0.1	0.2	0.1
μ momentum scale	<0.1	<0.1	<0.1	0.1	<0.1
Uncorrelated	2.2	1.3	1.4	1.7	0.8
Total sys. uncertainty	11	5.1	5.3	4.1	4.1
Luminosity	2.4	2.4	2.3	2.3	2.4
Statistics	14	11	10	8.8	5.1
Total	18	12	11	10	7.0

on other backgrounds are the theoretical uncertainties on the cross sections of the non-ZZ backgrounds estimated using simulation. They are 13% for $t\bar{t}+W$ [18], 12% for $t\bar{t}+V$ [18], 20% for VVV [19], and 15% for tZ [7]. Uncertainties labeled as "Uncorrelated" are from sources not correlated between flavor channels, including statistical uncertainties in simulation (including the top-like simulation used for the top estimate) and in the ZCR of the Fake Factor estimate.

The systematic uncertainties on A_{WZ} and C_{WZ} consist of the experimental systematic uncertainties described above (affecting the numerator of C_{WZ}), as well as theoretical uncertainties on the WZ prediction, related to renormalization (μ_R) and factorization (μ_F) scale, and choice of PDF; in addition, parton shower modeling uncertainties affect C_{WZ}. The nominal POWHEG WZ sample is used for determining these uncertainties, generated using the CT10 PDF set with dynamic QCD scales $\mu_R = \mu_F = m_{WZ}/2$. QCD scale uncertainties are estimated by varying μ_R and μ_F up and down by a factor of two around the nominal scale $m_{WZ}/2$ in all combinations satisfying $0.5 < \mu_R/\mu_F < 2$. PDF uncertainties are estimated using the CT10

eigenvector set, and by taking the envelope of CT10, CT14 [20], MMHT2014 [21] and NNPDF3.0 [22] NLO PDF sets. Parton shower uncertainties are obtained by showering the POWHEG simulation with both PYTHIA and SHERPA and using the difference as an uncertainty; the uncertainty here is taken from simulation studies for the 8 TeV measurement [7]. Theoretical uncertainties on C_{WZ} are negligible; the uncertainties on A_{WZ} are less than 5% (PDF) and less than 7% (scale).

8.9 Results

The data yields in the signal region are shown in Table 8.26, along with a summary of the background estimates, expected WZ, and all statistical, systematic and luminosity uncertainties associated with each process.

Validation Plots

The Z + jet/$Z\gamma$ and ZZ backgrounds, which together comprise around 75% of all WZ background, are validated by checking the agreement in a subset of the signal region enriched in these backgrounds by requiring $30 < m_{\mathrm{T}}^{W} < 50$ GeV and $E_{\mathrm{T}}^{\mathrm{miss}} < 40$ GeV. After scaling WZ by 1.18—see Fig. 8.21, the agreement in this region, which contains 45% background, including more than half of the total Z + jet/$Z\gamma$ background, is at the level of 5%, well below the statistical error of the data. Figure 8.19 shows the $E_{\mathrm{T}}^{\mathrm{miss}}$ distribution in the region $30 < m_{\mathrm{T}}^{W} < 50$ GeV, showing the agreement. The eee and $e\mu\mu$ channels are plotted together, as are the μee and $\mu\mu\mu$ channels; this is to demonstrate the performance of the Z + jet/$Z\gamma$ Fake Factor method, where fake electrons (muons) associated with the W boson are the dominant contribution. The Z + jet/$Z\gamma$ and ZZ backgrounds are modeled well in this region.

Figure 8.20 shows various reconstruction-level signal region distributions. The POWHEG WZ prediction is scaled by 1.18—see Fig. 8.21. The kinematic distributions are in good agreement between the data and signal+background predictions.

The Fiducial Cross Section Measurement

The cross section is calculated in each channel from the event yields and estimated background yields, using Eq. 8.23 and the correction factor C_{WZ} described in Sect. 8.6. The results of the fiducial cross section measurement in each channel are summarized in Table 8.27. The results of the W^+Z and W^-Z measurements are reproduced in Appendix D.2. The measurements from individual channels are combined using the χ^2 minimization described in Sect. 8.6; the resulting fiducial cross section is:

$$\begin{aligned} \sigma^{\mathrm{fid.}}_{W^{\pm}Z\to\ell'\nu\ell\ell} &= 63.2 \pm 3.2\,(\mathrm{stat.}) \pm 2.6\,(\mathrm{sys.}) \pm 1.5\,(\mathrm{lumi.})\ \mathrm{fb} \\ &= 63.2 \pm 4.4\ \mathrm{fb}. \end{aligned}$$

By comparison, the SM NLO prediction from Powheg + PYTHIA8 is $53.4^{+1.6}_{-1.2}$ (PDF)$^{+2.1}_{-1.6}$ (scale) fb. This prediction is generated using the CT10 PDF set, with

Table 8.26 Observed and expected numbers of events after the WZ inclusive selection described in Sect. 8.4. The expected number of WZ events, and the estimates of the background, are shown as well, with their statistical, theoretical, and luminosity uncertainties

Channel	eee		μee		$e\mu\mu$		$\mu\mu\mu$		All	
Data	98		122		166		183		569	
Total expected	102	±10	118	±9	126	±11	160	±12	506	±38
WZ (Powheg + PYTHIA8)	74	±6	96	±8	97	±8	129	±10	396	±32
$Z + j, Z\gamma$	16	±7	7	±5	14	±7	9	±5	45	±17
ZZ	6.7	±0.7	8.7	±1.0	8.5	±0.9	11.7	±1.2	36	±4
$t\bar{t} + V$	2.7	±0.4	3.2	±0.4	2.9	±0.4	3.4	±0.5	12.1	±1.6
$t\bar{t}$, Wt, $WW + j$	1.2	±0.8	2.0	±0.9	2.4	±0.9	3.6	±1.5	9.2	±3.1
tZ	1.28	±0.20	1.65	±0.26	1.63	±0.26	2.12	±0.34	6.7	±1.1
VVV	0.24	±0.04	0.29	±0.05	0.27	±0.04	0.34	±0.05	1.14	±0.18

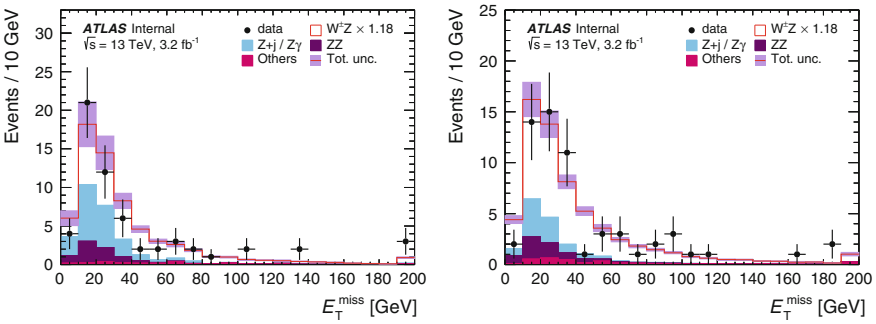

Fig. 8.19 Distribution of the missing transverse momentum in a subset of the WZ signal region containing events with $30 < m_{\mathrm{T}}^{W} < 50\,\mathrm{GeV}$, depicting eee and $e\mu\mu$ channels (left), and μee and $\mu\mu\mu$ channels (right). This region is enriched in ZZ, $Z+\mathrm{jet}$ and $Z\gamma$ compared to the rest of the SR. Backgrounds labeled "Others" consist of $t\bar{t}$, Wt, WW, tZ, $t\bar{t}V$, and VVV processes. The Powheg + PYTHIA8 MC prediction is used for the WZ signal contribution, scaled by a global factor of 1.18 to match the measured inclusive WZ cross section

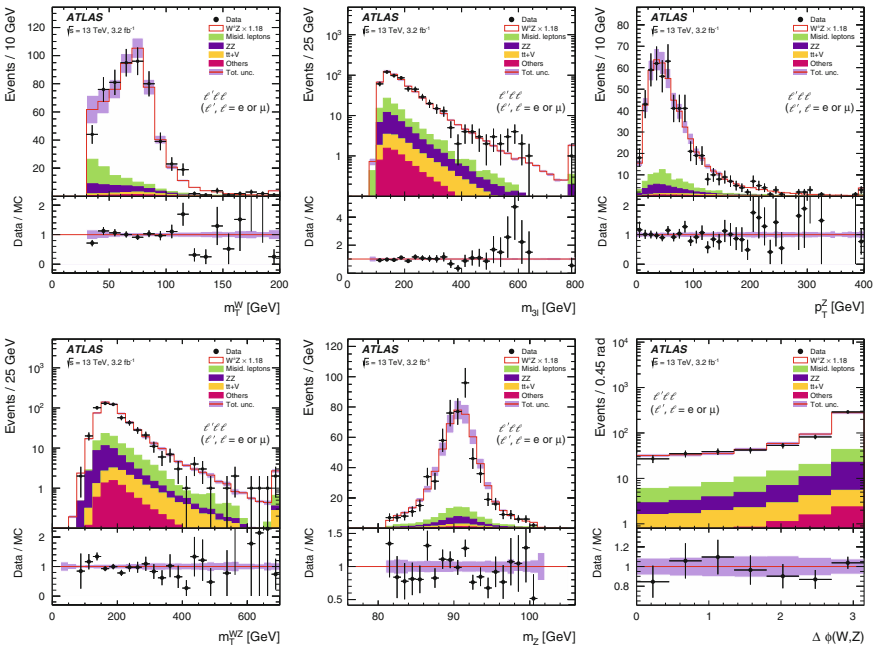

Fig. 8.20 Reconstructed signal-level distributions in the WZ signal region. The Powheg + PYTHIA8 MC prediction is used for the WZ signal contribution, scaled by a global factor of 1.18 to match the measured inclusive WZ cross section

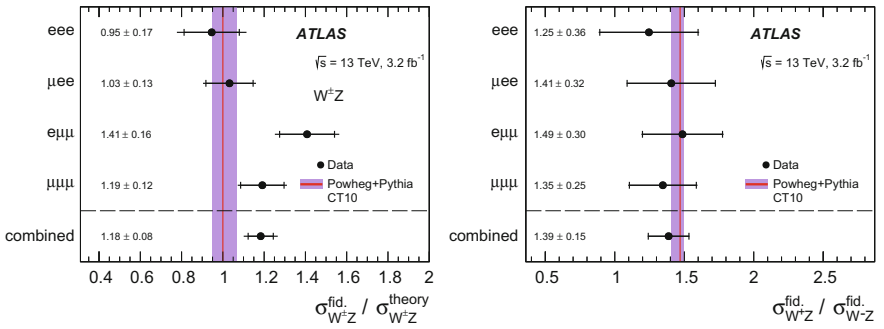

Fig. 8.21 Left: WZ fiducial cross section measurement comparisons, channel-by-channel, with the NLO theory prediction. Right: The W^+Z/W^-Z fiducial cross section ratio, compared to the NLO prediction

Table 8.27 Fiducial cross section results, in individual channels and after their combination. The NLO prediction is from Powheg + PYTHIA8

Channel	$\sigma^{\text{fid.}}$ [fb]	$\delta_{\text{stat.}}$ [%]	$\delta_{\text{sys.}}$ [%]	$\delta_{\text{lumi.}}$ [%]	$\delta_{\text{tot.}}$ [%]
$\sigma^{\text{fid.}}_{W^\pm Z \to \ell' \nu \ell \ell}$					
$e^\pm ee$	50.5	14.2	10.6	2.4	17.8
$\mu^\pm ee$	55.1	11.1	5.1	2.4	12.4
$e^\pm \mu\mu$	75.2	9.5	5.3	2.3	11.1
$\mu^\pm \mu\mu$	63.6	8.9	4.1	2.3	10.0
Combined	63.2	5.2	4.1	2.4	7.0
SM prediction	53.4	–	–	–	6.0

dynamic QCD scales $\mu_R = \mu_F = m_{WZ}/2$. PDF uncertainties are estimated using the CT10 eigenvector set, and by taking the envelope of CT10, CT14 [20], MMHT2014 [21] and NNPDF3.0 [22] NLO PDF sets. Scale uncertainties are evaluated by varying μ_R and μ_F up and down by a factor of two, using combinations satisfying $0.5 < \mu_R/\mu_F < 2$. Figure 8.21 shows the channel-by-channel comparisons between the 13 TeV measurement and the NLO prediction. A fiducial NNLO cross section prediction does not yet exist. The figure also shows the ratio of fiducial cross sections separately for W^+Z and W^-Z, along with the Powheg + PYTHIA8 predicted ratio; the data is in good agreement with the ratio prediction.

The combined fiducial cross section is extrapolated to the total phase space, defined in Sect. 8.2, using the acceptance factor A_{WZ} described in Sect. 8.6. The total cross section (including all leptonic and hadronic decay channels) is:

$$\begin{aligned} \sigma^{\text{tot.}}_{W^\pm Z} &= 50.6 \pm 2.6\,(\text{stat.}) \pm 2.0\,(\text{sys.}) \pm 0.9\,(\text{th.}) \pm 1.2\,(\text{lumi.})\text{pb} \\ &= 50.6 \pm 3.6\,\text{pb}. \end{aligned}$$

The SM NLO prediction from Powheg + PYTHIA8 is $42.4 \pm 0.8\,(\text{PDF}) \pm 1.6$ (scale) pb. A new NNLO calculation [2] obtained using MATRIX and using the NNPDF3.0 PDF set, with fixed scales $\mu_R = \mu_F = (m_W + m_Z)/2$, predicts $\sigma^{\text{tot.}}_{W^\pm Z} = 48.2^{+1.1}_{-1.0}\,(\text{scale})$ pb. Figure 8.22 shows the comparison between the ATLAS WZ measurements at $\sqrt{s} = 7$, 8, and 13 TeV, comparing with the NLO predictions in p–p and p–$\bar{p}$ collisions, and with the newest p–p NNLO prediction.

8.10 Prospects for Improving the WZ Measurement in 2016

One of the most promising ways in which the WZ measurement can be improved is through refinements in the $Z + \text{jet}/Z\gamma$ Fake Factor background estimate. Many of the fake background uncertainties are statistical in nature, and simply collecting more data will reduce these uncertainties. Table 8.28 shows the expected reduction of the Fake Factor estimate uncertainties with roughly 8 times more data in 2016, corresponding to the expected total collection of $25\,\text{fb}^{-1}$. The total uncertainty is reduced by 15%.

The remaining large systematic uncertainties include the electron composition uncertainty and the subtraction of the WZ/ZZ background in the Fake Factor Region; together these make up 25% of the total fake background uncertainty (the remaining uncertainties only contribute 10% in the projection scenario). These systematic uncertainties can be reduced by straightforward modifications to the event selection and the Fake Factor Method. An approach to improving the fake background determination includes the following:

1. Tightening the identification and isolation requirements on the lepton associated with the W boson. Fake leptons associated with the W account for 85% of $Z + \text{jet}/Z\gamma$ events and for 70% of $t\bar{t}$ events with a fake muon). In particular, the muon

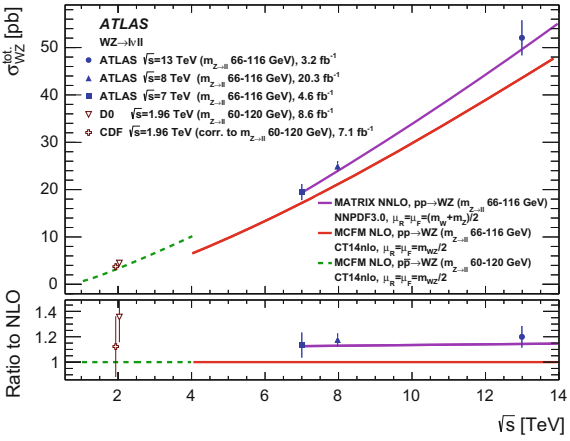

Fig. 8.22 ATLAS WZ measurements in p–p collisions, and CDF and D0 measurements in p–$\bar{p}$ collisions, compared to NLO and NNLO (in the p–p collision case) predictions

Table 8.28 Summary of the expected uncertainties, as a fraction of the total expected Z + jet, $Z\gamma$ and $t\bar{t}$ estimate, both in the 2015 data set and extrapolating the WZ reducible background estimate to 25 fb^{-1} of 13 TeV data

Uncertainties (%)		
Individual uncertainties	3.2 fb^{-1} dataset	25 fb^{-1} dataset
ZCR stat (data, MC)	2.8	1.0
Z FF WZ/ZZ subtraction	14.6	14.6
ZCR WZ/ZZ subtraction	0.8	0.8
Z muon FF stat	12.8	4.6
Z electron FF stat	12.2	4.4
Composition/closure (μ)	7.0	7.0
Composition/closure (ele)	20.9	20.9
Z FF $t\bar{t}$ μ SF MC+data stat	0.9	0.3
Z FF $t\bar{t}$ ele SF MC+data stat	1.0	0.4
ZCR $t\bar{t}$ region extrapolation	0.4	0.4
$t\bar{t}$ MC stat in SR	1.8	1.8
$t\bar{t}$ CR||SR mu SF MC+data stat	4.2	1.9
$t\bar{t}$ CR||SR ele SF MC+data stat	3.2	1.2
$t\bar{t}$ CR||SR extrapolation	0.3	0.3
Total uncertainty	32.4	27.4

isolation can be tightened from the Gradient Loose to the Gradient operating point.
2. Reducing the signal contamination in the Z Fake Factor Region with a fake muon, by lowering the maximum m_{T}^{W} requirement in that region. This is only possible when more data is available, and must be balanced with the low event yield of that region.
3. Improving the definition of the anti-id selection (denominator) of the electron fake factor to force the jet and γ fake factors closer to one another, in order to reduce the composition systematic uncertainty.

The last item can be achieved by tuning the anti-id electron definition using MC simulation until the jet and γ fake factors are identical in every p_{T} bin. However, using this procedure to change the selection criteria amounts to tuning the MC-based composition systematic uncertainty until it approaches 0. This approach would rely too much on the ability of the MC to accurately estimate the fake rates of the individual components, which we had tried to avoid in the first place by moving to data-driven methods. To avoid this consequence, the MC-based uncertainty should be replaced with a data-driven systematic treatment.

A data-driven composition systematic can be accomplished by understanding the fake composition in data using the nBlayerHits, impact parameter and isolation vari-

ables to enhance the denominator definition in either jet or γ fakes. The composition systematic can be estimated by modifying the denominator definition, using MC as a guide, to change the γ fraction by ± 20–50% (or some reasonable amount), and determining the resulting change in the Fake Factor result.

References

1. T. Gehrmann, M. Grazzini, S. Kallweit, P. Maierhfer, A. von Manteuffel, S. Pozzorini, D. Rathlev, and L. Tancredi, W^+W^- Production at hadron colliders in next to next to leading order QCD. Phys. Rev. Lett. **113**(21), 212001 (2014), arXiv:1408.5243 [hep-ph]
2. M. Grazzini, S. Kallweit, D. Rathlev, M. Wiesemann, $W^{\pm}Z$ production at hadron colliders in NNLO QCD. (2016), arXiv:1604.08576 [hep-ph]
3. F. Cascioli, T. Gehrmann, M. Grazzini, S. Kallweit, P. Maierhfer, A. von Manteuffel, S. Pozzorini, D. Rathlev, L. Tancredi, E. Weihs, ZZ production at hadron colliders in NNLO QCD. Phys. Lett. B **735**, 311–313 (2014), arXiv:1405.2219 [hep-ph]
4. C.D.F. Collaboration, T. Aaltonen et al., Measurement of the WZ Cross Section and Triple Gauge Couplings in $p\bar{p}$ Collisions at $\sqrt{s} = 1.96$ TeV. Phys. Rev. D **86**, 031104 (2012), arXiv:1202.6629 [hep-ex]
5. D0 Collaboration, V.M. Abazov et al., A measurement of the WZ and ZZ production cross sections using leptonic final states in 8.6 fb^{-1} of $p\bar{p}$ collisions. Phys. Rev. D **85**, 112005 (2012), arXiv:1201.5652 [hep-ex]
6. ATLAS Collaboration, Measurement of $W^{\pm}Z$ production in proton–proton collisions at $\sqrt{s} =$ 7 TeV with the ATLAS detector. Eur. Phys. J. C **72**, 2173 (2012), arXiv:1208.1390 [hep-ex]
7. ATLAS Collaboration, Measurements of $W^{\pm}Z$ production cross sections in pp collisions at $\sqrt{s} = 8$ TeV with the ATLAS detector and limits on anomalous gauge boson self-couplings. Phys. Rev. D **93**, 092004 (2016), arXiv:1603.02151 [hep-ex]
8. CMS Collaboration, Measurement of the WZ production cross section in pp collisions at sqrt(s) = 13 TeV, CMS-PAS-SMP-16-002 (2016), https://cdsweb.cern.ch/record/2201221
9. CMS Collaboration, *Measurement of WZ production rate*, CMS-PAS-SMP-12-006 (2013), https://cdsweb.cern.ch/record/1564318
10. ATLAS Collaboration, Measurement of the $W^{\pm}Z$ boson pair-production cross section in pp collisions at $\sqrt{s} = 13$ TeV with the ATLAS Detector. Phys. Lett. **B762**, 1–22 (2016), arXiv:1606.04017 [hep-ex]
11. ATLAS Collaboration, *Electron efficiency measurements with the ATLAS detector using the 2015 LHC proton-proton collision data*, ATLAS-CONF-2016-024 (2016), https://cds.cern.ch/record/2157687
12. ATLAS Collaboration, Muon reconstruction performance of the ATLAS detector in proton–proton collision data at $\sqrt{s}$ =13 TeV. Eur. Phys. J. **C76**(5), 292 (2016), arXiv:1603.05598 [hep-ex]
13. M. Cacciari, G.P. Salam, G. Soyez, The anti-k_t jet clustering algorithm. JHEP **04**, 063 (2008), arXiv:0802.1189 [hep-ph]
14. ATLAS Collaboration, *Performance of pile-up mitigation techniques for jets in pp collisions at* $\sqrt{s} = 8$ TeV *using the ATLAS detector*, arXiv:1510.03823 [hep-ex]
15. H1 Collaboration, F.D. Aaron et al., Measurement of the inclusive ep scattering cross section at low Q^2 and x at HERA. Eur. Phys. J. C **63**, 625–678 (2009), arXiv:0904.0929 [hep-ex]
16. K. Olive, P.D. Group, Review of particle physics. Chin. Phys. C **38**(9), 090001 (2014), http://stacks.iop.org/1674-1137/38/i=9/a=090001
17. ATLAS Collaboration, *Jet Calibration and Systematic Uncertainties for Jets Reconstructed in the ATLAS Detector at* $\sqrt{s} = 13$ TeV, ATL-PHYS-PUB-2015-015 (2015), https://cds.cern.ch/record/2037613

18. J. Alwall, R. Frederix, S. Frixione, V. Hirschi, F. Maltoni, O. Mattelaer, H.S. Shao, T. Stelzer, P. Torrielli, M. Zaro, The automated computation of tree-level and next-to-leading order differential cross sections, and their matching to parton shower simulations. JHEP **07**, 079 (2014), arXiv:1405.0301 [hep-ph]
19. ATLAS Collaboration, *Multi-boson simulation for* 13 TeV *ATLAS analyses*, ATL-PHYS-PUB-2016-002 (2016), http://cdsweb.cern.ch/record/2119986
20. S. Dulat, T.-J. Hou, J. Gao, M. Guzzi, J. Huston, P. Nadolsky, J. Pumplin, C. Schmidt, D. Stump, C.P. Yuan, New parton distribution functions from a global analysis of quantum chromodynamics. Phys. Rev. **D93**(3), 033006 (2016), arXiv:1506.07443 [hep-ph]
21. L.A. Harland-Lang, A.D. Martin, P. Motylinski, R.S. Thorne, Parton distributions in the LHC era: MMHT 2014 PDFs. Eur. Phys. J. **C75**(5), 204 (2015), arXiv:1412.3989 [hep-ph]
22. NNPDF Collaboration, R.D. Ball et al., Parton distributions for the LHC Run II. JHEP **04**, 040 (2015), arXiv:1410.8849 [hep-ph]

Chapter 9
Conclusions

This thesis presented fiducial and differential cross section measurements of the Higgs boson at $\sqrt{s} = 8\,\text{TeV}$ with the ATLAS detector, and fiducial and total cross section measurements of WZ diboson production at $\sqrt{s} = 13\,\text{TeV}$. The electron likelihood method of identification, first introduced in Run 1 and adapted for use in Run 2, is described in detail. Electron efficiency measurements of identification criteria are described as well, featuring methods developed in Run 1 and employed during Run 2 data taking.

The Higgs fiducial cross section and decay to four leptons (e or μ) at 8 TeV was measured to be $\sigma_{\text{fid}} = 2.11\ ^{+0.53}_{-0.47}\ (\text{stat})\ \pm 0.08\ (\text{syst})\,\text{fb}$, and can be compared to the theoretical prediction [1] of a Higgs with mass 125.4 GeV of $1.30 \pm 0.13\,\text{fb}$. Unfolded differential distributions of kinematic observables show no statistically significant deviation from the SM predictions according to a number of state-of-the-art generators.

The WZ fiducial cross section and decay to a leptonic channel in 13 TeV p–p collisions is measured to be $\sigma_{\text{fid}} = 63.2 \pm 3.2\ (\text{stat})\ \pm 2.6\ (\text{syst})\ \pm 1.5\ (\text{lumi})\,\text{fb}$. When extrapolated to the total phase space, the total cross section is $\sigma_{\text{tot}} = 50.6 \pm 2.6\ (\text{stat})\ \pm 2.0\ (\text{syst})\ \pm 0.9\ (\text{syst})\ \pm 1.2\ (\text{lumi})\,\text{pb}$, in good agreement with the recent NNLO calculation [2] predicting $48.2^{+1.1}_{-1.0}\,\text{pb}$.

References

1. LHC Higgs Cross Section Working Group Collaboration, J.R. Andersen et al. *Handbook of LHC Higgs Cross Sections: 3. Higgs Properties*, arXiv:1307.1347 [hep-ph]
2. M. Grazzini, S. Kallweit, D. Rathlev, M. Wiesemann, $W^{\pm}Z$ *production at hadron colliders in NNLO QCD*, arXiv:1604.08576 [hep-ph]

K. Brendlinger, *Physics with Electrons in the ATLAS Detector*, Springer Theses,
https://doi.org/10.1007/978-3-319-73930-4_9

Appendix A
Electron Identification

A.1 Correlation Between Electron Variables

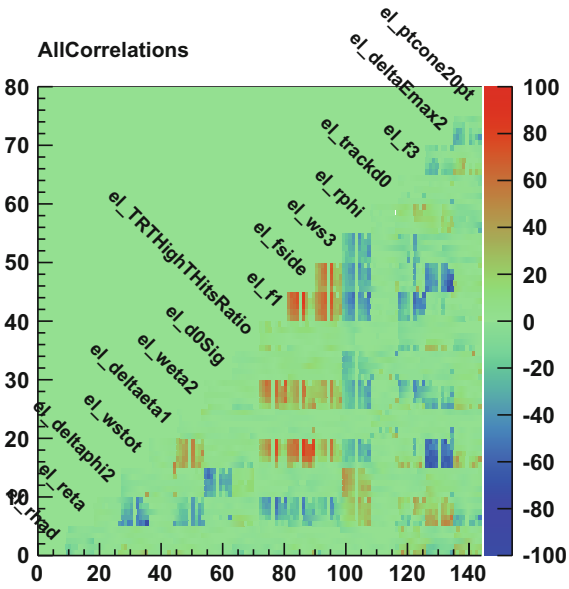

Fig. A.1 The electron correlations between variables for a representative sample of electron discriminants. The plot is arranged in blocks of 9×5 bins in $\eta \times E_{\mathrm{T}}$ in the range $10 < E_{\mathrm{T}} < 50\,\mathrm{GeV}$, using the nominal likelihood $|\eta|$ bins. (The crack, which appears as thin green lines, is excluded.) Each block represents the correlations between the variable label directly to the left and the variable label directly above it. The background correlations are not shown

K. Brendlinger, *Physics with Electrons in the ATLAS Detector*, Springer Theses,
https://doi.org/10.1007/978-3-319-73930-4

A.2 Electron Identification Variables

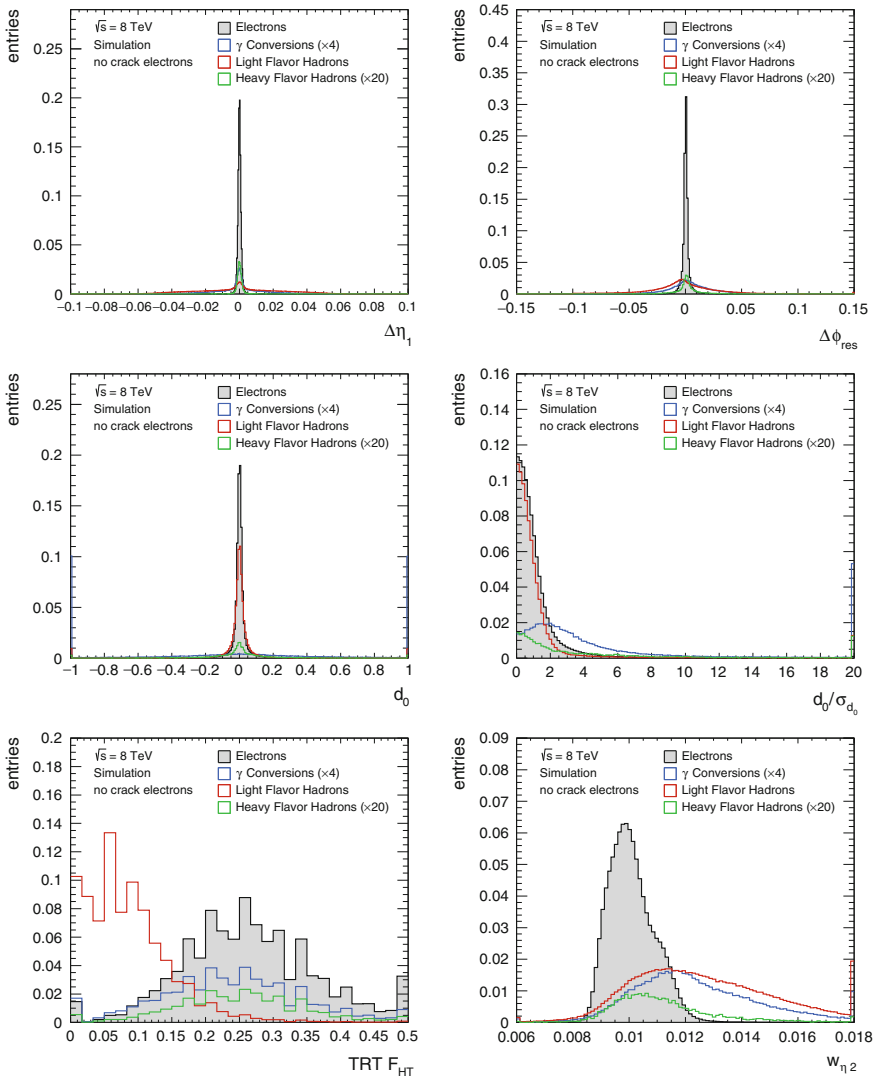

Fig. A.2 Electron identification variables (in 2012) comparing signal electrons from a $Z \rightarrow ee$ MC sample and backgrounds (converted photons, light flavor hadrons, and heavy flavor hadrons) taken from an MC sample (jf17) containing all $2 \rightarrow 2$ QCD processes

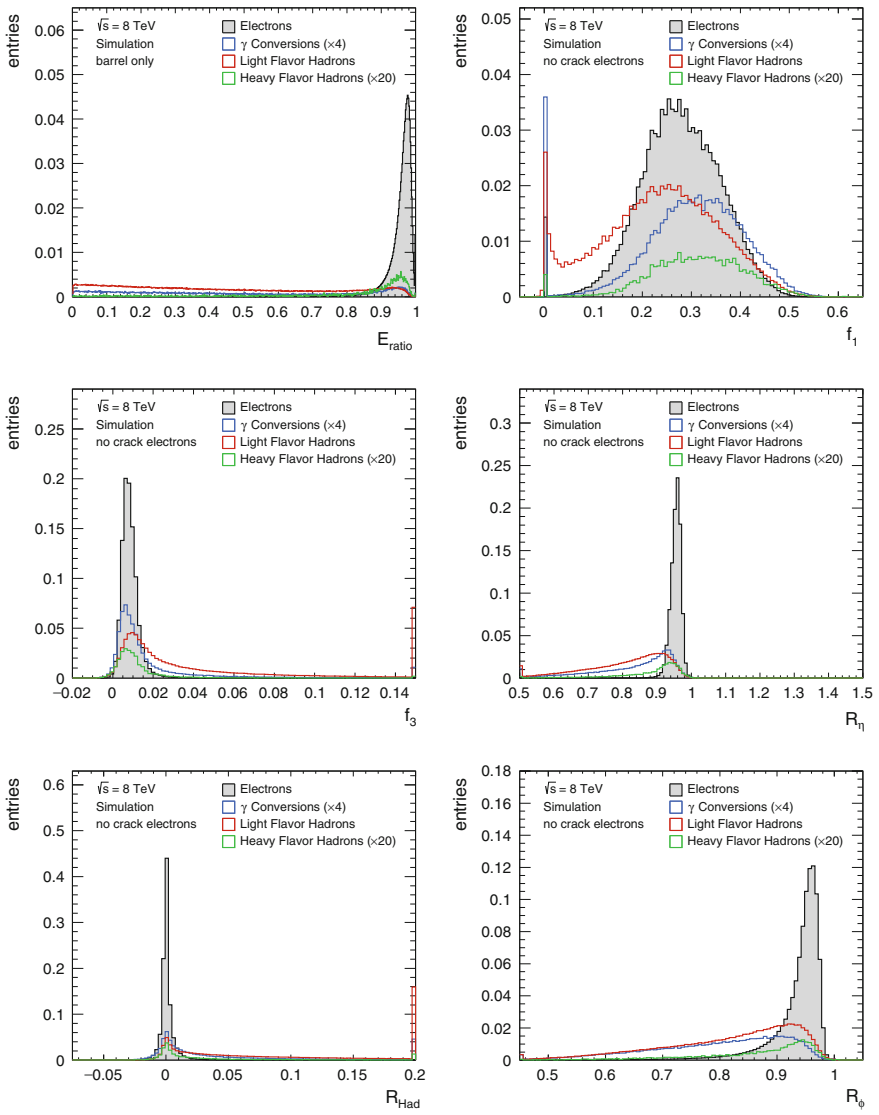

Fig. A.3 Electron identification variables (in 2012) comparing signal electrons from a $Z \rightarrow ee$ MC sample and backgrounds (converted photons, light flavor hadrons, and heavy flavor hadrons) taken from an MC sample (jf17) containing all $2 \rightarrow 2$ QCD processes

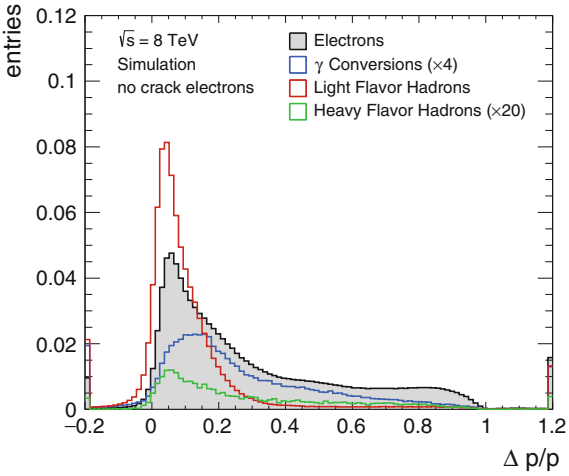

Fig. A.4 Electron identification variables (in 2012) comparing signal electrons from a $Z \rightarrow ee$ MC sample and backgrounds (converted photons, light flavor hadrons, and heavy flavor hadrons) taken from an MC sample (jf17) containing all $2 \rightarrow 2$ QCD processes

A.3 Shift and Width Parameters for 2015 MC

Table A.1 Width and shift parameters for 2015 MC. R_ϕ was not shifted in 2015, but shifts were derived after the likelihood menu was developed

Region	Shifts					Widths	
	f_1	f_3	R_η	$w_{\eta 2}$	R_ϕ *	$\Delta\eta_1$	$\Delta\phi_{\text{Res}}$
$0.0 < \lvert\eta\rvert < 0.6$	−0.00327	0.00125	−0.0033	0.000160	0.0016	1.2797	1.1947
$0.6 < \lvert\eta\rvert < 0.8$	−0.00563	0.00215	−0.0040	0.000192	0.0012	1.3207	0.9990
$0.8 < \lvert\eta\rvert < 1.15$	−0.00587	0.00249	−0.0047	0.000080	0.0032	1.4404	0.9966
$1.15 < \lvert\eta\rvert < 1.37$	−0.00697	0.00159	−0.0053	0.000112	0.0020	2.3864	1.0883
$1.37 < \lvert\eta\rvert < 1.52$	−0.00120	0.0	−0.0040	0.0	0.0008	2.1416	0.9990
$1.52 < \lvert\eta\rvert < 1.81$	0.00681	0.00227	−0.0060	0.000312	0.0024	2.2589	1.2992
$1.81 < \lvert\eta\rvert < 2.01$	−0.00240	0.00397	−0.0060	0.000376	0.0028	2.2757	1.3353
$2.01 < \lvert\eta\rvert < 2.37$	−0.00233	0.00623	−0.0080	0.000392	0.0028	2.1248	1.7113
$2.37 < \lvert\eta\rvert < 2.47$	−0.02567	0.02006	−0.0206	0.000592	−0.0004	2.2034	2.1612

A.4 Electron Supporting Triggers

Table A.2 Supporting triggers and effective prescales in 2012 and 2015

2012		
Trigger	Luminosity collected (nb)	Effective prescale
e24vhi_medium1	20517700.0	1.
e5_etcut	12335.7	1663.
e11_etcut	6315.39	3249.
g20_etcut	129.163	158851.
g24_etcut	2062.0	9950.
2015		
Trigger	Luminosity collected (nb)	Effective prescale
HLT_e24_lhmedium_iloose_L1EM20VH	3209050.0	1.
HLT_e5_etcut	3.5	921288.35
HLT_e10_etcut_L1EM7	27.4	117126.31
HLT_e15_etcut_L1EM7	81.4	39438.97
HLT_e20_etcut_L1EM12	190.9	16812.84
HLT_e25_etcut_L1EM15	358.7	8946.41
HLT_e30_etcut_L1EM15	601.5	5335.06
HLT_e40_etcut_L1EM15	1420.9	2258.46
HLT_e50_etcut_L1EM15	2862.7	1120.99
HLT_e60_etcut	5765.8	556.57
HLT_e80_etcut	14870.7	215.80
HLT_e100_etcut	33396.0	96.09
HLT_e120_etcut	67414.4	47.60
HLT_e5_lhvloose	41.0	78277.72
HLT_e10_lhvloose_L1EM7	93.9	34193.10
HLT_e15_lhvloose_L1EM7	422.3	7599.54
HLT_e20_lhvloose	8022.7	400
HLT_e25_lhvloose_L1EM15	2116.3	1516.33
HLT_e30_lhvloose_L1EM15	3637.6	882.18
HLT_e40_lhvloose_L1EM15	9149.1	350.75
HLT_e50_lhvloose_L1EM15	20479.2	156.70
HLT_e70_lhvloose	57534.1	55.78
HLT_e80_lhvloose	85505.6	37.53
HLT_e100_lhvloose	181762.0	17.66
HLT_e120_lhvloose	347573.0	9.23

A.5 Resolution of Electron Identification Variables at Trigger Level

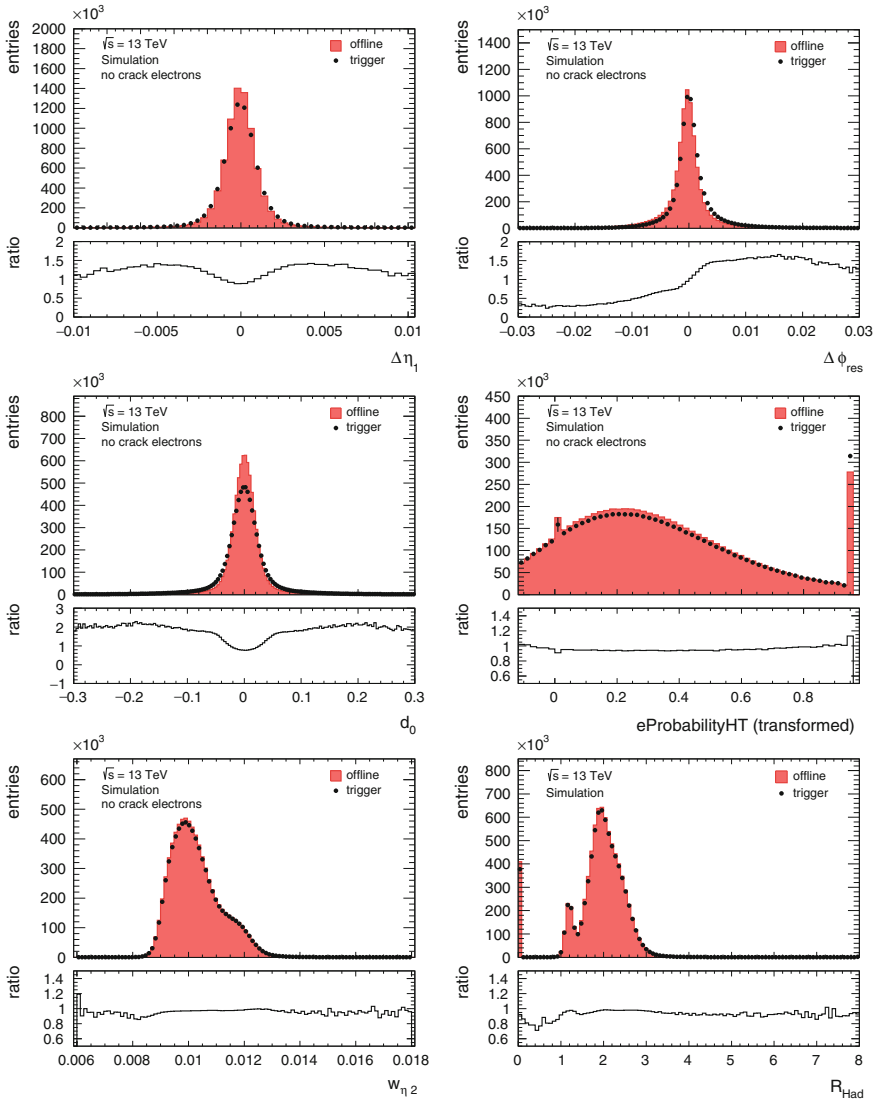

Fig. A.5 Online and offline electron identification variables (in 2015) for simulated samples of electrons from $Z \rightarrow ee$ at $\sqrt{s} = 13$ TeV

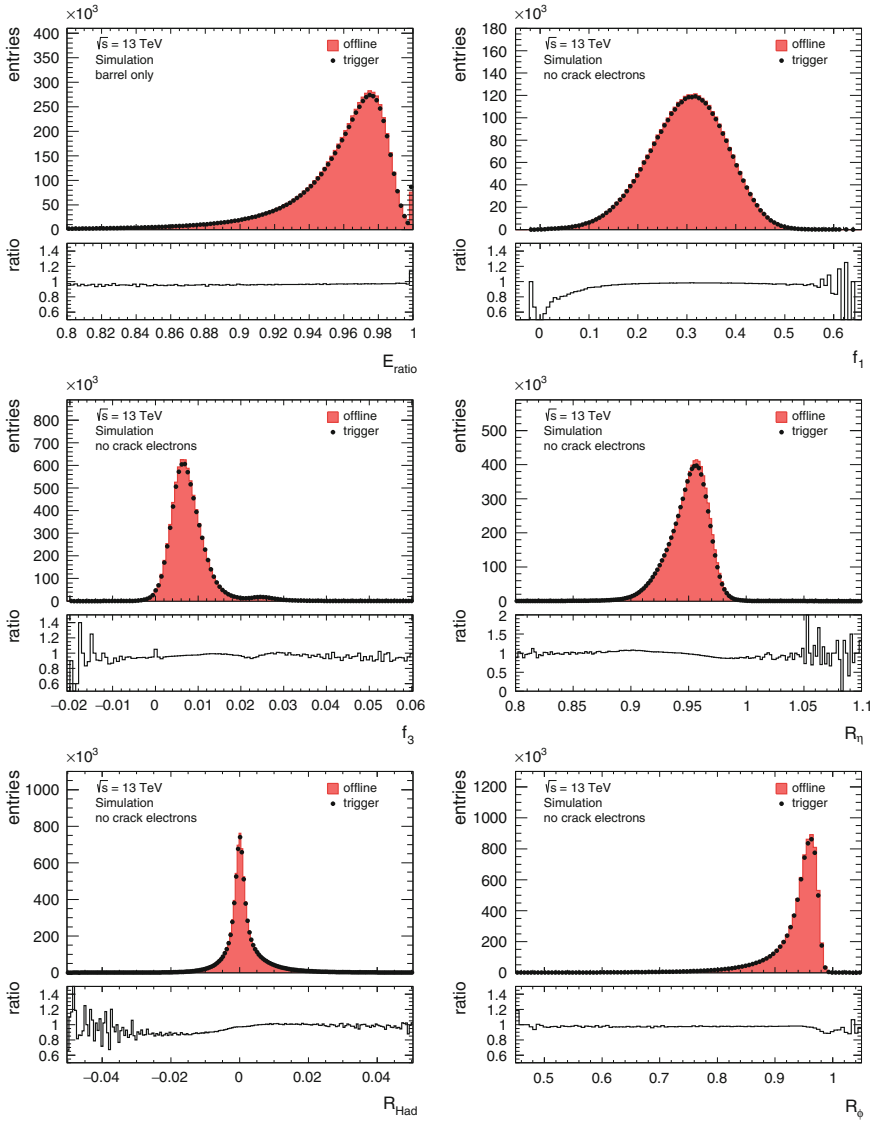

Fig. A.6 Online and offline electron identification variables (in 2015) for simulated samples of electrons from $Z \rightarrow ee$ at $\sqrt{s} = 13$ TeV

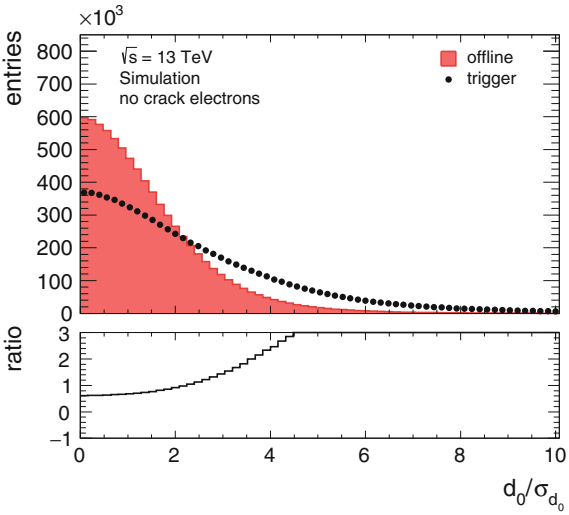

Fig. A.7 Online and offline electron identification variables (in 2015) for simulated samples of electrons from $Z \to ee$ at $\sqrt{s} = 13$ TeV

Appendix B
Electron Efficiency Measurements

B.1 Tag and Probe Methodology

This section describes the methodology behind the tag-and-probe method. To illustrate the method, we will seek the efficiency of a MEDIUM menu over the entire $\eta \times p_{\mathrm{T}}$ spectrum ($p_{\mathrm{T}} > 15\,\mathrm{GeV}$), using events collected with a TIGHT trigger with threshold $p_{\mathrm{T}} > 25\,\mathrm{GeV}$. We also assume for simplicity that the TIGHT trigger selection is a subset of the MEDIUM menu.

Given these conditions, there are 3 types of events in our sample and one type of event missing from the sample:

- N_{tt} = Number of Z events where both electrons pass tag requirement
- $N_{t,m!t}$ = Number of Z events where one electron passes the tag and the other electron passes MEDIUM but fails TIGHT
- $N_{t,!m}$ = Number of Z events where one electron passes the tag and the other electron fails MEDIUM.
- $N_{!m,!m}$ = Number of Z events where both electrons fail

We don't have $N_{!m,!m}$ events at our disposal, since we don't trigger on them. Now define ε_m and ε_t as the MEDIUM and TIGHT efficiencies, respectively, and $\varepsilon_{m!t}$ the efficiency of passing MEDIUM but failing TIGHT. Then

$$N_{t,m!t} = (2\varepsilon_t \varepsilon_{m!t}) N_Z \tag{B.1}$$

$$N_{t,t} = \varepsilon_t^2 N_Z \tag{B.2}$$

$$N_{t,!m} = 2\varepsilon_t (1 - \varepsilon_{m!t} - \varepsilon_t) N_Z \,. \tag{B.3}$$

Now we assert the following: that the final expression for the MEDIUM efficiency is:

$$\varepsilon = \frac{N_{t,m!t} + 2N_{tt}}{N_{t,m!t} + 2N_{tt} + N_{t,!m}} \,. \tag{B.4}$$

K. Brendlinger, *Physics with Electrons in the ATLAS Detector*, Springer Theses,
https://doi.org/10.1007/978-3-319-73930-4

The N_Z in each term of the numerator and denominator cancel. Making substitutions:

$$\begin{aligned}\varepsilon &= \frac{2\varepsilon_t\varepsilon_{m!t} + 2\varepsilon_t^2}{2\varepsilon_t^2 + 2\varepsilon_t\varepsilon_{m!t} + 2\varepsilon_t(1-\varepsilon_{m!t}-\varepsilon_t)} \\ &= \frac{\varepsilon_t(\varepsilon_{m!t}+\varepsilon_t)}{\varepsilon_t(\varepsilon_t+\varepsilon_{m!t}+1-\varepsilon_{m!t}-\varepsilon_t)} \\ &= \varepsilon_{m!t}+\varepsilon_t = \varepsilon_m\,, \end{aligned} \tag{B.5}$$

which is the quantity we sought.

This simple example can be extended to apply to measurements binned in p_{T} and η, with similar principles but more terms. Cases also exist in which the tag is not a subset of the probe (as in the case of measuring a TIGHT efficiency using a tag electron collected using a MEDIUM online trigger menu and passing MEDIUM offline requirements), or the tag is neither a subset nor a superset of the probe (as in the case of measuring trigger menus with trigger reconstruction inputs that have different resolutions, or measuring likelihood efficiencies calculated using cut-based trigger menus). These cases are left to the reader to verify.

Appendix C
$H \rightarrow ZZ^* \rightarrow 4\ell$ Measurement

C.1 Theoretical Differential Predictions from Powheg

Table C.1 Differential cross section in $p_{T4\ell}$ and theoretical uncertainties for the Higgs ggF process based on the POWHEG prediction (fb/GeV). MC stat uncertainties are taken from the statistical error on the nominal sample. The total error is taken as the MC stat, scale, PDF choice, and PDF eigenvector uncertainties added in quadrature

$p_{T4\ell}$ [GeV]	$0 < p_{\mathrm{T}} < 20$	$20 < p_{\mathrm{T}} < 50$	$50 < p_{\mathrm{T}} < 100$	$100 < p_{\mathrm{T}} < 200$
Diff xsec	0.0164	0.0129	0.0051	0.0012
MC stat	0.3%	0.3%	0.4%	0.6%
Scale up	19.7%	20.5%	19.3%	20.2%
Scale down	16.2%	15.6%	15.7%	16.2%
PDF choice up	1.4%	1.4%	1.4%	1.4%
PDF choice down	0.0%	0.0%	0.0%	0.0%
CT10 eigen up	1.2%	1.2%	1.2%	1.2%
CT10 eigen dn	1.1%	1.1%	1.1%	1.1%
Total err up	19.8%	20.6%	19.4%	20.3%
Total err dn	16.2%	15.6%	15.8%	16.3%

K. Brendlinger, *Physics with Electrons in the ATLAS Detector*, Springer Theses,
https://doi.org/10.1007/978-3-319-73930-4

Table C.2 Differential cross section in $|y|_{4\ell}$ and theoretical uncertainties for the Higgs ggF process based on the POWHEG prediction (fb). MC stat uncertainties are taken from the statistical error on the nominal sample. The total error is taken as the MC stat, scale, PDF choice, and PDF eigenvector uncertainties added in quadrature

$\|y_{4\ell}\|$	$0 < \|y\| < 0.3$	$0.3 < \|y\| < 0.65$	$0.65 < \|y\| < 1.0$	$1.0 < \|y\| < 1.4$	$1.4 < \|y\| < 2.4$
Diff xsec	0.7836	0.7474	0.6904	0.5891	0.2275
MC stat	0.4%	0.4%	0.4%	0.5%	0.4%
Scale up	19.5%	20.5%	20.6%	19.8%	19.4%
Scale down	16.1%	15.6%	15.9%	15.8%	16.1%
PDF choice up	1.6%	1.6%	1.7%	1.6%	0.7%
PDF choice down	0.1%	0.1%	0.0%	0.0%	0.0%
CT10 eigen up	2.4%	2.2%	1.8%	1.1%	0.9%
CT10 eigen dn	1.8%	1.7%	1.4%	1.1%	1.4%
Total err up	19.7%	20.7%	20.8%	19.9%	19.5%
Total err dn	16.2%	15.7%	16.0%	15.8%	16.2%

Table C.3 Differential cross section in m_{34} and theoretical uncertainties for the Higgs ggF process based on the POWHEG prediction (fb). MC stat uncertainties are taken from the statistical error on the nominal sample. The total error is taken as the MC stat, scale, PDF choice, and PDF eigenvector uncertainties added in quadrature

m_{34} [GeV]	$12 < m_{34} < 20$	$20 < m_{34} < 30$	$30 < m_{34} < 40$	$40 < m_{34} < 60$
Diff xsec	0.0244	0.0487	0.0303	0.0065
MC stat	0.5%	0.3%	0.4%	0.6%
Scale up	20.8%	19.3%	20.6%	19.8%
Scale down	15.8%	16.3%	15.5%	16.3%
PDF choice up	1.4%	1.4%	1.4%	1.4%
PDF choice down	−0.0%	−0.0%	−0.0%	−0.0%
CT10 eigen up	1.2%	1.2%	1.2%	1.2%
CT10 eigen dn	1.1%	1.1%	1.1%	1.1%
Total err up	20.9%	19.4%	20.6%	19.9%
Total err dn	15.9%	16.4%	15.6%	16.4%

Table C.4 Differential cross section in $|\cos(\theta^*)|$ and theoretical uncertainties for the Higgs ggF process based on the POWHEG prediction (fb). MC stat uncertainties are taken from the statistical error on the nominal sample. The total error is taken as the MC stat, scale, PDF choice, and PDF eigenvector uncertainties added in quadrature

$\|\cos(\theta^*)\|$	$0 < \|c\| < 0.2$	$0.2 < \|c\| < 0.4$	$0.4 < \|c\| < 0.6$	$0.6 < \|c\| < 0.8$	$0.8 < \|c\| < 1.0$
Diff xsec	1.1638	1.1549	1.1389	1.0877	1.0384
MC stat	0.4%	0.4%	0.4%	0.4%	0.4%
Scale up	20.3%	19.9%	18.9%	20.4%	20.2%
Scale down	15.3%	15.6%	16.7%	15.9%	15.9%
PDF choice up	1.4%	1.4%	1.4%	1.4%	1.4%
PDF choice down	0.0%	0.0%	0.0%	0.0%	0.0%
CT10 eigen up	1.2%	1.2%	1.3%	1.3%	1.3%
CT10 eigen dn	1.0%	1.0%	1.1%	1.1%	1.1%
Total err up	20.4%	20.0%	19.0%	20.5%	20.3%
Total err dn	15.4%	15.6%	16.7%	16.0%	15.9%

Table C.5 Differential cross section in N_{jets} and theoretical uncertainties for the Higgs ggF process based on the POWHEG prediction (fb). MC stat uncertainties are taken from the statistical error on the nominal sample. The Stewart-Tackmann procedure is used for the QCD scale uncertainty. The total error is taken as the MC stat, scale (ST), PDF choice, and PDF eigenvector uncertainties added in quadrature

N_{jets}	0 jets	1 jet	2 jets	$\geq$3 jets
Diff xsec	0.6121	0.3506	0.1104	0.0441
MC stat	0.3%	0.3%	0.6%	1.0%
Scale (ST) up	39.8%	30.1%	29.1%	20.6%
Scale (ST) down	32.0%	24.3%	23.6%	16.7%
PDF choice up	1.3%	1.4%	1.4%	1.4%
PDF choice down	0.0%	0.0%	0.0%	0.0%
CT10 eigen up	1.1%	1.2%	1.2%	1.2%
CT10 eigen dn	1.2%	1.0%	1.1%	1.1%
Total err up	39.8%	30.1%	29.2%	20.7%
Total err dn	32.0%	24.3%	23.6%	16.8%

Table C.6 Differential cross section in $p_{T,jet1}$ and theoretical uncertainties for the Higgs ggF process based on the POWHEG prediction (fb). MC stat uncertainties are taken from the statistical error on the nominal sample. The total error is taken as the MC stat, scale, PDF choice, and PDF eigenvector uncertainties added in quadrature

$p_{T,jet1}$ [GeV]	$0 < p_{T,jet} < 30$	$30 < p_{T,jet} < 50$	$50 < p_{T,jet} < 70$	$70 < p_{T,jet} < 140$
Diff xsec	0.0204	0.0101	0.0056	0.0021
MC stat	0.3%	0.4%	0.6%	0.5%
Scale up	19.7%	19.4%	21.8%	19.8%
Scale down	15.8%	16.3%	15.6%	16.4%
PDF choice up	1.3%	1.4%	1.4%	1.4%
PDF choice down	0.0%	0.0%	0.0%	0.0%
CT10 eigen up	1.1%	1.2%	1.2%	1.2%
CT10 eigen dn	1.2%	1.1%	1.1%	1.1%
Total err up	19.8%	19.5%	21.9%	19.9%
Total err dn	15.9%	16.4%	15.6%	16.4%

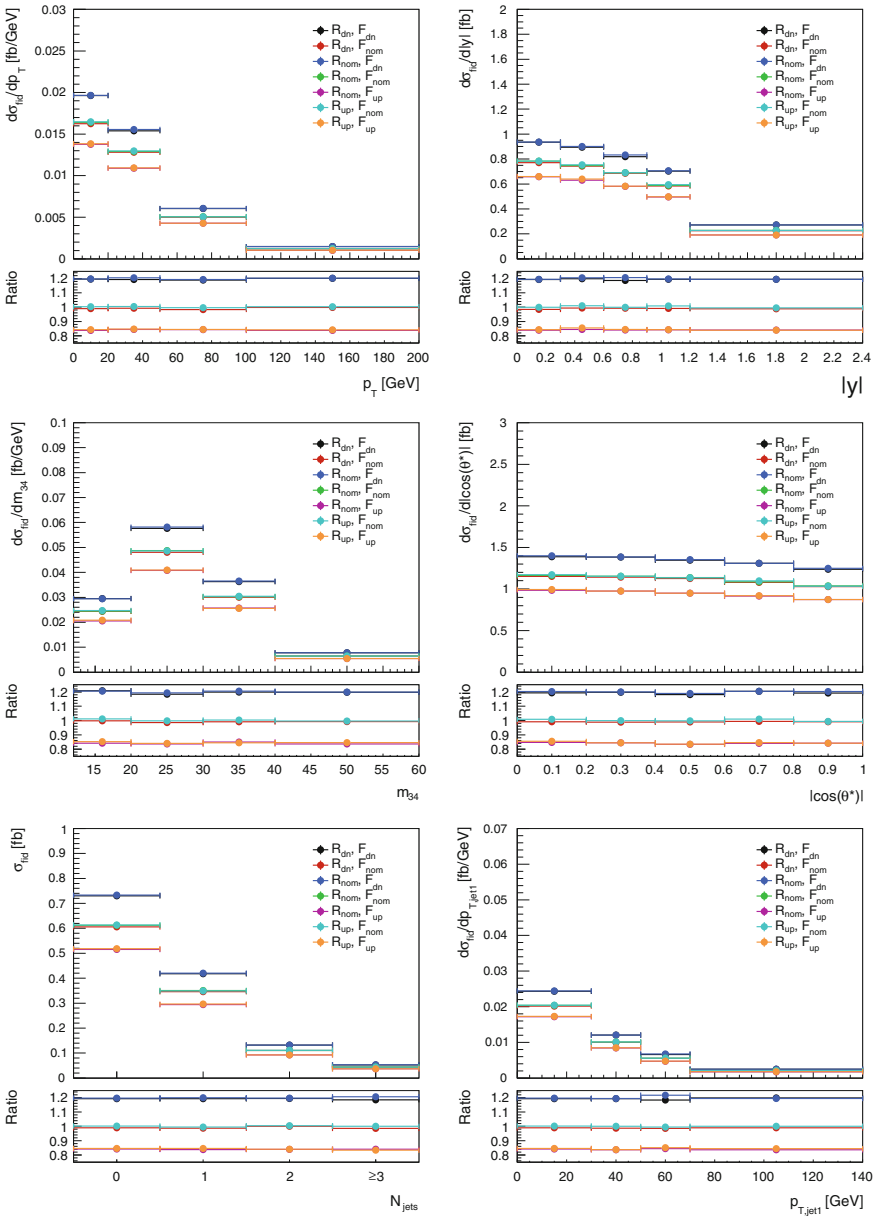

Fig. C.1 Comparisons of the 7 scale variations for a 125.4 GeV Higgs sample generated using POWHEG. The ratio plots underneath are with respect to the nominal (R_{nom}, F_{nom})

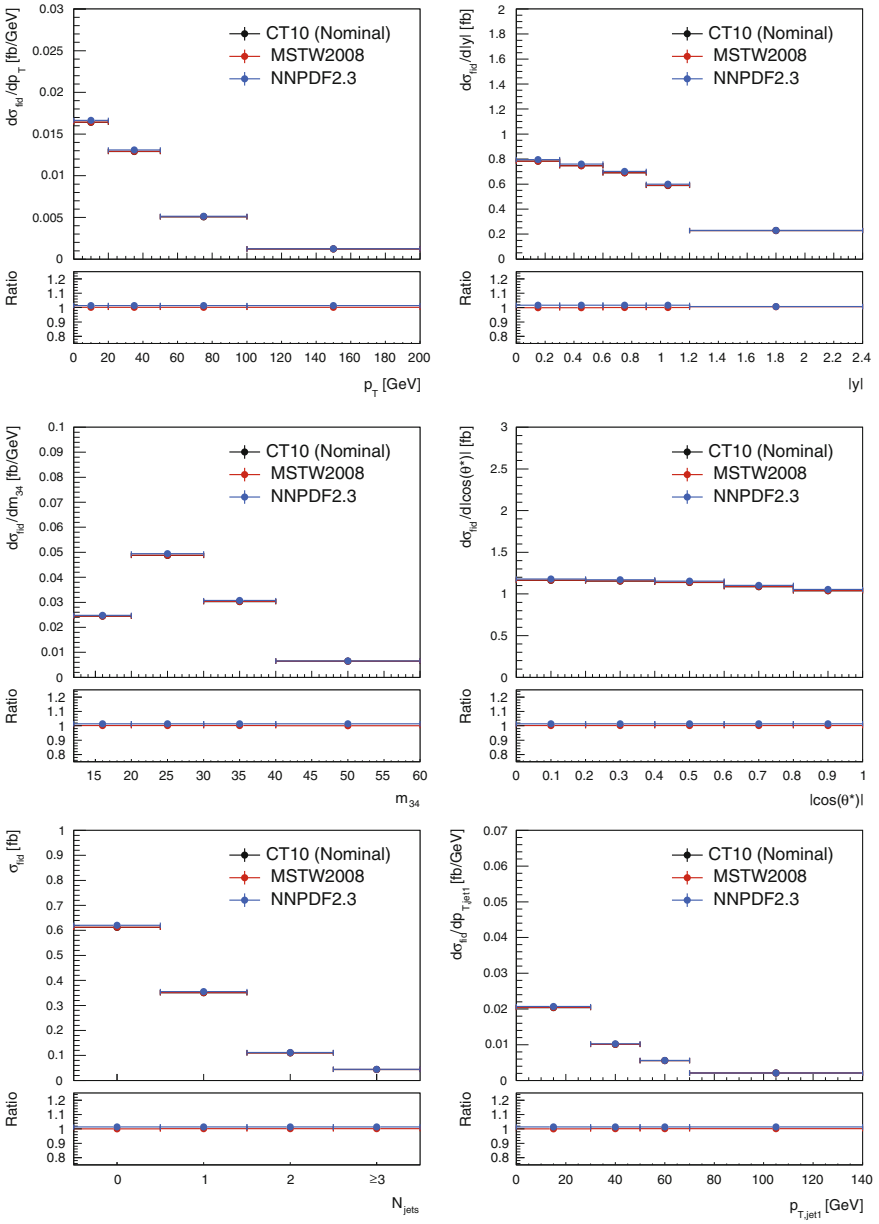

Fig. C.2 Comparisons of the nominal POWHEG generated sample (CT10) and the MSTW2008 and NNPDF2.1 PDF variations, for a 125.4 GeV Higgs. The ratio plots underneath are with respect to the nominal (CT10)

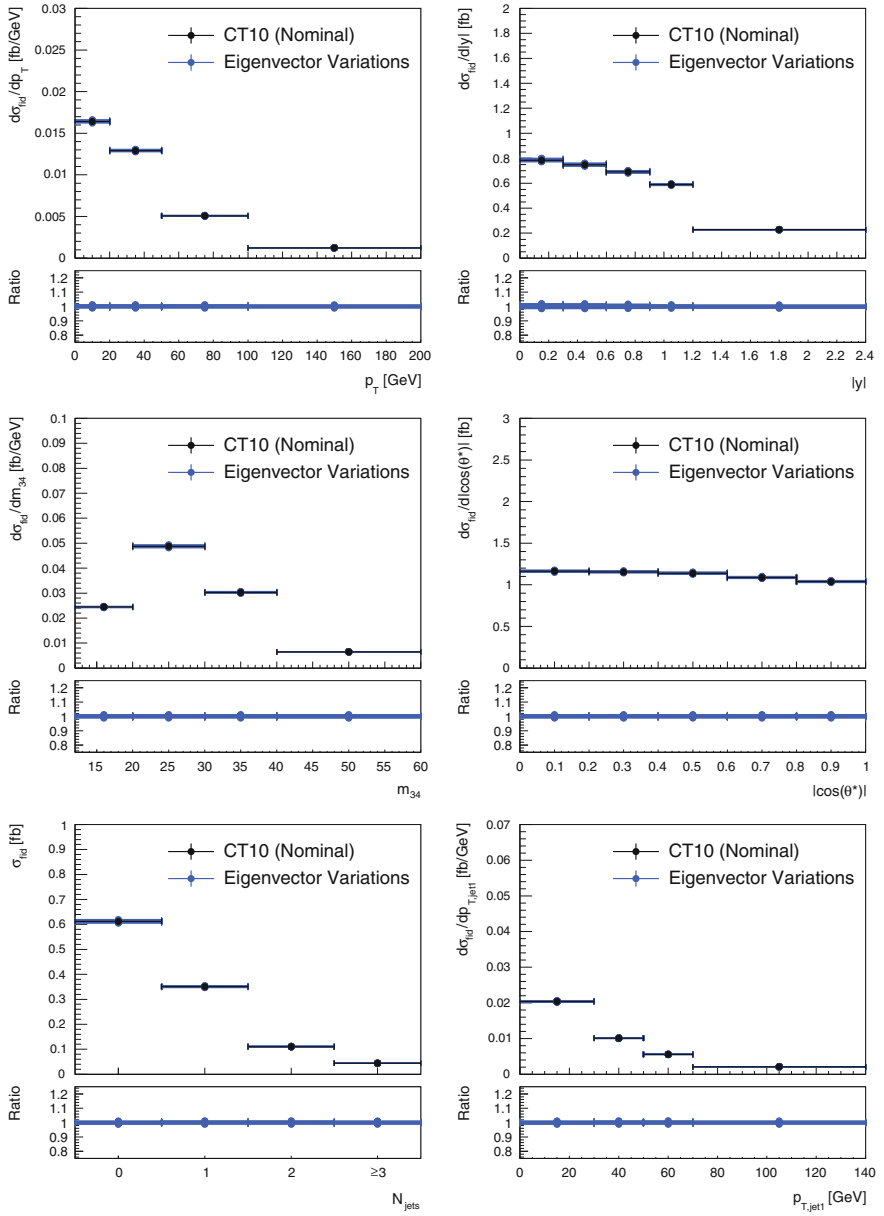

Fig. C.3 Comparisons of the nominal POWHEG generated sample and the 52 (26 up and 26 down) CT10 eigenvector variations, for a 125.4 GeV Higgs. The ratio plots underneath are with respect to the nominal eigenvector variation

C.2 Theoretical Differential Predictions from Minlo

Table C.7 Differential cross section in $p_{T4\ell}$ and theoretical uncertainties for the Higgs ggF process based on the Minlo prediction (fb/GeV). MC stat uncertainties are taken from the statistical error on the nominal sample. The total error is taken as the MC stat, scale, PDF choice, and PDF eigenvector uncertainties added in quadrature

$p_{T4\ell}$ [GeV]	$0 < p_{\mathrm{T}} < 20$	$20 < p_{\mathrm{T}} < 50$	$50 < p_{\mathrm{T}} < 100$	$100 < p_{\mathrm{T}} < 200$
Diff xsec	0.0204	0.0129	0.0042	0.0008
MC stat	0.5%	0.5%	0.6%	0.9%
Scale up	38.9%	28.3%	29.7%	28.9%
Scale down	13.5%	14.1%	17.1%	20.9%
PDF choice up	0.3%	1.4%	2.4%	2.9%
PDF choice down	2.9%	0.0%	0.0%	0.0%
CT10 eigen up	2.3%	1.2%	1.2%	2.5%
CT10 eigen dn	3.4%	1.4%	1.5%	2.5%
Total err up	39.0%	28.4%	29.8%	29.2%
Total err dn	14.2%	14.2%	17.2%	21.1%

Table C.8 Differential cross section in $|y|_{4\ell}$ and theoretical uncertainties for the Higgs ggF process based on the Minlo prediction (fb). MC stat uncertainties are taken from the statistical error on the nominal sample. The total error is taken as the MC stat, scale, PDF choice, and PDF eigenvector uncertainties added in quadrature

$\lvert y\rvert_{4\ell}$	$0 < \lvert y\rvert < 0.3$	$0.3 < \lvert y\rvert < 0.65$	$0.65 < \lvert y\rvert < 1.0$	$1.0 < \lvert y\rvert < 1.4$	$1.4 < \lvert y\rvert < 2.4$
Diff xsec	0.7830	0.7424	0.6905	0.5834	0.2236
MC stat	0.6%	0.6%	0.7%	0.7%	0.6%
Scale up	30.2%	32.3%	33.4%	32.7%	32.2%
Scale down	14.3%	14.6%	14.5%	14.5%	14.7%
PDF choice up	1.2%	1.1%	1.4%	1.3%	0.6%
PDF choice down	0.0%	0.0%	0.1%	0.0%	0.0%
CT10 eigen up	2.2%	2.0%	1.6%	0.9%	0.8%
CT10 eigen dn	2.2%	2.0%	1.8%	1.3%	1.9%
Total err up	30.3%	32.3%	33.4%	32.8%	32.2%
Total err dn	14.5%	14.7%	14.7%	14.5%	14.8%

Table C.9 Differential cross section in m_{34} and theoretical uncertainties for the Higgs ggF process based on the Minlo prediction (fb). MC stat uncertainties are taken from the statistical error on the nominal sample. The total error is taken as the MC stat, scale, PDF choice, and PDF eigenvector uncertainties added in quadrature

m_{34} [GeV]	$12 < m_{34} < 20$	$20 < m_{34} < 30$	$30 < m_{34} < 40$	$40 < m_{34} < 60$
Diff xsec	0.0244	0.0482	0.0302	0.0064
MC stat	0.7%	0.4%	0.6%	0.8%
Scale up	34.0%	32.4%	30.6%	31.3%
Scale down	14.8%	14.6%	14.2%	14.2%
PDF choice up	1.0%	1.1%	1.1%	1.1%
PDF choice down	−0.0%	−0.0%	−0.0%	−0.0%
CT10 eigen up	0.9%	1.0%	1.0%	1.0%
CT10 eigen dn	1.2%	1.3%	1.4%	1.5%
Total err up	34.0%	32.4%	30.7%	31.3%
Total err dn	14.9%	14.7%	14.3%	14.3%

Table C.10 Differential cross section in $|\cos(\theta^*)|$ and theoretical uncertainties for the Higgs ggF process based on the Minlo prediction (fb). MC stat uncertainties are taken from the statistical error on the nominal sample. The total error is taken as the MC stat, scale, PDF choice, and PDF eigenvector uncertainties added in quadrature

$\lvert\cos(\theta^*)\rvert$	$0 < \lvert c\rvert < 0.2$	$0.2 < \lvert c\rvert < 0.4$	$0.4 < \lvert c\rvert < 0.6$	$0.6 < \lvert c\rvert < 0.8$	$0.8 < \lvert c\rvert < 1.0$
Diff xsec	1.1692	1.1467	1.1256	1.0761	1.0249
MC stat	0.6%	0.6%	0.6%	0.6%	0.7%
Scale up	32.4%	32.9%	30.4%	31.1%	33.7%
Scale down	14.6%	14.6%	14.3%	14.3%	14.8%
PDF choice up	1.0%	1.1%	1.1%	1.1%	1.0%
PDF choice down	0.0%	0.0%	0.0%	0.0%	0.0%
CT10 eigen up	0.9%	1.0%	1.0%	1.0%	1.0%
CT10 eigen dn	1.4%	1.4%	1.3%	1.4%	1.4%
Total err up	32.5%	32.9%	30.5%	31.1%	33.7%
Total err dn	14.7%	14.7%	14.3%	14.4%	14.9%

Table C.11 Differential cross section in N_{jets} and theoretical uncertainties for the Higgs ggF process based on the Minlo prediction (fb). MC stat uncertainties are taken from the statistical error on the nominal sample. The Stewart-Tackmann procedure is used for the QCD scale uncertainty. The total error is taken as the MC stat, scale (ST), PDF choice, and PDF eigenvector uncertainties added in quadrature

N_{jets}	0 jets	1 jet	2 jets	$\geq$3 jets
Diff xsec	0.6834	0.3013	0.0927	0.0317
MC stat	0.4%	0.5%	0.8%	1.4%
Scale (ST) up	55.0%	42.6%	41.8%	30.1%
Scale (ST) down	25.9%	25.6%	26.4%	20.5%
PDF choice up	0.8%	1.9%	2.9%	2.6%
PDF choice down	1.3%	0.0%	0.0%	0.0%
CT10 eigen up	1.7%	1.0%	2.5%	4.2%
CT10 eigen dn	2.8%	1.3%	2.5%	3.9%
Total err up	55.0%	42.7%	41.9%	30.5%
Total err dn	26.1%	25.6%	26.6%	20.9%

Table C.12 Differential cross section in $p_{T,jet1}$ and theoretical uncertainties for the Higgs ggF process based on the Minlo prediction (fb). MC stat uncertainties are taken from the statistical error on the nominal sample. The total error is taken as the MC stat, scale, PDF choice, and PDF eigenvector uncertainties added in quadrature

$p_{T,jet1}$ [GeV]	$0 < p_{T,jet} < 30$	$30 < p_{T,jet} < 50$	$50 < p_{T,jet} < 70$	$70 < p_{T,jet} < 140$
Diff xsec	0.0228	0.0094	0.0047	0.0016
MC stat	0.4%	0.6%	0.8%	0.8%
Scale up	34.9%	28.4%	28.7%	30.1%
Scale down	13.8%	15.0%	16.8%	20.0%
PDF choice up	0.8%	1.8%	2.1%	2.6%
PDF choice down	1.3%	0.0%	0.0%	0.0%
CT10 eigen up	1.7%	1.0%	1.2%	2.0%
CT10 eigen dn	2.8%	1.2%	1.5%	2.1%
Total err up	34.9%	28.5%	28.8%	30.3%
Total err dn	14.1%	15.1%	16.9%	20.2%

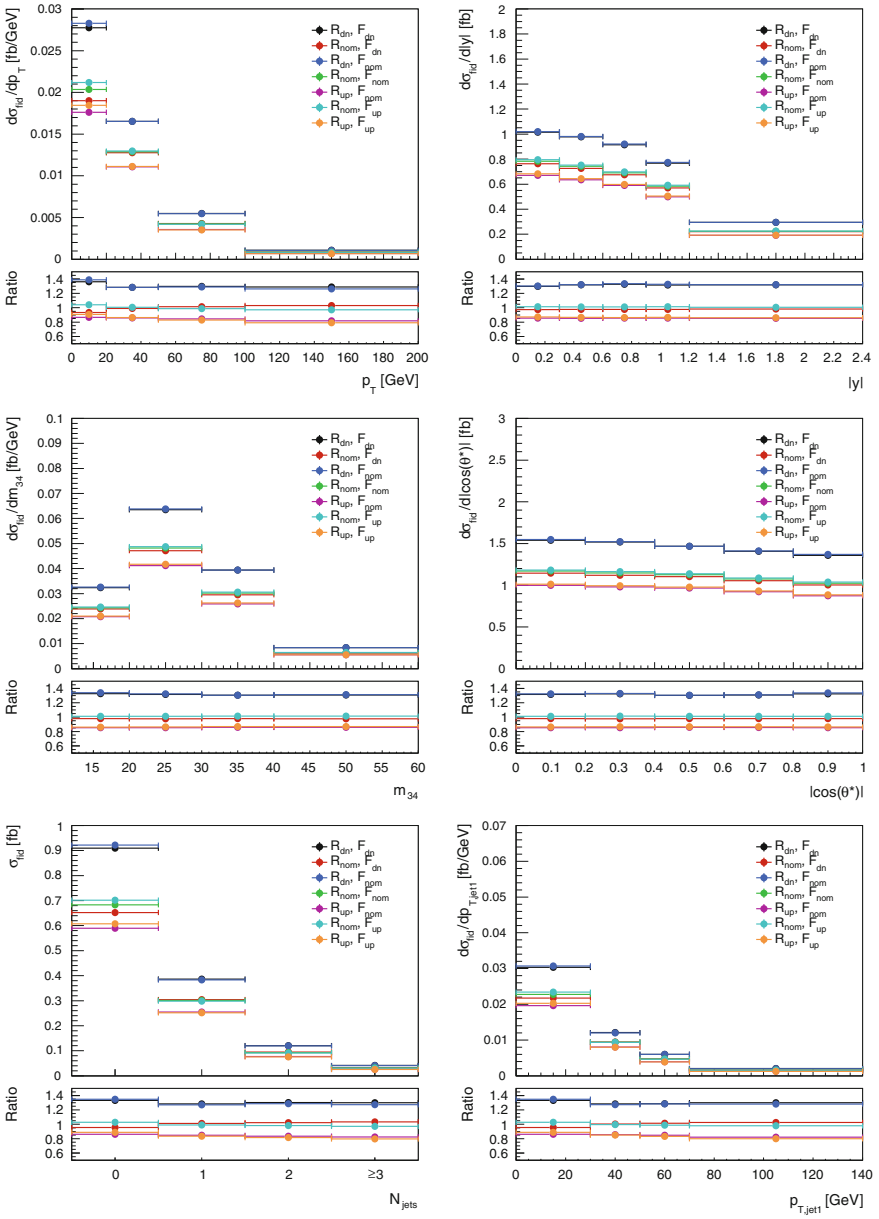

Fig. C.4 Comparisons of the 7 scale variations for a 125.4 GeV Higgs sample generated using H+1j. The ratio plots underneath are with respect to the nominal (R_{nom}, F_{nom})

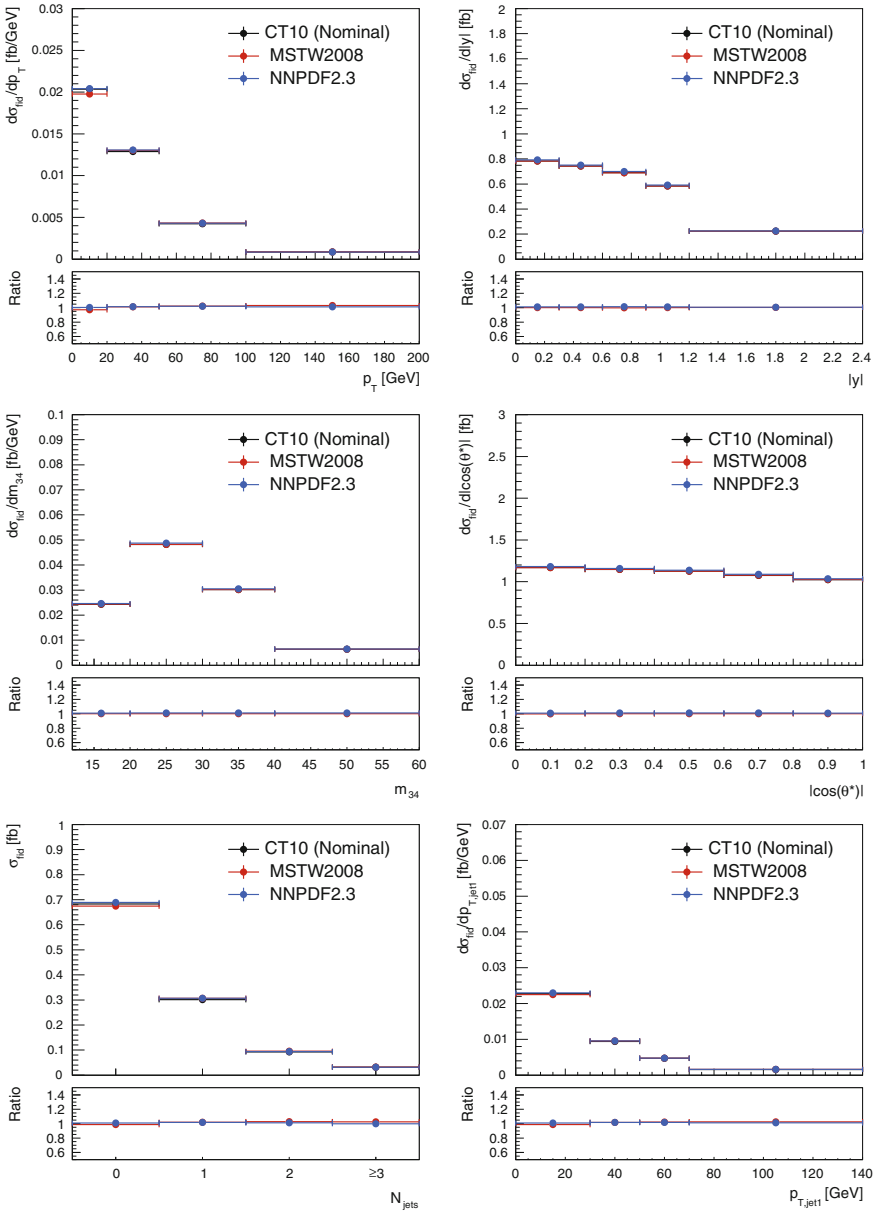

Fig. C.5 Comparisons of the nominal H+1j generated sample (CT10) and the MSTW2008 and NNPDF2.1 PDF variations, for a 125.4 GeV Higgs. The ratio plots underneath are with respect to the nominal (CT10)

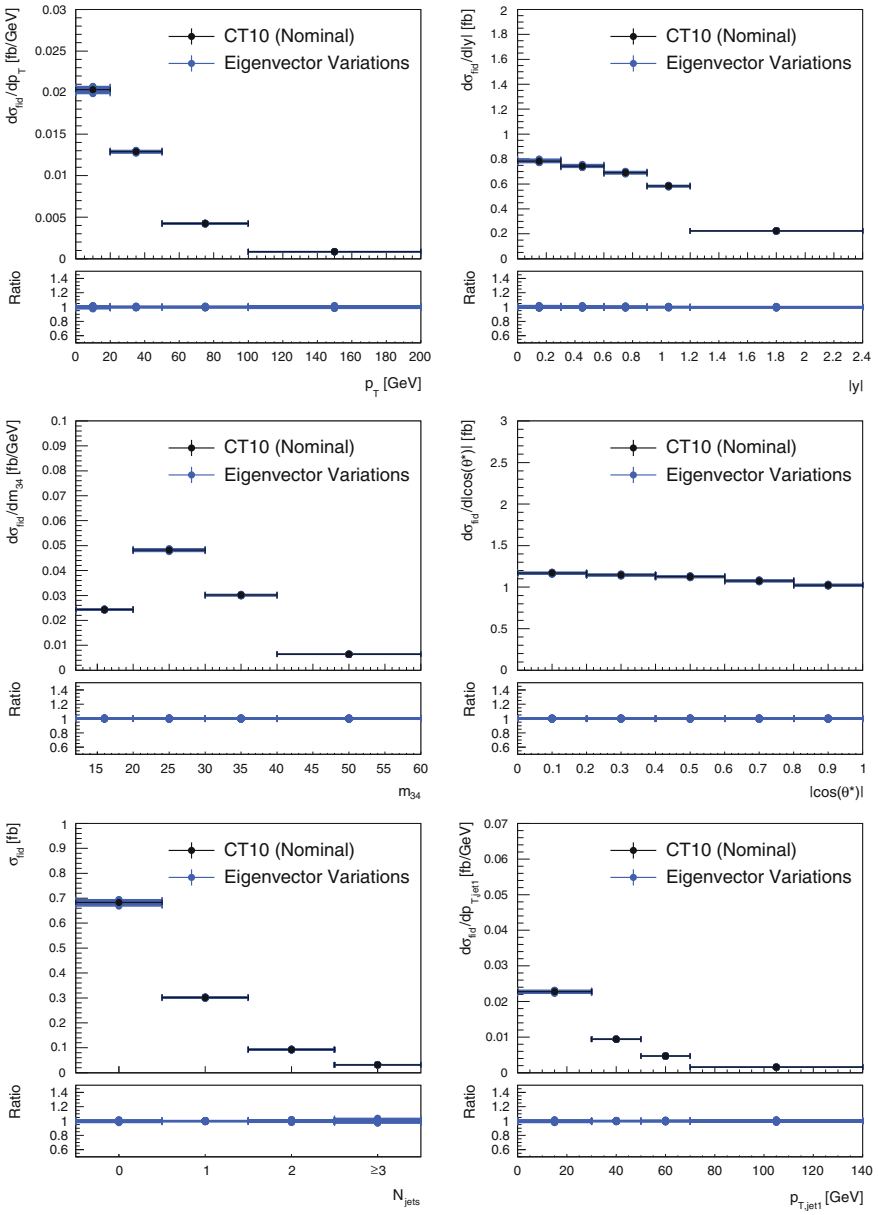

Fig. C.6 Comparisons of the nominal H+1j generated sample and the 52 (26 up and 26 down) CT10 eigenvector variations, for a 125.4 GeV Higgs. The ratio plots underneath are with respect to the nominal eigenvector variation

C.3 Theoretical Differential Predictions from HRes2

Table C.13 Differential cross section in $p_{T4\ell}$ and theoretical uncertainties for the Higgs ggF process based on the HRES2 prediction (fb/GeV). MC statistical uncertainties are taken from the statistical error on the nominal sample. The total error is calculated as described in the text

$p_{T4\ell}$ [GeV]	$0 < p_{\mathrm{T}} < 20$	$20 < p_{\mathrm{T}} < 50$	$50 < p_{\mathrm{T}} < 100$	$100 < p_{\mathrm{T}} < 200$
Diff xsec	0.0229	0.0142	0.0038	0.0006
MC stat	1.7%	1.5%	2.8%	2.8%
Scale up	9.6%	10.6%	17.3%	22.9%
Scale down	6.6%	10.8%	14.6%	19.6%
PDF choice up	4.5%	7.3%	6.9%	5.5%
PDF choice down	2.3%	0.0%	0.0%	0.0%
MSTW eigenvector up	5.9%	0.9%	1.8%	0.8%
MSTW eigenvector down	1.6%	1.8%	1.8%	2.4%
Total err up	12.3%	13.1%	19.0%	23.7%
Total err down	7.4%	11.0%	15.0%	19.9%

Table C.14 Differential cross section in $|y_{4\ell}|$ and theoretical uncertainties for the Higgs ggF process based on the HRES2 prediction (fb/GeV). MC statistical uncertainties are taken from the statistical error on the nominal sample. The total error is calculated as described in the text

$\lvert y_{4\ell}\rvert$	$0 < \lvert y\rvert < 0.3$	$0.3 < \lvert y\rvert < 0.65$	$0.65 < \lvert y\rvert < 1.0$	$1.0 < \lvert y\rvert < 1.4$	$1.4 < \lvert y\rvert < 2.4$
Diff xsec	0.8024	0.7748	0.6993	0.6183	0.2278
MC stat	2.6%	2.6%	3.1%	3.2%	2.5%
Scale up	11.6%	11.3%	13.6%	10.4%	11.8%
Scale down	10.4%	10.2%	9.3%	10.4%	9.0%
PDF choice up	7.1%	5.6%	8.3%	5.8%	5.7%
PDF choice down	0.6%	1.1%	0.0%	2.0%	0.0%
MSTW up	6.0%	3.5%	8.4%	3.0%	6.2%
MSTW down	1.5%	2.8%	0.1%	4.4%	0.7%
Total err up	15.1%	13.4%	18.3%	12.7%	14.7%
Total err down	10.8%	10.9%	9.8%	11.9%	9.4%

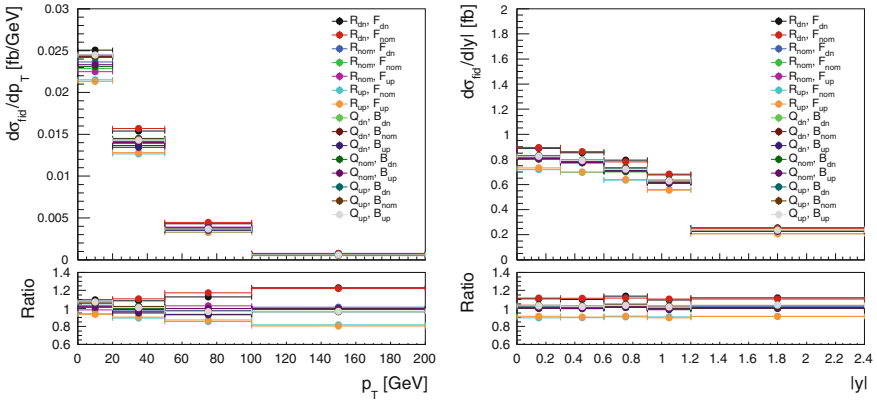

Fig. C.7 Comparisons of the 15 scale variations for a 125.4 GeV Higgs sample generated using HRES2. The ratio plots underneath are with respect to the nominal (R_{nom}, F_{nom})

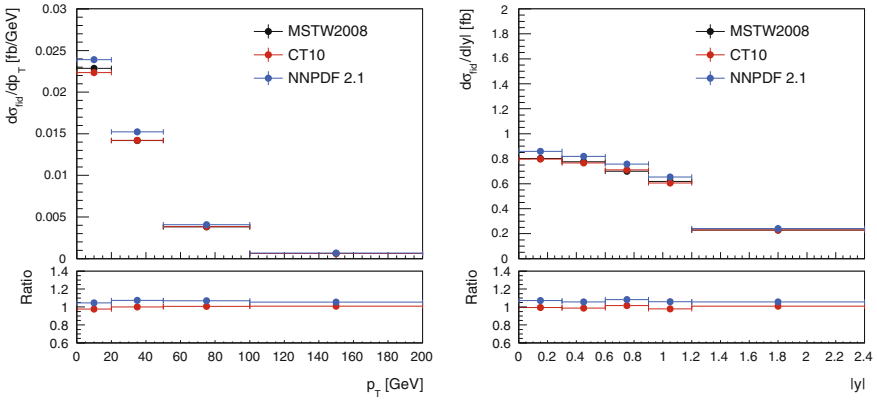

Fig. C.8 Comparisons of the nominal HRES2 generated sample (MSTW) and the CT10 and NNPDF2.1 PDF variations, for a 125.4 GeV Higgs. The ratio plots underneath are with respect to the nominal variation (MSTW2008)

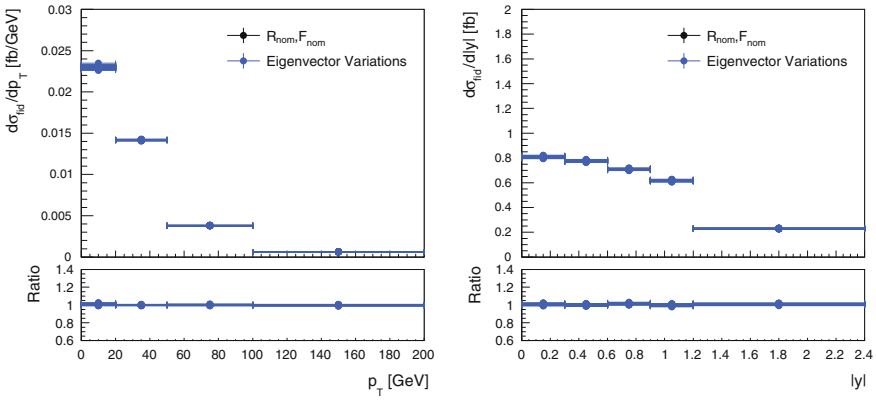

Fig. C.9 Comparisons of the nominal HRES2 generated sample and the 40 (20 up and 20 down) MSTW eigenvector variations, for a 125.4 GeV Higgs. The ratio plots underneath are with respect to the nominal eigenvector variation

Appendix D
WZ Measurement

D.1 Reducible Background Estimates for W^+Z and W^-Z Selection

Table D.1 shows a summary of the Z+jet/$Z\gamma$ fake factor estimate, split into W^+Z and W^-Z channels (the same fake factors described in the previous section are used).

Table D.1 Fake factor final results: the final estimate, split into W^+Z and W^-Z channels

W^+Z					
Channels	eee	$e\mu\mu$	μee	$\mu\mu\mu$	All
$N_{LTT} \cdot F$	$6.83 \pm 0.55 \pm 1.51$	$6.75 \pm 0.55 \pm 1.66$	$3.51 \pm 0.32 \pm 1.94$	$2.85 \pm 0.30 \pm 1.30$	$19.95 \pm 0.89 \pm 4.51$
$N_{TLT} \cdot F$	$0.40 \pm 0.22 \pm 0.12$	–	–	$0.16 \pm 0.10 \pm 0.13$	$0.56 \pm 0.24 \pm 0.18$
$N_{TTL} \cdot F$	$2.13 \pm 0.51 \pm 0.23$	–	–	$1.41 \pm 0.43 \pm 0.25$	$3.54 \pm 0.67 \pm 0.35$
Total	$9.37 \pm 0.78 \pm 1.74$	$6.75 \pm 0.55 \pm 1.66$	$3.51 \pm 0.32 \pm 1.94$	$4.42 \pm 0.53 \pm 1.62$	$24.05 \pm 1.14 \pm 4.90$
W^-Z					
$N_{LTT} \cdot F$	$5.30 \pm 0.48 \pm 1.31$	$7.24 \pm 0.56 \pm 1.75$	$2.99 \pm 0.30 \pm 1.52$	$3.37 \pm 0.31 \pm 1.63$	$18.89 \pm 0.85 \pm 4.39$
$N_{TLT} \cdot F$	$0.67 \pm 0.25 \pm 0.13$	–	–	$0.21 \pm 0.10 \pm 0.15$	$0.89 \pm 0.27 \pm 0.20$
$N_{TTL} \cdot F$	$0.59 \pm 0.37 \pm 0.09$	–	–	$0.70 \pm 0.35 \pm 0.13$	$1.29 \pm 0.51 \pm 0.16$
Total	$6.57 \pm 0.65 \pm 1.50$	$7.24 \pm 0.56 \pm 1.75$	$2.99 \pm 0.30 \pm 1.52$	$4.28 \pm 0.48 \pm 1.88$	$21.07 \pm 1.03 \pm 4.71$

Table D.2 shows a summary of the $t\bar{t}$ estimate, split into W^+Z and W^-Z channels.

Table D.3 shows a full summary of results and statistical/systematic uncertainties, broken down into W^+Z and W^-Z channels. The last column indicates whether a

K. Brendlinger, *Physics with Electrons in the ATLAS Detector*, Springer Theses,
https://doi.org/10.1007/978-3-319-73930-4

Table D.2 $t\bar{t}$ final results: the final estimate, split into W^+Z and W^-Z channels

W^+Z					
Channels	eee	$e\mu\mu$	μee	$\mu\mu\mu$	Total
$t\bar{t}$ MC×SF, μ-fake	0.00 ± 0.00	1.09 ± 0.37	0.27 ± 0.19	2.25 ± 0.56	3.62 ± 0.69
$t\bar{t}$ MC×SF, e-fake	0.58 ± 0.16	0.08 ± 0.06	0.60 ± 0.17	0.00 ± 0.00	1.26 ± 0.24
$t\bar{t}$ MC×SF, total	0.58 ± 0.16	1.17 ± 0.37	0.87 ± 0.25	2.25 ± 0.56	4.88 ± 0.73
μ-fake uncertainty	0.00	0.39	0.10	0.80	1.28
e-fake uncertainty	0.35	0.05	0.36	0.00	0.76
W^-Z					
$t\bar{t}$ MC×SF, μ-fake	0.00 ± 0.00	0.74 ± 0.28	0.54 ± 0.27	1.33 ± 0.44	2.61 ± 0.59
$t\bar{t}$ MC×SF, e-fake	0.65 ± 0.18	0.46 ± 0.16	0.55 ± 0.17	0.00 ± 0.00	1.67 ± 0.29
$t\bar{t}$ MC×SF, total	0.65 ± 0.18	1.21 ± 0.32	1.10 ± 0.32	1.33 ± 0.44	4.28 ± 0.66
μ-fake uncertainty	0.00	0.26	0.19	0.47	0.92
e-fake uncertainty	0.39	0.28	0.33	0.00	1.00

Table D.3 Summary of Z+jet/$Z\gamma$ and $t\bar{t}$ yields and systematics, split into W^+Z and W^-Z. The last column details whether the uncertainty is assumed to be 100% correlated across W^+Z and W^-Z channels

	W^+Z					W^-Z					
Channels	eee	$e\mu\mu$	μee	$\mu\mu\mu$	All	eee	$e\mu\mu$	μee	$\mu\mu\mu$	All	Correlation
Z+jet/$Z\gamma$	9.37	6.75	3.51	4.42	24.05	6.57	7.24	2.99	4.28	21.07	–
$t\bar{t}$	0.58	1.17	0.87	2.25	4.88	0.65	1.21	1.10	1.33	4.28	–
Total yield	9.95	7.92	4.38	6.67	28.93	7.22	8.45	4.09	5.61	25.35	–
ZCR stat (data, MC)	0.78	0.55	0.32	0.53	1.14	0.65	0.56	0.30	0.48	1.03	No
Z FF WZ subtraction	0.87	0.81	1.28	1.10	4.05	0.72	0.85	1.01	1.27	3.85	Yes
ZCR WZ subtraction	0.14	0.05	0.01	0.05	0.26	0.11	0.04	0.01	0.04	0.19	Yes
Z muon FF stat	–	–	1.94	1.62	3.54	–	–	1.52	1.88	3.41	Yes
Z electron FF stat	1.74	1.66	–	–	3.38	1.50	1.75	–	–	3.25	Yes
Composition/closure (μ)	0.00	0.00	0.92	1.08	2.00	–	–	0.76	1.06	1.82	Yes
Composition/closure (ele)	3.52	2.53	0.00	0.00	6.04	2.57	2.70	–	–	5.28	Yes
Z FF $t\bar{t}$ μ SF MC+data stat	–	–	0.06	0.20	0.26	–	–	0.07	0.19	0.26	Yes
Z FF $t\bar{t}$ ele SF MC+data stat	0.18	0.07	–	–	0.25	0.19	0.07	–	–	0.26	Yes
ZCR $t\bar{t}$ region extrapolation	0.05	0.01	0.02	0.03	0.11	0.05	0.01	0.02	0.03	0.11	
$t\bar{t}$ MC stat	0.16	0.37	0.25	0.56	0.73	0.18	0.32	0.32	0.44	0.66	No
$t\bar{t}$ region mu SF MC+data stat	–	0.39	0.10	0.80	1.28	–	0.26	0.19	0.47	0.92	Yes
$t\bar{t}$ region ele SF MC+data stat	0.35	0.05	0.36	–	0.76	0.39	0.28	0.33	0.00	1.00	Yes
$t\bar{t}$ region extrapolation	0.02	0.03	0.01	0.03	0.09	0.02	0.03	0.01	0.02	0.08	
Total uncertainty	4.12	3.23	2.56	2.51	9.23	3.17	3.41	2.06	2.64	8.47	–
Total uncertainty (%)	41.4	40.8	58.5	37.6	31.9	43.9	40.4	50.4	47.0	33.4	–

given uncertainty should be treated as correlated between W^+Z and W^-Z, for the purposes of the W^+Z/W^-Z ratio measurement.

D.2 W^+Z and W^-Z Production Cross Section Results

Table D.4 Fiducial cross section results for W^+Z and W^-Z

$\sigma^{\text{fid.}}_{W^+Z\to\ell'\nu\ell\ell}$					
e^+ee	28.0	19.2	11.2	2.4	22.3
μ^+ee	32.2	14.4	5.0	2.4	15.3
$e^+\mu\mu$	45.0	12.1	4.6	2.3	13.1
$\mu^+\mu\mu$	36.5	11.6	4.1	2.3	12.5
Combined	36.7	6.7	3.9	2.3	8.1
SM prediction	31.8	—	—	—	5.8
$\sigma^{\text{fid.}}_{W^-Z\to\ell'\nu\ell\ell}$					
e^-ee	22.5	21.0	10.5	2.4	23.6
μ^-ee	22.9	17.5	5.8	2.4	18.5
$e^-\mu\mu$	30.2	15.2	6.9	2.3	16.8
$\mu^-\mu\mu$	27.1	13.7	5.0	2.4	14.7
Combined	26.1	8.1	4.7	2.4	9.6
SM prediction	21.6	—	—	—	7.9

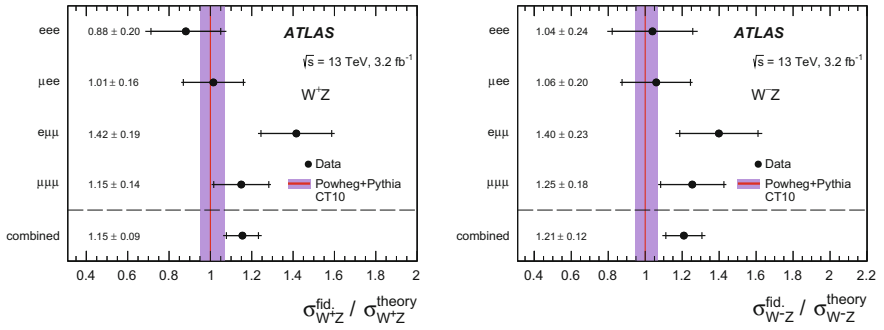

Fig. D.1 Separate W^+Z and W^-Z cross section comparisons with the NLO prediction, presented channel-by-channel and in total

D.3 Modeling of N_{jets} Distributions in Reducible Backgrounds

In order to calculate unfolded differential WZ N_{jets} distributions, the N_{jets} distributions of the Z+jet/$Z\gamma$ and $t\bar{t}$ reducible backgrounds must be estimated. The Fake Factor Method predicts kinematic distributions (including N_{jets}) for the Z+jet/$Z\gamma$ background; likewise, the procedure developed to estimate $t\bar{t}$ in the SR can also give an estimate of N_{jets} for its target background. These estimates are summarized in Tables D.5 and D.6 for jets within $|\eta| < 4.5$ and $|\eta| < 2.5$, respectively. This section describes the tests performed to validate the N_{jets} distributions for these processes.

In the Z+jet/$Z\gamma$ Fake Factor procedure, events weighted by the p_{T}-dependent fake factor can be used to estimate kinematic distributions. If the variable in question has no correlation with fake leptons in the event, then events in the ZCR weighted by the fake factor should faithfully reproduce the shape and normalization of the distribution. However, since the type of jet(s) produced in association with the Z boson can influence both the N_{jets} distribution and the composition of the fake lepton, it is possible that the procedure would fail to reproduce the correct N_{jets} distribution. Fixing this problem would require understanding and correcting for the correlation between N_{jets} and the fake factors of different fake composition components. Thus, the nominal procedure's ability to reproduce the correct N_{jets} distribution should be explicitly tested.

To validate the N_{jets} distribution predicted by the Fake Factor Method, the MC closure test of Sect. 8.5.2.3 is extended by comparing the N_{jets} distribution produced by the all-MC Fake Factor procedure to the out-of-the-box MC N_{jets} distribution. Figure D.2 shows the comparison (with jets defined up to $|\eta| < 4.5$); the distributions are compatible within statistical error. Other corrections to the Fake Factor method, such as the WZ/ZZ subtraction component and the $t\bar{t}$ subtraction component, are small (we will comment on the $t\bar{t}$ component below). Based on this test we conclude that the Fake Factor method should adequately describe the N_{jets} distribution of

Table D.5 Estimates of $t\bar{t}/Wt/WW$ (using the top CR) and of $Z + j/Z\gamma$ (using the FF method) in exclusive jet multiplicity bins. Jets have $|\eta| < 4.5$. Only statistical uncertainties are shown

$\|\eta\| < 4.5$	0 jets	1 jet	2 jets	3 jets	$\geqslant 4$ jets
$t\bar{t}/Wt/WW$	0.65 ± 0.26	2.87 ± 0.52	2.66 ± 0.53	1.29 ± 0.35	1.68 ± 0.48
$Z + j/Z\gamma$	16.99 ± 0.88	13.36 ± 0.85	8.56 ± 0.69	4.09 ± 0.51	2.12 ± 0.36

Table D.6 Estimates of $t\bar{t}/Wt/WW$ (using the top CR) and of $Z + j/Z\gamma$ (using the FF method) in exclusive jet multiplicity bins. Jets have $|\eta| < 2.5$. Only statistical uncertainties are shown

$\|\eta\| < 2.5$	0 jets	1 jet	2 jets	3 jets	$\geqslant 4$ jets
$t\bar{t}/Wt/WW$	0.69 ± 0.26	3.16 ± 0.54	3.13 ± 0.60	1.23 ± 0.36	0.95 ± 0.34
$Z + j/Z\gamma$	18.73 ± 0.92	13.70 ± 0.87	7.92 ± 0.68	3.16 ± 0.46	1.61 ± 0.31

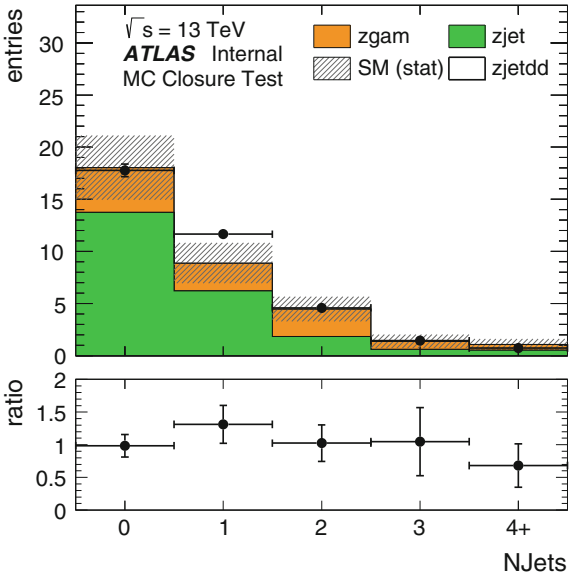

Fig. D.2 The Z+jet/$Z\gamma$ Fake Factor closure test, extended to validate the method's ability to predict the N_{jets} distribution. The "data" (labeled "zjetdd") is the Fake Factor prediction based on events in the ZCR, weighted by the Fake Factor, in an MC-only procedure. The stacked MC (Z+jet and $Z\gamma$) represents the out-of-the box MC Z+jet/$Z\gamma$ estimate in the SR. The Fake Factor Method models the N_{jets} distribution well according to this test

Z+jet/$Z\gamma$ in the SR, and thus we assign no further uncertainty on the shape of the distribution.

The procedure to estimate $t\bar{t}$ by normalizing MC in dedicated control regions can also be used to predict the $t\bar{t}$ N_{jets} distribution. In this procedure, the N_{jets} distribution is taken directly from MC (weighted by the data-MC scale factors derived in the $t\bar{t}$ control regions). To validate the MC modeling of the N_{jets} distributions, we can check the agreement with data in the $t\bar{t}$ control regions.

Figure D.3 compares the N_{jets} distributions in both the top-CR||ZCR and the top-CR||SR, for both e-fake and μ-fake channels. Jets are defined up to $|\eta| < 4.5$. Focusing on the top-CR||ZCR, we find good agreement between the shapes of the MC and the data, within statistical errors. Though the statistics of the top-CR||SR are limited, the general N_{jets} shape of data events in that region is also compatible with MC. Based on these validation plots, we conclude that the MC adequately describes the $t\bar{t}$ N_{jets} distribution, and therefore no additional shape uncertainties are considered. The agreement in the top-CR||ZCR also supports the assertion that shape uncertainties associated with the $t\bar{t}$ subtraction component in the Fake Factor procedure are also small.

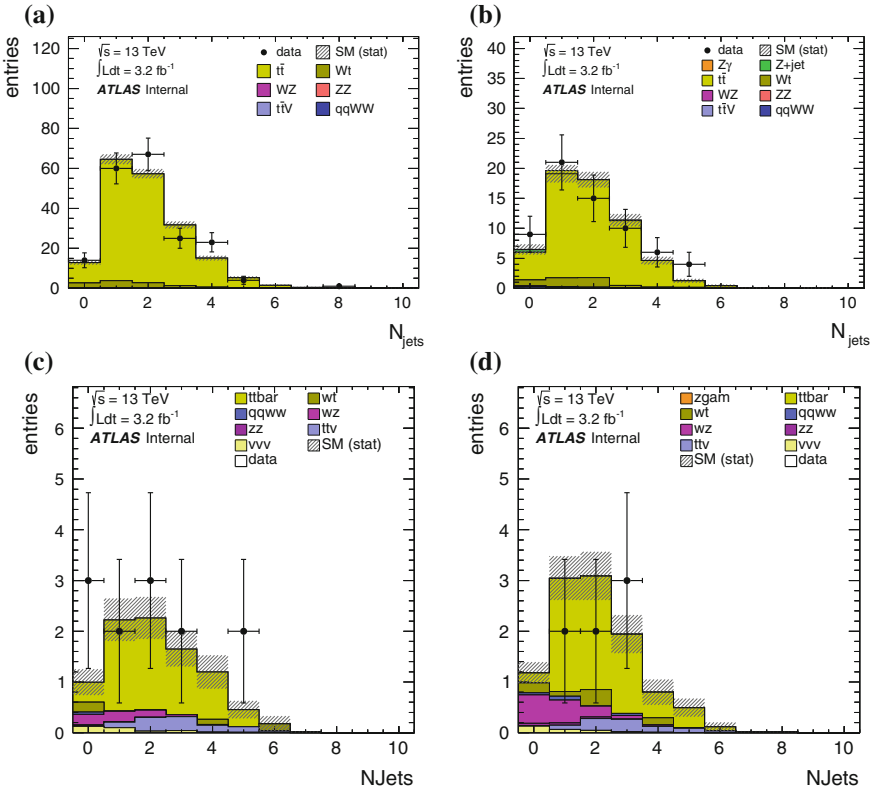

Fig. D.3 Top: Data-MC agreement of the N_{jets} distribution in the $t\bar{t}$ control regions. The $\mu^{\pm}e^{\mp}\mu^{\pm}$ $+\mu^{\pm}\mu^{\pm}e^{\mp}$ channels of the top-CR||ZCR (**a**), and the $e^{\pm}e^{\pm}\mu^{\mp}$ $+e^{\pm}\mu^{\mp}e^{\pm}$ channels of the top-CR||ZCR (**b**) are shown, combining the LTT, TLT and TTL regions within each channel. The $\mu^{\pm}e^{\mp}\mu^{\pm}$ $+\mu^{\pm}\mu^{\pm}e^{\mp}$ channels of the top-CR||SR (**c**) and the $e^{\pm}e^{\pm}\mu^{\mp}$ $+e^{\pm}\mu^{\mp}e^{\pm}$ channels of the top-CR||SR (**d**) are also shown. The $t\bar{t}$ MC is not corrected by the data-MC scale factor in these plots

D.4 Result of WZ Unfolded N_{jets} Distribution

Figures D.4 and D.5 show N_{jets}-related reconstruction-level results and the unfolded N_{jets} distribution.

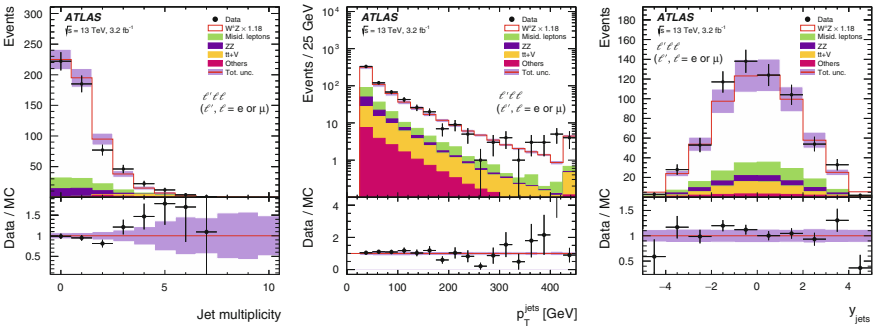

Fig. D.4 Reconstruction-level jet distributions in the WZ signal region. Left: jet multiplicity; center: the p_T of the jets, where every jet in the event is plotted; right: the rapidity of the jets, where again every jet in the event is represented

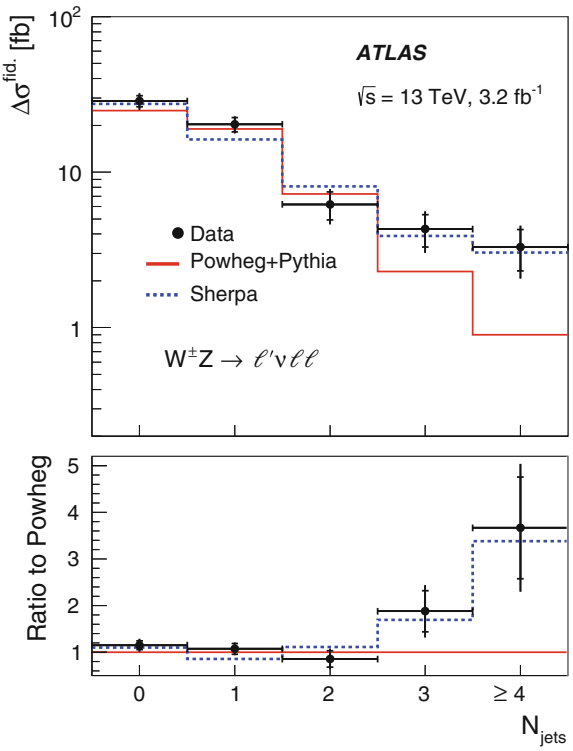

Fig. D.5 The unfolded WZ fiducial differential N_{jets} distribution [1]

Reference

1. ATLAS Collaboration, Measurement of the $W^{\pm}Z$ boson pair-production cross section in pp collisions at $\sqrt{s} = 13$ TeV with the ATLAS detector. Phys. Lett. **B762**, 1–22 (2016), arXiv:1606.04017 [hep-ex]